



**Rapid Phase-contrast Magnetic
Resonance Imaging Using Spiral
Trajectories and Parallel Imaging**

Jennifer Anne Steeden

A dissertation submitted in partial fulfillment of the
requirements for the degree of
Doctor of Philosophy
of
University College London.

Department of Medical Physics and Bioengineering University
College London
2010

I, Jennifer Anne Steeden confirm that the work presented in this thesis is my own.
Where information has been derived from other sources, I confirm that this has been
indicated in the thesis.

A handwritten signature in black ink, appearing to read "J Steeden", with a long horizontal flourish extending to the right.

ABSTRACT

Phase contrast (PC) MRI is a proven method of measuring blood flow in the clinical environment. Traditionally, PCMR data is acquired using cardiac gated Cartesian sequences. However, these sequences are time consuming and difficult to perform in patients with irregular heart rates. The work of my thesis covers three alternative PC sequences, all using undersampled spiral sequences with SENSE reconstruction algorithms.

The first piece of work investigates real-time spiral PCMR. The spiral flow sequence was validated at rest by comparing stroke volumes in the aorta of healthy volunteers, against a retrospectively gated Cartesian sequence. By combining flow data with simultaneous blood pressure measurements during exercise, this sequence was used to quantify the hemodynamic response to physical stress.

The second piece of work investigates improvements in spatial or temporal resolution for real-time PCMR, by splitting the acquisition of flow-compensated and flow-encoded data into separate short blocks. The data is then retrospectively matched in cardio-respiratory space, to remove background phase offsets. This sequence was validated (at rest) in an adult population. The improved spatial resolution was shown to provide more accurate flow measurements than standard real-time flow measurements, in a paediatric population.

The third piece of work investigates prospectively triggered spiral PCMR to achieve high spatio-temporal resolution, within a short breath-hold. Flow volumes, regurgitation fraction and shunt ratios were compared from a high spatial-resolution, free breathing retrospectively gated Cartesian sequence with 3 averages (~2.5 minute scan time), a low spatial-resolution breath-hold retrospectively gated Cartesian sequence (~20 second scan time), and the (high spatial-resolution) prospectively triggered spiral sequence (~6 second scan time). It was shown that accurate flow

measurements can be made in the aorta, pulmonary artery and pulmonary branches, within manageable breath-hold times for children and sick adults. This sequence may improve patient compliance and increase patient throughput.

ACKNOWLEDGEMENTS

First and foremost I would like to thank Vivek Muthurangu for all of his help, support and advice over the last two years. His continuous enthusiasm, dedication and never-ending supply of ideas has provided great encouragement and motivation. Vivek has been especially helpful in proof-reading manuscripts and is always pushing me to do the best that I can. Without his help none of these studies would have been possible.

I would also like to thank David Atkinson for his endless support, physics knowledge and for proof-reading all of my long-winded documents. His patience and ability to teach have been greatly appreciated.

In addition I would like to thank the following people for their support and advice during my work: Michael Hansen, for all of his help in the early days; Andrew Taylor, for his continued support and proof-reading of manuscripts; Freddy Odille, for his efficiency and brilliant segmentation tool (which has saved many hours of tedious circle-drawing time); and Peter Gatehouse, for all of his help in anything MRI-related. Furthermore, I would like to thank the radiographers at ICH, who have helped with scanning during these 3 years: Wendy Norman, Rod Jones, Catherine Bull and Romina Linton.

I am also grateful to all of the volunteers and patients who have taken part in the studies described in this thesis, and to the British Heart Foundation for providing financial support towards the running of the scanner. Additional thanks must go to EPSRC for funding my PhD.

Last, but by no means least, I would like to thank Mike and my family, without whom none of this would have been possible. And of course, the Caterham for keeping Mike out of my hair whilst writing my thesis!

CONTENTS

DECLARATION OF ORIGINALITY	3
ABSTRACT	3
ACKNOWLEDGEMENTS	5
CONTENTS	6
LIST OF FIGURES	13
LIST OF TABLES	24
LIST OF ABBREVIATIONS	26
CHAPTER 1 Principles of Magnetic Resonance Imaging	28
1.1 Introduction	29
1.2 Nuclear Magnetic Resonance	30
1.2.1 Quantum Mechanics Description of NMR.....	30
1.2.2 Classical Description of NMR.....	34
1.2.2.1 Rotating Frame of Reference	36
1.2.2.2 RF-Pulses	36
1.2.2.3 Signal Detection	38
1.3 Magnetic Resonance Imaging	39
1.3.1 Spatial Encoding.....	39
1.3.2 K-space	39
1.3.3 Pulse Sequences.....	41
1.3.4 Slice Selection	41
1.3.5 Fourier Imaging.....	42

1.3.5.1	Frequency-Encoding	42
1.3.5.2	Phase-Encoding.....	43
1.3.5.3	General Localization	43
1.3.6	K-space Trajectories	44
1.3.7	Spiral Trajectories	45
1.3.8	Gridding.....	48
1.4	Parallel Imaging	50
1.4.1	Coil Sensitivities.....	51
1.4.2	SENSE.....	53
1.4.2.1	Cartesian SENSE.....	54
1.4.2.2	Non-Cartesian SENSE	55
1.4.2.3	Regularization	60
1.4.2.4	Preconditioning	61
1.5	Cardiac Imaging	63
1.5.1	Respiratory Motion.....	63
1.5.2	Cardiac Motion.....	64
1.6	Flow Measurements	67
1.6.1	Implementation of Phase-Contrast Imaging.....	68
1.6.2	Accuracy of PCMR	70
1.6.3	Concomitant Gradients in Flow Imaging	73
1.6.4	Additional Phase Offsets	74
CHAPTER 2 Real-time Flow Measurements		76
2.1	Introduction	77
2.1.1	Aims	79
2.1.2	Personal Contribution.....	79
2.2	Literature Review	81
2.2.1	Real-time Flow Measurements.....	81
2.2.1.1	Efficient Trajectories.....	81
2.2.1.2	Parallel Imaging	84
2.2.2	Performing MRI During Exercise	87
2.2.3	Measurement of Ventricular Function During Exercise	91
2.2.4	Assessment of Hemodynamic Parameters Using MRI	94

2.2.4.1	Measuring Vascular Resistance Using MRI	95
2.2.4.2	Measuring Vascular Compliance Using MRI	96
2.2.5	Summary.....	96
2.3	Development	98
2.3.1	Real-time PCMR Sequence	98
2.3.1.1	Spiral Sequence	98
2.3.1.2	Flow Encoding	101
2.3.1.3	Data Undersampling.....	102
2.3.2	SENSE Reconstruction.....	103
2.3.2.1	Calculation of Coil Sensitivity Information	104
2.3.3	Concomitant Gradient Correction	107
2.3.4	Residual Phase Offsets	108
2.3.5	Optimisation of Sequence Parameters.....	110
2.3.6	Development of OsiriX Plug-ins	112
2.3.6.1	Analysis of Flow Data.....	112
2.3.6.2	Analysis of Hemodynamic Parameters	114
2.4	In-vitro Validation.....	116
2.4.1	Standard Flow Sequence	116
2.4.2	Real-time Spiral Sequence	117
2.4.3	Image Analysis	118
2.4.4	In-vitro Results	119
2.4.4.1	Flow Assessment.....	119
2.4.4.2	Image Quality.....	121
2.5	In-vivo Experiments	122
2.5.1	Study Population	122
2.5.2	MR Protocol	122
2.5.2.1	Standard Flow Assessment.....	124
2.5.2.2	Real-time Flow Assessment.....	125
2.5.2.3	Real-time Volume Assessment	126
2.5.3	Data Analysis.....	127
2.5.4	Image Quality	127
2.5.5	In-vivo Validation	128
2.5.6	Vascular Response To Exercise	130
2.6	Discussion	133

2.6.1	Hemodynamic Response to Exercise	134
2.6.2	Limitations.....	135
2.6.3	Conclusion.....	135
2.7	Automatic Segmentation Propagation of Real-Time PCMR	136
2.8	Hemodynamic Response To Mental Stress Using Real-time PCMR	141
2.9	Clinical Use	144
CHAPTER 3 Split-Acquisition Flow Measurements		145
3.1	Introduction	146
3.1.1	Aims	147
3.1.2	Personal Contribution.....	147
3.2	Literature Review	148
3.2.1	Reference-less Flow Measurements.....	148
3.2.2	Splitting the Acquisition of Flow Data.....	150
3.2.3	Matching MR images	152
3.2.4	Summary.....	153
3.3	Development	154
3.3.1	Split-acquisition Scheme	154
3.3.2	Matching Technique.....	155
3.3.3	Development of Image Quality Assessment Tools	157
3.3.3.1	Calculation of Estimated SNR	158
3.3.3.2	Calculation of Estimated VNR.....	158
3.3.3.3	OsiriX Plug-in Implementation	159
3.3.3.4	Calculation of Edge Sharpness.....	161
3.4	Optimisation of Sequence Parameters.....	162
3.4.1	In-vitro Validation	163
3.5	Adult Protocol	165
3.5.1	Cardiac Gated PCMR	166
3.5.2	Interleaved Spiral Real-time PCMR.....	166
3.5.3	Split-acquisition Real-time CINE PCMR	166
3.5.4	Experiments.....	168
3.5.5	Data Analysis.....	168
3.6	Accuracy of Matching.....	169

3.6.1	‘Simulated Split-acquisition’ Reconstruction.....	169
3.6.1.1	Results	170
3.6.2	Importance of Matching	172
3.6.2.1	Results	172
3.7	Image Quality	175
3.8	In-vivo Validation	178
3.9	Paediatric Utility	181
3.9.1	Paediatric Results	182
3.10	Discussion	184
3.10.1	Accuracy of Matching	184
3.10.2	Image Quality	185
3.10.3	Adult In-vivo Validation	185
3.10.4	Paediatric Utility.....	186
3.10.5	Advantages of Split-acquisition PCMR	186
3.10.6	Limitations.....	187
3.10.7	Conclusion.....	188
CHAPTER 4 Rapid Gated Flow Measurements		189
4.1	Introduction	190
4.1.1	Aims	191
4.1.2	Personal Contribution.....	191
4.2	Literature Review	193
4.2.1	Summary.....	200
4.3	Development	201
4.3.1	Cardiac Triggering.....	201
4.3.2	Stimulated Echo’s.....	202
4.3.3	Automating the UI.....	205
4.3.4	Analysis of Flow Data	207
4.3.5	SNR measurements	209
4.3.6	Edge sharpness	212
4.3.7	Residual Background Phase Correction	214
4.3.8	Recording Physiological Data	221
4.4	Optimisation of Sequence Parameters.....	222

4.4.1	Interleave Ordering.....	222
4.5	In-vitro Validation.....	224
4.5.1	In-vitro protocol.....	224
4.5.2	Image Analysis.....	224
4.5.3	In-vitro Results.....	225
4.6	In-vivo Protocol.....	228
4.6.1	Patient population.....	228
4.6.2	MR protocol.....	229
4.6.2.1	Reference Free-breathing Sequence.....	230
4.6.2.2	Standard Breath-hold Sequence.....	230
4.6.2.3	Spiral SENSE Breath-hold Sequence.....	230
4.6.3	Image Analysis.....	231
4.6.4	Statistical analysis.....	232
4.7	In-vivo Results.....	233
4.7.1	Physiological Data.....	233
4.7.2	Functional Assessment.....	235
4.8	Image Quality.....	245
4.9	Discussion.....	247
4.9.1	Spiral SENSE PCMR.....	247
4.9.2	Comparison of sequences.....	248
4.9.3	Image quality.....	248
4.9.4	Limitations.....	249
4.9.5	Conclusion.....	249
CHAPTER 5 Conclusions and Future Work		250
5.1	Summary.....	251
5.2	Future Work.....	253
5.2.1	Reducing the FOV.....	253
5.2.1.1	Improved Coil Configurations.....	254
5.2.1.2	RF-Shielding.....	254
5.2.1.3	Spatially-selective RF-pulses.....	255
5.2.1.4	Saturation bands.....	256
5.2.2	Speeding up the Reconstruction.....	256

5.2.3	4D Flow Measurements.....	258
5.2.4	Fourier Velocity Encoding and Fourier Acceleration Encoding.....	261
5.3	Conclusion.....	263
REFERENCES		264
APPENDIX 1		279
APPENDIX 2		287
APPENDIX 3		295
APPENDIX 4		303
APPENDIX 5		311

LIST OF FIGURES

Figure 1.1: Zeeman splitting for a spin- $\frac{1}{2}$ system.....	32
Figure 1.2: Magnetic moment vectors. Top: spins precess with random phase, bottom; spins align in direction of an external magnetic field.....	33
Figure 1.3: Precession of the spin-vector about a static magnetic field.....	34
Figure 1.4: Free induction decay simulated in MATLAB.....	38
Figure 1.5: Effect of gradients on the precessional frequency of spins. a) In a constant field all of the spins precess at the same frequency – there is no difference in the phase of the MR signal. b) When a linear gradient is applied, the precessional frequency is dependent on position – the phase of the MR signal is proportional to the spins position.....	40
Figure 1.6: Slice selection; an RF-pulse is applied simultaneously with a linear gradient on the z-axis	41
Figure 1.7: a) Sequence diagram of a basic Cartesian gradient echo sequence. b) Corresponding k-space trajectory	42
Figure 1.8: Common k-space trajectories; a) Cartesian, b) EPI, c) Radial, d) Spiral	45
Figure 1.9: Example of an efficient spiral trajectory. The gradients are slew- rate limited in the centre of k-space, and gradient amplitude limited at the edge of k-space.....	47
Figure 1.10: Undersampling of Cartesian k-space data a) Fully sampled data, b) corresponding 2-fold undersampled data.....	50
Figure 1.11: Simulated effect of Cartesian undersampling, performed in MATLAB.....	50
Figure 1.12: Basic Cartesian SENSE by direct unfolding. Simulation made in MATLAB.....	55
Figure 1.13: Undersampling of spiral k-space data a) Fully sampled data, b) corresponding 2-fold undersampled spiral data	56

Figure 1.14: Simulated effect of spiral undersampling, performed in MATLAB.....	56
Figure 1.15: Implementation of iterative CG image reconstruction	59
Figure 1.16: Prospective Cardiac gating; the RR-interval is divided into sub-sections	64
Figure 1.17: Data acquisition in; a) prospective ECG gating, b) retrospective ECG gating. In both sequences, one segment is acquired repeatedly in each R-wave. On detection of an R-wave the segment is changed.....	66
Figure 1.18: A balanced bipolar gradient causes a phase shift which is proportional to the velocity of the spins.....	68
Figure 1.19: Example of a Cartesian PC sequence. Each line is acquired with flow-compensated and flow-encoded gradients before moving to the next line in k-space.....	70
Figure 1.20: Example of a PC data in the ascending aorta of a healthy volunteer.....	70
Figure 1.21: From Greil, et al. (40). A linear relationship was found between the number of pixels in the vessel of interest and the percentage flow error.....	72
Figure 2.1: From Lurz, et al. (86). Agreement in RV to LV stroke volumes for; a) standard real-time and b) radial k-t real-time sequences.....	93
Figure 2.2: A sequence diagram showing the interleaved flow-compensated and flow-encoded readouts for one spiral interleave	101
Figure 2.3: The sequence->special tab on the UI contains user-defined parameters, including the desired acceleration factor, the regularisation factor (λ) and reconstruction limit (ϵ).....	102
Figure 2.4: Calculation of coil sensitivity information from an undersampled spiral sequence (SENSE $\times 4$). The coil sensitivities are calculated by dividing of the filtered average image for each coil by the homogeneous image.....	105
Figure 2.5: A Tukey filter, simulated in MATLAB.....	106
Figure 2.6: Effect of Maxwell correction on water phantoms imaged with 12 spiral interleaves, undersampled by a factor of 2, VENC = 100cm/s. Note the different scales	108

Figure 2.7: Residual phase offsets (after Maxwell correction) from an oblique slice in a water phantom, VENC: 100cm/s. Effect of varying; a) TE, b) rise time (RT) of the flow-encoding gradients. Values in brackets give the actual TE	109
Figure 2.8: Acquisition of data for the optimised sequence with 8 spiral interleaves, undersampled by a factor of 4. — represents flow-compensated data, and \sim represents flow-encoded data. Note the rotation of the spiral interleaves	111
Figure 2.9: Resultant image quality from the optimised sequence in a resolution phantom (circular object on left of image), with a bottle of oil (square object on right of image).....	112
Figure 2.10: In-house plug-in developed for analysis of real-time flow data using OsiriX	114
Figure 2.11: Figure from (63). Calculation of compliance, by optimisation of two-element Windkessel model	115
Figure 2.12: Photograph of rubber tubing vessel phantom used for in-vitro validation.....	116
Figure 2.13: Comparison of flow profiles in-vitro.....	119
Figure 2.14: Example of data analysis for real-time sequence using the OsiriX plug-in	120
Figure 2.15: Comparison of pump output in-vitro between the reference flow sequence and real-time flow sequence. a) Correlation of flow measured from both techniques. b) Bland-Altman plot of the difference in flow measured using both techniques.....	120
Figure 2.16: Examples of images acquired in-vitro from; a) the standard PCMR sequence and b) the real-time sequence.....	121
Figure 2.17: Photograph of a subject performing exercise on the ergometer, within the MRI scanner at ICH	123
Figure 2.18: Coils used for imaging in-vivo; one body-matrix coil on top of the subject, and one underneath	123
Figure 2.19: Figure from (63). The timeline of the MRI protocol at rest and during each exercise level	124
Figure 2.20: Figure from (63). Magnitude (top) and phase (bottom) images from; a) reference gated flow sequence at rest, b) real-time flow	

sequence at rest, and c) real-time flow sequence during exercise at 8W	128
Figure 2.21: Figure from (63). Comparison of aortic stroke volumes from reference standard PCMR and real-time spiral PCMR, at rest. a) Correlation of flow measured from both techniques. b) Bland-Altman plot of the difference in flow measured using both techniques.....	129
Figure 2.22: Comparison of stroke volumes in-vivo, at rest calculated from real-time k-t SENSE (LV stroke volume) and real-time spiral PCMR (aortic stroke volume). a) Correlation of flow measured from both techniques. b) Bland-Altman plot of the difference in flow measured using both techniques	129
Figure 2.23: Comparison of stroke volumes in-vivo, at 8W of exercise calculated from real-time k-t SENSE (LV stroke volume) and real-time spiral PCMR (aortic stroke volume). a) Correlation of flow measured from both techniques. b) Bland-Altman plot of the difference in flow measured using both techniques	130
Figure 2.24: Measured responses to exercise. All points are mean values, and standard deviation is shown with error bars. Effect of exercise on a) heart rate, b) stroke volume, c) cardiac output, d) systolic BP, e) diastolic BP, f) mean BP, g) systemic vascular resistance, and h) arterial compliance. Figures a)c)g)h) from (63)	132
Figure 2.25: Figure from (105). Example of manual and semi-automatic segmentations from two observers, at rest (a, b) and during exercise (c,d). Segmentations are show in a hybrid space-time view (a, c) and in multiple frames (c,d) chosen at times indicated by the red vertical lines	139
Figure 2.26: Figure from (107). A screenshot of the MIST test, showing; a) an example mathematical problem, b) a timer bar, c) possible answers (0-9) and d) feedback box. f) The ‘performance bar’, shows the ‘average’ score e) marked above the bar and the participants score g) below the bar.....	142
Figure 2.27: Flow curve measured using the real-time PCMR sequence, in a subject with an irregular heart rate.....	144

Figure 3.1: From Nielson, et al. (111). Top row shows manually drawn ROI's through the smooth background phase offsets. These images were corrected using a 2 nd order polynomial fit (middle and bottom row)	149
Figure 3.2: Acquisition of flow data for split-acquisition technique	154
Figure 3.3: Effect of the Tukey filter on the magnitude images. a) Magnitude image before Tukey filter, b) Windowed magnitude image after Tukey Filter	155
Figure 3.4: Figure from (109). Pipeline of data acquisition and reconstruction for the proposed split-acquisition real-time CINE PCMR technique	157
Figure 3.5: OsiriX plug-in developed for calculation of estimated SNR and VNR. a) First a ROI drawn in stationary tissue in an average magnitude image. b) The stationary ROI is copied to all magnitude frames (left). A ROI is then drawn in the vessel of interest in the average magnitude image. c) The semi-automatic segmentation tool is used to propagate the segmentation of the vessel through all magnitude frames. Estimated SNR and VNR are calculated in the frame with maximum flow (as indicated on the UI)	160
Figure 3.6: OsiriX plug-in used to calculate edge sharpness	161
Figure 3.7: Examples of image quality in a resolution phantom (circular object on left of image), with a bottle of oil (square object on right of image) from the optimised split-acquisition sequences, a) HTR sequence, b) HSR sequence	163
Figure 3.8: Comparison of flow profiles from the pulsatile flow pump between the four sequences tested	163
Figure 3.9: Comparison of 'conventional' and 'simulated split-acquisition' reconstructions of the same in-vivo data. a) Correlation of flow measured from both reconstruction techniques. b) Bland-Altman plot of the difference in flow measured using both reconstruction techniques	170
Figure 3.10: Figure from (109). Comparison of flow profiles from one interleaved real-time PCMR adult patient data set, reconstructed	

using the ‘conventional’ and ‘simulated split-acquisition’ reconstruction methods	171
Figure 3.11: Comparison of flow profiles from one patient with an irregular heart rate. Top: flow throughout the 6 seconds of interleaved real- time PCMR data (calculated from standard reconstruction). Bottom: Flow profiles as calculated from ‘conventional’ and ‘simulated split-acquisition’ reconstruction methods	171
Figure 3.12: Matching error between a single flow-encoded frame and all flow-compensated frames from both blocks	173
Figure 3.13: Correlation between normalized matching metric and flow error in all adult subjects.....	173
Figure 3.14: Figure from (109). Comparison of image quality from the sequences. Arrows indicate image blurring	175
Figure 3.15: Figure from (109). Comparison of flow profiles from all four sequences in one adult volunteer.....	178
Figure 3.16: Correlation (left) and Bland-Altman analysis (right) of stroke volumes in adult population calculated from: a)-b) cardiac gated PCMR vs. standard real-time PCMR, c)-d) cardiac gated PCMR vs. HTR split-acquisition PCMR, e)-f) cardiac gated PCMR vs. HSR split-acquisition PCMR	179
Figure 3.17: Correlation (left) and Bland-Altman analysis (right) of stroke volumes in paediatric population, calculated from: a)-b) cardiac gated PCMR vs. standard real-time PCMR, c)-d) cardiac gated PCMR vs. HSR split-acquisition PCMR	183
Figure 4.1: From paediatric study by Beerbaum, et al. (123). Comparison of stroke volumes in the aorta for the reference sequence vs. SENSE $\times 2$ sequence; a) Correlation between the two sequences b) Bland- Altman analysis (data log-transformed).....	194
Figure 4.2: From adult study by Beerbaum, et al. (119). Comparison of stroke volumes in the pulmonary artery for a reference sequence vs. SENSE $\times 2$ sequence; a) Correlation between the two sequences b) Bland-Altman analysis (data log-transformed).....	195
Figure 4.3: From Prakash, et al. (124). Correlation (left) and Bland-Altman analysis (right) between conventional PCMR sequence (SENSE	

×1) and SENSE ×2 sequence, as found in a)-b) the aorta, c)-d) the pulmonary artery	197
Figure 4.4: From Lew, et al. (125). Resultant image quality from a SENSE×3 sequence; a) magnitude, b) phase. A lot of noise is observed in these images, which Lew, et al. believe comes from noise in the coil sensitivity maps	198
Figure 4.5: The physiological tab was enabled on the UI.....	201
Figure 4.6: Hashing artefact observed when acquiring more than one spiral interleave per RR-interval, in a) Magnitude image, and b) Phase image. The large circular object is a water phantom, and the two smaller objects are oil (right) and butter (left)	203
Figure 4.7: From Bernstein, et al. (36). Gradient echo image of a uniform spherical phantom, with no phase-encoding rewriter gradient (i.e. the phase encode gradient is used as a spoiler). The striped pattern demonstrates the spatially non-uniform spoiling caused as the phase-encode gradients produce spatially varying fields	204
Figure 4.8: Sequence diagram of resultant sequence, showing rewriter gradients after all spiral gradients, which null the zeroth-order moments of all gradients on the x and y axes	205
Figure 4.9: Example of a normal flow profile (plotted with linear interpolation) from a retrospectively-gated PCMR sequence, and the prospectively-triggered spiral PCMR sequence. It can be seen that, for this subject, the last 90 ms at the end of diastole is not captured by the prospectively-triggered sequence	207
Figure 4.10: Abnormal flow profile, with regurgitant flow during diastole. A cubic interpolation is performed between the acquired data points, and a linear interpolation is used between the last and first points, to ensure the flow profile filled the entire RR-interval	208
Figure 4.11: OsiriX plug-in developed to analyse flow from the prospectively-triggered PCMR sequence. In this subject 22 cardiac phases are captured, meaning the last acquired point is at time 673 ms. As the RR-interval is 867 ms, data for the remaining 167 ms was predicted using linear interpolation.....	209

- Figure 4.12: Plug-in for SNR quantification, showing the average signal intensity in the stationary ROI (I_A) in the black line, the exponential fitted curve in red, and the corrected signal intensity in green, for a prospectively-triggered spiral PCMR data set..... 210
- Figure 4.13: SNR measurements with exponential curve fitting from; top) retrospectively-gated Cartesian PCMR sequence, bottom) prospectively-triggered spiral PCMR sequence..... 211
- Figure 4.14: Example of edge sharpness calculation for one data set, using; a) fifth-order polynomial fit, b) Savitzky–Golay filter. It can be seen that polynomial fit detects an artificial edge. The Savitzky–Golay filter detects the vessel border correctly..... 213
- Figure 4.15: Phase correction plug-in as implemented in OsiriX. a) An average magnitude image is formed (left). Using the threshold from the UI, the $\text{mask}_{\text{MAGNITUDE}}$ is formed (right). Blue pixels show pixels not in the mask. b) The standard deviation of the phase data through all cardiac phases is calculated, and masked using the $\text{mask}_{\text{MAGNITUDE}}$ (left). Using the threshold from the UI the $\text{mask}_{\text{FINAL}}$ is formed (right). c) An average phase image is formed and masked with the $\text{mask}_{\text{FINAL}}$ (left). The pixel values remaining in this image are used to calculate the quadratic correction surface (right). d) The quadratic surface is subtracted from all phase images to correct for offsets. Left; uncorrected average phase image, middle; quadratic surface, right; corrected average phase image. e) Flow analysis is carried out for the uncorrected and corrected phase series, plotted in black and red, respectively..... 217
- Figure 4.16: Phase offsets observed in a stationary water phantom, with identical imaging parameters to those used in the subject from Figure 4.15. The flow volume plug-in was used to calculate the average flow offset caused by the phase offsets (left) 218
- Figure 4.17: Background phase correction for a prospectively-triggered spiral sequence. a) Calculation of quadratic surface, left; average phase image with final mask, middle; quadratic correction surface, right; average phase image with background phase correction. b)

Flow analysis for the uncorrected and corrected phase series, plotted in green and blue, respectively.....	219
Figure 4.18: Flow analysis for the uncorrected and corrected phase series for a subject with no background phase offsets. It can be seen that the background phase correction has not added artificial phase to the data	220
Figure 4.19: Example of physiological data acquired for one subject during the prospectively-triggered spiral PCMR sequence. It can be seen that the sequence correctly triggers at the R-wave in each heart-beat. The respiratory data shows little variation over the 6 second scan.....	221
Figure 4.20: The optimised sequence uses a total of 36 spiral interleaves, with 2 interleaves acquired in each RR-interval, undersampled by a factor of 3. The sampling pattern is rotated in each cardiac phase (P, indicated along the top). In total 6 RR-intervals are required to collect all of the data (indicated in gray along the left). The coloured numbers in the boxes, represent which spiral interleaves were acquired – for each spiral interleave the flow-compensated data was acquired first, followed by the flow-encoded data.....	223
Figure 4.21: Comparison of flow profiles in-vitro.....	226
Figure 4.22: Comparison of pump output in-vitro between retrospectively-gated Cartesian sequence and prospectively-triggered spiral sequence. a) Correlation of flow measured from both techniques. b) Bland-Altman plot of the difference in flow measured using both techniques.....	227
Figure 4.23: Respiratory data recorded from two subjects, for all three sequences. These subjects were able to complete the short breath-hold for the spiral sequence, however were only able to complete about half of the breath-hold for the standard breath-hold sequence. Note: different time axis.	234
Figure 4.24: Comparison of flow profiles from all three sequences for one patient, for; a) AAO, b) MPA, c) RPA, d) LPA.....	235

Figure 4.25: Comparisons of stroke volumes in all vessels between reference free-breathing PCMR (FB-PCMR) and standard breath-hold PCMR (BH-PCMR) (top), and between free-breathing PCMR and spiral breath-hold PCMR (SP-PCMR) (bottom). Scatter plots shown on the left and associated Bland-Altman analysis shown on the right	236
Figure 4.26: Bland-Altman analysis comparing stroke volumes in the aorta, MPA and pulmonary branches between reference free-breathing and standard breath-hold PCMR (left), and between free-breathing PCMR and spiral breath-hold PCMR (right)	238
Figure 4.27: Comparisons of stroke volumes in all vessels between reference free-breathing PCMR (FB-PCMR) and standard breath-hold PCMR (BH-PCMR) (top), and between free-breathing PCMR and spiral breath-hold PCMR (SP-PCMR) (bottom). Scatter plots shown on the left and associated Bland-Altman analysis shown on the right	239
Figure 4.28: Comparisons of Q_p/Q_s ratio in all vessels between reference free-breathing PCMR (FB-PCMR) and standard breath-hold PCMR (BH-PCMR) (top), and between free-breathing PCMR and spiral breath-hold PCMR (SP-PCMR) (bottom). Scatter plots shown on the left and associated Bland-Altman analysis shown on the right	241
Figure 4.29: Comparisons of RPA/LPA ratio in all vessels between reference free-breathing PCMR (FB-PCMR) and standard breath-hold PCMR (BH-PCMR) (top), and between free-breathing PCMR and spiral breath-hold PCMR (SP-PCMR) (bottom). Scatter plots shown on the left and associated Bland-Altman analysis shown on the right.	242
Figure 4.30: Comparisons of intra-observe variability between the three sequences. a) Scatter plot for all three sequences, as well as Bland-Altman analysis for b) reference free-breathing sequence, c) standard breath-hold sequence, and d) spiral breath-hold sequence	243

Figure 4.31: Comparisons of inter-observe variability between the three sequences. a) Scatter plot for all three sequences, as well as Bland-Altman analysis for b) reference free-breathing sequence, c) standard breath-hold sequence, and d) spiral breath-hold sequence	244
Figure 4.32: Examples of image quality from the three sequences	246
Figure 5.1: From (134). Accusorb shields for the arms (left) and the torso (right).....	254
Figure 5.2: Effect of <i>Accusorb</i> RF arm shields in the same subject, from the real-time PCMR sequence described in chapter 2, at rest and during exercise	255
Figure 5.3: Sequence diagram for spiral 4D PCMR sequence. + indicates flow-compensated gradients, * indicates flow-encoding gradients	258
Figure 5.4: Comparison of flow profiles between standard PCMR and the 4D CINE PCMR sequence.....	260
Figure 5.5: Streamlines from the 4D PCMR sequence performed in MATLAB. a) Streamlines seeded in the left ventricle, showing path through aorta, b) Streamlines seeded in the ascending and descending aorta, showing the aortic arch	260

LIST OF TABLES

Table 1.1: Properties of some relevant NMR-active nuclei.....	31
Table 2.1: Adapted from Beleslin, et al. (60), showing comparison of side effects from exercise and Dobutamine in the same group of patients	78
Table 2.2: Sequence parameters used by Nayak, et al. (64)	82
Table 2.3: Sequence parameters used by Klein, et al. (65).....	83
Table 2.4: Sequence parameters used by Körperich, et al. (66).....	84
Table 2.5: Sequence parameters used by Nezfati, et al. (69)	86
Table 2.6: Sequence parameters used by Hjortdal, et al. (81).....	88
Table 2.7: Sequence parameters used by Pedersen, et al. (82)	90
Table 2.8: Sequence parameters used by Lurz, et al. (86)	91
Table 2.9: Standard PCMR sequence parameters, in-vitro	117
Table 2.10: Real-time Spiral PCMR sequence parameters, in-vitro	118
Table 2.11: Standard PCMR sequence parameters, in-vivo	125
Table 2.12: Real-time spiral PCMR sequence parameters, in-vivo	125
Table 2.13: Real-time volume assessment sequence parameters, in-vivo	126
Table 2.14: Response to Exercise	131
Table 2.15: Results from (105) showing stroke volumes calculated from manual vs. automatic segmentations.....	138
Table 2.16: Sequence parameters used in mental stress study by Jones, et al. (107)	142
Table 3.1: Sequence parameters used by Gatehouse, et al. (7).....	151
Table 3.2: Sequence Parameters for all four sequences tested, in adult study.....	167
Table 3.3: Estimated SNR, VNR and edge sharpness measures for all four sequences.....	177
Table 3.4: Flow volumes for all four sequences tested, in the adult population.....	178
Table 3.5: Sequence Parameters for all three sequences tested, in the paediatric study	181

Table 3.6: Flow volumes for all three sequences tested, in the paediatric population.....	182
Table 4.1: Sequence parameters used by Beerbaum, et al. (123) in paediatric study	193
Table 4.2: Sequence parameters used by Prakash, et al. (124)	196
Table 4.3: Sequence parameters used by Lew, et al. (125).....	198
Table 4.4: Sequence parameters in-vitro, for retrospectively-gated Cartesian sequence and prospectively-triggered spiral sequence.....	225
Table 4.5: Imaging parameters.....	231
Table 4.6: Comparison of stroke volumes calculated from the three sequences	237
Table 4.7: Comparison of regurgitation fraction calculated from the three sequences.....	239
Table 4.8: Comparison of Q_P/Q_S and RPA/LPA ratios calculated from the three sequences.....	240
Table 4.9: Image Quality - estimated SNR, VNR and edge sharpness measures for all sequences	245
Table 5.1: Sequence parameters used for 4D PCMR sequence.....	259

LIST OF ABBREVIATIONS

1D	One dimensional
2D	Two dimensional
3D	Three dimensional
4D	Four dimensional
AAO	Ascending aorta
ACL	Auto-calibration lines
ANOVA	Analysis of variance
BP	Blood pressure
bpm	Beats per minute
BW	Bandwidth
C	Compliance
CG	Conjugate gradient
CPU	Central processing unit
ECG	Electrocardiogram
EPI	Echo planar imaging
FAE	Fourier acceleration encoding
FFT	Fast Fourier transform
FOV	Field-of-view
FVE	Fourier velocity encoding
GRAPPA	Generalized autocalibrating partially parallel acquisitions
GPU	Graphics processing unit
HSR	High spatial resolution
HTR	High temporal resolution
ICH	Institute of Child Health
IVC	Inferior vena cava
LPA	Left pulmonary artery
LV	Left ventricle

MIST	Montreal Imaging Stress Task
MPA	Main pulmonary artery
MRI	Magnetic resonance imaging
NFFT	Non-equispaced fast Fourier transform
NMR	Nuclear magnetic resonance
NSA	Number of signal averages
PC	Phase contrast
PCMR	Phase contrast magnetic resonance
PVR	Pulmonary vascular resistance
Q_p/Q_s	Ratio of flow in the pulmonary artery to flow in the aorta
R	Resistance
RF	Radio-frequency
ROI	Region of interest
RPA	Right pulmonary artery
RV	Right ventricle
SENSE	Sensitivity encoding
SNR	Signal-to-noise ratio
SV	Stroke volume
SVC	Superior vena cava
SVR	Systemic vascular resistance
TE	Echo time
TR	Repetition time
TSENSE	Temporal filtering combined with spatial sensitivity encoding
UCL	University College London
UI	User interface
UNFOLD	UNaliasing by Fourier-encoding the Overlaps using the temporal Dimension
VENC	Velocity encoding
VNR	Velocity-to-noise ratio
VOI	Vessel of interest

CHAPTER 1

Principles of Magnetic Resonance Imaging

1.1 Introduction

The fundamental physical principles of nuclear magnetic resonance (NMR) were discovered independently by Felix Bloch (1) and Edward Purcell (2), in 1946. They theorized that any spinning charged particle creates an electromagnetic field.

Paul Lauterbur produced the first magnetic resonance (MR) images using the principles of NMR in 1973 (3). Since then MRI has become a common method of medical imaging, which is used clinically in a wide variety of specialties.

MRI is a non-invasive, non-ionising medical imaging modality, which;

- Allows an arbitrary selection of scan plane
- Has good penetration depth
- Can produce truly 3D images with high resolution
- Has good inherent soft tissue contrast
- Allows visualization of structures
- Allows quantification of function, e.g. flow

1.2 Nuclear Magnetic Resonance

NMR can be described in terms of quantum mechanics or more simply using a classical description.

1.2.1 Quantum Mechanics Description of NMR

Elementary particles possess an intrinsic angular momentum, \vec{J} , called *spin*. As a nucleus, such as a proton has an electric charge, this spinning charged particle has a magnetic moment (1, 2). The magnetic moment, $\vec{\mu}$, is related to the angular momentum, by;

$$\vec{\mu} = \gamma \vec{J} \quad \text{Equation 1.1}$$

where γ is a nucleus dependent, physical constant, called the *gyromagnetic ratio*. The magnitude of the spins magnetic momentum, $|\mu|$, can be calculated by;

$$|\mu| = \gamma \hbar \sqrt{I(I+1)} \quad \text{Equation 1.2}$$

where \hbar is Planck's constant (1.055×10^{-34} Js), and I is the nuclear spin quantum number.

A commonly used constant related to the gyromagnetic ratio is γ , where;

$$\gamma = \frac{\gamma}{2\pi} \quad \text{Equation 1.3}$$

Values of NMR-relevant I and γ are given in Table 1.1. Note: Nuclei are only NMR-active if $I \neq 0$, i.e. the nuclei must have an odd mass number, or an odd charge number.

Nucleus	Spin, I	Gyromagnetic ratio, γ (MHz/T)
1H	1/2	42.58
^{13}C	1/2	10.71
^{19}F	1/2	40.05
^{31}P	1/2	11.26

Table 1.1: Properties of some relevant NMR-active nuclei

Due to thermal random motion there is no net-magnetic moment in the absence of an external magnetic field. However, when an external magnetic field is applied, the spins become quantized into $(2I + 1)$ energy levels. These quantum levels, m_I , are;

$$m_I = -I, -I + 1, \dots, I \quad \text{Equation 1.4}$$

The most common nuclei used in MRI is hydrogen (1H), as this has a natural abundance in the body. From Table 1.1 it can be seen that for a hydrogen nuclei; $I = 1/2$. From Equation 1.4 we can see that 1H has two energy states when an external magnetic field is applied; $+1/2$ and $-1/2$. These two states are aligned in opposite directions, often referred to as *parallel* and *anti-parallel* (to the external magnetic field), or *spin-up* and *spin-down*. While the orientation of $\vec{\mu}$ is quantized along the direction of the magnetic field, the spins continue to precess randomly about the z-axis, at an angular frequency, ω_0 , where;

$$\omega_0 = \gamma B_0 \quad \text{Equation 1.5}$$

This is the *Larmor equation*, which underpins NMR.

The energy states, E , are proportional to the strength of the external magnetic field applied, B_0 , by;

$$E = I \gamma \hbar B_0 \quad \text{Equation 1.6}$$

Therefore, for 1H a transition between the two states represents a change in energy of;

$$\Delta E = \gamma \hbar B_0 \quad \text{Equation 1.7}$$

This non-zero difference in energy levels is known as *Zeeman splitting*;

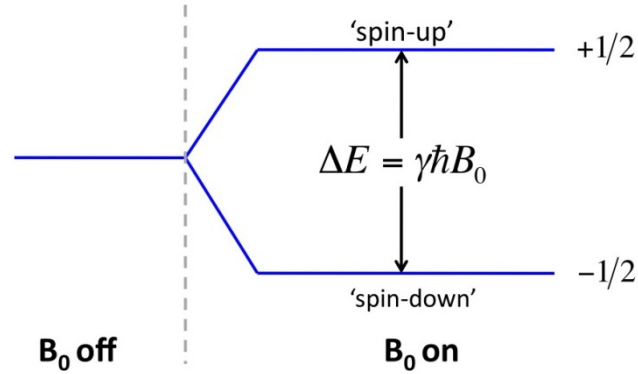


Figure 1.1: Zeeman splitting for a spin- $\frac{1}{2}$ system

A transition between the two energy states can be induced by absorption or emission of electromagnetic radiation of frequency, ω_0 , such that;

$$\hbar\omega_0 = \Delta E = \gamma \hbar B_0 \quad \text{Equation 1.8}$$

This is known as the *resonance condition*.

In reality there is not just one, but are many nuclei all of which occupy a particular spin state. According to the Boltzmann relationship;

$$\frac{N_{+1/2}}{N_{-1/2}} = \exp\left(\frac{\Delta E}{kT_S}\right) \quad \text{Equation 1.9}$$

$$= \exp\left(\frac{\gamma \hbar B_0}{kT_S}\right) \quad \text{(from Equation 1.7)} \quad \text{Equation 1.10}$$

$$\approx 1 + \frac{\gamma \hbar B_0}{kT_S} \quad \text{(providing } kT_S \gg \gamma \hbar B_0) \quad \text{Equation 1.11}$$

$$N_{+1/2} - N_{-1/2} \approx N_S \left(\frac{\gamma \hbar B_0}{2kT_S} \right) \quad \text{Equation 1.12}$$

where k is the Boltzmann constant (1.38×10^{-23} J/K), T_S is the absolute temperature of the spin system (in Kelvin), $N_{+1/2}$ is the number of spins in the higher energy state, $N_{-1/2}$ is the number of spins in the lower energy state, and N_S is the total number of spins in the spin system. From Equation 1.12 it can be seen that there are slightly more spins in the lower energy state. The resulting bulk magnetization, \vec{M} , can be calculated as;

$$\vec{M} = \sum_{n=1}^{N_S} \vec{\mu}_n \quad \text{Equation 1.13}$$

$$= \left(\sum_{n=1}^{N_S} \vec{\mu}_{x,n} \right) \vec{x} + \left(\sum_{n=1}^{N_S} \vec{\mu}_{y,n} \right) \vec{y} + \left(\sum_{n=1}^{N_S} \vec{\mu}_{z,n} \right) \vec{z} \quad \text{Equation 1.14}$$

Assuming B_0 is applied on the z -axis, the \vec{x} and \vec{y} terms are zero. This is because the projection of $\vec{\mu}_n$ onto the transverse plane has a random phase, while it precesses about \vec{z} . Therefore, by substituting Equation 1.2 into Equation 1.14 we get;

$$\vec{M} = \left(\sum_{n=1}^{N_{+1/2}} \frac{1}{2} \gamma \hbar - \sum_{n=1}^{N_{-1/2}} \frac{1}{2} \gamma \hbar \right) \vec{z} \quad \text{Equation 1.15}$$

$$= \frac{1}{2} (N_{+1/2} - N_{-1/2}) \gamma \hbar \vec{z} \quad \text{Equation 1.16}$$

Equation 1.16 shows that \vec{M} points exactly along the positive direction of the z -axis at thermal equilibrium.

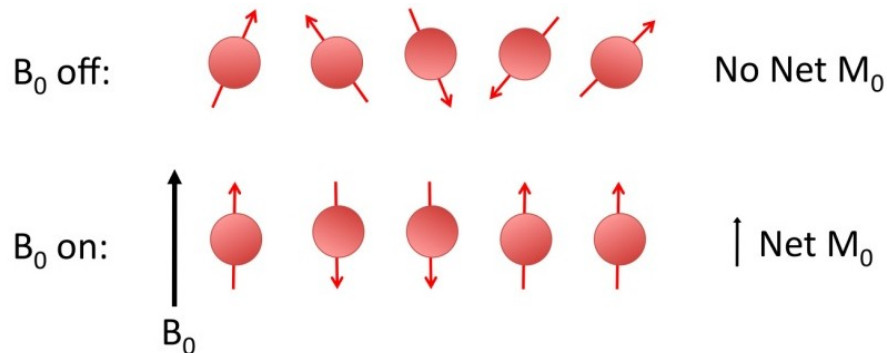


Figure 1.2: Magnetic moment vectors. Top: spins precess with random phase, bottom; spins align in direction of an external magnetic field

It is not possible to measure \vec{M} when it is aligned with the main magnetic field, however each magnetic moment vector also has a microscopic transverse component. It is possible to achieve phase coherence between the spins (thereby introducing a transverse component of \vec{M}), by introducing an oscillating magnetic field (B_1) perpendicular to the main field. The frequency of B_1 must be such that it induces a change in the energy state of the spins (see Equation 1.5 and Equation 1.8), i.e. it must have a frequency equal to ω_0 . As ω_0 is in the radio-frequency range, B_1 is often referred to as an *RF-pulse*.

Treating the behaviour of all the spins in the system in terms of the net magnetic vector, \vec{M} , allows us to transfer to the classical description of NMR.

1.2.2 Classical Description of NMR

When \vec{M} is aligned with an external magnetic field, it continues to precess about the z -axis, at the frequency ω_0 , as shown in Figure 1.3;

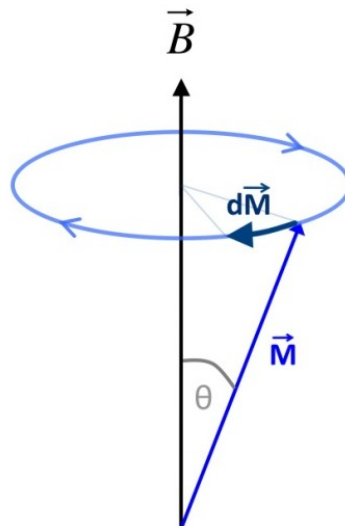


Figure 1.3: Precession of the spin-vector about a static magnetic field

This time-dependent behaviour of \vec{M} , in the presence of an applied magnetic field, \vec{B} , can be described by the Bloch equation;

$$\frac{d\vec{M}}{dt} = \gamma \vec{M} \cdot \vec{B} \quad \text{Equation 1.17}$$

When a constant field, B_0 , is applied on the z -axis, $\vec{B} = B_0 \vec{z}$, Equation 1.17 can be written as the following component equations;

$$\left. \begin{aligned} \frac{dM_x}{dt} &= \gamma M_y \cdot B_0 \\ \frac{dM_y}{dt} &= -\gamma M_x \cdot B_0 \\ \frac{dM_z}{dt} &= 0 \end{aligned} \right\} \quad \text{Equation 1.18}$$

Where $\omega_0 = \gamma B_0$, the complete set of solutions is;

$$\left. \begin{aligned} M_x(t) &= M_x(0)\cos(\omega_0 t) - M_y(0)\sin(\omega_0 t) \\ M_y(t) &= M_x(0)\sin(\omega_0 t) + M_y(0)\cos(\omega_0 t) \\ M_z(t) &= M_z(0) \end{aligned} \right\} \quad \text{Equation 1.19}$$

These equations describe the precession of \vec{M} about the z -axis, at frequency ω_0 , as previously shown in Figure 1.3.

1.2.2.1 Rotating Frame of Reference

In order to simplify the effect of RF-pulses and relaxation mechanisms, the *rotating frame of reference* is commonly used (denoted as x' , y' , and z'). This reference frame rotates about the z -axis at the Larmor frequency, ω_0 . It is mathematically related to the stationary frame by;

$$\left. \begin{aligned} \vec{x}' &\equiv \vec{x} \cdot \cos(\omega t) - \vec{y} \cdot \sin(\omega t) \\ \vec{y}' &\equiv -\vec{x} \cdot \sin(\omega t) + \vec{y} \cdot \cos(\omega t) \\ \vec{z}' &\equiv \vec{z} \end{aligned} \right\} \text{Equation 1.20}$$

In this rotating frame, spins which are rotating at the Larmor frequency appear to be stationary, while those at a higher or lower frequency gain or lose phase, respectively. \vec{M} can now be viewed as a static vector, \vec{M}' .

1.2.2.2 RF-Pulses

In the static frame of reference, a typical B_1 field takes the form;

$$\vec{B}_1(t) = 2B_1^e(t) \cos(\omega_{rf}t) \vec{x} \quad \text{Equation 1.21}$$

where B_1^e is the pulse envelope function. Mathematically this can be decomposed into two circularly polarized fields (perpendicular to the z -axis). Assuming the counter-clockwise rotation exerts negligible effects, Equation 1.21 can be re-written as;

$$\vec{B}_1(t) = B_1^e(t) \left[\vec{x} \cdot \cos(\omega_{rf}t) - \vec{y} \cdot \sin(\omega_{rf}t) \right] \quad \text{Equation 1.22}$$

By viewing the RF-pulse in the rotating frame of reference (see Equation 1.20), Equation 1.22 can be re-written as;

$$\vec{B}_1'(t) = B_1^e(t) \vec{x}' \quad \text{Equation 1.23}$$

Substituting Equation 1.23 into the Bloch equation (Equation 1.17), gives;

$$\left. \begin{aligned} \frac{dM_{x'}}{dt} &= 0 \\ \frac{dM_{y'}}{dt} &= \gamma B_1^e(t) M_{z'} \\ \frac{dM_{z'}}{dt} &= -\gamma B_1^e(t) M_{y'} \end{aligned} \right\} \text{Equation 1.24}$$

For an RF-pulse under the starting conditions $M_{x'}(0) = M_{y'}(0) = 0$ and $M_{z'}(0) = M_z^0$, the bulk magnetization is therefore;

$$\left. \begin{aligned} M_{x'}(t) &= 0 \\ M_{y'}(t) &= M_z^0 \sin \left(\int_{t=0}^{\tau} \gamma B_1^e(t) dt \right) \\ M_{z'}(t) &= M_z^0 \cos \left(\int_{t=0}^{\tau} \gamma B_1^e(t) dt \right) \end{aligned} \right\} \text{Equation 1.25}$$

where τ is the RF-pulse duration. Combining these equations with Equation 1.20 it can be seen that the bulk magnetization vector precesses (or *nutates*) about the x' -axis with angular velocity;

$$\vec{\omega}_1 = -\gamma \vec{B}_1 \quad \text{Equation 1.26}$$

This is called *forced precession*. As a result, the bulk magnetization vector is tipped onto the x - y plane, where it can be measured.

The flip angle (α) of an RF-pulse is defined as the angle between \vec{M} and the z -axis immediately after the RF-pulse has terminated. From Equation 1.25 it can be seen that α depends on the magnitude of B_1 and τ , by;

$$\alpha = \int_{t=0}^{\tau} \gamma B_1^e(t) dt \quad \text{Equation 1.27}$$

1.2.2.3 Signal Detection

After \vec{M} has been excited using an RF-pulse, it can be measured on the x - y plane. By placing RF-receive coils in the x - y plane, the time-varying bulk magnetization vector induces a voltage in these coils, proportional to \vec{M}_{xy} .

The voltage induced varies at the Larmor frequency and decays exponentially with time due to magnetization relaxation. In the absence of any additional magnetic gradients, this signal is known as the *free induction decay*.

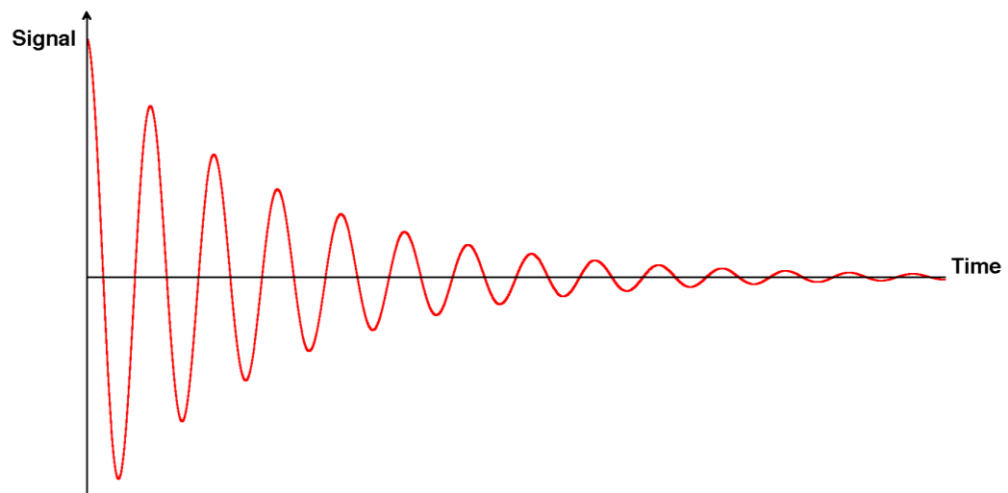


Figure 1.4: Free induction decay simulated in MATLAB

1.3 Magnetic Resonance Imaging

The signal received in MRI is the sum of the magnetization from all of the excited spins within the object (see Equation 1.13). In a static homogeneous field, after an RF-pulse, \vec{M}' remains along the x' -axis – this reveals no information about the location of the individual spins.

1.3.1 Spatial Encoding

By manipulating the spatial variation of the magnetic field in a known way using gradient coils, it is possible to achieve spatial encoding of the MR signal. These gradient coils vary the magnetic field linearly across the imaging volume. By extending the Larmor equation (Equation 1.5) it can be seen that the addition of a linearly varying gradient \vec{G}_r across an imaging volume has the effect of altering the precessional frequency of the spins depending on their position (\vec{r});

$$\omega(\vec{r}) = \gamma(B_0 + \vec{G}_r \cdot \vec{r}) \quad \text{Equation 1.28}$$

This is shown in Figure 1.5.

1.3.2 K-space

The received signal (after demodulation) from an object after a single RF-excitation is now seen to be related to its 3D position;

$$S(t) = \iiint \rho(\vec{r}) \exp(-j\gamma \vec{G}_r \cdot \vec{r} t) d\vec{r} \quad \text{Equation 1.29}$$

where ρ is the proton density. The reciprocal space is defined, \vec{k} , where;

$$\vec{k}(t) = \gamma \int_0^t \vec{G}(\tau) d\tau \quad \text{Equation 1.30}$$

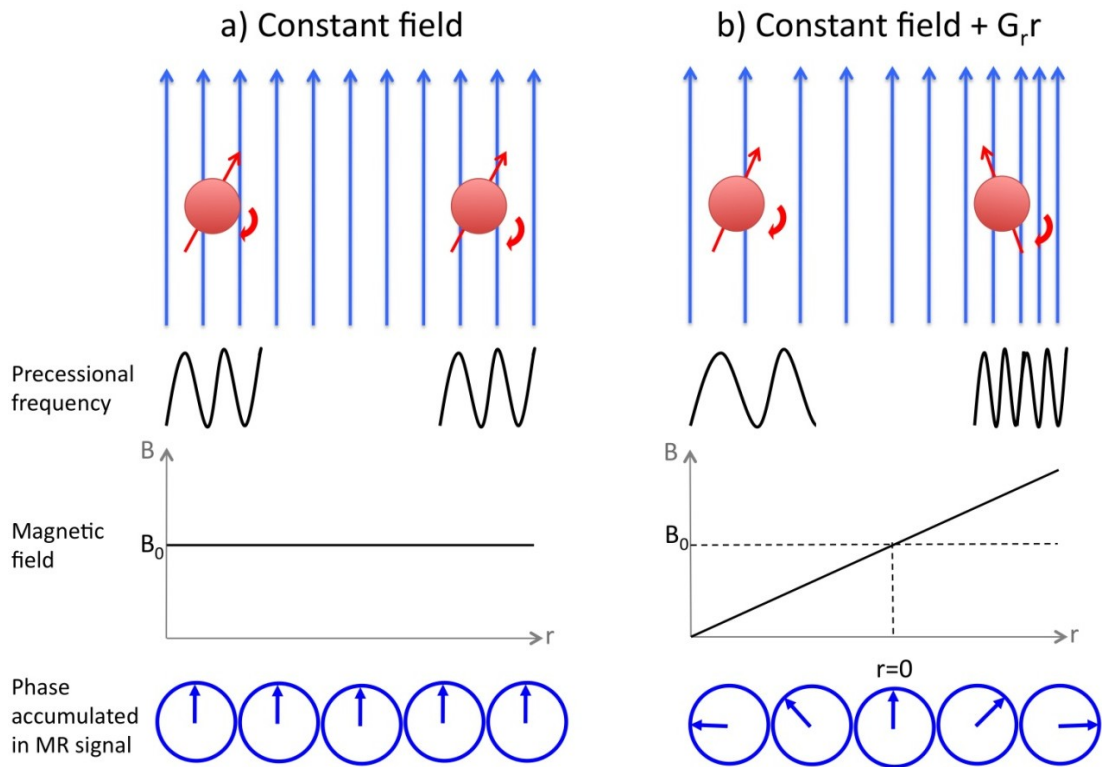


Figure 1.5: Effect of gradients on the precessional frequency of spins. a) In a constant field all of the spins precess at the same frequency – there is no difference in the phase of the MR signal. b) When a linear gradient is applied, the precessional frequency is dependent on position – the phase of the MR signal is proportional to the spins position

The Fourier relationship between the received signal and the position of the spins (the proton density) is obvious from Equation 1.29;

$$S(\vec{k}) = \iiint \rho(\vec{r}) \exp(-j\vec{k}\vec{r}) d\vec{r} \quad \text{Equation 1.31}$$

$$\rho(\vec{r}) = \iiint S(\vec{k}) \exp(j\vec{k}\vec{r}) d\vec{k} \quad \text{Equation 1.32}$$

The raw data is therefore collected in *k-space*, where the centre of *k-space* contains low spatial frequencies and at the periphery contains high spatial frequencies. To transform this raw data from *k-space* into image space, the inverse Fourier transform must be used. Normally the *fast Fourier transform* (FFT) is used, due to its computational efficiency.

There are some MRI techniques which sample *k-space* in 3D as described in Equation 1.31 and Equation 1.32, however most techniques reduce the problem to 2D by applying slice selection (see section 1.3.4), in the *z*-direction.

1.3.3 Pulse Sequences

A pulse sequence is a set of defined RF and gradient pulses, which control how k-space is filled. Parameters normally used when describing pulse sequences include *echo time* (TE) and *repetition time* (TR). TE is defined as the time between the RF-pulse and the point we pass through the centre of k-space. TR is defined as the time between excitatory RF-pulses.

1.3.4 Slice Selection

In order to selectively excite spins in a single imaging plane, a linear gradient is applied simultaneously with the RF-pulse. As described in section 1.2.1 an RF-pulse only affects spins, which are precessing at the frequency of the RF-pulse. Therefore by applying a linear gradient (shown in Figure 1.6 on the z -axis) at the same time as the RF-pulse, only a band of spins are excited (along the z -axis). The slice thickness is dependent on the bandwidth of the RF-pulse and the gradient strength, as seen in Figure 1.6;

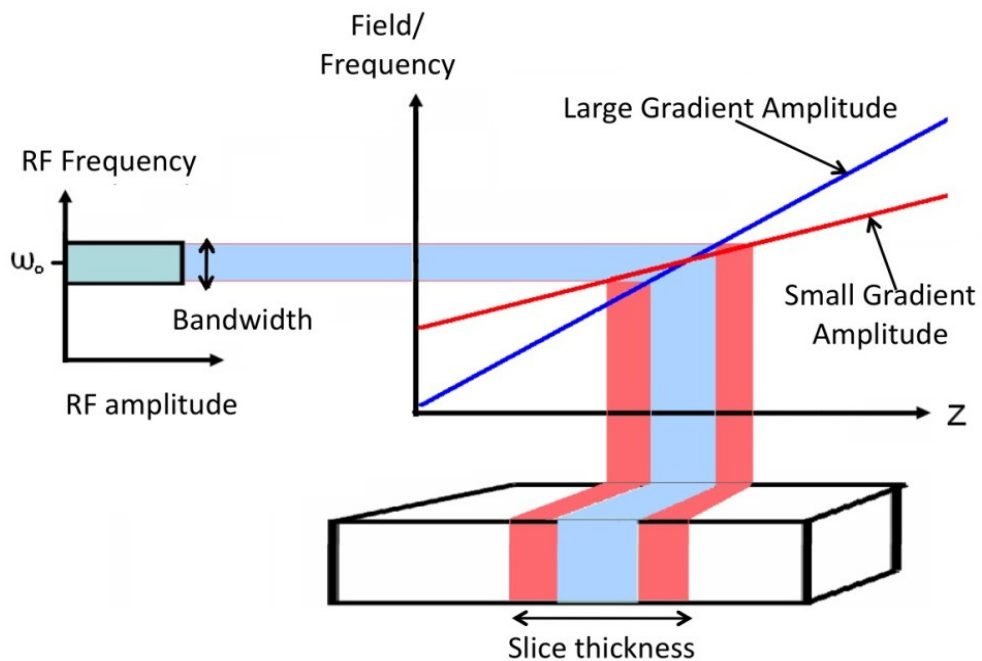


Figure 1.6: Slice selection; an RF-pulse is applied simultaneously with a linear gradient on the z -axis

1.3.5 Fourier Imaging

After slice selection, the problem has been reduced to just two dimensions. From Equation 1.30 it can be seen that the position in k -space is proportional to the time-integral of the gradient vector (also known as the *zeroth-order gradient moment*). This means that the (x and y) gradients that are applied, define our trajectory in (2D) k -space. In conventional Cartesian imaging, data is acquired one row at a time (see Figure 1.7). After slice selection, a *phase-encoding gradient* is first applied on the y -axis – this moves us up/down in k -space. A *readout gradient* is then applied on the x -axis to move us across k -space, while the ADC is on (i.e. data is acquired). This sequence of gradients is repeated with a different phase-encoding gradient for each row in k -space.

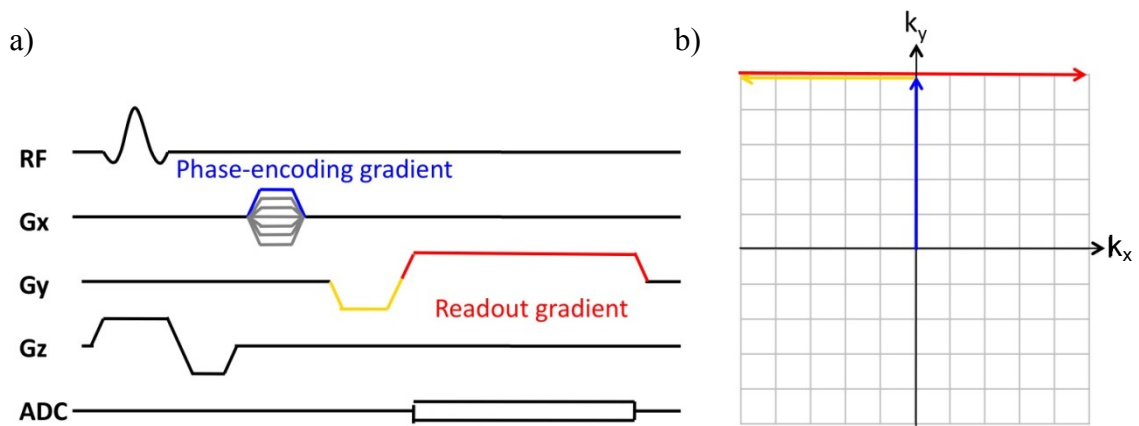


Figure 1.7: a) Sequence diagram of a basic Cartesian gradient echo sequence. b) Corresponding k -space trajectory

1.3.5.1 Frequency-Encoding

In Cartesian imaging *frequency-encoding* is often used to explain how the signal is encoded in the x -direction. As described in section 1.3.1, the application of the readout gradient on the x -axis, causes the frequency of the spins to be linearly related to their spatial location (in the x -direction) (see Equation 1.28).

From Equation 1.29 the signal resulting from the readout gradient (G_x) can be written as;

$$S(t) = \int_{\text{object}} \rho_0 \exp\left(-j\gamma \vec{G}_x \cdot \vec{x} t\right) d\vec{x} \quad \text{Equation 1.33}$$

1.3.5.2 Phase-Encoding

In Cartesian imaging *phase-encoding* is often used to explain how the signal is encoded in the y -direction. The phase-encoding gradient is applied before the readout (see Figure 1.7). Like the frequency-encoding (or readout) gradient, this causes the frequency of the spins to be linearly related to their spatial location (in the y -direction), while the gradient is on. When the phase-encoding gradient is turned off, spins from different y -positions have accumulated different phase angles. The signal during and after the phase-encoding gradient, can be written as;

$$dS(y,t) = \begin{cases} \rho(y) \exp\left(-j\gamma G_y \cdot y t\right) & 0 \leq t \leq T_{pe} \\ \rho(y) \exp\left(-j\gamma G_y \cdot y T_{pe}\right) & T_{pe} \leq t \end{cases} \quad \text{Equation 1.34}$$

where T_{pe} is the total time of the phase-encoding gradient. It can be seen that the signal after the phase-encode gradient will have an initial phase (ϕ) of;

$$\phi(y) = -\gamma G_y \cdot y T_{pe} \quad \text{Equation 1.35}$$

1.3.5.3 General Localization

Describing frequency and phase encoding differently does not translate well to non-Cartesian imaging. In fact, frequency and phase encoding are the same.

Expanding Equation 1.31 for a 2D problem we get;

$$S(k_x, k_y) = \iint \rho(x, y) \exp(j2\pi x k_x) \exp(j2\pi y k_y) dx dy \quad \text{Equation 1.36}$$

Combining Equation 1.30 and Equation 1.36 we get;

$$S(k_x, k_y) = \iint \rho(x, y) \cdot \exp\left(-j\gamma x \int_0^x G_x(\tau) d\tau\right) \cdot \exp\left(-j\gamma y \int_0^y G_y(\tau) d\tau\right) dx dy \quad \text{Equation 1.37}$$

It can be seen that the rate at which the spins dephase depends on their position (in x and y) and the amplitude of the gradient waveforms (G_x and G_y) at time τ . Therefore, spins accumulate a phase over time depending on their 2D location, according to the equation;

$$\phi(x, y) = -\gamma \left(x \int_0^x G_x(\tau) d\tau + y \int_0^y G_y(\tau) d\tau \right) \quad \text{Equation 1.38}$$

1.3.6 K-space Trajectories

There are many different paths that can be taken, to acquire all of the data in k-space. Collecting data in a Cartesian grid (see Figure 1.7) is popular because the gradient design is simple and the data is robust to many artefacts. Also, k-space data must be on a uniform rectilinear grid in order to use the FFT. Acquiring data in this way is very slow as only a small portion of k-space is covered after each excitation, and there are a large number of excitations (equal to the number of lines in k_y).

Methods of speeding up acquisition, while maintaining data on a Cartesian grid include the use of *echo planar imaging* (EPI), see Figure 1.8. Single shot EPI is possible where the entire k-space is filled after one excitation, or segmented EPI can be used where a part of k-space is filled after each excitation.

Non-Cartesian trajectories may offer more efficient methods of covering k-space, or non-uniform coverage of k-space. The most common non-Cartesian trajectories include radial and spiral acquisitions (see Figure 1.8);

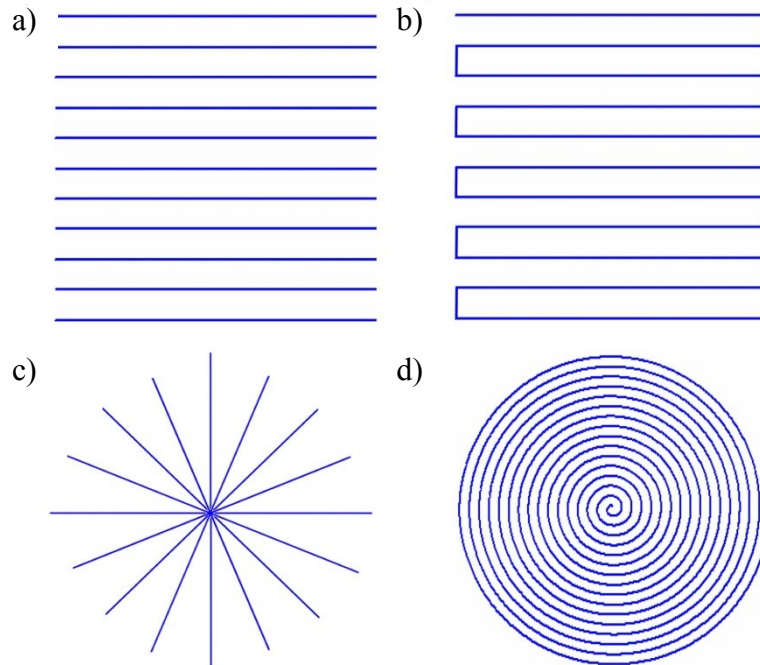


Figure 1.8: Common k-space trajectories; a) Cartesian, b) EPI, c) Radial, d) Spiral

Both radial and spiral sequences oversample the centre of k-space, which reduces their sensitivity to motion, and can be useful when using parallel imaging techniques (see section 1.4). In this work we will focus on the use of spiral trajectories, as they have desirable properties for flow imaging (see section 1.6)

1.3.7 Spiral Trajectories

Spiral trajectories (4, 5) provide a highly efficient method of traversing k-space, as a large proportion of k-space can be covered after just one excitation. As spiral trajectories start in the centre of k-space they have a very short TE, therefore spins have very little time to dephase due to motion, before the centre of k-space is acquired – this is especially important in flow imaging (6, 7).

To acquire data on a spiral trajectory, the required gradient waveforms are sinusoidal in shape and must be both frequency and amplitude modulated. The Archimedean spiral (where the radius is directly proportional to the amount of rotation) is a popular trajectory design, as the resulting k-space density is fairly uniform. The desired Archimedes spiral trajectory can be designed using the following formula (5);

$$\vec{k}(t) = \lambda \theta(t) \cdot \exp(j\theta(t)) \quad \text{Equation 1.39}$$

where $\theta(t)$ describes the azimuth angle evolution over time (in radians), and λ is a constant which describes the rate of spiral growth towards the edge of k-space.

To prevent aliasing, the distance between two spiral arms (Δk) should not be greater than the Nyquist sampling ratio;

$$\Delta k = \frac{1}{FOV} = \lambda 2\pi \quad \text{Equation 1.40}$$

$$\lambda = \frac{N_{int}}{2\pi \cdot FOV} \quad \text{Equation 1.41}$$

where N_{int} is the total number of desired interleaves. A spiral trajectory that has multiple interleaves uses the same trajectory for each interleave, however each interleave is rotated by a multiple of $2\pi/N_{int}$ radians.

To ensure we reach the edge of k-space, the final value of θ must equal to;

$$\theta_{final} = \frac{k_{max}}{\lambda} = \frac{1}{2\Delta x \cdot \lambda} \quad \text{Equation 1.42}$$

It is possible to design spiral trajectories with constant angular velocity, or with constant linear velocity, however the gradient amplitude is not great enough to fulfil either of these trajectories. To achieve the most efficient spiral trajectory the gradients must be limited by the slew rate at the start of the readout, however once the maximum gradient amplitude has been reached, this then limits the gradient waveforms (as seen in Figure 1.9).

Equation 1.39 can be solved by differentiation (5, 8). There are many ways to optimise the spirals. One solution can be realized by (4, 5, 9);

$$\theta(t) = \frac{1}{\sqrt{\alpha + (1-\alpha)t'}} \quad \text{Equation 1.43}$$

where α is used to tune the spiral between constant angular velocity (when $\alpha = 1$, $\theta \propto t$) and constant linear velocity (when $\alpha = 0$, $\theta \propto \sqrt{t}$). Unfortunately it is difficult to optimise α so that the resulting trajectories cover k-space as efficiently as possible (9). A more efficient solution is obtained by solving for the gradient amplitude and slew rate given the hardware limitations (5, 8). Unfortunately there is no analytical solution to these equations making them computationally expensive, as they must be solved iteratively. This is discussed further in section 2.3.1.1.

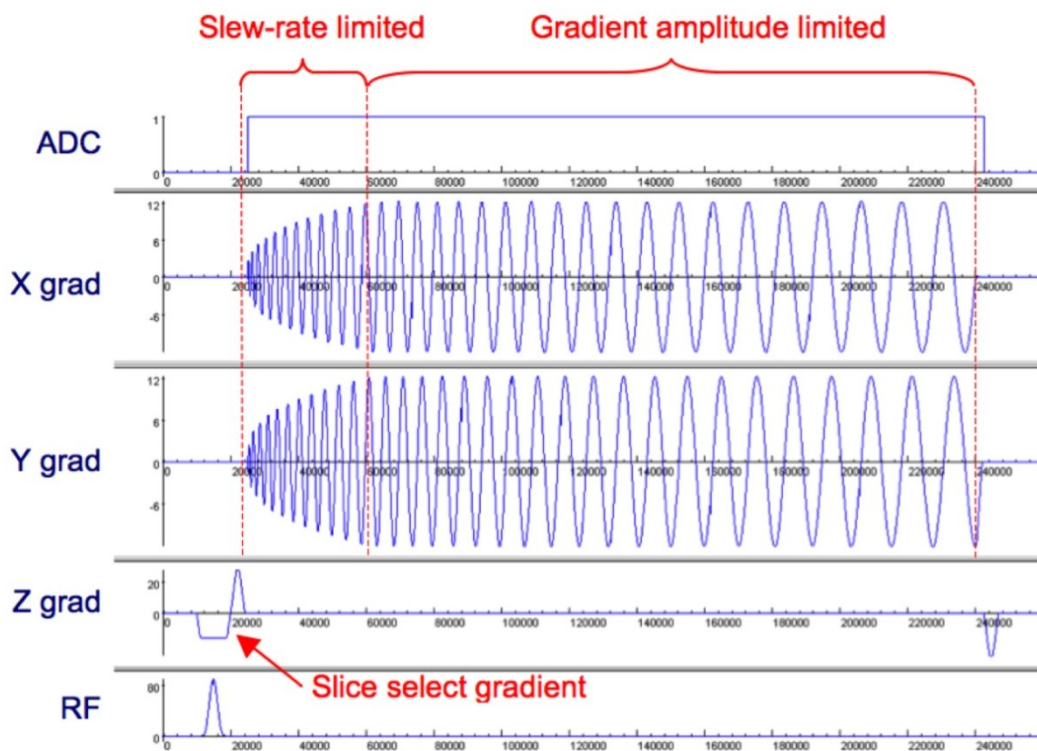


Figure 1.9: Example of an efficient spiral trajectory. The gradients are slew-rate limited in the centre of k-space, and gradient amplitude limited at the edge of k-space

1.3.8 Gridding

K-space data that is acquired using non-Cartesian trajectories (or non-uniform trajectories), requires the data to be re-sampled onto a uniform rectangular grid before reconstruction using the FFT. It is possible to perform nearest neighbour interpolation or bilinear interpolation of the data onto a Cartesian grid, however this is prone to artefacts. Alternatively, *gridding* can be used (10, 11).

Gridding uses a window function, \hat{C} , which is convolved with the measured data, \hat{M} , and sampled onto a unit-spaced grid;

$$\hat{G} = (\hat{C} * \hat{M}) \cdot III \quad \text{Equation 1.44}$$

where the 2D comb function, III , is defined as;

$$III(x, y) = \sum_i \sum_j \delta(x-i, y-j) \quad \text{Equation 1.45}$$

The ideal window function (or *convolution kernel*) is a *sinc* kernel, however as this is an infinite function the computation is impractical. The choice of kernel is a trade-off between processing time and interpolation accuracy (12). In MRI a *Kaiser-Bessel* kernel is commonly used (typical width: 3-5 grid points) (12, 13), as it has minimal residual aliasing and allows a relatively short computation time. It also has an analytic expression for its properties in the Fourier domain. The Kaiser-Bessel kernel is defined as (12);

$$C(u) = \frac{1}{w} I_0 \left[\beta \sqrt{1 - (2u/w)^2} \right] \quad \text{Equation 1.46}$$

$$c(x) = \frac{\sin \sqrt{\pi^2 w^2 x^2 - \beta^2}}{\sqrt{\pi^2 w^2 x^2 - \beta^2}} \quad \text{Equation 1.47}$$

where $C(u) \xleftrightarrow{FT} c(x)$, w is the window width, $I_0[\]$ is the modified Bessel function, and β is a constant that determines the shape of the window. After gridding has been performed, the data can be transformed into image space using a 2D inverse FFT. It is

necessary to divide the resultant image by the Fourier transform of the convolution kernel, to remove the apodization caused by the convolution.

For non-uniform sampling patterns it is also necessary to perform density correction to account for undersampling/oversampling. This correction is performed by multiplying the data by a set of weights (an area density function), prior to convolution with the window function. For a spiral trajectory these weights (W) can be numerically estimated (6) as;

$$W(t) = \left| \vec{G}(t) \right| \cdot \left| \left[\sin(\arg(\vec{G}(t))) - \sin(\arg(\vec{k}(t))) \right] \right| \quad \text{Equation 1.48}$$

1.4 Parallel Imaging

It is possible to speed up MR acquisition by undersampling the data. In Cartesian imaging this is normally achieved by missing out entire lines in k-space (in the phase-encode direction) as seen in Figure 1.10;

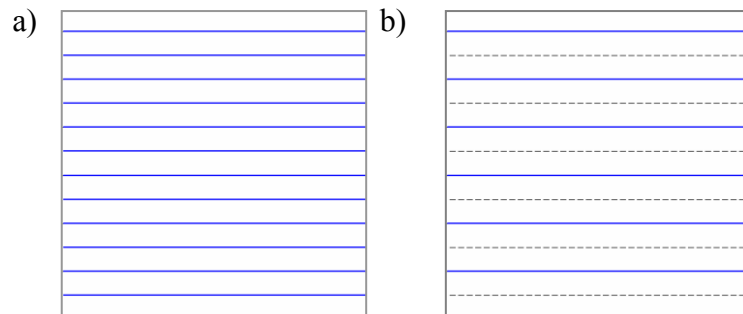


Figure 1.10: Undersampling of Cartesian k-space data a) Fully sampled data, b) corresponding 2-fold undersampled data

The increase in distance between the k-space lines causes an effective decrease in the FOV, as;

$$\Delta k = \frac{1}{FOV} \quad \text{Equation 1.49}$$

This causes aliasing to occur in the reconstructed images, as replicas of the subject appear along the phase-encode direction, spaced at FOV/acceleration factor, as seen in Figure 1.11;

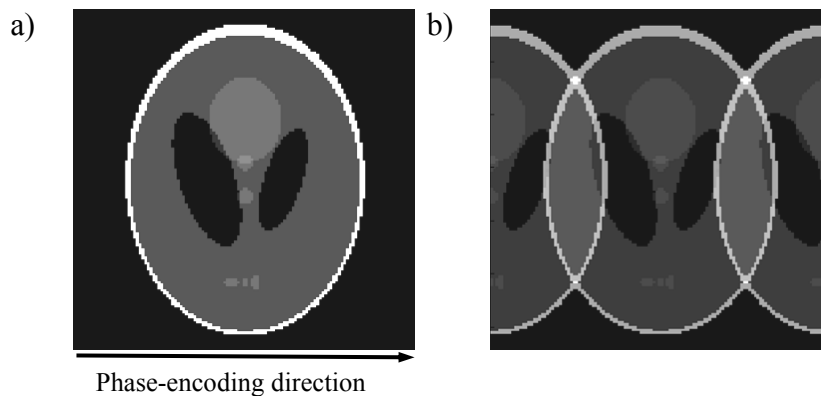


Figure 1.11: Simulated effect of Cartesian undersampling, performed in MATLAB. a) Fully-sampled, b) 2-fold acceleration

Parallel-imaging, so called because data is acquired simultaneously (i.e. in parallel) using multiple coils, can be used to remove aliasing from undersampled data. Parallel-imaging uses the spatial dependence of the individual coils (the *coil sensitivities*) to imply information about origin of the signal, and unwrap the aliasing.

There are many different parallel-imaging algorithms, however they can be divided into two main categories;

- Those that unwrap the data in the image domain
- Those that unwrap the data in the Fourier domain

Parallel-imaging algorithms that unwrap data in image space include;

- SENSE (sensitivity encoding) (14)
- K-t SENSE (15)
- TSENSE (temporal filtering combined with spatial sensitivity encoding) (16)

Parallel-imaging algorithms that unwrap data in k-space include;

- SMASH (Simultaneous acquisition of spatial harmonics) (17)
- GRAPPA (Generalized autocalibrating partially parallel acquisitions) (18)
- K-t GRAPPA (19)

In this work we will focus on the use of SENSE.

1.4.1 Coil Sensitivities

To measure the coil sensitivities low resolution, full FOV images are required from each of the coils, and from a homogeneous coil (14). The coil sensitivity, C_γ of the γ^{th} coil, is calculated by dividing the low resolution, full FOV image from the γ^{th} coil (I_γ), by the low resolution, full FOV image from the homogeneous coil (I_H);

$$C_\gamma = I_\gamma / I_H \quad \text{Equation 1.50}$$

The homogeneous image, I_H , may be acquired using the body coil. Alternatively, an estimated homogeneous image can be formed from the complex sum-of-squares of all coil images;

$$I_H(x, y) = \sqrt{\sum_{\gamma=1}^{n_c} I_{\gamma(x,y)} I_{\gamma(x,y)}^*} \quad \text{Equation 1.51}$$

The low-resolution images necessary to calculate the coil sensitivities may be acquired in a separate scan, however this requires additional scan time and is prone to errors if the subject moves between the scans.

Alternatively, the coil sensitivities can be calculated from the acquired data itself. This can be achieved in many different ways, as reviewed in (20). Commonly self-calibrated SENSE is used, where variable density k-space data is acquired (21-23). A small number of fully sampled lines in the centre of k-space are used to produce low-resolution reference images. However, the need for additional scan lines decreases the temporal resolution or increases the scan time.

Another approach is TSENSE (16) which uses the UNFOLD method (24) to provide temporal filtering. The UNFOLD technique interleaves the k-space lines in sequential images. The images reconstructed from any single frame contain aliasing, however the aliased component is shifted between frames. This means that the aliasing can be removed by temporal low-pass filtering of the data.

Using the sum-of-squares method to calculate the homogeneous coil (see Equation 1.51), TSENSE allows all coil sensitivity information to be calculated without any additional scans, or additional scan lines. In order to ensure high signal-to-noise coil sensitivity information, the un-aliased images may be averaged over multiple measurements as is performed in k-t SENSE (15).

1.4.2 SENSE

SENSE (14) uses a linear encoding matrix, E , to describe the transformation from the ideal image ρ (matrix size: $n_m \times n_m$) to the acquired aliased values from each coil, S_γ (number of samples: n_k);

$$S_\gamma = E_\gamma \rho \quad \text{Equation 1.52}$$

In Cartesian SENSE, E includes the inverse FFT at the k-space positions used to acquire the data (this defines the aliasing), and the coil sensitivity information. E (size: $n_c n_k \times n_m^2$) can be written as;

$$E_{(\gamma,k),\rho} = C_\gamma(r_\rho) \exp(jK_k r_\rho) \quad \text{Equation 1.53}$$

where r_ρ denotes the position of the ρ^{th} voxel and K_k is the k^{th} sampling position in k-space.

The reconstruction of ρ is performed using a linear reconstruction matrix, F , where;

$$\rho = \sum_\gamma S_\gamma F_\gamma \quad \text{Equation 1.54}$$

F (size: $n_m^2 \times n_c n_k$) is estimated under a *weak voxel criterion*, which approximates the shape of the voxel function by the unit impulse function. This gives;

$$FE = Id \quad \text{Equation 1.55}$$

where Id denotes an identity matrix (size: $n_m \times n_m$). F is therefore, often over-determined ($n_c n_k - n_m^2$ remaining degrees of freedom). The least squares method is used to chose the solution with minimum errors in every equation, by;

$$F = (E^H E)^{-1} E^H \quad \text{Equation 1.56}$$

where E^H is the complex conjugate transpose of E .

By combining Equation 1.54 and Equation 1.56, we get the least-squares SENSE algorithm;

$$\rho = (E^H E)^{-1} E^H S \quad \text{Equation 1.57}$$

In this work we have omitted the noise matrix to simplify the reconstruction. This results in an SNR penalty, however the unfolding is still ensured (14).

1.4.2.1 Cartesian SENSE

SENSE reconstruction of an accelerated Cartesian data set, can be efficiently performed by direct unfolding of the aliased images in the image domain, as seen in Figure 1.12. The formula derived in Figure 1.12, is a simplified version of Equation 1.57, where the reconstruction matrix (E) is just the inverse of the coil sensitivity data.

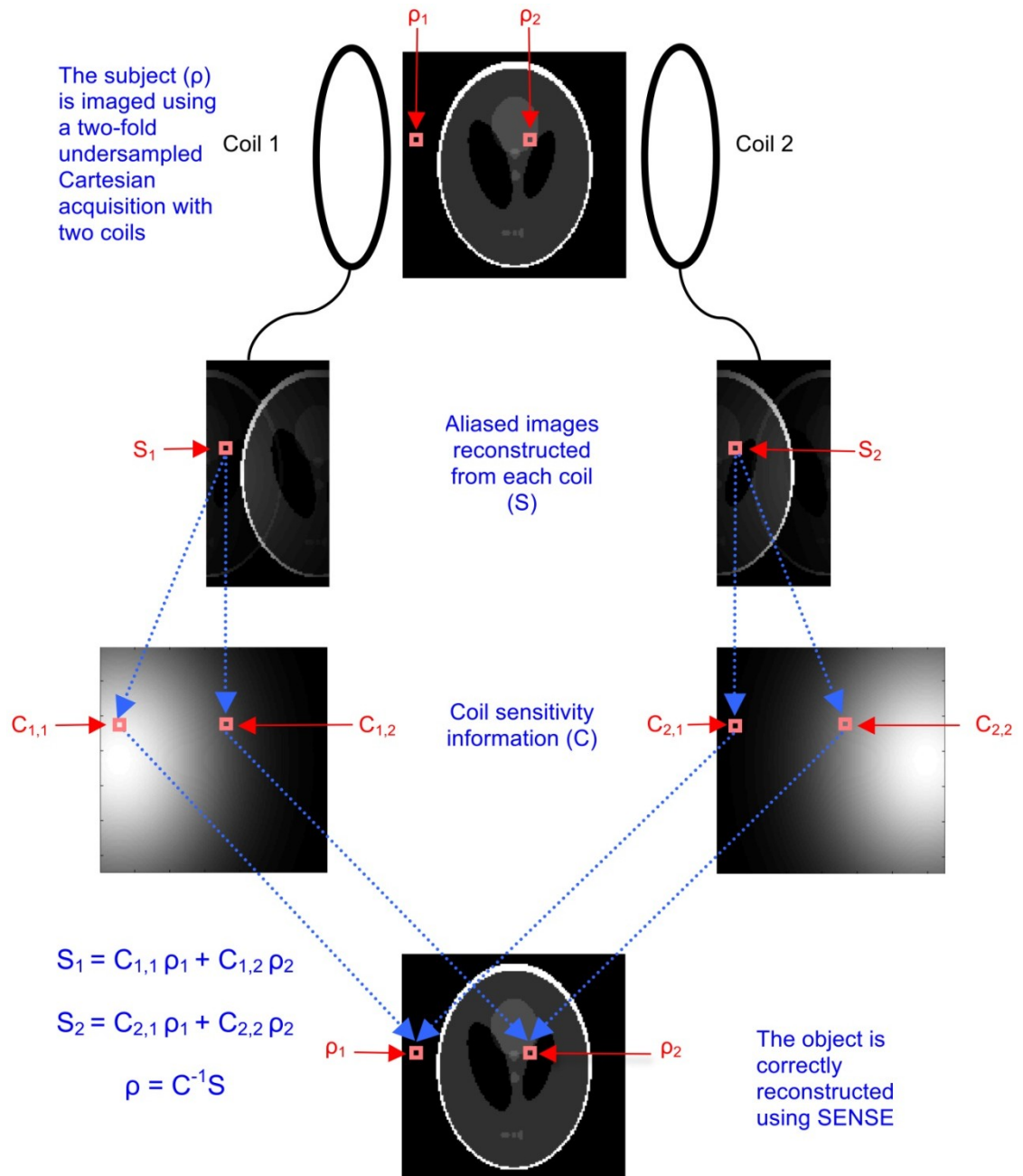


Figure 1.12: Basic Cartesian SENSE by direct unfolding. Simulation made in MATLAB

1.4.2.2 Non-Cartesian SENSE

It is also possible to perform parallel-imaging for data acquired using non-Cartesian trajectories. For example, in an interleaved spiral sequence it is possible to miss out entire spiral readouts, as seen in Figure 1.13.

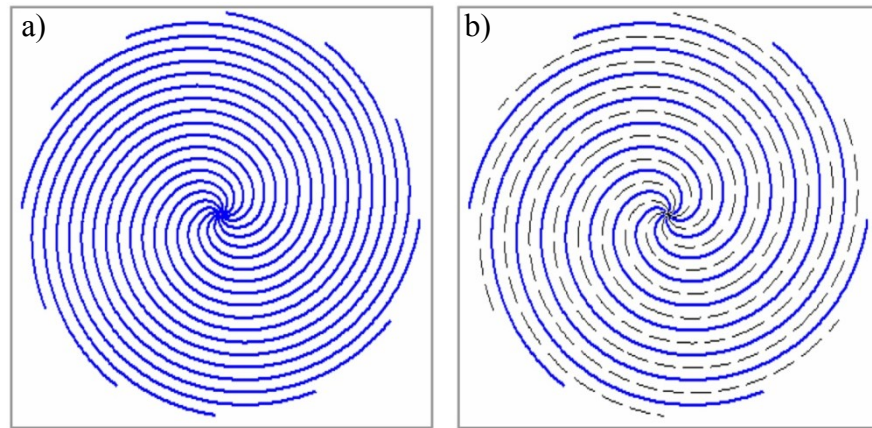


Figure 1.13: Undersampling of spiral k-space data a) Fully sampled data, b) corresponding 2-fold undersampled spiral data

However, undersampled spiral data causes aliasing in the form of streaks and swirls that are not related to the anatomical region that generated the aliasing;

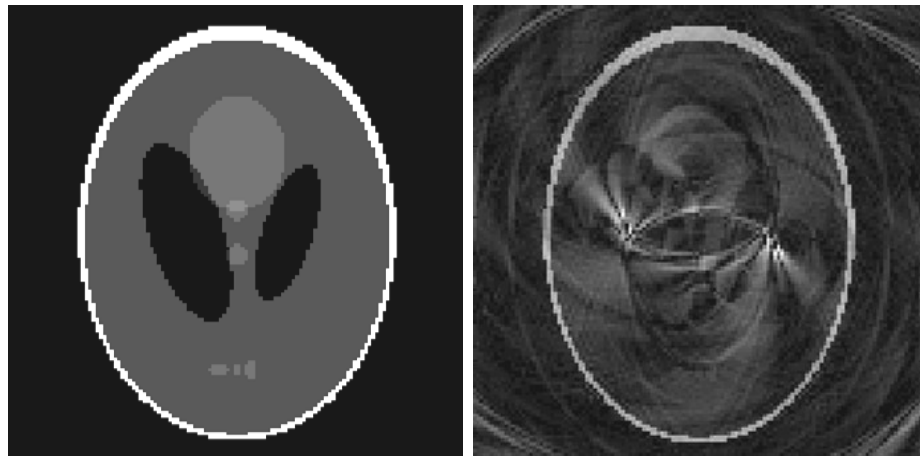


Figure 1.14: Simulated effect of spiral undersampling, performed in MATLAB. a) Fully sampled with 12 spiral interleaves, b) corresponding 2-fold undersampled data

This makes direct unfolding of the data, as seen in Figure 1.12, impossible. Solving Equation 1.57 is numerically challenging as the matrices are very large. A more efficient solution is to solve Equation 1.57 iteratively (13). Typically, the conjugate-gradient (CG) method is used, which solves linear systems in the form;

$$Ax=b$$

Equation 1.58

where x is an unknown vector, and A is a coefficient matrix. The CG converges safely given that A is square, symmetric and positive-definite.

The CG is an iterative method, which can be summarized (13, 25, 26) as;

$$\begin{array}{l}
 d_{(0)} = r_{(0)} = b - Ax_{(0)} \\
 \text{for } (i = 0, 1, 2 \dots) \\
 \quad \alpha_{(i)} = \frac{r_{(i)}^T r_{(i)}}{r_{(i)}^T r_{(i)}} \quad \{\text{compute step length}\} \\
 \quad x_{(i+1)} = x_{(i)} + \alpha_{(i)} d_{(i)} \quad \{\text{update solution}\} \\
 \quad r_{(i+1)} = r_{(i)} - \alpha_{(i)} A d_{(i)} \quad \{\text{compute new residual}\} \\
 \quad \beta_{(i+1)} = \frac{r_{(i+1)}^T r_{(i+1)}}{r_{(i)}^T r_{(i)}} \\
 \quad d_{(i+1)} = r_{(i+1)} + \beta_{(i+1)} d_{(i)} \quad \{\text{compute new search direction}\} \\
 \text{end}
 \end{array}
 \quad \left. \vphantom{\begin{array}{l} \\ \\ \\ \\ \\ \\ \end{array}} \right\} \text{Equation 1.59}$$

where i is the iteration number, d is the search direction, r is the residual (how far we are away from the correct b , which also indicates the direction of steepest descent), α is a scalar determining the step length and β is the Gram-Schmidt orthogonal basis. The initial guess at the solution, $x_{(0)}$, is commonly a matrix of zeros (size: $n_m \times n_m$).

Each iteration of the conjugate gradient results in a refined approximation of x to the exact solution. A convergence check is often performed to limit the time taken for the iterative process. This convergence check is based on the value of α . When the required accuracy (ϵ) is reached ($\alpha < \epsilon$), or the number of iterations exceeds a predefined maximum number of iterations, then the current estimate is used.

From Equation 1.57 and Equation 1.58, for the CG SENSE algorithm;

$$A = E^H E \quad \text{Equation 1.60}$$

$$x = \rho \quad \text{Equation 1.61}$$

$$b = E^H S \quad \text{Equation 1.62}$$

In non-Cartesian SENSE, the encoding matrix, E , consists of;

- Multiplication with the coil sensitivities
- Deapodization; division by the Fourier transform of the gridding kernel (see section 1.3.8)
- Transformation to k-space using the inverse FFT
- Back-gridding of the data onto the experimental k-space trajectory, by convolution with a gridding kernel

The conjugate of the encoding matrix, E^H , therefore consists of;

- Multiplication by weights, W , to perform density correction (see section 1.3.8)
- Gridding onto a Cartesian grid, using convolution with a gridding kernel (see section 1.3.8)
- Transformation into the image domain using the FFT
- Deapodization; division by the Fourier transform of the gridding kernel (see section 1.3.8)
- Multiplication by the complex conjugate of the coil sensitivities

The implementation of the iterative CG SENSE algorithm is shown in Figure 1.15.

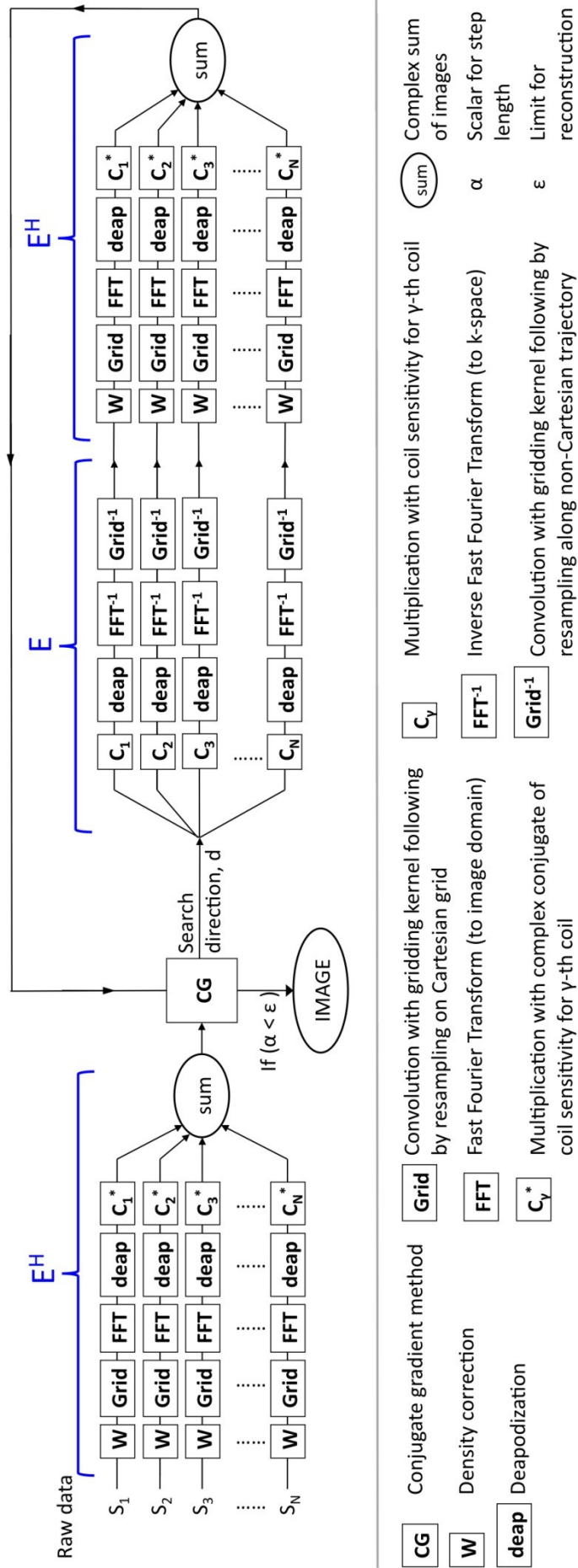


Figure 1.15: Implementation of iterative CG image reconstruction

1.4.2.3 Regularization

The image reconstruction problem often becomes ill-conditioned (27) due to high acceleration factors and/or sub-optimal geometry of the coils, which leads to amplification of noise. It is possible to improve the conditioning of the problem with the use of regularization, which constrains the solution based on some prior knowledge (28). From Equation 1.52 it can be seen that we desire a solution that satisfies;

$$\min \|E\rho - S\|_2 \quad \text{Equation 1.63}$$

where $\|\bullet\|_2$ is the L2-norm. By adding a constraint, we can look for a solution that satisfies (29);

$$\rho_\lambda = \arg \min_{\rho} \left\{ \|E\rho - S\|_2 + \lambda \|L(\rho - \rho_0)\|_2 \right\} \quad \text{Equation 1.64}$$

where λ controls the trade-off between data consistency and regularization, L is a linear transform (chosen to reduce the sensitivity to noise), and ρ_0 is a prior estimate of the solution. This is called *Tikhonov regularization* (28, 29).

The simplest form of Tikhonov regularization is called *zeroth-order regularization*, where L is an identity matrix (29-31). However, the optimal choice of L is a diagonal matrix, with the inverse of the expected signal along the diagonal;

$$L^H L = \theta^{-1} \quad \text{Equation 1.65}$$

where θ is the signal covariance matrix (32, 33).

Equation 1.64 can be re-written as;

$$\left. \begin{aligned} E(\rho - \rho_0) &= S - E\rho_0 \\ \lambda L(\rho - \rho_0) &= 0 \end{aligned} \right\} \quad \text{Equation 1.66}$$

Writing Equation 1.66 in stacked form we get;

$$\tilde{E}\tilde{\rho} = \tilde{S} \quad \text{Equation 1.67}$$

where;

$$\left. \begin{aligned} \tilde{E} &= \begin{bmatrix} E \\ \lambda L \end{bmatrix} \\ \tilde{\rho} &= \rho - \rho_0 \\ \tilde{S} &= \begin{bmatrix} S - E\rho_0 \\ 0 \end{bmatrix} \end{aligned} \right\} \quad \text{Equation 1.68}$$

Equation 1.67 can be solved using the least squares algorithm, in a similar fashion to Equation 1.57;

$$\tilde{\rho} = (\tilde{E}^H \tilde{E})^{-1} \tilde{E}^H \tilde{S} \quad \text{Equation 1.69}$$

Substituting Equation 1.68 into Equation 1.69 we get;

$$\tilde{\rho} = (E^H E + \lambda^2 L^H L)^{-1} E^H (S - E\rho_0) \quad \text{Equation 1.70}$$

$$\rho = \rho_0 + (E^H E + \lambda^2 L^H L)^{-1} E^H (S - E\rho_0) \quad \text{Equation 1.71}$$

1.4.2.4 Preconditioning

In addition to regularization, it is possible to incorporate preconditioning into the iterative SENSE algorithm (34). Preconditioning aims to make Equation 1.62 closer to the desired solution, therefore reducing the number of iterations in the CG. The addition of a diagonal preconditioning matrix (D), to Equation 1.70 gives;

$$D^{-1}\tilde{\rho} = D(E^H ED + \lambda^2 L^H LD)^{-1} DE^H (S - E\rho_0) \quad \text{Equation 1.72}$$

D can be calculated from the coil sensitivity information, and the regularization information (34) by;

$$D_{(x,y)} = \sqrt{\frac{1}{N_{ft} \sum_{\gamma=1}^{N_c} C_{\gamma,xy} C_{\gamma,xy}^* + \text{diag}(\lambda^2 L^H L)_{xy}}} \quad \text{Equation 1.73}$$

where N_{ft} is the number of elements in the final image.

The final CG algorithm with regularization and preconditioning, can be written as;

$$D_{(x,y)} = \sqrt{\frac{1}{N_{ft} \sum_{\gamma=1}^{N_c} C_{\gamma,xy} C_{\gamma,xy}^* + \text{diag}(\lambda^2 \theta^{-1})_{xy}}} \quad \left. \begin{array}{l} \text{\{from Equation 1.73} \\ \text{\& Equation 1.65\}} \end{array} \right\} \text{Equation 1.74}$$

$$d_{(0)} = r_{(0)} = D(E^H (S - E\rho_{(0)}))$$

for ($i = 0, 1, 2 \dots$)

$$q_{(i)} = D(E^H E D d_{(i)} + \lambda^2 \theta^{-1} D d_{(i)})$$

$$\alpha_{(i)} = \frac{r_{(i)}^T r_{(i)}}{d_{(i)}^T q_{(i)}}$$

$$\tilde{\rho}_{(i+1)} = \tilde{\rho}_{(i)} + \alpha_{(i)} d_{(i)}$$

$$r_{(i+1)} = r_{(i)} - q_{(i)}$$

$$\beta_{(i+1)} = \frac{r_{(i+1)}^T r_{(i+1)}}{r_{(i)}^T r_{(i)}}$$

$$d_{(i+1)} = r_{(i+1)} + \beta_{(i+1)} d_{(i)}$$

end

$$\rho = D\tilde{\rho}_{final} + \rho_0$$

1.5 Cardiac Imaging

MRI is an inherently slow imaging methodology, hence it can take seconds to acquire a single two-dimensional image. This makes MR data susceptible to artefacts caused by cardiac and respiratory motion (35). These artefacts must be minimized to obtain images of diagnostic quality

1.5.1 Respiratory Motion

There are three main techniques to reduce respiratory artefacts;

- Multiple signal averages
- Breath-hold imaging
- Respiratory gating

The simplest way to minimize respiratory artefacts is to increase the *number of signal averages* (NSA's). This technique reinforces the signal intensity in static anatomy, however reduces the signal intensity of ghosts caused by the moving anatomy. To achieve good artefact reduction the number of NSA's is often set to 3 (or greater), giving a three-fold increase in total scan time.

If the total imaging time is short (< 25 seconds), it may be possible to perform the scan within a single breath-hold. For certain applications it is also possible to split the acquisition into multiple breath-holds (e.g. for multiple slices), however the breath-hold positions may vary, resulting in inconsistent data. Additionally, many children and sick adults are unable to complete long breath-holds.

Respiratory gating uses navigator information (from respiratory bellows or from a respiratory navigator signal) to only acquire data when the subject is in the same respiratory position. The success of this technique is dependent on the regularity of the patient's respiratory pattern. Generally respiratory gating also results a three-fold increase in total scan time (36).

1.5.2 Cardiac Motion

Cardiac motion is normally compensated by the use of cardiac gating. Normally an electrocardiogram (ECG) signal is used to synchronize the acquisition of data with the cardiac motion. This enables multiple phases of the cardiac cycle to be sampled. There are two main types of cardiac gating;

- Prospective gating
- Retrospective gating

In prospective gating the R-wave of the ECG signal is used to trigger the start of the data acquisition, over multiple heart-beats. Within each RR-interval there is an operator-selected trigger-delay, an acquisition window, and a trigger-window, as shown in Figure 1.16;

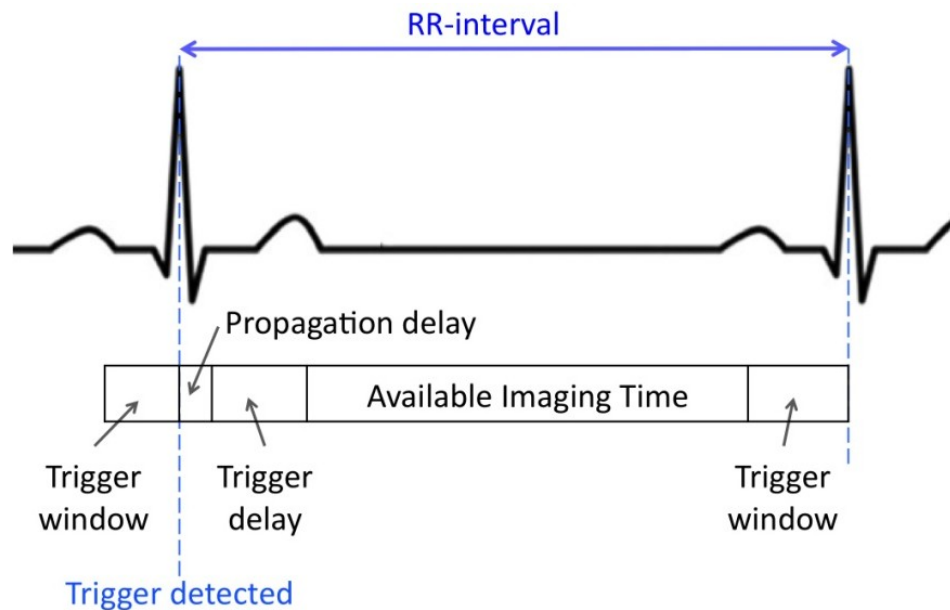


Figure 1.16: Prospective Cardiac gating; the RR-interval is divided into sub-sections

The trigger-window is the time after the data acquisition, when the pulse sequence is waiting for a valid trigger. This is necessary to account for heart rate variability. Once an R-wave is detected the trigger-window closes. A subsequent trigger-delay may be selected by the user to restrict acquisition of data to diastole, however this may be set to zero to maximize acquisition efficiency. In the remainder of the RR-interval, the pulse sequence is played out. Prospectively gated sequences always exclude late diastole, because of the need for a trigger-window.

In retrospective gating, data is continuously acquired over multiple heart-beats, and stored with the simultaneous ECG data. As the MRI data is sampled at arbitrary points in the cardiac cycle, post-processing is required to retrospectively interpolate the data to pre-determined, fixed points in the cardiac cycle. The benefit of retrospective gating is that it can provide data from the whole cardiac cycle.

In both prospective and retrospective gating, the detection of an R-wave causes a change in the line, or group of lines (known as a segment) that is acquired (37), as seen in Figure 1.17.

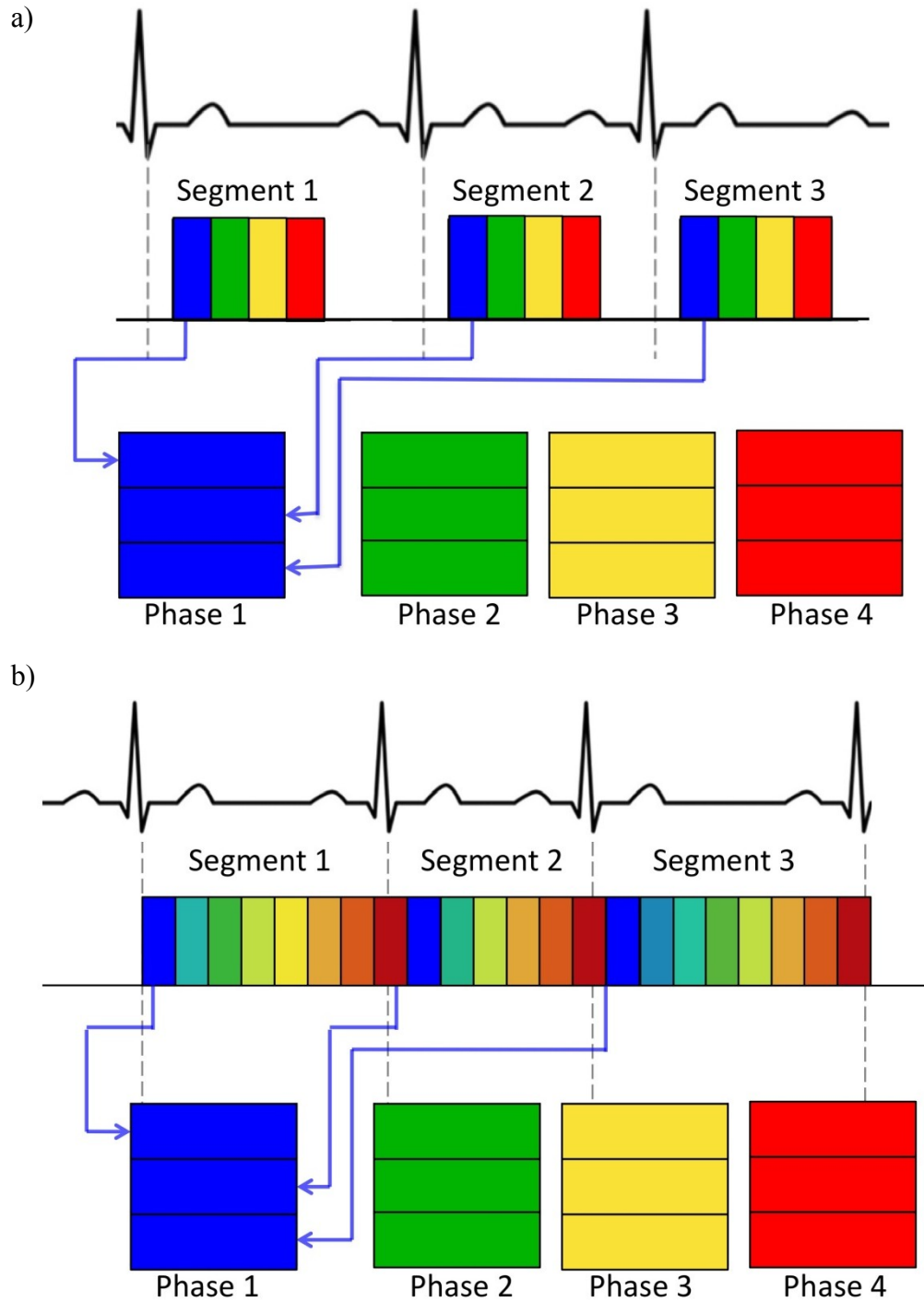


Figure 1.17: Data acquisition in; a) prospective ECG gating, b) retrospective ECG gating. In both sequences, one segment is acquired repeatedly in each R-wave. On detection of an R-wave the segment is changed.

Common problems with ECG-gated acquisitions include;

- Inaccurate R-wave detection
- Irregular heart rates (arrhythmias)

1.6 Flow Measurements

As described in section 1.3.1 the linear magnetic gradients used for spatial encoding in MRI alter the resonant frequency of spins depending on their position, \vec{r} (see Equation 1.28). This makes MRI inherently motion sensitive. As previously demonstrated, spatial encoding is achieved as spins accumulate a phase over time depending on their location. In its general form Equation 1.38 can be written as;

$$\phi(t) = \gamma \int_{t_0}^t \vec{G}(\tau) \vec{r}(\tau) d\tau \quad \text{Equation 1.75}$$

By performing a Taylor expansion of Equation 1.75, it can be seen that the phase accumulated by a spin is linearly proportional to its velocity (38);

$$\phi(t) = \gamma \vec{r}_0 \int_{t_0}^t \vec{G}(\tau) d\tau + \gamma \vec{v}_0 \int_{t_0}^t \vec{G}(\tau) \tau d\tau + \dots + \gamma \frac{1}{n!} \int_{t_0}^t \vec{G}(\tau) \tau^n d\tau \quad \text{Equation 1.76}$$

where r_0 is the initial displacement of the spin along the direction of the gradient, and v_0 is the initial velocity of the spin in the direction of the gradient.

As the n^{th} -order moment of a gradient, M_n , is defined as;

$$M_n = \gamma \int_{t_0}^t \vec{G}(\tau) \tau^n d\tau \quad \text{Equation 1.77}$$

it can be seen that the sensitivity of MRI to the velocity of spins is related to the first-order gradient moment (M_1);

$$\phi(t) = \gamma \left(\vec{r}_0 M_0 + \vec{v}_0 M_1 + \dots + \frac{1}{n!} \left(\frac{d^n r}{dt^n} \right)_{t=0} M_n \right) \quad \text{Equation 1.78}$$

The encoding of velocity into the phase of an MR signal is known as *phase-contrast* (PC) imaging (39).

1.6.1 Implementation of Phase-Contrast Imaging

Assuming there is no accelerative or higher order motion of spins, Equation 1.78 simplifies to;

$$\phi(t) = \gamma(\vec{r}_0 M_0 + \vec{v}_0 M_1) \quad \text{Equation 1.79}$$

It is possible to remove the effect of displacement (r_0) on the phase of signal, with the use of a bi-polar gradient with two lobes of equal area but opposite polarity. The net area of the bi-polar gradient is therefore zero, i.e. M_0 is zero. In this case Equation 1.79 can be simplified to;

$$\phi(t) = \gamma \vec{v}_0 M_1 \quad \text{Equation 1.80}$$

From Equation 1.80 it can be seen that the resulting phase is only related to the velocity of the spins;

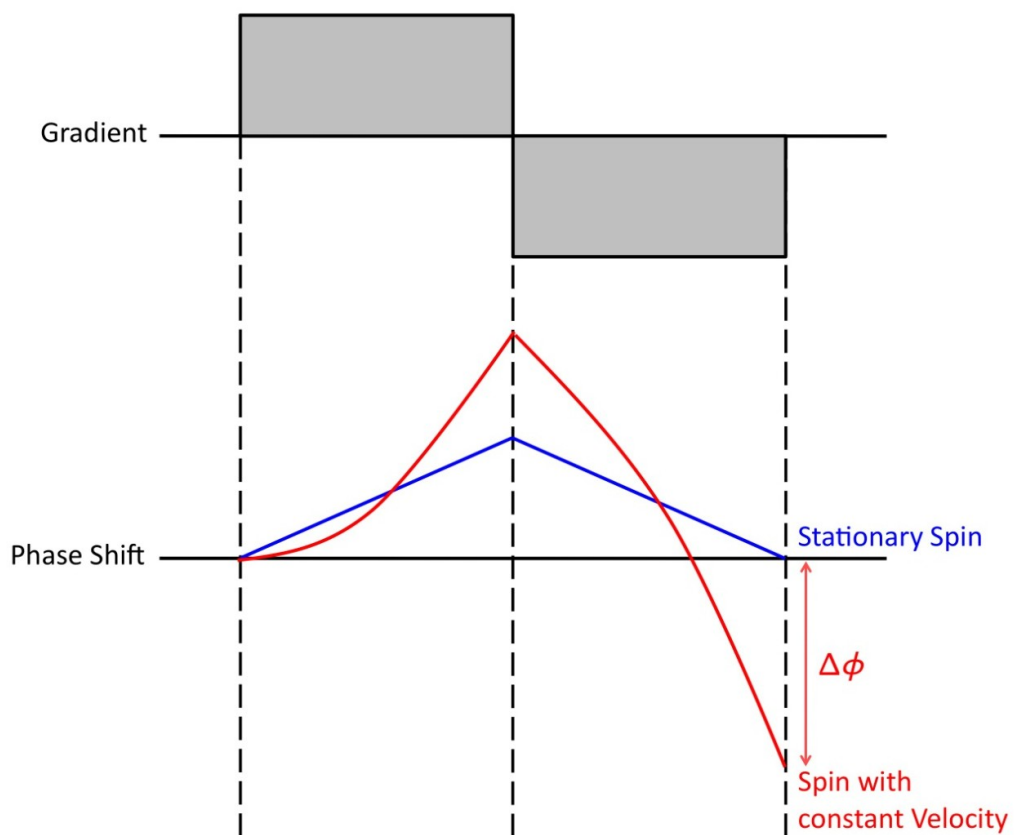


Figure 1.18: A balanced bipolar gradient causes a phase shift which is proportional to the velocity of the spins

Unfortunately phase offsets may arise from additional sources, e.g. B_0 inhomogeneities, susceptibility effects, concomitant gradients or eddy currents. In order to remove these additional phase offsets, normally two interleaved measurements are made with different first-order gradient moments. The phase of the resultant images is subtracted, thereby subtracting out the background phase offsets. The phase difference in PCMR is therefore commonly expressed as a difference in the first-order moments of the two images, ΔM_1 ;

$$\Delta\phi = \gamma \vec{v}_0 \cdot \Delta M_1 \quad \text{Equation 1.81}$$

The value of ΔM_1 determines the maximum velocity that can correctly be encoded in PCMR before aliasing occurs – this is often referred to as the *velocity encoding* (VENC). A spin travelling at \pm VENC (m/s) will cause a phase shift of $\pm \pi$ radians, as;

$$VENC = \frac{\pi}{\gamma \Delta M_1} \quad \text{Equation 1.82}$$

Although alternative encoding strategies are possible, it is common to acquire one data set with velocity-compensated gradients (i.e. with a VENC of zero) and the other data set with velocity-encoded gradients (i.e. with the desired VENC). This is called *asymmetric encoding*.

It is possible to measure flow in any direction, however most commonly flow is measured through-plane. This is achieved by placing the flow gradients on the z -axis after the slice-select gradient. Here the flow gradients can be combined with the slice-select rewriter gradient to minimize the TE. Conventionally each line in k -space is acquired using flow-compensated gradients, and then with flow-encoded gradients, before moving to the next line in k -space, as seen for a Cartesian sequence in Figure 1.19.

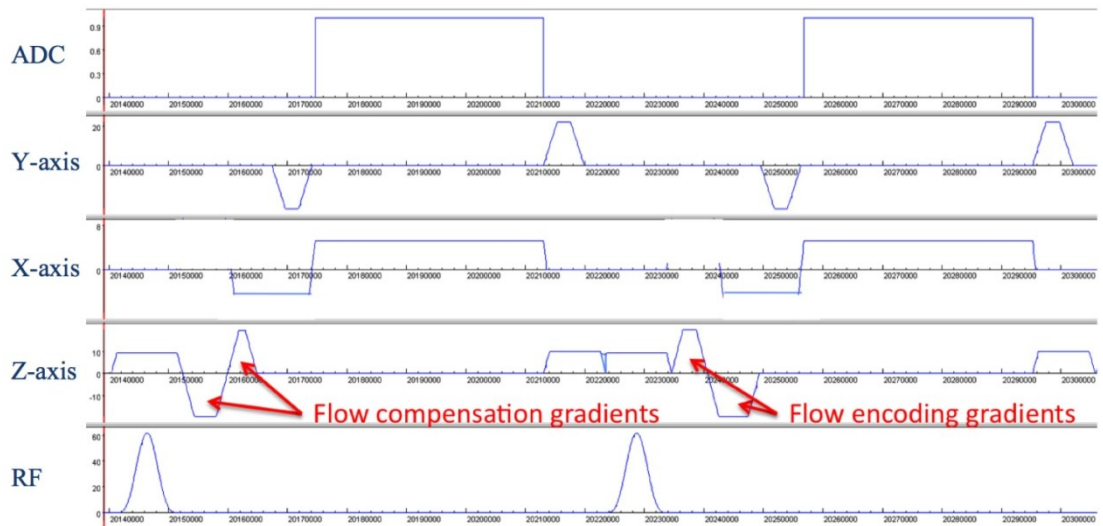


Figure 1.19: Example of a Cartesian PC sequence. Each line is acquired with flow-compensated and flow-encoded gradients before moving to the next line in k-space

Every PC acquisition yields a magnitude image and a phase image. The magnitude image gives information about the anatomy and is used for segmentation. The phase image gives the velocity of blood in each voxel and can be used to calculate flow volumes.

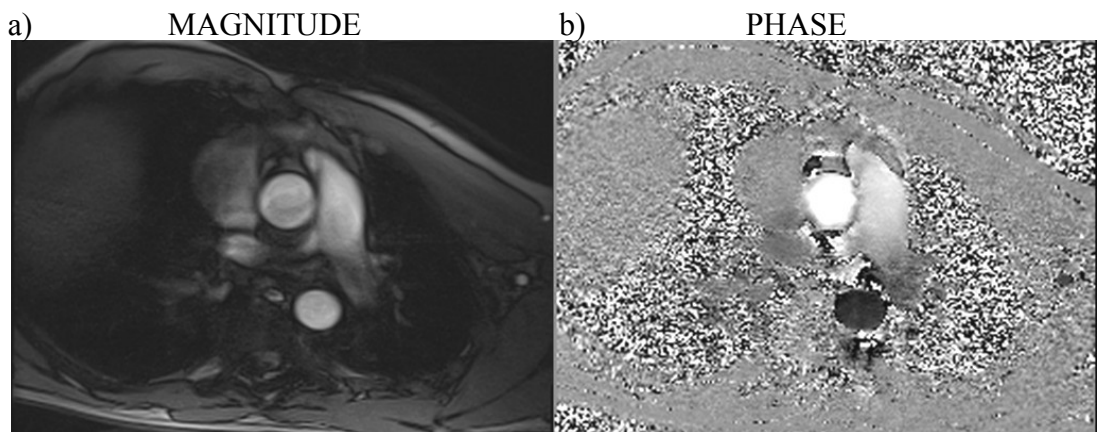


Figure 1.20: Example of a PC data in the ascending aorta of a healthy volunteer

1.6.2 Accuracy of PCMR

In the clinical environment, measures of stroke volume, cardiac output and regurgitation fraction from flow measurements are used to determine patient diagnosis and treatment.

The accuracy of PCMR depends on;

- Adequate temporal resolution to accurately detect the peak velocities
- Adequate spatial resolution to prevent partial-volume effects (see below)
- The spins within each voxel to be travelling at the same velocity, to prevent intravoxel dephasing (see below)
- A suitable match between the velocities in the vessel of interest and the chosen VENC;
 - If the VENC is too small, then wrap occurs where the phase shift is greater than $\pm \pi$
 - If the VENC is too large, then noise may mask the true velocities
- The angle of the imaging plane to the main direction of flow – for through-plane flow the most precise measurements are obtained if the plane is orthogonal to the direction of flow
- Complete subtraction of background phase offsets
- The accuracy of vessel segmentation

Partial-volume effects are observed when there are both stationary and flowing spins within a voxel, e.g. in voxels that are on vessel boundaries. This results in overestimation of flow because the signal intensity from the blood pool is greater than that from surrounding tissue, causing the velocity of the flowing spins to be weighted more heavily than the stationary spins. The smaller the vessel (or the larger the pixels), the larger the relative number of pixels influenced by partial-volume effects.

Intravoxel dephasing occurs when there are spins with different velocities within a voxel, causing destruction of phase coherence. Intravoxel dephasing may be caused by accelerative spins, turbulent spins or magnetic field inhomogeneity. Both partial-volume effects and intravoxel dephasing can be reduced by increasing the spatial resolution of the images.

Greil, et al. (40) investigated the effect of the above parameters on the accuracy of PCMR in a pulsatile flow phantom. They found that mean percentage error did not differ significantly with;

- Slice thickness (4, 6, 8 mm, $p = 0.4$)
- Slice inclination (0° , 10° , 20° , 30° , 40° , $p = 0.09$)
- RF-flip angle (10° , 15° , 20° , 30° , 40° , $p = 0.19$)
- VENC (1.0, 1.5, 2.0, 2.5, 3.0, 3.5, 4.0 m/s, $p = 0.82$)

However, they found that as the spatial resolution was decreased (by increasing the FOV), the error percentage grew linearly ($y = 0.35x - 7.6$), as shown in Figure 2.21;

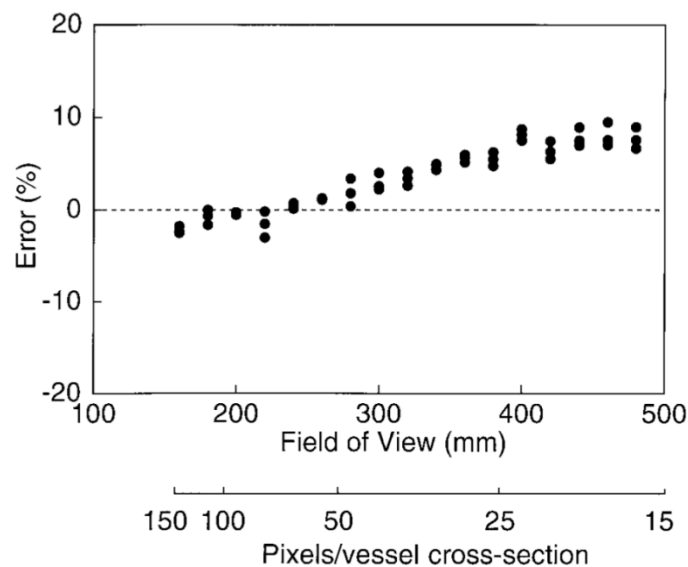


Figure 1.21: From Greil, et al. (40). A linear relationship was found between the number of pixels in the vessel of interest and the percentage flow error

Where there were only 16 pixels in the cross section of the vessel, the flow velocity was overestimated by an average of 9.0 %. Greil, et al. concluded that providing the spatial resolution is great enough, PCMR is an accurate and robust method of measuring flow (40).

Tang, et al. (41) have also shown that the accuracy of flow measurements improves as spatial resolution increases. They showed that there must be at least 16 isotropic voxels within the vessel of interest to achieve flow measurements within 10 % of the true value.

1.6.3 Concomitant Gradients in Flow Imaging

Concomitant gradients (also known as *Maxwell* gradients) are unintentional gradients with nonlinear spatial dependence, which occur in addition to the desired linear magnetic field gradients. These concomitant gradients are instantaneous with the applied gradients (unlike eddy currents which can last beyond the applied gradients), and are a consequence of Maxwell's equations for the divergence and curl of the magnetic field.

Concomitant gradients cause undesired phase offsets in images and therefore incorrect velocity measurements in PCMR. The concomitant gradient field can be calculated (42) as;

$$B_c(x, y, z, t) = \frac{1}{2B_0} \left\{ \begin{array}{l} G_x^2 z^2 + G_y^2 z^2 + G_z^2 \frac{x^2 + y^2}{4} \\ - G_x G_z xz - G_y G_z yz \end{array} \right\} \quad \text{Equation 1.83}$$

Causing a phase accumulation of;

$$\Delta\phi_c(x, y, z, t) = \gamma \int B_c(x, y, z, t) dt \quad \text{Equation 1.84}$$

From Equation 1.83 and Equation 1.84 the residual phase in PCMR caused by concomitant gradients (after the phase difference calculation) can be calculated as (42);

$$\Delta\phi_c(x, y, z) = Az^2 + B(x^2 + y^2) + Cxz + Dyz \quad \text{Equation 1.85}$$

$$\left. \begin{aligned} A &= \frac{\gamma}{2B_0} \int \left\{ [G_x^2(t) + G_y^2(t)]_{f_{e1}} - [G_x^2(t) + G_y^2(t)]_{f_{e2}} \right\} dt \\ B &= \frac{\gamma}{8B_0} \int \left\{ G_z^2(t)_{f_{e1}} - G_z^2(t)_{f_{e2}} \right\} dt \\ C &= \frac{\gamma}{2B_0} \int \left\{ [G_x(t)G_z(t)]_{f_{e1}} - [G_x(t)G_z(t)]_{f_{e2}} \right\} dt \\ D &= \frac{\gamma}{2B_0} \int \left\{ [G_y(t)G_z(t)]_{f_{e1}} - [G_y(t)G_z(t)]_{f_{e2}} \right\} dt \end{aligned} \right\} \quad \text{Equation 1.86}$$

where $fe1$ is the first flow image and $fe2$ is the second flow image. The integrals are evaluated over a time period from the end of the RF-excitation pulse, to the beginning of the ADC readout.

Maxwell gradients also affect all imaging gradients, and may play an important part in spiral imaging (43). In spiral imaging the effect of concomitant gradients is much harder to correct, as each point in the readout has to be corrected by a different phase offset.

1.6.4 Additional Phase Offsets

Additional phase offsets in PC imaging have been widely observed after phase subtraction (44-48). These phase offsets may arise from inhomogeneities in the magnetic field or eddy current effects. They are affected by the imaging position, VENC, maximum gradient amplitude and maximum gradient slew rate, amongst others. Like concomitant gradients, these phase offsets cause incorrect velocity measurements in PCMR.

Gatehouse, et al. (48) performed a multi-centre, multi-vendor study into background phase offsets in PC acquisitions from 12 systems. In this study no post-processing was carried out to correct for phase offsets. In a static phantom, located up to 70 mm from the magnet isocenter, the phase offset over a circular region-of-interest with 30 mm diameter, gave a velocity offset from 0.4 cm/s to 4.9 cm/s. Over all planes and systems the average velocity offset was 2.7 cm/s – this represents 1.8 % of the 150 cm/s VENC used.

Gatehouse, et al. (48) suggest a 5 % error in volume to be the limit of acceptability. Therefore in an 80 mL/cycle stroke volume, the limit of acceptability is 4 mL/cycle error. In theory, in a great vessel of diameter 30 mm, an average velocity offset of 2.7 cm/s would cause a 19.1 mL/cycle error in stroke volume (with a heart rate of 60 bpm). This is ~5 times the 4 mL/cycle limit of acceptability, demonstrating the importance of background phase correction in PCMR.

Commonly manual post processing techniques are used to remove additional phase offsets. One such method involves estimation of the phase offset from a region of stationary tissue near to the vessel of interest (40, 46, 49). Unfortunately this method does not work well in the great vessels, as there is very little surrounding stationary tissue.

Alternatively, a separate scan can be performed on a stationary phantom with identical imaging parameters (45, 50, 51). From these images the phase offsets in the same region as the vessel can be calculated. This method is time consuming and inconvenient in clinical practice, as it must be carried out for every PC image acquired.

A semi-automated method described by Walker, et al. assumes the phase offsets vary linearly in space (52). The phase offsets can be predicted by fitting a plane through the stationary pixels in the phase image. This plane is subtracted from the velocity images to correct for phase offsets. This technique is widely used however the phase offsets are often assumed to be of a low-order (40, 46, 47, 53, 54). This technique can be completely automated, however it does not work for very noisy data or in images where there is very little stationary tissue.

CHAPTER 2

Real-time Flow Measurements

2.1 Introduction

Exercise is a powerful stimulator of the cardiovascular system and can be used to unmask subtle changes in early hypertensive disease (55). Exercise testing is a common medical exam carried out to assess for cardiac disease, where the patient is placed on a treadmill and the level of exercise is progressively increased. Routinely, only blood pressure (BP) and heart rate response are measured during exercise (55). These are not sensitive markers of early vascular dysfunction and thus the full potential of exercise stress testing is not achieved. It would be advantageous if systemic vascular resistance (R) and total arterial compliance (C) could also be measured during exercise (see section 2.2.4). This requires quantification of flow, as well as blood pressure measurements.

Cardiac gated PCMR is a proven method of measuring blood flow at rest (56-59). However, gated flow sequences are not reliable during exercise due to excessive motion. Additionally, gated sequences average data from multiple heart-beats, which prohibits the assessment of short-term changes in flow patterns which occur during exercise.

A pharmacological stress test can be used instead of exercise, to increase the load on the heart, e.g. using Dobutamine or Adenosine. Pharmacological stress tests are important in subjects with physical limitations, e.g. severe arthritis, prior injury or reduced exercise tolerance. However, exercise testing is advantageous over pharmacological stress tests due to the physiologic effects of exercise. Although, there are possible side-effects to both exercise and pharmacological agents, generally fewer side effects are observed in response to exercise than to pharmacological agents. Table 2.1 shows a comparison of side effects from exercise testing and Dobutamine testing in the same group of patients (N=136) as found by Beleslin, et al. (60). In this study at least one symptom was observed in 46% of patients during exercise and in 79% of patients during pharmacological stress tests using Dobutamine. Of these, serious symptoms were found in 3% of patients during exercise and in 11% of patients during pharmacological stress tests using Dobutamine.

	Exercise (%)	Dobutamine (%)
Any symptom	46	79
Shivering/chilling	0	52
Flushing	0	8
Shortness of breath	14	7
Headache	10	4
Premature Ventricular Contractions	13	32
Serious symptom	3	11
Hypotension	1	6
Tachycardia	2	3
Atrial Fibrillation	0	1
Atrioventricular block	0	1

Table 2.1: Adapted from Beleslin, et al. (60), showing comparison of side effects from exercise and Dobutamine in the same group of patients

Previous exercise studies have been carried out using MRI. These have mostly used cardiac gated sequences, hence required suspension of exercise during imaging (see section 2.2.2). This is non-physiological (61) and makes ramped exercise protocols difficult to perform (where the exercise intensity is increased throughout the exam). A better approach may be to use real-time imaging where data is acquired within one heart-beat, rather than averaging data over many heart-beats (see section 2.2.1). Real-time MR is less susceptible to motion (caused either by exercise or breathing) and can be performed without cardiac gating, making it more suited to imaging during exercise. However, real-time imaging may come at the cost of low temporal or low spatial resolution, which may affect its accuracy at high heart rates present during exercise.

The high temporal resolution required for real-time imaging during exercise can be achieved through efficient k-space filling, combined with parallel imaging. In this study we investigated the use of an undersampled spiral PCMR sequence, reconstructed using an iterative SENSE algorithm, to measure the hemodynamic response to exercise.

2.1.1 Aims

The aims of this study were to:

- Develop a real-time spiral SENSE PCMR sequence with a high temporal resolution
- Develop an iterative CG SENSE, PCMR reconstruction algorithm
- Validate the real-time flow sequence in-vitro and in-vivo
- Demonstrate the feasibility of using this sequence to measure cardiac output during exercise
- Combine the flow measurements from the real-time spiral SENSE PCMR sequence with non-invasive pressure measurements to calculate vascular resistance and compliance

2.1.2 Personal Contribution

To fulfil the above aims I have:

- Designed and developed a uniform density spiral sequence with data undersampling, for PCMR measurements (see section 2.3.1) in the Siemens, IDEA environment. The spiral trajectory is calculated based on code developed by Brian Hargreaves (62)
- Optimised the spiral sequence to achieve a high temporal resolution with adequate image quality (see section 2.3.5), as well as reducing background phase offsets (see section 2.3.4)
- Designed and developed an iterative CG reconstruction for spiral SENSE PCMR data (see section 2.3.2) in the Siemens, ICE environment (also prototyped in MATLAB). This is based on code for iterative CG reconstruction of radial k-t SENSE data, developed by Michael Hansen. Specifically, it uses Michael Hansen's gridding algorithm
- Implemented concomitant gradient correction (see section 2.3.3)
- Performed in-vitro validation of the sequence, in a pulsatile flow pump (see section 2.4)

- Performed in-vivo validation of the sequence, in 20 healthy volunteers, at rest (see section 2.5.5)
- Used the sequence to measure flow in 20 healthy volunteers at rest and at two different exercise levels (see section 2.5). This data was combined with simultaneous blood pressure measurements to quantify resistance and compliance (see section 2.5.6)
- Developed a plug-in for OsiriX (the OsiriX Foundation, Geneva, Switzerland), to analyse real-time flow data (see section 2.3.6.1)
- Developed a plug-in for OsiriX to quantify resistance and compliance (see section 2.3.6.2)

The results from this work have been published by J. Steeden, D. Atkinson, A. Taylor and V. Muthurangu, in the *Journal of Magnetic Resonance Imaging*, 2010, **31**(4), entitled; “Assessing vascular response to exercise using a combination of real-time spiral phase-contrast MR and noninvasive blood pressure measurements” (63) (see Appendix 1).

2.2 Literature Review

In this section, literature on the following areas will be discussed:

- Real-time flow measurements
- Performing MRI during exercise
- Assessment of hemodynamic parameters using MRI

2.2.1 Real-time Flow Measurements

Real-time flow measurements have been achieved through the use of efficient trajectories (including EPI and spirals) and more recently through the use of parallel imaging.

2.2.1.1 Efficient Trajectories

In 2000, Nayak, et al. (64) developed a real-time PCMR sequence using spiral trajectories, with a sliding window reconstruction. Sliding window is a view sharing technique where intermediate images are formed whenever a new line is acquired.

A water-selective spectral-spatial excitation pulse (duration 7 ms) was used to avoid blurring from off-resonant fat signals. The sequence parameters are shown in Table 2.2.

Nayak, et al. showed a good correlation (within 5 %) between a reference standard PCMR sequence and the spiral flow sequence, in a constant flow phantom with through-plane and in-plane flow measurements. Experiments in a pulsatile flow pump showed that the spiral sequence was able to accurately capture the shape and peak of the velocity waveform, compared to continuous-wave Doppler ultrasound.

Sequence Parameters	
TE/TR	8/30 ms
Spiral interleaves	3
Flip angle	30°
FOV	200 mm
Matrix	87×87
VENC	242 cm/sec
Temporal resolution	180 ms (~6 frames/sec)
Spatial resolution	2.4×2.4 mm

Table 2.2: Sequence parameters used by Nayak, et al. (64)

The temporal resolution achieved by Nayak, et al. is low, meaning that the sequence is unlikely to accurately detect the peak flow. The low temporal resolution is partly due to the long spectral-spatial excitation pulse (7 ms), as well as long spiral readouts (16 ms), giving a long TR of 30 ms. The long excitation and long readout may also cause signal reduction in areas of flow, as high velocity spins may not experience the full excitation, or may move significantly during the readout. However, the use of a spectral-spatial pulse does allow for a small FOV without wrap artefacts.

Non-spiral trajectories have also been used for real-time flow imaging. Klein, et al. (65) used a turbo gradient-echo EPI PCMR sequence to measure flow in 47 patients. In large and medium sized vessels (with diameters 20-55 mm and 6-13 mm, respectively) vessel diameter, peak velocity and flow volumes were quantified. The sequence parameters for the real-time EPI sequence are shown in Table 2.3, where the EPI factor is the number of lines acquired per EPI readout. The flow results were compared to a reference standard (free-breathing, retrospectively-gated) PCMR sequence.

Sequence Parameters	
TE/TR	6.8/15.5 ms
EPI factor	9
Flip angle	20°
FOV	200-350 mm
Matrix	64×128
VENC	200 cm/sec
Temporal resolution	124 ms (~8 frames/sec)
Spatial resolution	~4.7×2.3 mm

Table 2.3: Sequence parameters used by Klein, et al. (65).

Klein, et al. found a reasonably good agreement between the reference standard PCMR sequence and their EPI flow sequence, for large and medium size vessels in terms of vessel diameter ($r = 0.97$ and $r = 0.71$, relative difference; 4 % and 16 % respectively) and peak velocity ($r = 0.88$ and $r = 0.81$, relative difference; 10 % and 14 % respectively). The flow volumes correlated reasonably well in large vessels ($r = 0.87$, relative difference; 16 %) but not in the medium size vessels ($r = 0.64$, relative difference; 31 %).

This study achieved low temporal and low spatial resolution imaging, without any data undersampling or data sharing. The sequence was not accurate in terms of stroke volume, in medium vessels. This significant difference is most likely to be due to low spatial resolution of the EPI sequence, which resulted in ~6 cross sectional pixels within the vessel. As discussed in section 1.6.2, Tang, et al. (41) have shown that there must be at least 16 voxels within the vessel of interest to achieve flow measurements within 10 % of the true value. This study demonstrates the need for good spatial resolution to prevent partial volume effects and ensure accurate flow volume measurements.

From these studies it can be seen that the temporal resolution achieved by efficient trajectories alone, is not adequate for real-time imaging.

2.2.1.2 Parallel Imaging

Further increases in temporal resolution for real-time PCMR have been achieved by combining efficient trajectories with parallel imaging, including SENSE.

In 2004 Körperich, et al. (66) developed a free-breathing, real-time, single-shot EPI PCMR sequence, accelerated with SENSE. The sequence parameters were;

Sequence Parameters	
TE/TR	4.9/19.4 ms
EPI factor	19
Half-scan factor	0.6
SENSE factor	4
Flip angle	40°
FOV	300×340 mm
Matrix	112×128
VENC	200 cm/sec
Temporal resolution	39 ms (~25 frames/sec)
Spatial resolution	~2.7×2.7 mm

Table 2.4: Sequence parameters used by Körperich, et al. (66)

The *half-scan factor* used in this study (also known as *partial-Fourier acquisition*) indicates how much of k-space is filled. A half-scan factor of 0.6, only acquires 60 % of k-space (one entire half and only a small proportion of the other half). The remaining lines are zero padded (a more advanced *homodyne reconstruction* cannot be used for PCMR as this results in the loss of the phase data (36)). If the object is real, its Fourier transform is Hermitian, i.e.

$$S(-k_x, -k_y) = S^*(k_x, k_y) \quad \text{Equation 2.1}$$

where * denotes the complex conjugation. Unfortunately this assumption is never true because unwanted phase shifts cause the reconstructed object to be complex. As flowing spins cause phase shifts, PCMR data is always complex, hence its Fourier

transform is not Hermitian. This is likely to result in errors in the phase of PCMR data if the half-scan factor is lower than 75 % (36).

Körperich, et al. validated this real-time EPI PCMR sequence using a pulsatile flow phantom, by comparison of 6 flow volumes with the *bucket and stopwatch* method. Despite the low half-scan factor used, a good correlation was found ($r = 0.999$) with a moderate overestimation ($y = 1.26x + 0.03$) and relative differences of 12.8-28.1 % ($p < 0.006$).

In-vivo experiments were carried out in 14 paediatric patients (age: 5.2 ± 2.0 years) with cardiac left-to-right shunt. The Q_P/Q_S ratio (ratio of flow in the pulmonary artery to flow in the aorta) was calculated from a reference standard (free-breathing, retrospectively-gated) PCMR sequence and from the real-time EPI PCMR sequence (Q_P/Q_S ratio; 1.91 ± 0.64 vs. 1.94 ± 0.68 , respectively). Comparison of the stroke volumes from the two sequences found negligible difference in the pulmonary artery (3 %) and aorta (2 %).

By combining a SENSE factor of 4 with a half-Fourier technique, Körperich, et al. were able to achieve high temporal resolution imaging (39 ms). However, in this study it was necessary to perform a separate scan (< 1 minute) to calculate the coil sensitivities.

Körperich, et al. performed 1D SENSE (as the data was only undersampled the in the phase-encode direction) using a 5-element cardiac coil for signal detection. Four-fold acceleration seems to be very high for 1D SENSE, as the acceleration factor in SENSE is bound by the number of independent coils used in the direction of the undersampling (14, 67). However it is likely that the technique was successful due to the large FOV used (300×340 mm) in small children (average age: 5.2 years). As these children are likely to be much smaller than the FOV, this means that in the undersampled images, many pixels will have less than 4 aliases (i.e. the acceleration factor is effectively less than 4), simplifying the reconstruction.

In 2005 Nezafat, et al. (68) described a real-time auto-calibrated spiral TSENSE sequence. In this study the spiral interleaves were rotated in each phase, so that by combining the raw data from R (acceleration factor) frames, a fully sampled, full FOV image could be reconstructed. This allowed adaptive coil sensitivities to be calculated from the acquired data, removing the need for an additional scan (see section 1.4.1).

Nezafat, et al. measured flow in the ascending aorta and in the aortic valve of one healthy volunteer, using the sequence parameters shown in Table 2.5. No validation of the spiral sequence is shown.

Sequence Parameters	Ascending Aorta	Aortic Valve
TE/TR	2.3/15.2 ms	15.2 ms
Spiral interleaves	8	?
SENSE factor	4	3
Flip angle	30°	30°
FOV	340×340 mm	260×260 mm
Slice thickness	10 mm	10 mm
Matrix	?	256×256
VENC	150 cm/sec	150 cm/sec
Temporal resolution	60.8 ms (~16 frames/sec)	91.2 ms (~11 frames/sec)
Spatial resolution	?	1.8×1.8 mm

Table 2.5: Sequence parameters used by Nezafat, et al. (69)

There are several limitations to this study, including;

- Demonstration of the technique in just one healthy volunteer
- No validation of the sequence
- Low temporal resolution achieved, especially in the aortic valve (91.2 ms)
- Reconstruction of data offline, in MATLAB

From these studies it can be seen that by combining efficient trajectories with parallel imaging, it is possible to achieve high temporal and spatial imaging. Körperich, et al. (66) demonstrated high resolution imaging in small children with the use of partial-Fourier EPI trajectories, undersampled by SENSE. Unfortunately, EPI trajectories have a long TE which is not optimal for flow imaging, as moving spins have a long time to dephase before the centre of k-space is sampled. Spiral trajectories have a much shorter TE, as they start in the centre of k-space, making them optimal for flow imaging (6, 7). Additionally spiral sequences allow undersampling in 2D, unlike EPI. Nezafat, et al. (69) used spiral trajectories undersampled by SENSE, however the temporal resolution achieved (60.8-91.2 ms) is not adequate for imaging high heart rates expected during exercise.

We wish to achieve high temporal resolution real-time PCMR imaging, using spiral trajectories because of the short TE's possible. We wish to calculate the coil sensitivities from the data itself, not from a separate pre-scan as performed by Körperich, et al. (66). We will also reconstruct the data on-line, unlike Nezafat, et al. (69), as this will allow the user to view the images and repeat the scan if necessary. Reconstructing the data on-line will make the real-time sequence clinically useful, and allows all images to be stored and backed-up with the remaining images from the study.

2.2.2 Performing MRI During Exercise

Studies investigating the response to exercise with MRI often use supine ergometers, as it is not possible for subjects to be upright within a conventional MRI scanner. Most studies require ECG gating to achieve suitable spatial and temporal resolution. In these studies the subjects are normally required to suspend exercise, in order to perform MRI measurements. This is non-physiological, as cardiac dynamics change rapidly after exercise (61). Studies have shown a greater sensitivity to disease at peak exercise than post-exercise, e.g. Dymond, et al. (70) found 100 % vs. 70 % sensitivity using radionuclide angiography and by Hecht, et al. (71) found 100 % vs. 78 % sensitivity using echocardiography. Suspension of exercise also makes ramped exercise protocols difficult to perform.

Studies that have performed PCMR with gated sequences, immediately after supine exercise include Mohiaddin, et al. in 1999 (72), Pederson, et al. in 1999 (73) and 2002 (74) and Jekic, et al in 2008 (75).

Studies by Taylor, et al. in 2002 (76), Cheng, et al. in 2003 (77), 2004 (78), 2005 (79) and Tenforde, et al. in 2010 (80) have performed cardiac gated flow measurements during the continuation of upright exercise (using a 0.5 T open-bore MRI system). This upright cycling position enables higher levels of exercise in a more natural and comfortable exercise position, however there are very few vertical, open-bore magnet systems. Additionally, the low magnetic field strength used results in low SNR images.

There are very few studies that use real-time PCMR sequences (without the use of ECG gating) to acquire data during continuation of exercise. One such study was performed by Hjortdal, et al. (81). They used a real-time, segmented EPI sequence to investigate the influence of exercise on flow, in 11 paediatric patients (age: 12.4 ± 4.6 years). The sequence parameters were;

Sequence Parameters	
TE/TR	4-5/12-13 ms
EPI segments	13
Half-scan factor	0.8
FOV	90×136 mm
Slice thickness	5-7 mm
Matrix	26×64
VENC	50-120 cm/sec
Temporal resolution	48-56 ms (~20 frames/sec)
Spatial resolution	3.4×2.1 mm

Table 2.6: Sequence parameters used by Hjortdal, et al. (81)

Flow was measured at rest and at two exercise levels (0.5 and 1.0 W/kg) in the inferior vena cava (IVC), superior vena cava (SVC) and in the ascending aorta. For each real-time flow measurement 120 consecutive PC images were acquired. Blood flow and stroke volume were quantified over two respiratory cycles. It was found that mean aortic and IVC flow rates increased significantly with increased exercise, however SVC flow was unchanged. The study was able to separately quantify inspiratory and expiratory flow to demonstrate that in total Cavopulmonary connection (TCPC) patients, inspiration facilitates IVC flow at rest but less so during exercise.

In this study high temporal resolution real-time imaging was achieved using efficient EPI trajectories, without parallel-imaging – this was possible due to the very small imaging matrix used. Additionally, partial-Fourier acquisition was used which may introduce errors into the PCMR phase data. However, the combined IVC and SVC flow was comparable to the measured aortic flow (< 6 % difference), indicating the accuracy of the sequence. The separate quantification of flow during inspiration and expiration would not have been possible without the use of a real-time sequence.

Hjortdal, et al. (81) were able to use a small FOV (90×136 mm) with a small matrix (26×64) as they were imaging paediatric patients (mean age: 12.4 years) with a single 18-cm receiver coil.

In 2010, Pedersen, et al. (82) extended the sequence developed by Hjortdal, et al. to use parallel-imaging. A five-element cardiac coil was used, to allow SENSE factors of 2-3. The acceleration of data acquisition was used to image over a larger FOV using a bigger matrix, while maintaining the temporal and spatial resolution. The actual FOV or matrix size are not stated, however the remaining sequence parameters are assumed to be the same as (81) in Table 2.6, unless otherwise stated in Table 2.7.

Sequence Parameters	
TE	4.8-5.0 ms
SENSE factor	2-3
Temporal resolution	48-52 ms (~20 frames/sec)
Spatial resolution	3.20×2.0 mm

Table 2.7: Sequence parameters used by Pedersen, et al. (82)

In 7 patients (median age: 18 years) and in 7 control subjects (median age: 19 years), flow was measured in the ascending aorta and in the descending aorta. Real-time flow measurements were acquired at rest and at two exercise levels (0.5 and 1.0 W/kg). No validation of the sequence has been carried out, and there are very few details on the implementation. However, Pedersen, et al. have achieved a relatively high temporal and spatial resolution with the use of efficient EPI trajectories, a half-scan factor of 0.8, plus a SENSE acceleration of 2-3.

We wish to develop a real-time PCMR sequence, to measure flow during continuation of exercise as performed by Hjortdal, et al. (81) and Pedersen, et al. (82). Instead of using an EPI sequence, we will use a spiral trajectory with a short TE. We do not want to use a partial-Fourier acquisition, as this is known to introduce errors into the phase of PCMR measurements (36). It is felt that the temporal resolution of the studies described here, is still too low to ensure that the peak flow is accurately captured during exercise.

Gatehouse, et al. (83) suggest that at rest, the accuracy of PCMR is retained if the temporal resolution is less than 60 ms. At a heart rate of 70 bpm, this is the equivalent of ~14 frames/cycle. At a heart rate of 104 bpm (as found by Hjortdal, et al. (81) at 1.0 W/kg of exercise), to ensure 14 frames/cycle a temporal resolution of ~40 ms would be necessary.

2.2.3 Measurement of Ventricular Function During Exercise

In addition to PCMR measurements during exercise, previous studies have quantified ventricular volumes using MRI, during exercise. Again, most studies use gated sequences and require suspension of exercise, including Roest, et al. in 2001 (84) and 2003 (85).

However, Lurz, et al. (86) measured right and left ventricular volumes using two real-time sequences;

- A Cartesian SSFP sequence, with 75% partial-Fourier, accelerated 2-fold using GRAPPA (“standard real-time” sequence)
- A radial sequence, accelerated 8-fold using k-t SENSE (“radial k-t real-time” sequence)

The sequence parameters are shown in Table 2.8;

	Standard real-time	Radial k-t real-time
TE/TR	0.9/2.0 ms	1.1/2.3 ms
Half-scan factor	0.75	-
GRAPPA (ACL)	2 (16)	-
k-t SENSE factor	-	8
Flip angle	41-47°	43-65°
FOV	~380×320 mm	~380×380 mm
Rectangular FOV	~85 %	100 %
Slice thickness	10 mm	10 mm
Number of slices	10-12	10-12
Matrix	128×82	128×128
Temporal resolution	~80 ms (~13 frames/sec)	~35.5 ms (~28 frames/sec)
Spatial resolution	3.1×3.9 mm	3.0×3.0 mm

Table 2.8: Sequence parameters used by Lurz, et al. (86)

GRAPPA is a parallel-imaging method that removes the aliasing in k-space. The centre of k-space is fully sampled, by acquiring additional auto-calibration lines (ACL), which are used to calculate the coil sensitivity information.

K-t SENSE is a variant of SENSE, which also uses spatiotemporal correlations to constrain the reconstruction (15), allowing higher acceleration factors to be achieved than is possible with SENSE. These spatiotemporal correlations are derived from a low spatial resolution alias-free training data set.

For the radial k-t SENSE sequence, 16 radial projections were acquired in each frame. The sampling pattern was rotated in each frame so that 8 consecutive frames comprised a fully sampled k-space (with 128 radial projections). The centre $1/8^{\text{th}}$ of each frame was used as a low resolution, alias-free, training data for the k-t SENSE algorithm. This sequence has previously been validated at rest (87). These studies were carried out at UCL Institute of Child Health (ICH), and this sequence is used in section 2.5.2.3 to validate our real-time flow sequence.

Lurz, et al. measured ventricular volumes using both real-time sequences in 12 healthy volunteers (mean age: 32.5 years), at rest and during continuation of exercise (at 7.5 W, 15.0 W and 22.5 W). Accuracy of the sequences was determined by assessing the agreement between right ventricular (RV) stroke volume and left ventricular (LV) stroke volume. The agreement of RV to LV stroke volumes was found to be greater during exercise with the radial k-t real-time sequence than with the standard real-time sequence (standard deviation of difference: ± 3.43 vs. ± 8.97 mL/cycle, respectively; $F = 6.85$, $p < 0.001$). Bland Altman analyses for both of the sequences are seen in Figure 2.1, showing a smaller bias and lower limits of agreement for the radial k-t sequence, compared to the standard real-time sequence.

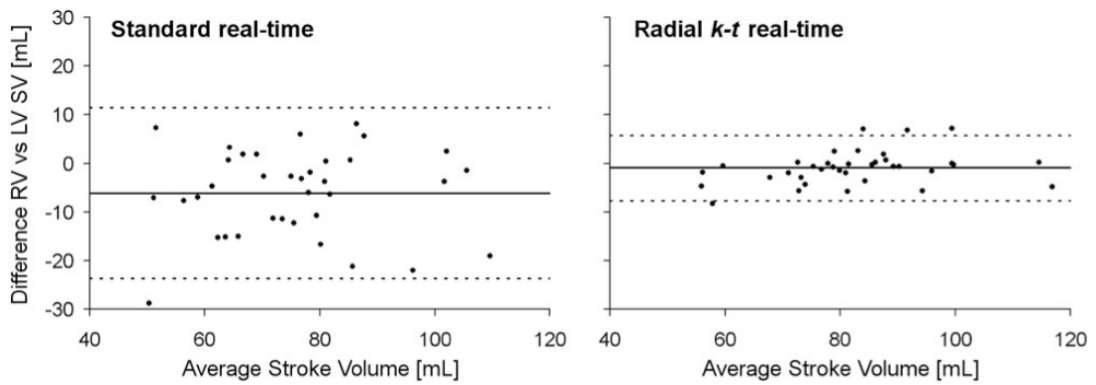


Figure 2.1: From Lurz, et al. (86). Agreement in RV to LV stroke volumes for; a) standard real-time and b) radial k-t real-time sequences

Lurz, et al. also found that the image quality and motion fidelity of the radial k-t real-time sequence was greater than that of the standard real-time sequence. This was because of the higher temporal resolution achieved by the radial k-t real-time sequence. Additionally the artefacts caused by the radial sequence (radial streaks) were less visually disturbing.

This study achieved high temporal and spatial resolution imaging with the use of radial trajectories, undersampled by a factor of 8. The data was reconstructed using an iterative CG k-t SENSE algorithm. The sequence was demonstrated to be accurate in adults, even during exercise.

Lurz. et al, demonstrated that high temporal resolution is important in real-time imaging to ensure accurate quantification of ventricular volumes during exercise. The agreement in LV and RV stroke volume was significantly worse from the standard real-time sequence than the radial k-t real-time sequence (temporal resolution; 80 ms vs. 35 ms). The average heart rates found in this study at 22.5 W of exercise was 154 bpm – at this heart rate the standard real-time sequence could only capture ~5 frames/cycle, whereas the radial k-t real-time sequence could capture ~11 frames/cycle.

2.2.4 Assessment of Hemodynamic Parameters Using MRI

In this study we are interested in quantifying systemic vascular resistance (R) and vascular compliance (C). R (measured in mmHg/L/min, also known as *Woods units*, WU) is the amount of resistance to flow that must be overcome to push blood through the peripheral circulatory system. R is calculated by;

$$R = \frac{\text{mean arterial blood pressure}}{\text{cardiac output}} \quad \text{Equation 2.2}$$

Compliance is a measure of the ability of the wall of a blood vessel to distend and increase volume, with increasing transmural pressure. A simple approximation of compliance (C_{SV}) is;

$$C_{SV} = \frac{\text{stroke volume}}{\text{pulse pressure}} \quad \text{Equation 2.3}$$

however C_{SV} is thought to overestimate true arterial compliance (88). The pulse pressure method (C_{PPM}) is thought to give a more accurate estimation of true compliance by parameter optimization of the two-element Windkessel model (89). The two-element Windkessel model is;

$$\dot{Q}(t) = \frac{P(t)}{R} + C \frac{dP(t)}{dt} \quad \text{Equation 2.4}$$

where P is pressure and $\dot{Q}(t)$ is the flow curve.

Normally R and C are calculated using invasive catheter manometers to measure pressure, and using the Fick method to quantify flow from invasive oximetry data. Unfortunately, the Fick method is considered to be inaccurate, especially in the presence of high blood flow and high concentrations of oxygen.

In the pulmonary vasculature, accurate PCMR flow measurements have been combined with invasive pressure measurements to calculate vascular resistance (90) and compliance (91).

2.2.4.1 Measuring Vascular Resistance Using MRI

In 2004 Muthurangu, et al. (90) measured pulmonary vascular resistance by combining PCMR flow measurements with simultaneous invasive pressure measurements. PCMR was carried out using a retrospectively-gated, Cartesian sequence during free-breathing. Three NSA's were used to reduce respiratory artefacts. Imaging was performed at the midpoint of the pulmonary artery.

The vascular resistance measurements derived from MR were compared to those derived from the Fick method in 15 patients. Muthurangu. et al, showed reasonable agreement between Fick and MRI-derived resistance at 30 % oxygen ($r = 0.91$, bias = 2.3 %), however at 100 % oxygen there was less agreement between the methods ($r = 0.59$, bias = 54.2 %). It was believed that these errors were from inaccuracies in the Fick method, rather than the MR. This study by Muthurangu, et al. demonstrated the feasibility of quantifying vascular resistance using PCMR.

We wish to use this principle to quantifying vascular resistance, by combining non-invasive cuff-based oscillometric blood pressure measurements with real-time PCMR measurements. By acquiring data during exercise we will be able to analyse the response of vascular resistance to exercise – this has not been previously carried out.

2.2.4.2 Measuring Vascular Compliance Using MRI

Muthurangu, et al. (91) also measured vascular compliance using the same protocol as described above. C_{SV} (Equation 2.3) was compared to C_{PPM} calculated from parameter optimization of the two-element Windkessel model (Equation 2.4). In this study C_{PPM} was found by generating a series of modelled pressure curves (P) using values of C between 0.001 and 7.0 mL/mmHg. C_{PPM} was taken to be the value that produced the best match with the actual pulse pressure. This is discussed further in section 2.3.6.2.

Compliance was measured in 17 patients. Correlation between C_{SV} and C_{PPM} was found to be excellent ($r > 0.97$), however there was a systemic bias (of 61 %), giving a significant difference between the two methods. This overestimation of C_{SV} has been previously observed (88, 89), due to oversimplification of the model. This study by Muthurangu, et al. demonstrated the feasibility of quantifying vascular compliance using PCMR.

We wish to use this principle to quantifying vascular compliance using the pulse pressure method, by combining non-invasive cuff-based oscillometric blood pressure measurements with real-time PCMR measurements. By acquiring data during exercise we will be able to analyse the vascular compliance response to exercise – this has not been previously carried out.

2.2.5 Summary

From the literature review it can be seen that:

- Spiral trajectories have previously been combined with PCMR to successfully measure flow in real-time with MRI
- Without the use of data undersampling, the temporal resolution achieved is insufficient for real-time imaging
- Data undersampling with a SENSE reconstruction algorithm have been successfully used to measure flow in real-time with a high temporal resolution

- A few studies have measured flow-volume response to exercise using MRI, however many of these studies do not acquire data in real-time
- A few studies have combined MRI flow measurements with invasive blood pressure measurement in order to quantify pulmonary vascular resistance and compliance

We wish to combine these principles to develop a high temporal resolution real-time undersampled spiral PCMR sequence, with a SENSE reconstruction algorithm. We will use this sequence to measure flow volume response to continued exercise in the ascending aorta. By combining non-invasive blood pressure measurements with the real-time PCMR data we aim to measure the hemodynamic response to exercise using MRI, for the first time.

We aim to achieve a higher temporal resolution than most of the studies described, to ensure that peak flow is accurately captured during the high heart rates expected during exercise. As described above, we aim to achieve a temporal resolution of ~ 40 ms, as this would ensure ~ 14 frames/cycle a heart rate of 110 bpm.

2.3 Development

This section discusses what was developed for this study.

2.3.1 Real-time PCMR Sequence

It is possible to accelerate the acquisition of MR data by the use of efficient trajectories (section 1.3.6) as well as parallel imaging (section 1.4).

2.3.1.1 Spiral Sequence

In this study a uniform density spiral sequence was developed by integrating code by Brain Hargreaves (62) to calculate the spiral trajectories, into an MRI pulse sequence. This code takes into account the required;

- FOV
- Number of interleaves
- Maximum slew rate
- Maximum gradient amplitude
- Sampling period (Bandwidth)
- K-space radius

The equations describing spiral trajectories have been presented in section 1.3.7. The code by Hargreaves calculates an Archimedes spiral trajectory (Equation 1.39) solving θ (which describes the azimuth angle evolution over time) as a function of time using an iterative process. This iterative process is described below.

By differentiation of Equation 1.39 we get an expression for the gradient amplitude vector;

$$\vec{G} = \frac{2\pi\lambda}{\gamma} e^{j\theta} (\dot{\theta} + j\theta\dot{\theta}) \quad \text{Equation 2.5}$$

where $\dot{\theta}$ is the first derivative of θ with respect to time. Differentiation again gives an expression for the slew-rate vector;

$$\vec{S} = \frac{2\pi\lambda}{\gamma} e^{j\theta} [(\ddot{\theta} - j\theta\dot{\theta}^2) + j(2\dot{\theta}^2 + j\theta\ddot{\theta})] \quad \text{Equation 2.6}$$

where $\ddot{\theta}$ is the second derivative of θ with respect to time.

At first the trajectory is slew rate limited, and so Equation 2.5 is solved for $\ddot{\theta}$ (as the maximum slew rate is known), giving $\dot{\theta}$ and θ by discrete integration. The iterative loop then uses these values to solve for $\ddot{\theta}$ at the next time point. Once the maximum gradient amplitude is reached, Equation 2.6 is solved for $\dot{\theta}$. The iterative calculation repeats until the maximum k-space radius is reached.

The same spiral trajectory is used for each interleave, however for the m^{th} interleave (where there are N interleaves in total) the trajectory is rotated by an angle, α (radians);

$$\alpha = \frac{2\pi m}{N} \quad \text{Equation 2.7}$$

The resultant spiral trajectories have been presented in Figure 1.9.

The maximum slew rate is set at 95 % of the slew rate achievable by the system (obtained from the system properties in run time). As the maximum gradient amplitude determines our sampling frequency, the maximum gradient amplitude is calculated (from the Bandwidth/pixel as on the UI) as;

$$G_{\max} = \frac{\text{bandwidth per pixel}}{\text{pixel size} \times \gamma} \quad \text{Equation 2.8}$$

A check is performed to ensure that this value does not exceed 80 % of the maximum gradient amplitude achievable by the system. The maximum k-space radius is calculated in run time as;

$$k_r^{\max} = \frac{\text{matrix size}}{2 \cdot \text{FOV}} \quad \text{Equation 2.9}$$

In our implementation a non-selective RF-excitation (*sinc*) pulse is used, with a short duration (of 600 μs) to ensure a short TE. We do not apply rewinder gradients after the spiral readouts, as it is possible to achieve a shorter TR without these gradients. However, RF-spoiling and gradient spoiling (on the z-axis) are carried out to reduce residual transverse magnetisation.

To prevent a flash artefact in the first few frames, we applied 1 second of dummy pulses (where the gradients are played out but the ADC is not turned on), prior to the start of data acquisition.

2.3.1.2 Flow Encoding

The flow encoding gradients were added to the spiral sequence. We decided to use an asymmetric encoding, as this allowed coil sensitivity data to be calculated from just the flow-compensated data. In this way the magnitude of the coil sensitivity data is free of flow artefacts, and the phase is independent of the flow.

The flow-compensated and flow-encoded readouts were interleaved in their acquisition to maintain temporal coherence. This means that each spiral interleave is acquired once with flow-compensated gradients and once with flow-encoding gradients, before moving to the next spiral interleave (as presented in Figure 1.19).

As we are interested in through-plane flow, the flow-encoding gradients were added to the z -axis. To minimize the TE, the flow-encoding gradients were combined with the slice-select rewinder gradient. The resulting sequence diagram can be seen in Figure 2.2;

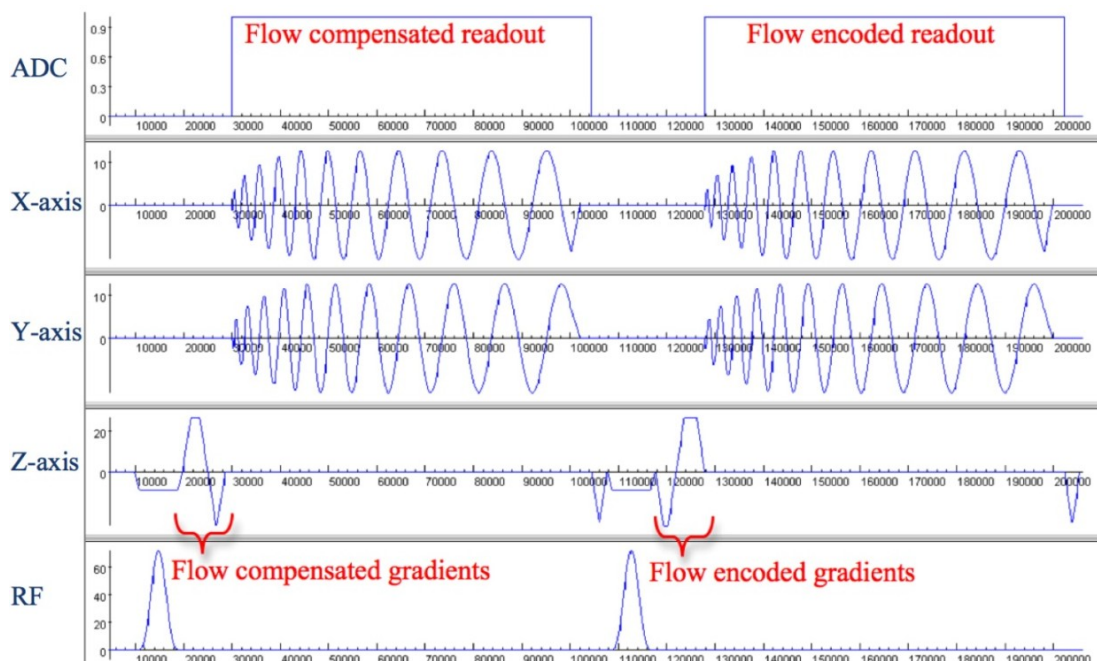


Figure 2.2: A sequence diagram showing the interleaved flow-compensated and flow-encoded readouts for one spiral interleave

2.3.1.3 Data Undersampling

In this study we wanted to calculate the coil sensitivity data from the undersampled data itself, rather than from a separate pre-scan (see section 1.4.1). As we are using uniform density spiral trajectories the centre of k-space is not fully sampled, therefore cannot be used to calculate the coil sensitivity maps. It was decided to use a variant of TSENSE (16) (see section 1.4.1) where the k-space lines in sequential repetitions are interleaved (see Figure 2.8).

In this implementation the desired acceleration factor, is specified by the user from the UI;

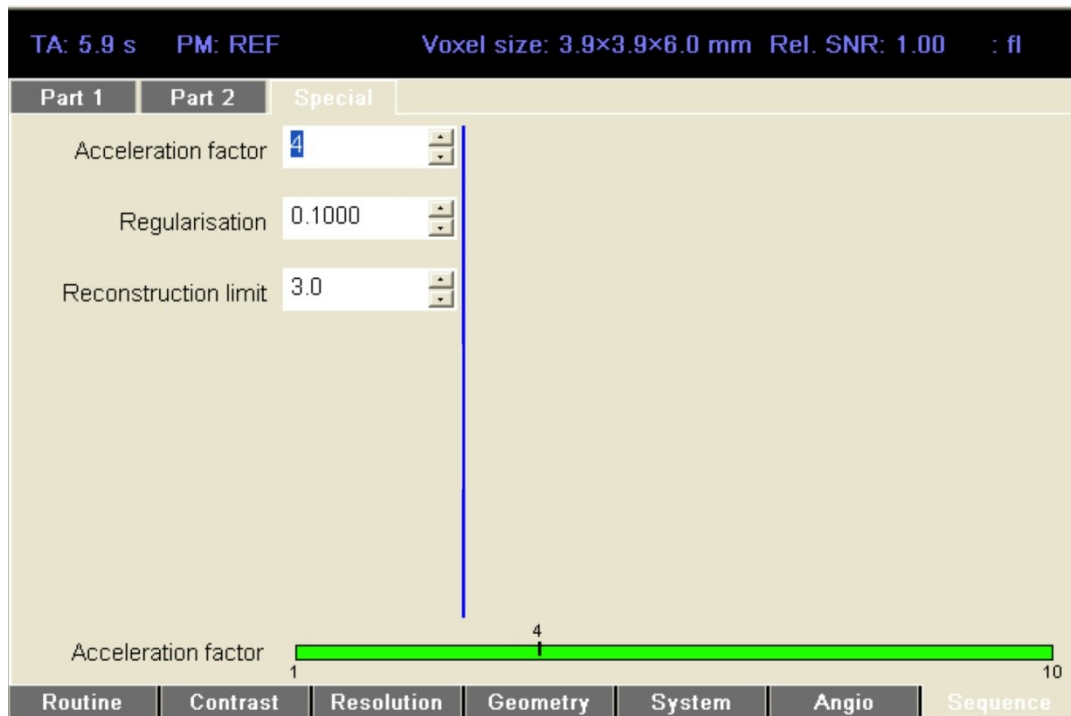


Figure 2.3: The sequence->special tab on the UI contains user-defined parameters, including the desired acceleration factor, the regularisation factor (λ) and reconstruction limit (ϵ).

2.3.2 SENSE Reconstruction

In order for the sequence to be clinically useful, it is necessary for the undersampled data to be reconstructed online, in the Siemens ICE environment (ICE VB15, two AMD Opteron processors, clock-speed: 3.2GHz, cache: 6MB). An iterative SENSE algorithm was used (section 1.4.2.2), with regularization (section 1.4.2.3) and preconditioning (section 1.4.2.4) to improve the speed of convergence. The conjugate gradient algorithm described in Equation 1.75 was implemented in ICE, however in this study we did not use any prior information (this is the same as setting ρ_0 to zero in Equation 1.75).

Gridding (see section 1.3.8) was performed by convolution with a Kaiser-Bessel kernel (see Equation 1.46 and Equation 1.47). The kernel width was chosen at $w = 4$, to give a good compromise between image quality and calculation time, where $\beta = 5.7567$ from the optimal values in (12). To remove aliasing at the edges of the images, an oversampling factor of 1.25 was used. This means that the FOV was increased by a factor of 1.25, by gridding the data onto a smaller grid, and the outer portion of the image was ignored. A look-up-table was used to store the gridding kernel (with 10000 steps), to optimise calculation time. This code was written by Michael Hansen, but adapted to handle spiral trajectories (rather than radial trajectories).

The spiral trajectory is calculated within the ICE environment by calling the trajectory function used in the sequence, with the same input parameters. The gridding weights (see section 1.3.8) are calculated analytically using Equation 1.48 within ICE.

2.3.2.1 Calculation of Coil Sensitivity Information

The coil sensitivity data and signal covariance (θ) required for the reconstruction algorithm (see section 1.4.1) were calculated directly from the raw data. Specifically, using just the flow-compensated data, the following steps were carried out to calculate the coil sensitivity data;

- For all repetitions and all channels;
 - Grid the undersampled data
 - Perform 2D inverse FFT to image space
- For all channels;
 - Calculate average image from all repetitions*
 - Perform 2D FFT to k-space
 - Apply 2D Tukey Filter (see below) to smooth the image
 - Perform 2D inverse FFT to image space (we will denote these images as I_γ)
- Calculate homogeneous image (I_H) (see Equation 1.51) as the complex square-root-sum-of-squares of all coil images, I_γ
- Calculate the coil sensitivities for each coil, C_γ ;
 - Divide I_γ by I_H

Examples of images from the steps above are shown in Figure 2.4.

In TSENSE adaptive coil sensitivity maps are used, by combining just R frames (in the step marked with a *). However these coil sensitivity maps tend to be noisy and this noise propagates through the reconstruction. We propose to calculate the coil sensitivity maps from all frames (similar to k-t SENSE (15)) so that high SNR coil sensitivity maps are achieved.

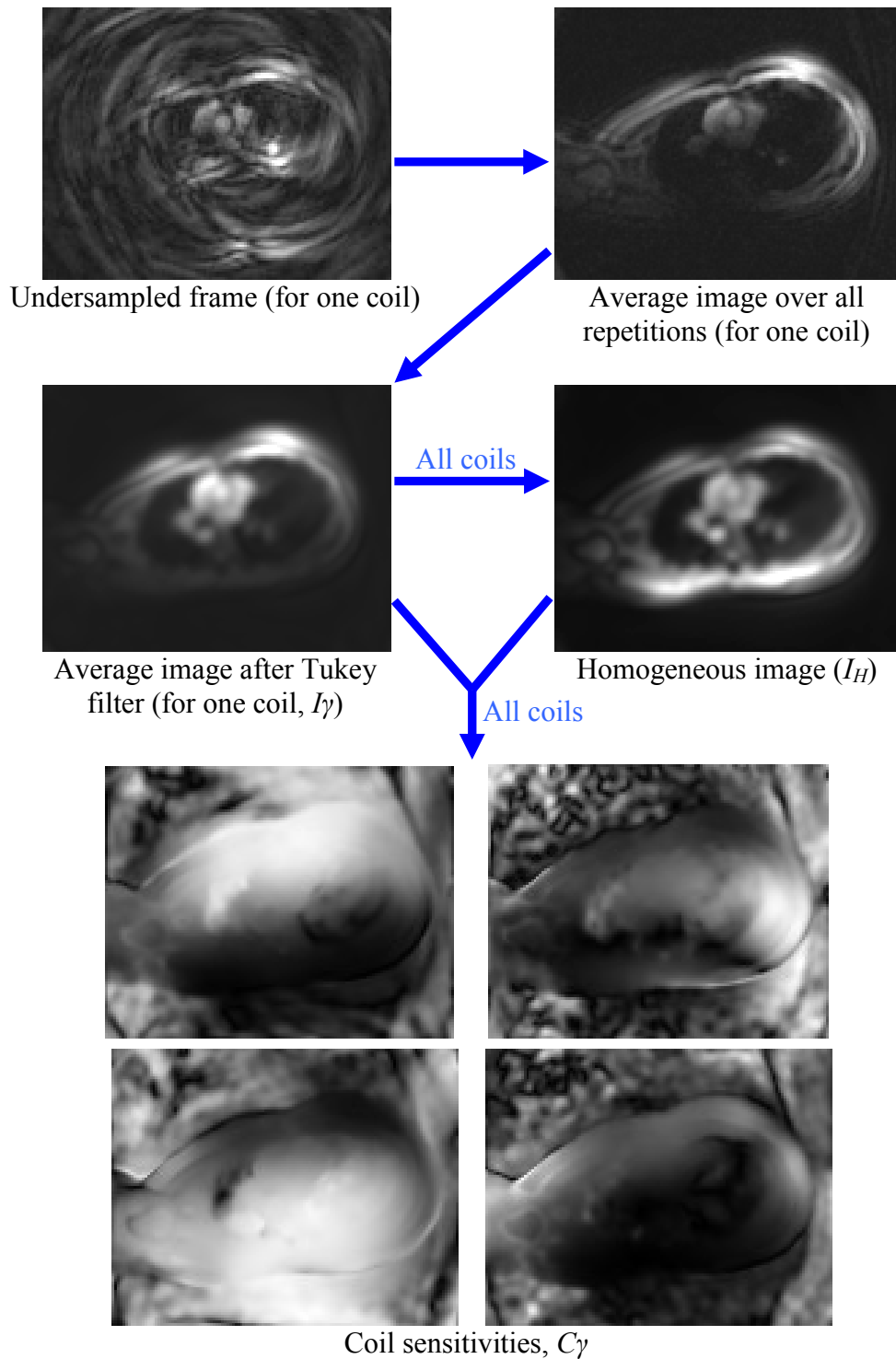


Figure 2.4: Calculation of coil sensitivity information from an undersampled spiral sequence (SENSE $\times 4$). The coil sensitivities are calculated by dividing of the filtered average image for each coil by the homogeneous image

An adapted Tukey filter was used to generate low-resolution images, by weighting the k-space data to maintain low frequency data and attenuate high frequency data. In this Tukey filter the user can control the flat top radius (r) and transition width (T), as shown in Figure 2.5;

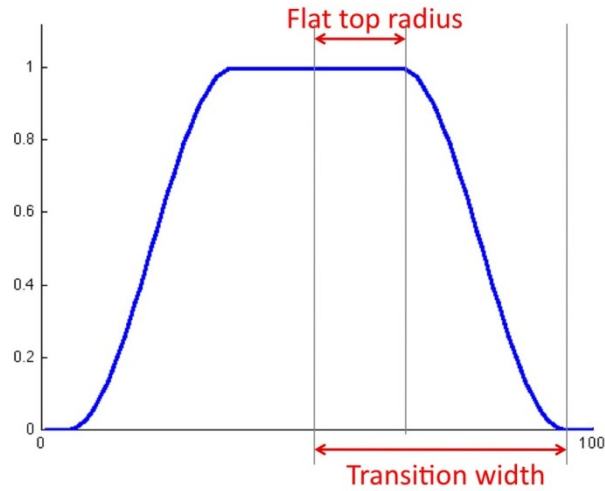


Figure 2.5: A Tukey filter, simulated in MATLAB

This filter is described as;

$$\omega_0(n) = \begin{cases} 1 & \text{when } n < r \\ \frac{1}{2} + \frac{\cos\left(\pi \left| \frac{n-r}{T} \right| \right)}{2} & \text{when } r \leq n \leq (r+T) \\ 0 & \text{when } n > (r+T) \end{cases} \quad \text{Equation 2.10}$$

The Tukey filter used to calculate the coil sensitivity data uses parameters: $r = 0$ and $T = \text{matrix_size}/2$.

The signal covariance (θ) used in the regularisation and preconditioning (see section 1.4.2.3 and section 1.4.2.4) was found from the expected signal, L (see Equation 1.65). In this study L was calculated in the same way as I_H except without the Tukey filtering.

2.3.3 Concomitant Gradient Correction

The effect of the concomitant field (see section 1.6.3) is small (52 ppm at 1.5 T with a gradient amplitude of 10 mT/m and a 20 cm distance from isocenter), and is thus largely neglected in most imaging situations (42). However in this study we are using a low-field system (1.5 T) with a high amplitude gradient system (40 mT/m) and for this application are generally interested in performing off-centre imaging. Therefore, concomitant magnetic fields were observed to be important in the resultant PCMR images, as seen in Figure 2.6. Maxwell correction was performed to remove the effects of concomitant gradients originating from the flow encoding gradients (42).

The residual phase in PCMR caused by concomitant gradients (after the phase difference calculation) has been presented in Equation 1.84 and Equation 1.85. In Figure 2.6 residual phase offsets result in velocity errors up to 20 cm/s at the edge of the image – this is one-fifth of the 100cm/s VENC used to acquire these images.

In Figure 2.6 Maxwell correction is observed to remove the phase offset in transverse, coronal and sagittal slices. The phase offset in the oblique slice is reduced by Maxwell correction, but is not completely removed.

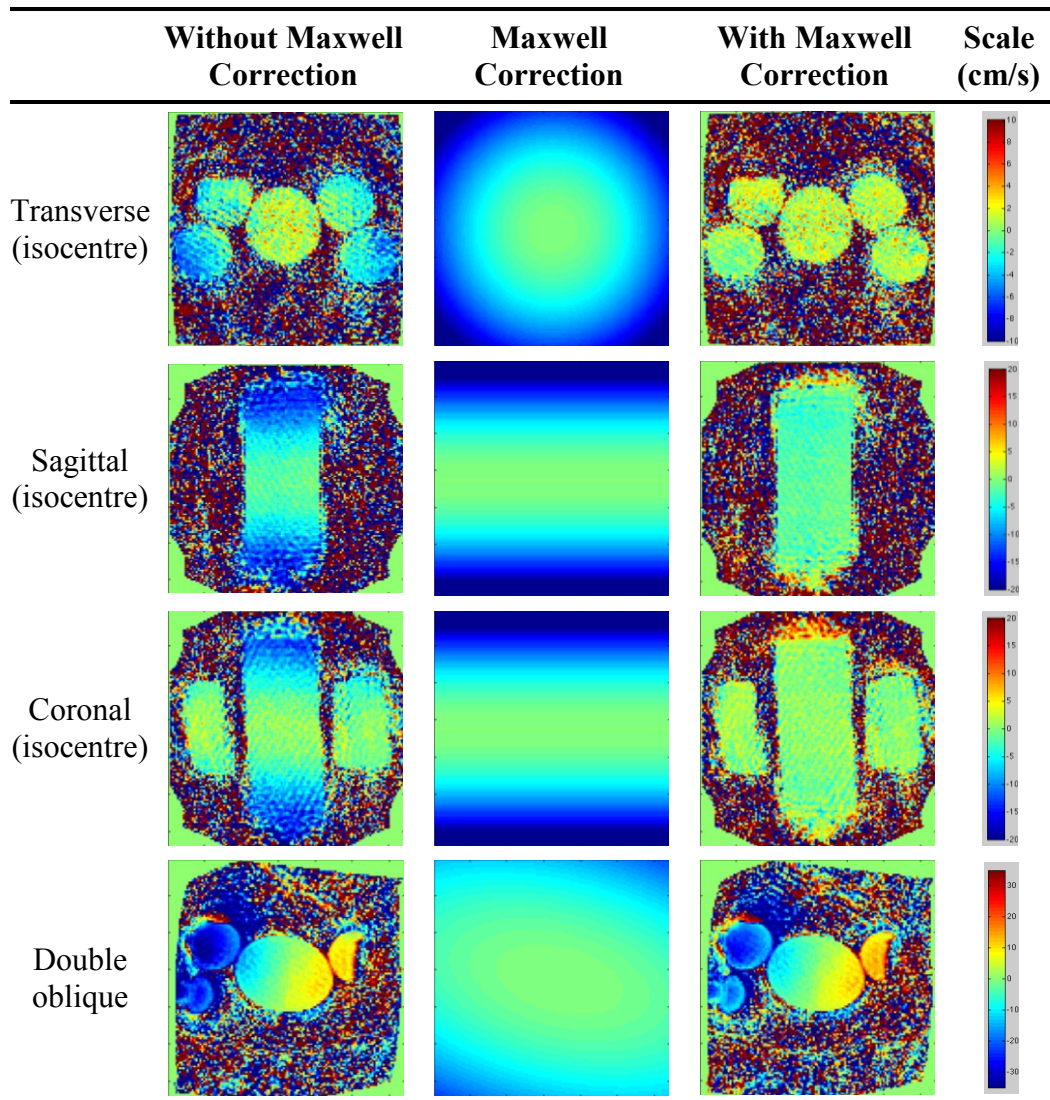


Figure 2.6: Effect of Maxwell correction on water phantoms imaged with 12 spiral interleaves, undersampled by a factor of 2, VENC = 100cm/s. Note the different scales

2.3.4 Residual Phase Offsets

Maxwell correction did not completely remove background phase offsets when imaging a double oblique slice. This suggests that there may be additional residual background phase offsets from other sources (as discussed in section 1.6.4).

It was observed that by varying the TE and the slew rate of the flow encoding gradients, it was possible to alter these additional phase offsets (see Figure 2.7).

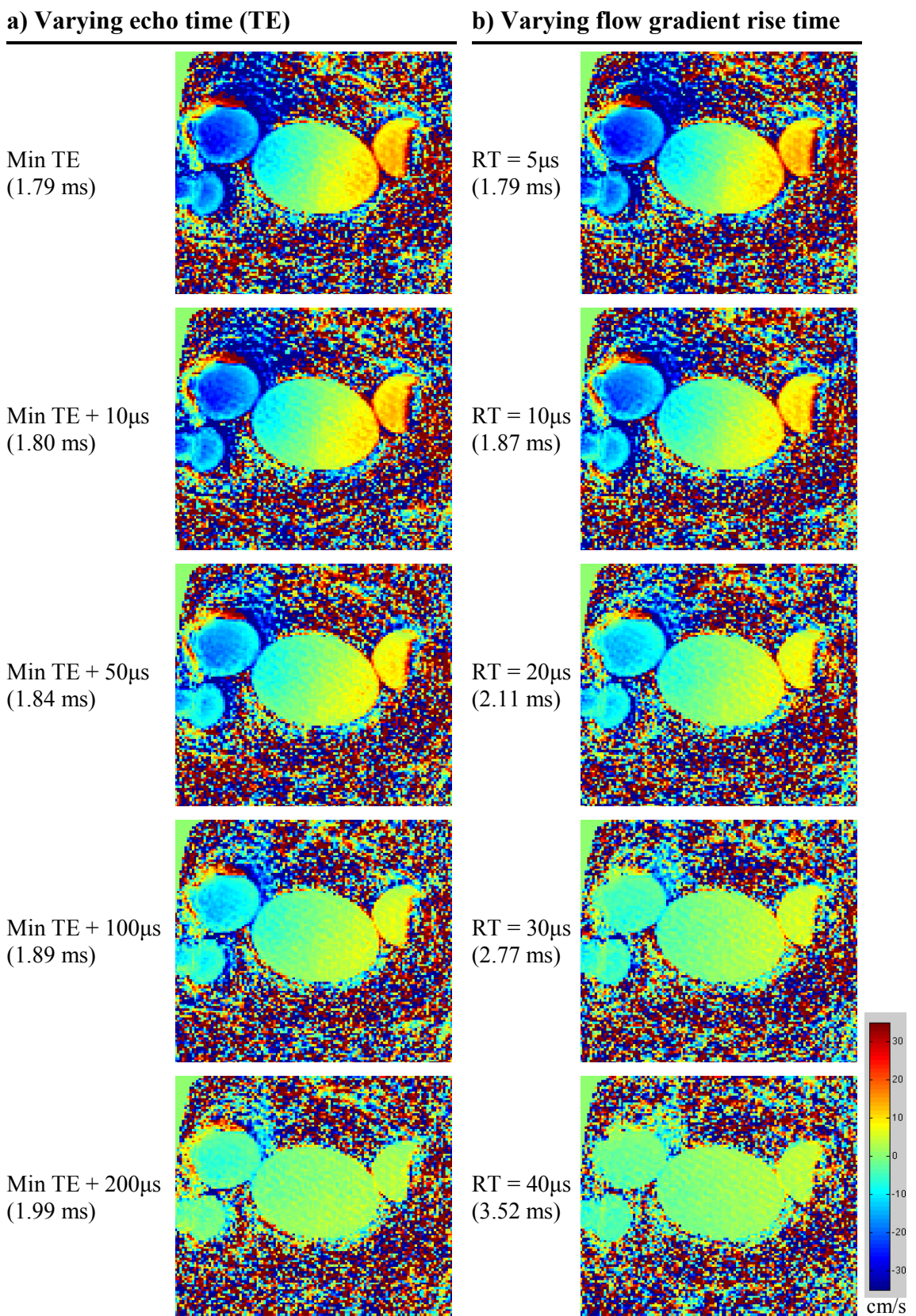


Figure 2.7: Residual phase offsets (after Maxwell correction) from an oblique slice in a water phantom, VENC: 100cm/s. Effect of varying; a) TE, b) rise time (RT) of the flow-encoding gradients. Values in brackets give the actual TE

Figure 2.7a) shows that the phase offsets decreased when a delay was inserted between the end of the flow gradients and the beginning of the readout. Figure 2.7b shows that (with no additional TE delay) the phase offsets could be decreased, by lengthening the rise time of the flow gradients – this is the same as reducing the slew rate of the flow gradients. These observations imply that these additional phase offsets may be a result of residual eddy currents from the flow-compensation/flow-encoding gradients. By introducing a TE delay, these eddy currents have time to decay before the beginning of the readout. By decreasing the slew rate of the gradients, less eddy currents are produced.

Optimisation of the TE delay and ramp-up times, found that we were able to achieve low residual phase offsets for most imaging planes (when imaging the aorta) using a ramp-up time of 10 μs , with an additional TE delay of 400 μs , within a short TE (TE = 2.27 ms for the experiment shown in Figure 2.7 with a VENC of 100 cm/s).

2.3.5 Optimisation of Sequence Parameters

Adequate temporal resolution is essential to ensure accurate flow measurements. In this study we wanted to acquire each phase-contrast frame in ~ 40 ms (as discussed in section 2.2.2).

As we do not use a spatially selective excitation, when imaging the ascending aorta the RF-pulse also excites spins in the arms of the subject. If the FOV is smaller than the subject, the reconstruction algorithm would not be able to distinguish between aliasing caused by undersampling of data and aliasing caused by wrapping of signal from outside the FOV. Therefore in this study it was necessary to use a large FOV, to also include the arms of all subjects. The FOV was therefore set at 500 mm, as we were imaging adult subjects.

In spiral imaging it is necessary to keep the readout times relatively short to ensure signal throughout the entire readout, and to reduce cumulative trajectory errors (which were observed to lead to image rotation and blurring).

With these requirements we were able to optimise the sequence parameters for our application. This was done by varying the sequence parameters, and comparing the resultant temporal resolution and image quality (by visual inspection). The parameters for the optimised sequence were;

- 128 matrix
- 8 spiral interleaves
- 4-fold acceleration
- 1775 Hz/pixel bandwidth
- 7 mm slice thickness
- 15° Flip angle
- 10^{-3} reconstruction limit (ϵ)
- 0.1 regularisation factor (λ)

With these settings a temporal resolution of 40.4 ms (with a VENC of 200 cm/s) and a spatial resolution of 3.9×3.9 mm was achieved. In this optimised sequence, data is acquired according to Figure 2.8;

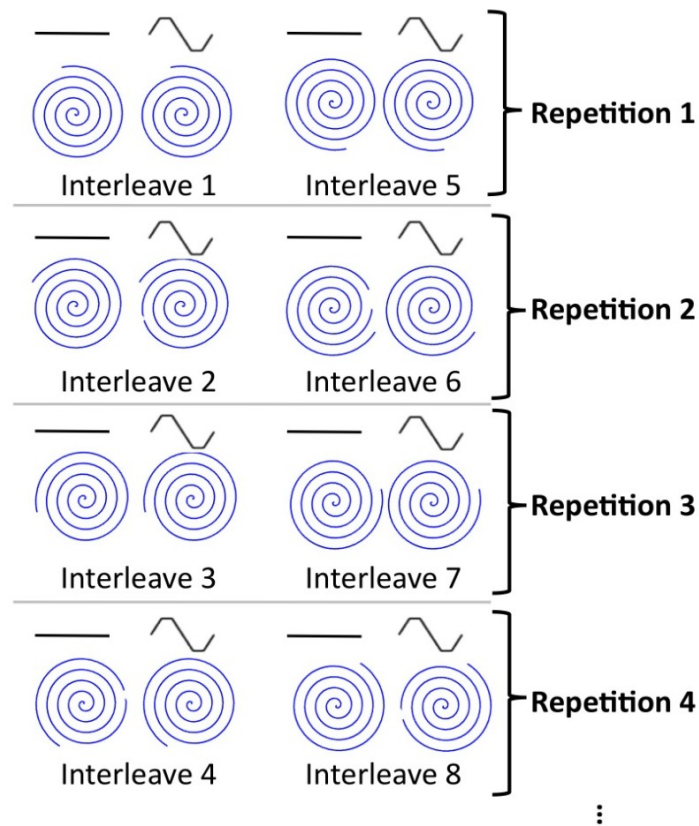


Figure 2.8: Acquisition of data for the optimised sequence with 8 spiral interleaves, undersampled by a factor of 4. — represents flow-compensated data, and \sim represents flow-encoded data. Note the rotation of the spiral interleaves

The resulting images from a resolution phantom can be seen in Figure 2.9;

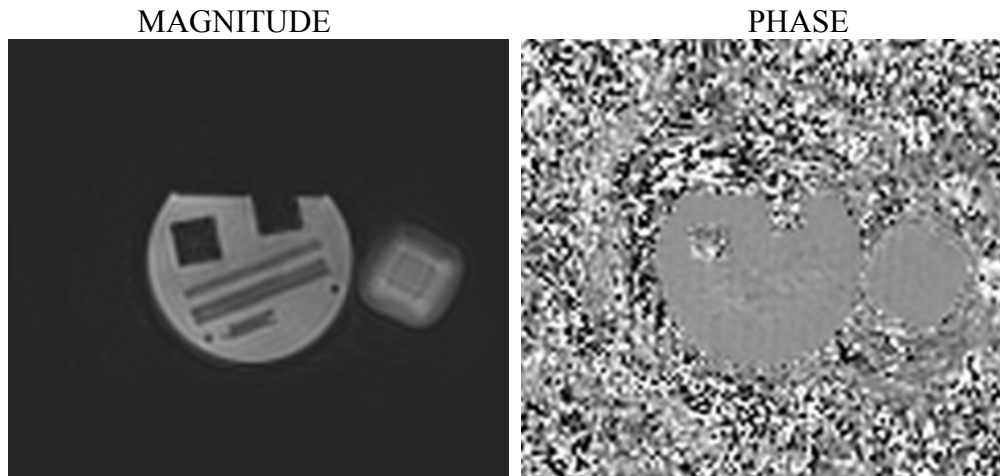


Figure 2.9: Resultant image quality from the optimised sequence in a resolution phantom (circular object on left of image), with a bottle of oil (square object on right of image)

2.3.6 Development of OsiriX Plug-ins

In order to analyse the resultant phase-contrast data, a plug-in was developed for the open-source software, OsiriX. This allows calculation of the flow velocities, flow volumes, as well as vascular resistance and compliance.

2.3.6.1 Analysis of Flow Data

When analysing flow data, segmentation is performed on the magnitude images, and then copied across to the phase images. As already discussed, the pixel intensities in the phase image are proportional to the velocity of the blood. The flow volume is therefore calculated by multiplying the velocity in each pixel by the pixel area. The flow volume of a vessel, is calculated by summing the flow volumes from all pixels within the vessel.

To calculate the stroke volume (or net forward flow) for a vessel, it is necessary to integrate the flow volume over one cardiac cycle. As the data is acquired in real-time, we must first select one cardiac cycle and calculate the stroke volume for this cycle. This is done automatically in the plug-in by;

- Detecting the peaks within the flow volume curve (these are plotted in green dots on the plug-in, see Figure 2.10. The peak-threshold can be adjusted by the user if the peaks are not correctly detected)
- Calculating the RR-interval, as the time per PC frame (temporal resolution) multiplied by the average number of frames per cycle
- For the cardiac cycle selected by the user (from the UI);
 - Find the points in the flow curve which represent the relevant cardiac cycle (these points can be adjusted by the user if the algorithm does not correctly detect the cycle, see Figure 2.10)
 - Integrating the flow volume curve for the selected cardiac cycle to a temporal resolution of 1 ms (by Fourier interpolation)
 - Calculate forward flow by summing the positive flow values in the integrated flow curve
 - Calculate backward flow by summing the negative flow values in the integrated flow curve
 - Calculate net forward flow by summing the all flow values in the integrated flow curve

The plug-in for analyzing the real-time flow data is shown in Figure 2.10.

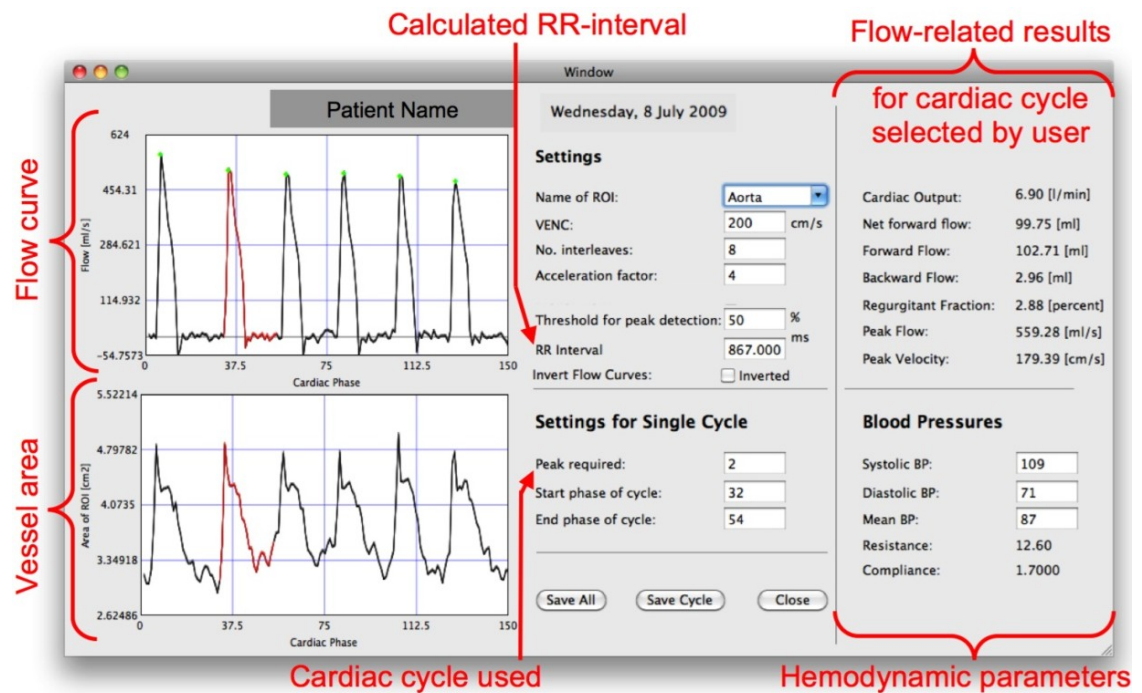


Figure 2.10: In-house plug-in developed for analysis of real-time flow data using OsiriX

2.3.6.2 Analysis of Hemodynamic Parameters

This plug-in can also be used to calculate the vascular resistance and compliance by combining the flow data (from the single cycle selected), with the blood pressure measurements (as seen in Figure 2.10).

Vascular resistance is calculated by dividing the mean blood pressure by the cardiac output (see section 2.2.4.1). Compliance was calculated using an optimization of the two-element Windkessel model (Equation 2.4), in the same way as Muthurangu, et al. (91) (see section 2.2.4.2). Specifically, a flow curve $\dot{Q}(t)$ with 50 cardiac cycles was created by repeating the single flow curve selected from the UI. $\dot{Q}(t)$ and the calculated resistance (R) were used as inputs to the Windkessel model. A series of modelled pressure curves (P) were generated using values of compliance (C) between 0.1 and 5.0 mL/mmHg in increments of 0.01. For a given C , Equation 2.4 was integrated using the initial condition $P(0) = 0$. This generated a 50-cycle pressure curve, which had stabilized and was independent of the initial condition by the 40th cycle. Therefore the modelled systolic and diastolic pressures ($P_{systole_computed}$ and $P_{diastole_computed}$) were calculated from the maximum and minimum pressures

respectively, between the 40th and 50th cycles. The modelled pulse pressure ($PP_{computed}$) was calculated as $P_{systole_computed}$ minus $P_{diastole_computed}$. Compliance was taken to be the value that produced the best match between $PP_{computed}$ and the actual pulse pressure (PP_{actual}) as seen in Figure 2.11;

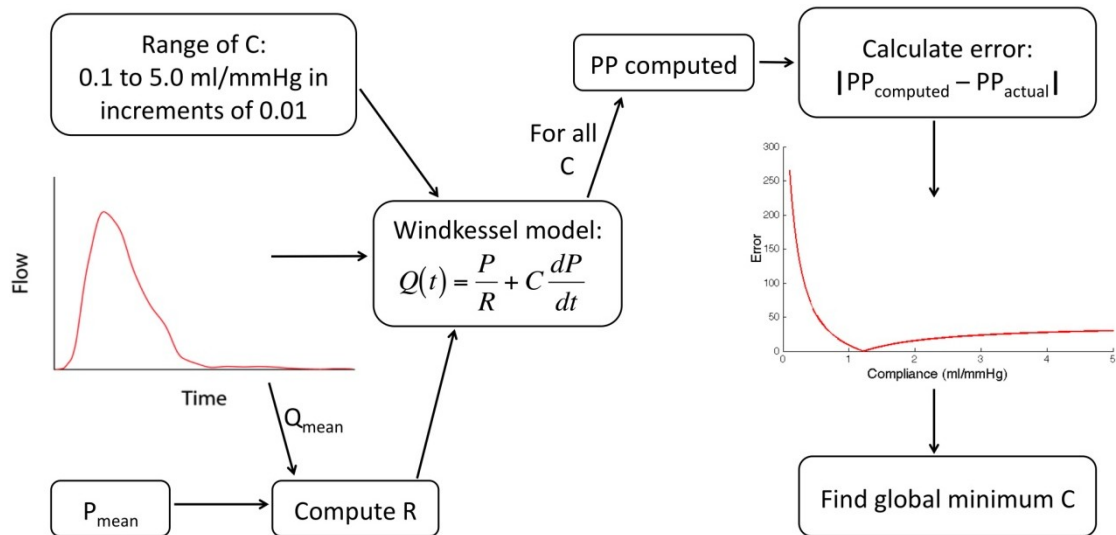


Figure 2.11: Figure from (63). Calculation of compliance, by optimisation of two-element Windkessel model

2.4 In-vitro Validation

To validate the undersampled spiral PCMR sequence, an experiment was carried out using a pulsatile flow pump (Harvard Medical Systems) connected to a distensible rubber tubing vessel phantom, as seen in Figure 2.12;



Figure 2.12: Photograph of rubber tubing vessel phantom used for in-vitro validation

The output from the pump was varied from 2.8-6.8 L/min, by changing the stroke volume (50-90 mL/cycle) and the pump rate (60-85 bpm). Flow was quantified at 14 different output volumes.

PCMR images were acquired using a standard, retrospectively-gated Cartesian sequence and the real-time spiral sequence, at the mid-point of the phantom with a transverse imaging plane. Two three-element spine coils (below the phantom) and two three-element body-matrix coils (above the phantom) were used for imaging.

2.4.1 Standard Flow Sequence

Standard flow quantification was performed using a (vendor supplied) retrospectively-gated, velocity-encoded gradient echo sequence with sequence parameters shown in Table 2.9. The sequence was gated from an external square wave signal generated by the flow pump.

This sequence has been well validated in many previous studies against the gold-standard stop-watch cylinder method of measuring flow (57, 59, 90, 92, 93). Therefore in this study the flow volumes measured from this sequence are assumed to be the true flow volumes.

Sequence Parameters	
TE/TR	3.4/7.0 ms
GRAPPA (ACL)	2 (24)
Flip angle	30°
FOV	320×240 mm
Rectangular FOV	75 %
Asymmetric echo	77 %
Slice thickness	7 mm
Matrix	256×192
Pixel Bandwidth	390 Hz/pixel
VENC	50 cm/s
NSA	2
Temporal resolution	27.9 ms (36 frames/sec)
Spatial resolution	1.3×1.3 mm
Scan Time	~2.0 mins

Table 2.9: Standard PCMR sequence parameters, in-vitro

Asymmetric echo uses the same principle as partial-Fourier but in the readout dimension.

2.4.2 Real-time Spiral Sequence

Real-time flow quantification was performed using the in-house real-time spiral PCMR sequence (optimised in section 2.3.5). The sequence parameters are shown in Table 2.10.

Sequence Parameters	
TE/TR	2.7/11.2 ms
Spiral Interleaves	8
SENSE factor	4
Flip angle	15°
FOV	300 mm
Slice thickness	7 mm
Matrix	128×128
Pixel Bandwidth	1775 Hz/pixel
VENC	50 cm/s
Temporal resolution	44.8 ms (22 frames/sec)
Spatial resolution	2.3×2.3 mm
Scan Time	~4 sec

Table 2.10: Real-time Spiral PCMR sequence parameters, in-vitro

For each scan, 80 consecutive frames were acquired. Reconstruction time online for each scan was ~3 minutes.

2.4.3 Image Analysis

All images were processed in OsiriX. Flow images were manually segmented (by J.A.S. using the modulus images) and the pump output was measured. For the real-time sequence a single cycle was used for calculation of flow volumes.

Results are expressed as the mean \pm standard deviation. Measurements of agreement between the standard flow sequence and the real-time flow sequence were performed using Bland-Altman analysis, as well as calculation of correlation coefficients. All statistical analysis was performed using GraphPad Prism (GraphPad Software Inc., San Diego, CA).

2.4.4 In-vitro Results

For each experiment pump output was calculated using both sequences.

2.4.4.1 Flow Assessment

There was good agreement between the standard gated flow sequence and the real-time flow sequence, throughout the cycle as seen in Figure 2.13;

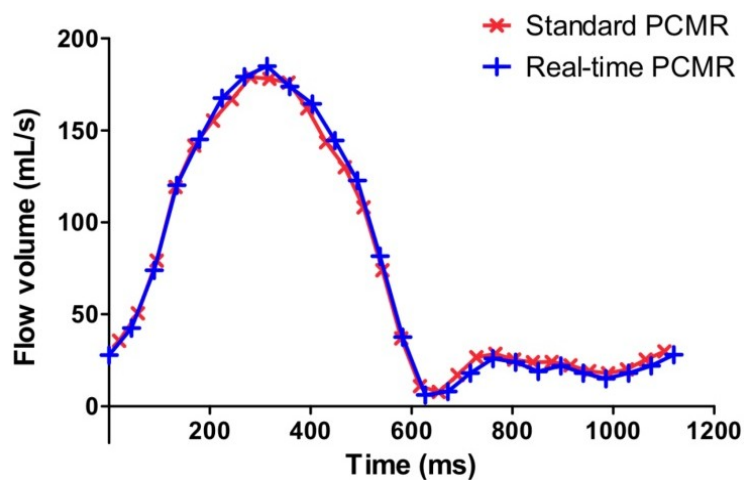


Figure 2.13: Comparison of flow profiles in-vitro

Figure 2.14 shows the use of the OsiriX plug-in (described in section 2.3.6.1) for analysis of the real-time PCMR data for one experiment.

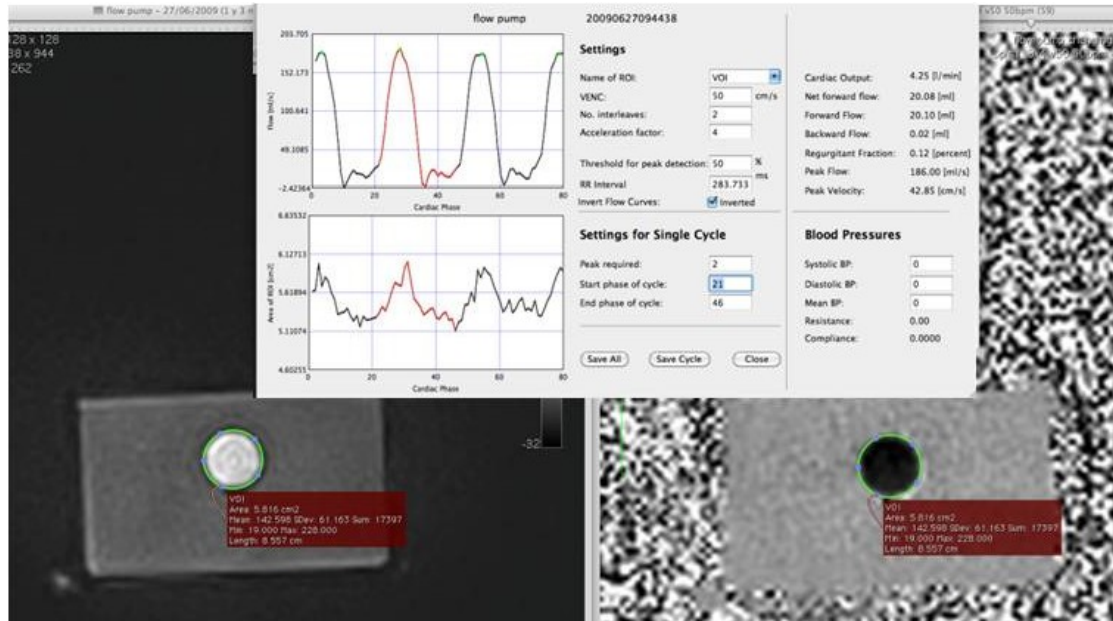


Figure 2.14: Example of data analysis for real-time sequence using the OsiriX plug-in

A good agreement was found between the pump output calculated from the reference PCMR and real-time PCMR sequence (5.09 ± 1.28 L/min vs. 5.17 ± 1.30 L/min, respectively). Bland-Altman analysis of the pump output found the bias was -0.08 L/min, with limits of agreement from -0.34 to 0.18 L/min (as seen in Figure 2.15). The correlation coefficient was 0.995 ($p < 0.005$).

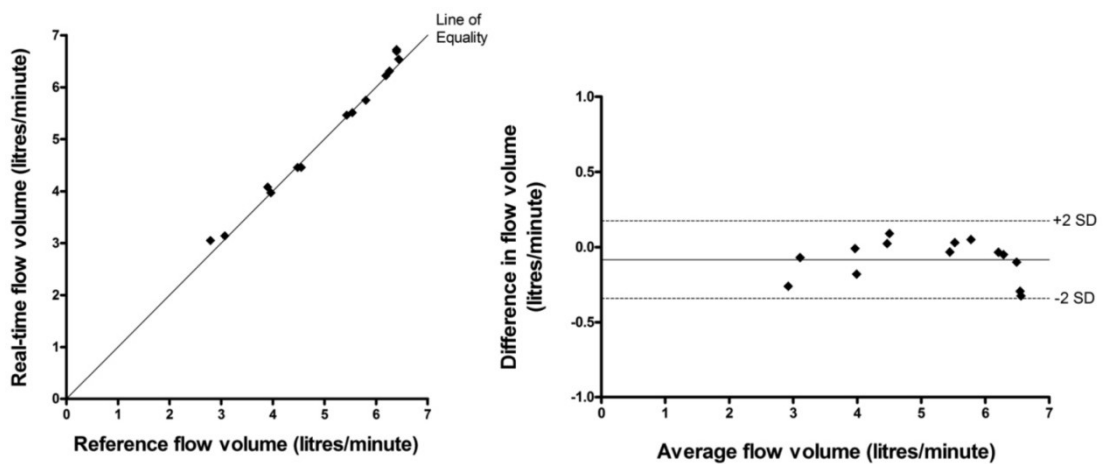


Figure 2.15: Comparison of pump output in-vitro between the reference flow sequence and real-time flow sequence. a) Correlation of flow measured from both techniques. b) Bland-Altman plot of the difference in flow measured using both techniques

2.4.4.2 Image Quality

Small residual aliasing artefacts were visible at the edges of all real-time spiral flow images, however no aliasing was seen over the vessel phantom. Additionally, some image blurring was observed and this is attributed to the sensitivity of spiral trajectories to off-resonance effects and small k-space trajectory errors. Figure 2.16 shows an example of the image quality from the standard PCMR sequence and the real-time PCMR sequence.

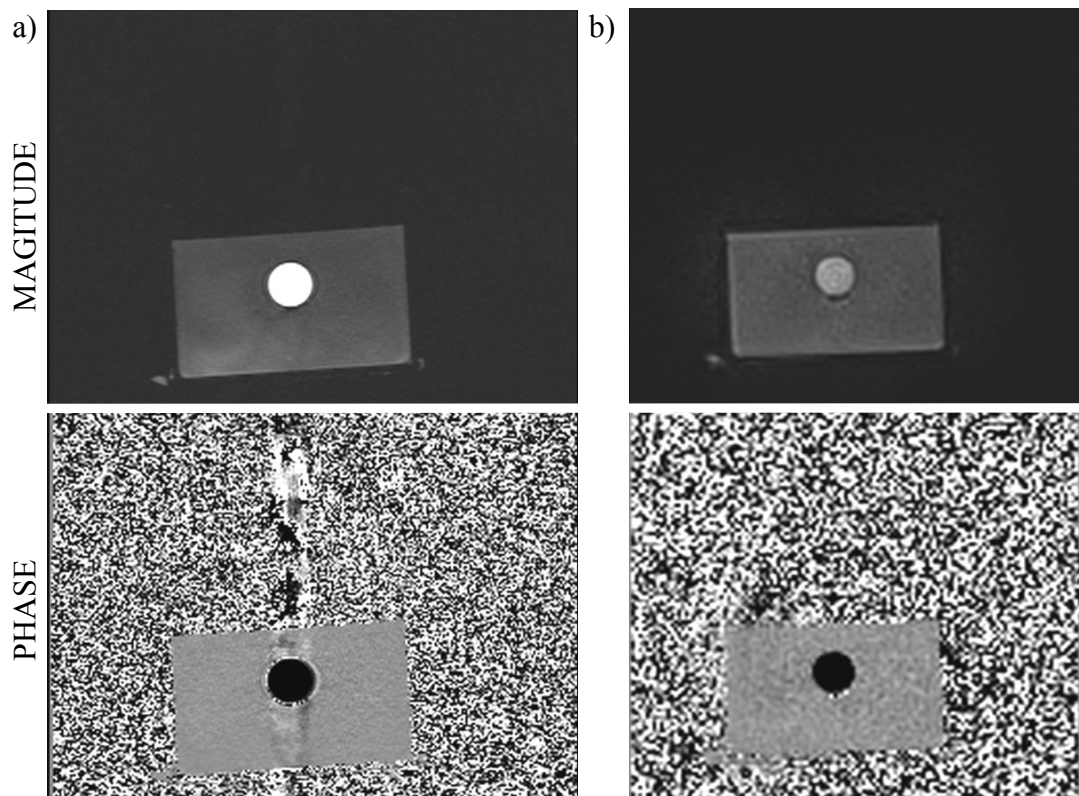


Figure 2.16: Examples of images acquired in-vitro from; a) the standard PCMR sequence and b) the real-time sequence

2.5 In-vivo Experiments

Validation of the real-time flow sequence, as well as hemodynamic response to exercise was performed in-vivo.

2.5.1 Study Population

Twenty healthy volunteers (9 Male: 11 Female) were recruited for this study between May and July 2009. The median age was 27.6 ± 6.8 years (range: 21.9-49.2 years). Exclusion criteria were;

- i. Cardiovascular disease (assessed by clinical history)
- ii. Illness that prevented exercise (i.e. joint disease)
- iii. Contraindications for MR such as MR-incompatible implants, or pregnancy

The local research ethics committee approved the study and written consent was obtained from all volunteers.

2.5.2 MR Protocol

Exercise was performed with an MR-compatible ergometer (MR cardiac ergometer Up/Down, Lode, Groningen, Netherlands), as seen in Figure 2.18 and Figure 2.17. The participants were placed supine in the MR scanner, with their feet strapped into the peddles and the upper leg strapped to supports on the ergometer, prior to the scan. Exercise consisted of an up-ward and down-ward motion of the pedals. This type of exercise is designed to minimize motion artefacts, as motion is restricted to the lower legs.



Figure 2.17: Photograph of a subject performing exercise on the ergometer, within the MRI scanner at ICH

All imaging was performed using two six-element body-matrix coils (one on top of the subject and one underneath the subject), as seen in Figure 2.18. It is not possible to use the standard spine coil underneath the subject, as this coil must be removed to accommodate the exercise ergometer on the scanner table.



Figure 2.18: Coils used for imaging in-vivo; one body-matrix coil on top of the subject, and one underneath

The imaging protocol at rest and at two exercise levels (4W and 8W) is shown in Figure 2.19;

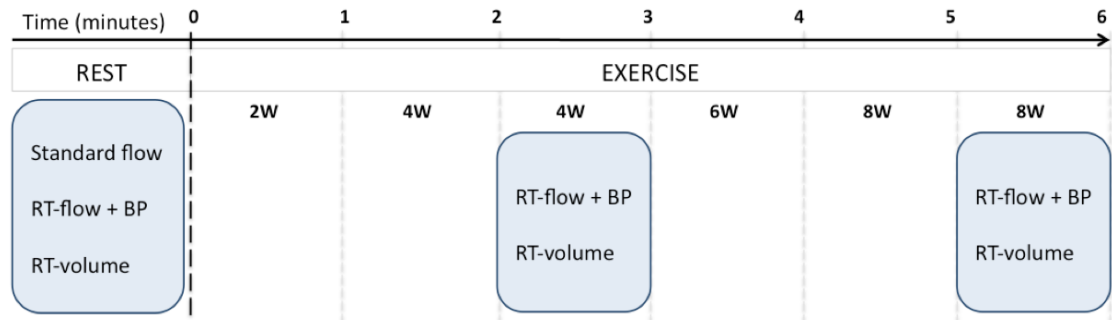


Figure 2.19: Figure from (63). The timeline of the MRI protocol at rest and during each exercise level

Exercise intensity was increased incrementally during the scan. All exercise data was acquired during free breathing and during the course of exercise. Brachial artery systolic, mean and diastolic blood pressure was measured with a cuff based oscillometric device (Datex Ohmeda, Finland) during acquisition of all real-time PCMR data.

2.5.2.1 Standard Flow Assessment

Standard aortic flow quantification was performed at rest using a retrospectively-gated, velocity-encoded gradient echo sequence (as previously described for the in-vitro experiment in section 2.4.1). The parameters are assumed to be the same as Table 2.9 unless otherwise stated in Table 2.11.

The imaging plane was located in the ascending aorta, as it passes the bifurcation of the pulmonary arteries. The scan was performed during free breathing. In this study the flow volumes measured from this sequence are assumed to be the true flow volumes.

Sequence Parameters	
TE/TR	3.2/7.0 ms
FOV	~320×240 mm
VENC	180 cm/s
NSA	3
Temporal resolution	27.1 ms (37 frames/sec)
Spatial resolution	~1.3×1.3 mm
Scan Time	~2.5 mins

Table 2.11: Standard PCMR sequence parameters, in-vivo

2.5.2.2 Real-time Flow Assessment

Real-time flow quantification was performed using the spiral PCMR sequence (as previously described in the in-vitro experiment in section 2.4.2). The parameters are assumed to be the same as Table 2.10 unless otherwise stated;

Sequence Parameters	
TE/TR	1.8/10.1 ms
FOV	500 mm
VENC	200 cm/s
Temporal resolution	40.4 ms (25 frames/sec)
Spatial resolution	3.9×3.9 mm
Scan Time	~6 sec

Table 2.12: Real-time spiral PCMR sequence parameters, in-vivo

The imaging plane was the same as the reference PCMR sequence. For each scan, 152 consecutive frames were acquired. Reconstruction for each scan took ~5 minutes.

2.5.2.3 Real-time Volume Assessment

Ventricular volumes were assessed using the real-time radial k-t SENSE sequence described in section 2.2.3. The sequence parameters are shown in Table 2.13;

Sequence Parameters	Radial k-t real-time
TE/TR	1.2/2.5 ms
k-t SENSE factor	8
Flip angle	38°
FOV	~380×380 mm
Slice thickness	10 mm
Number of slices	11-13
Matrix	128×128
Radial Spokes	128
Pixel Bandwidth	1500 Hz/pixel
Temporal resolution	~35.5 ms (~28 frames/sec)
Spatial resolution	3.0×3.0 mm
Scan time	~30 sec

Table 2.13: Real-time volume assessment sequence parameters, in-vivo

Eleven to 13 contiguous slices were acquired in the short axis to ensure coverage of the ventricle. Real-time data for each slice was acquired for 1.5 seconds and the slice was then automatically moved down the ventricle. This sequence has previously been validated at rest (87) and during exercise (86).

2.5.3 Data Analysis

All images were processed using in-house plug-ins for OsiriX. Measurement of ventricular stroke volume was performed by Vivek Muthurangu, as described in (86, 87). Flow images were manually segmented (by J.A.S. using the modulus images) and stroke volume and cardiac output were measured. By combining the flow data with blood pressure measurements, resistance and compliance were quantified (as described in 2.3.6.2).

All results are expressed as the mean \pm standard deviation. Measurements of agreement between the standard flow sequence and the real-time flow sequence, and also between the real-time k-t ventricular volume sequence and the real-time flow sequence, were performed using Bland-Altman analysis, as well as calculation of correlation coefficients. Two-tailed Student's t-tests were used to compare the hemodynamic responses at different exercise levels. All statistical analysis was performed using GraphPad Prism.

2.5.4 Image Quality

Small residual aliasing artefacts were visible in all real-time spiral flow images. Motion artefacts due to free breathing and continuation of exercise were not significant between images acquired at rest and at 8 W of continuous exercise. This is due to the very high temporal resolution achieved and because there is limited motion in the torso during the up-down exercise performed.

Additionally some image blurring was observed, which is attributed to the sensitivity of spiral trajectories to off-resonance effects and small k-space trajectory errors. Figure 2.20 shows examples of the image quality from the real-time flow sequence at rest and during exercise.

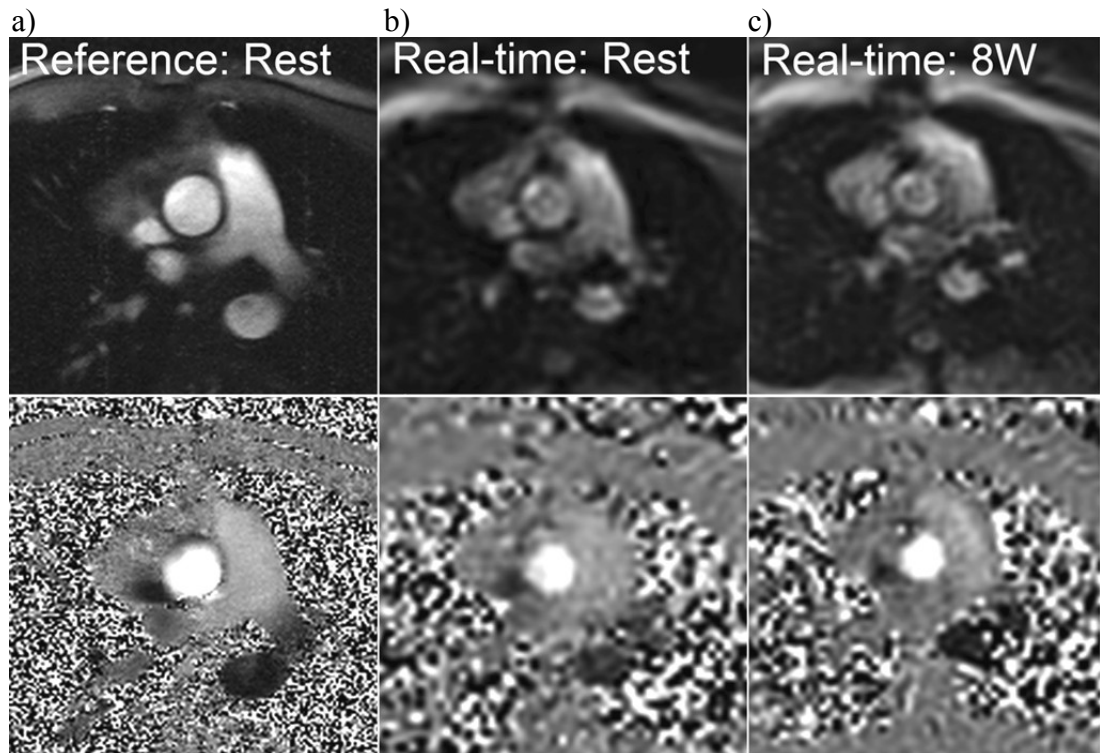


Figure 2.20: Figure from (63). Magnitude (top) and phase (bottom) images from; a) reference gated flow sequence at rest, b) real-time flow sequence at rest, and c) real-time flow sequence during exercise at 8W

2.5.5 In-vivo Validation

At rest the flow volumes calculated from the real-time spiral PCMR sequence were compared to those from the standard PCMR sequence. A good agreement in stroke volumes was found, $r = 0.994$, $p < 0.005$. Bland Altman analysis found a bias of -0.58 mL/cycle and limits of agreement from -4.71 to 3.56 mL/cycle, as shown in Figure 2.21.

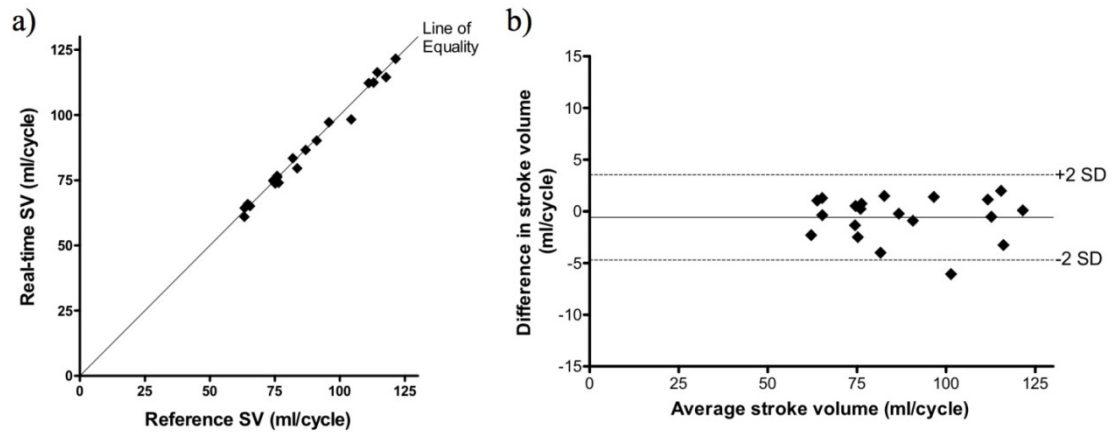


Figure 2.21: Figure from (63). Comparison of aortic stroke volumes from reference standard PCMR and real-time spiral PCMR, at rest. a) Correlation of flow measured from both techniques. b) Bland-Altman plot of the difference in flow measured using both techniques

At rest and during exercise, aortic flow volumes calculated from the real-time spiral PCMR sequence were compared with left ventricular stroke volumes from the real-time k-t SENSE volume measurements. At rest, Bland-Altman assessment found a bias of -2.04 mL/cycle and limits of agreement from -8.29 to 4.21 mL/cycle. The correlation coefficient between the two data sets was 0.988 ($p < 0.005$), as seen in Figure 2.22;

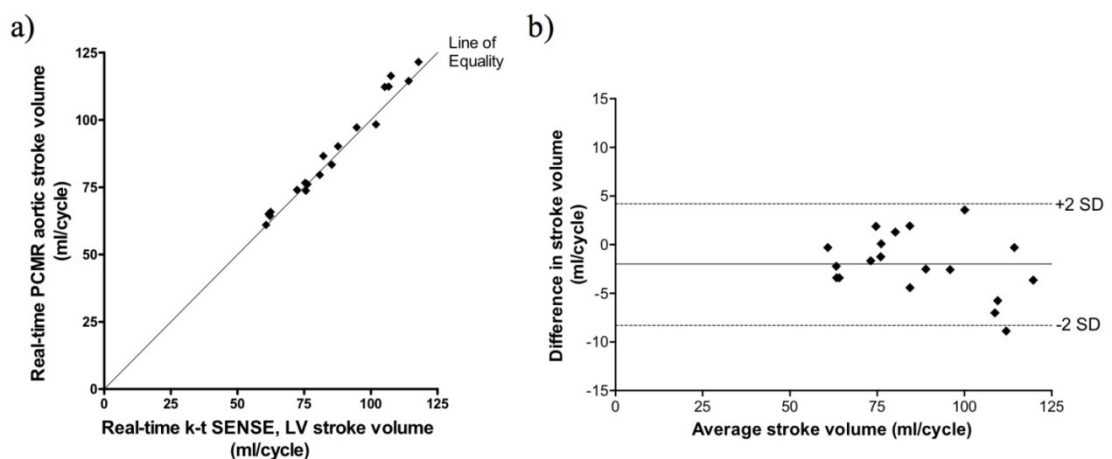


Figure 2.22: Comparison of stroke volumes in-vivo, at rest calculated from real-time k-t SENSE (LV stroke volume) and real-time spiral PCMR (aortic stroke volume). a) Correlation of flow measured from both techniques. b) Bland-Altman plot of the difference in flow measured using both techniques

During exercise at 8W, Bland-Altman assessment found a bias of 0.83 mL/cycle, with limits of agreement from -4.18 to 5.84 mL/cycle and a correlation coefficient of 0.984 ($p < 0.005$), as seen in Figure 2.23;

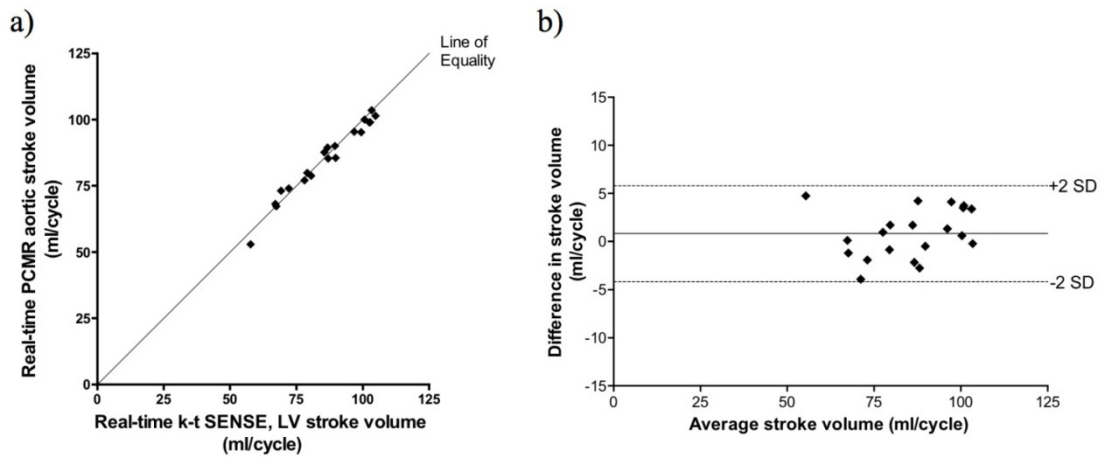


Figure 2.23: Comparison of stroke volumes in-vivo, at 8W of exercise calculated from real-time k-t SENSE (LV stroke volume) and real-time spiral PCMR (aortic stroke volume). a) Correlation of flow measured from both techniques. b) Bland-Altman plot of the difference in flow measured using both techniques

2.5.6 Vascular Response To Exercise

All participants successfully completed the exercise protocol. Blood pressure and MR flow data was measured on all subjects at rest, and at 4 W and 8 W of exercise. This data was used to calculate vascular resistance and compliance successfully in all subjects, at rest and during exercise.

Table 2.14 and Figure 2.24 show the average measured responses to exercise, which demonstrate the expected behaviour (94). Heart rate, cardiac output, and systolic and mean blood pressure increased significantly between rest and 4 W of exercise. Conversely, R and C decreased significantly between rest and 4 W. Between 4 W and 8 W heart rate, cardiac output and R changed significantly. There was no change in stroke volume or diastolic blood pressure during either stage of exercise.

	Rest⁺	4W⁺	8W⁺	P* (0W-4W)	P* (4W-8W)	P* (0W-8W)
Heart rate (bpm)	68.2 (12.5)	99.2 (15.8)	108.6 (21.2)	<.001	<.001	<.001
Stroke volume (ml/cycle)	87.2 (19.5)	85.1 (16.2)	85.2 (13.6)	0.3	0.97	0.41
Cardiac output (L/min)	5.8 (1.4)	8.3 (1.6)	9.1 (1.7)	<.001	0.002	<.001
Systolic BP (mmHg)	112.5 (10.4)	137.2 (15.2)	134.6 (21.0)	<.001	0.5	<.001
Diastolic BP (mmHg)	64.8 (6.0)	66.3 (12.3)	64.3 (13.1)	0.54	0.46	0.85
Mean BP (mmHg)	83.9 (6.8)	95.5 (9.4)	95.3 (8.9)	<.001	0.91	<.001
Vascular resistance (WU)	15.2 (2.9)	11.8 (2.5)	10.7 (1.7)	<.001	0.007	<.001
Arterial compliance (mL/mmHg)	1.00 (0.23)	0.62 (0.23)	0.63 (0.21)	<.001	0.8	<.001

+ Mean from all volunteers (standard deviation) * Paired t-test

Table 2.14: Response to Exercise

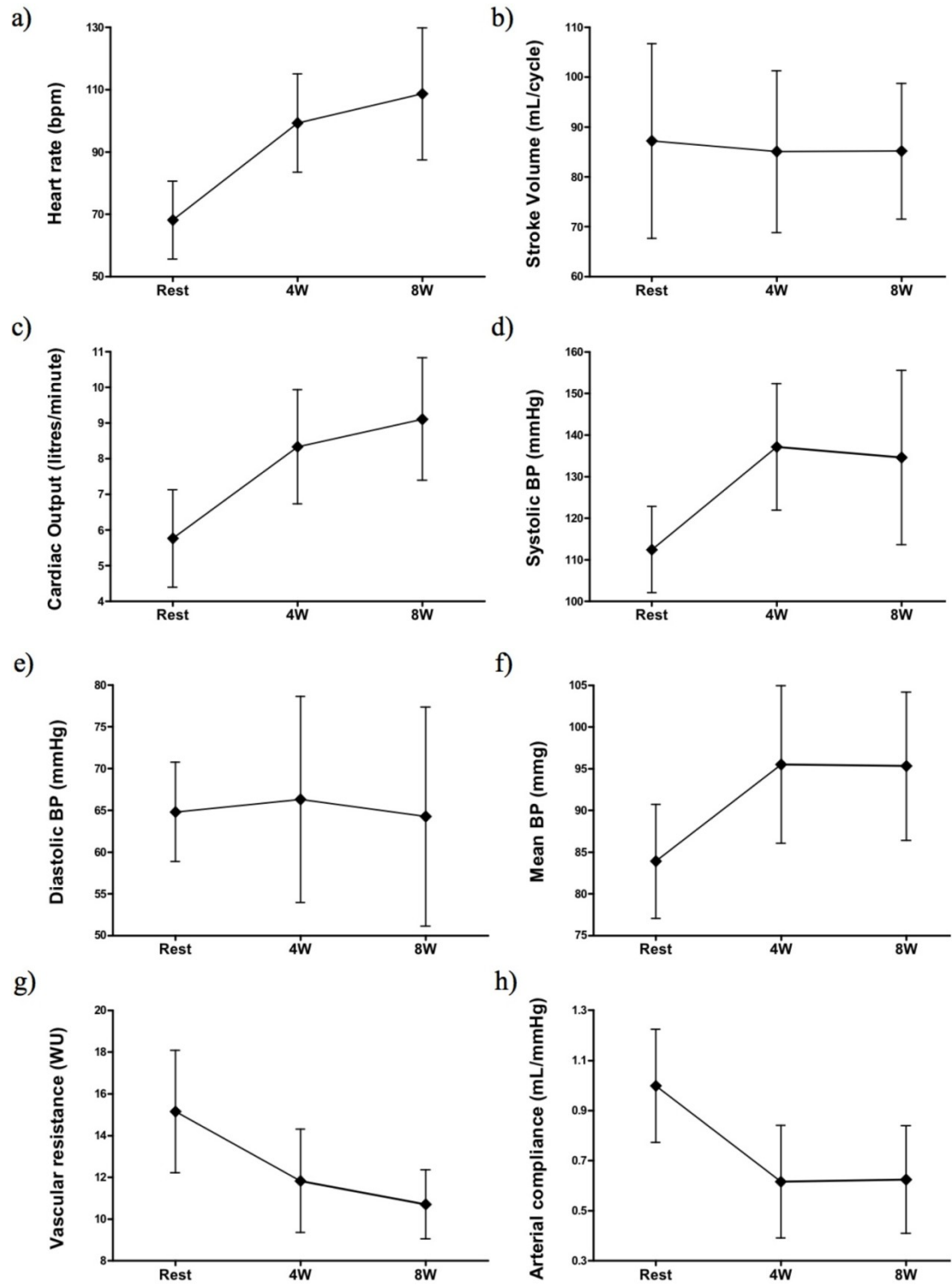


Figure 2.24: Measured responses to exercise. All points are mean values, and standard deviation is shown with error bars. Effect of exercise on a) heart rate, b) stroke volume, c) cardiac output, d) systolic BP, e) diastolic BP, f) mean BP, g) systemic vascular resistance, and h) arterial compliance. Figures a)c)g)h) from (63)

2.6 Discussion

The main findings of this study were;

- i) Real-time PCMR, achieved using an undersampled spiral sequence reconstructed using SENSE, is an accurate method of measuring aortic flow at rest and during exercise
- ii) MR flow data can be successfully combined with simultaneous blood pressure measurements to quantify hemodynamic responses to exercise in healthy volunteers

Exercise may be used to unmask early signs of vascular disease in at-risk groups. The ability to non-invasively measure vascular resistance and compliance further improves the sensitivity of exercise testing. Thus, this technique may allow the identification of at-risk individuals (90, 91). Impedance Cardiography offers an alternative method of measuring flow in real-time, however it is often unreliable and is not as accurate as MRI (95).

Gated flow sequences are unreliable during exercise due to excessive motion. A more robust solution is real-time imaging (81, 86). However, real-time sequences generally have a lower temporal resolution than gated sequences. This is problematic for exercise studies due to the high heart rates arising during physical stress. In this study adequate temporal resolution was achieved in three ways;

1. Spatial resolution was sacrificed, requiring less coverage of k-space and thus allowing quicker filling of k-space
2. A spiral trajectory was used, which allowed more efficient filling of k-space
3. K-space was undersampled and reconstructed using a SENSE algorithm

The resultant images have a low spatial resolution with an improved high temporal resolution, and minimal residual aliasing. Increased breathing during exercise caused little visual difference in image quality between scans acquired at rest and in exercise due to the high temporal resolution achieved. However, breathing is known to affect the stroke volume (96). In the standard flow sequence, variations in stroke volume

from breathing are averaged out, however when analyzing the real-time stroke volumes, a single flow cycle was chosen for comparison. This may explain some of the differences in flow volumes found between the two techniques.

Despite compromising the spatial resolution and using an undersampled non-Cartesian trajectory, there was good agreement with the reference flow sequence and the real-time ventricular volumes. Thus, this sequence is a robust method for assessing aortic flow during exercise.

2.6.1 Hemodynamic Response to Exercise

Using the real-time flow sequence we were able to demonstrate an increase in cardiac output at 4 W and 8 W, driven by an increase in heart rate rather than stroke volume. It has previously been observed that in raised leg supine exercise at a low intensity level, increased cardiac output was driven by heart rate rather than stroke volume (97). The low exercise levels undertaken may explain why stroke volume did not significantly change, compared to previous supine exercise studies which have used higher exercise levels including 7.5 W, 15.0 W and 22.5 W (86). Nevertheless, we were able to elicit a fall in R and C in this normal population.

To our knowledge, this is the first time vascular resistance and compliance have been quantified using MR during exercise. Previously, R and C have been assessed in the pulmonary vasculature by combining MR flow data at rest and simultaneous invasive blood pressure measurements (90, 91). We have extended these well-validated techniques to the systemic vasculature during exercise. It has been hypothesized that a lower than normal fall in R, in response to exercise is an indicator of early vascular disease (94, 98). An excessive drop in C during exercise may also predispose to vascular disease. Further work is required to demonstrate abnormal vascular responses in a patient population using this technique.

2.6.2 Limitations

In this study vascular response was only measured during mild, supine exercise. Increasing the exercise intensity may increase the sensitivity to subtle vascular abnormalities. Unfortunately, as exercise intensity increases it may become more difficult to accurately measure blood pressure non-invasively. However, it should be noted that we were able to elicit a response during mild exercise.

The other limitations of this technique are the low spatial resolution and long reconstruction times. Spatial resolution could be increased by the use of a smaller FOV, which here was set high to include the arms. This could be achieved by the use of spatially-selective excitations or saturation bands, which would conversely decrease temporal resolution (see section 5.2.1). Additionally, RF-shielding of the arms and torso or improved coil configurations, may allow a smaller FOV without affecting the temporal resolution (see section 5.2.1). Alternative reconstruction algorithms, which take advantage of spatiotemporal correlations (e.g. k-t SENSE (99)), may allow an increase in matrix size without a large temporal penalty. Reconstruction times could be improved by the use of newer multi-processor graphics cards (100), which are well suited to complex iterative reconstruction (see section 5.2.2).

2.6.3 Conclusion

In conclusion, we have shown that it is possible to measure the hemodynamic response to exercise using a combination of real-time MR flow and simultaneous blood pressure measurements. It is hoped that this technique could be used to identify individuals at risk of developing cardiovascular disease and thus allow early medical intervention.

2.7 Automatic Segmentation Propagation of Real-Time PCMR

Post-processing of real-time PCMR images is challenging as they have low spatial resolution, low SNR, as well as misalignments from frame to frame due to free breathing. The high temporal resolution means that hundreds of frames can be acquired in a few seconds. This makes computer-assisted segmentation tools desirable.

Existing methods for automated segmentation of vessels include;

- Adaptive thresholding (101)
- Graph searching (102)
- Active contours (103)
- Model-based approaches for small vessels (104)

Transferring these approaches to real-time images is challenging.

Freddy Odille (105) investigated the use of accurate, fully deformable nonrigid registration for segmentation of the real-time data acquired in section 2.5. The results from this work are in press in the *Journal of Magnetic Resonance Imaging*, 2010, by F. Odille, J. Steeden, V. Muthurangu and D. Atkinson, entitled; “Automatic Segmentation Propagation of the Aorta in Real-Time Phase Contrast MRI using Nonrigid Registration” (105) (see Appendix 2).

The registration provides displacement fields that describe motion between a reference frame and every other frame of the temporal series. A contour drawn manually in the reference frame can therefore be automatically propagated to the other frames, resulting in a fast segmentation of the whole real-time sequence of images.

The registration-based segmentation was integrated into an OsiriX plug-in. The registration was limited to a rectangular region-of-interest (ROI), of size 9×9 cm², selected around the reference contour to save computation time. To decrease the sensitivity of the algorithm to intensity changes from inflow enhancement, a

histogram matching was applied to all images of the time series before running the registration.

For ten randomly selected volunteer data sets from section 2.5 (at rest and exercise at 4 W), two observers (F.O. and J.A.S.) performed manual segmentation (M1 and M2) and automatic segmentation (A1 and A2). The segmentation errors were quantified using Dice score (106) (the intersection area divided by the mean area of the ROI's) and stroke volume measurements.

A high Dice score (of 0.886 ± 0.039) was found when comparing automatic and manual segmentations. Additionally, a good correlation coefficient between SV measurements was found at rest and exercise, as seen in Table 2.15.

	M1 vs. M2	A1 vs. A2	M vs. A^a
Rest			
Correlation coefficient	0.988	0.983	0.987
Bias (mL/cycle)	2.64 ± 3.31	0.54 ± 3.94	– 0.82 ± 3.83 -1.36 ± 3.07 1.82 ± 3.11 1.28 ± 3.73
Wilcoxon signed rank test	p = 0.02	p = 0.23	– p = 1.00 p = 0.28 p = 0.11 p = 0.28
Exercise			
Correlation coefficient	0.960	0.945	0.958
Bias (mL/cycle)	3.24 ± 4.10	1.17 ± 5.04	– -1.47 ± 4.52 -2.64 ± 5.43 1.77 ± 3.35 0.60 ± 3.70
Wilcoxon signed rank test	p = 0.01	p = 0.49	– p = 0.23 p = 0.28 p = 0.11 p = 0.63

^a Results from all combinations: M₁ vs. A₁, M₁ vs. A₂, M₂ vs. A₁, M₂ vs. A₂.

Table 2.15: Results from (105) showing stroke volumes calculated from manual vs. automatic segmentations

Figure 2.25 shows an example of manual and semi-automatic segmentations from the two observers;

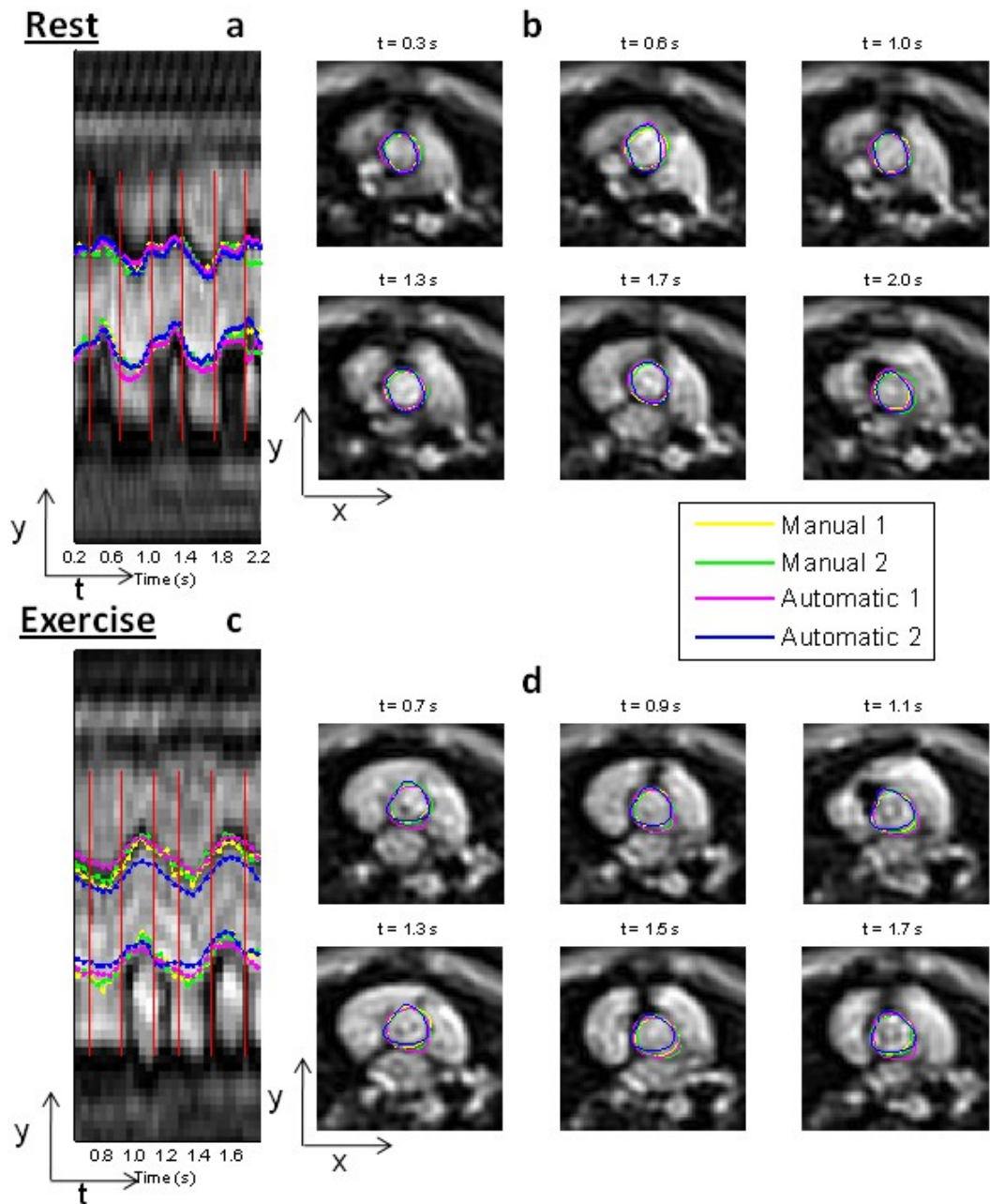


Figure 2.25: Figure from (105). Example of manual and semi-automatic segmentations from two observers, at rest (a, b) and during exercise (c,d). Segmentations are show in a hybrid space-time view (a, c) and in multiple frames (c,d) chosen at times indicated by the red vertical lines

It can be seen that the semi-automatic segmentations were accurate when compared to manually drawn ROI's, in terms of Dice score and stroke volume measures. This is true at rest and in exercise, demonstrating that this technique works even in the presence of significant movement in the vessel of interest. The variability of the semi-automatic segmentation is partly limited by the intrinsic variability of the initial manual segmentation. This may explain why the semi-automatic method does not provide a better reproducibility. The lower A1 vs. A2 bias suggests that the semi-automatic segmentation technique is less likely to suffer from systematic inter-observer error.

The main advantage of this technique is the possibility to accurately segment hundreds of images in ~10 seconds. This is compared to up to 30 minutes when segmenting all frames manually.

2.8 Hemodynamic Response To Mental Stress Using Real-time PCMR

This novel real-time PCMR sequence was also used in the first study to measure the hemodynamic response to mental stress using MRI, by Alexander Jones (107). This work aims to help understand the underlying links between mental stress and the development of cardiovascular disease. The results from this work are in press in *Journal of Magnetic Resonance Imaging*, 2010, by A. Jones, J. Steeden, J. Pruessner, A. Taylor, A. Deanfield and V. Muthurangu, entitled; “Detailed Assessment of The Hemodynamic Response to Psychosocial Stress using Real-Time MRI” (107) (see Appendix 3).

Standard cardiac-gated sequences are unsuitable for mental stress studies, due to their;

- Long acquisition times
- Motion intolerance
- Insensitivity to short-term changes in flow patterns

Therefore, real-time measurements are necessary when imaging during mental stress tasks.

In this study the Montreal Imaging Stress Task (MIST) (108) was used to evoke a neuroendocrine stress response, while the subject was in the scanner. Mental arithmetic tasks were displayed on a computer screen (Figure 2.26), visible to the participants using a mirror. Answers were selected from a circularly arranged set of numbers (0-9) using a fibre-optic mouse. Regardless of the participant’s performance, the ‘performance bar’ was negatively biased such that they appeared to perform poorly in comparison to the average score.

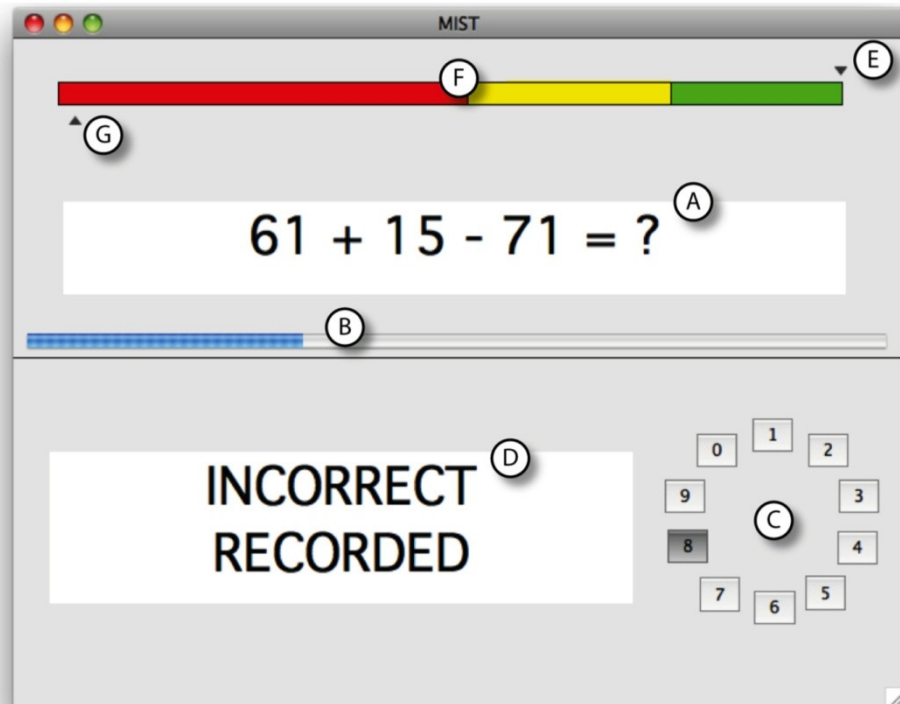


Figure 2.26: Figure from (107). A screenshot of the MIST test, showing; a) an example mathematical problem, b) a timer bar, c) possible answers (0-9) and d) feedback box. f) The ‘performance bar’, shows the ‘average’ score e) marked above the bar and the participants score g) below the bar

Flow was measured using the real-time spiral SENSE PCMR sequence using the same parameters as in Table 2.10, unless otherwise stated;

Sequence Parameters	
TE/TR	1.93/9.63 ms
Flip angle	25°
Pixel bandwidth	1860 Hz/pixel
VENC	180 cm/s
Temporal resolution	38.5 ms (~26 frames/sec)

Table 2.16: Sequence parameters used in mental stress study by Jones, et al. (107)

For each measurement, 76 consecutive frames were acquired over ~3 seconds. Simultaneous oscillometric blood pressure measures were used to calculate systemic vascular resistance and arterial compliance.

Twenty-two healthy, non-smoking volunteers (11 male: 11 female) with a median age of 36.2 (range: 25.9-63.7) years were recruited. It was found that in response to stress, blood pressure increased due to increased cardiac output and reduced compliance. As stroke volume did not significantly change, the increase in cardiac output was solely due to the increase in heart rate. Greater blood pressure responses were observed in male subjects, than in female subjects, due to a greater increase in cardiac output and higher vascular resistance. Older participants were observed to have greater blood pressure responses, due to a greater decrease in total arterial compliance.

This study showed the possibility of comprehensively assessing the cardiovascular response to mental stress using a combination of the MIST test and real-time PCMR. The findings suggest stress exposes relationships of cardiovascular function with age and sex, which were not seen at rest. It is thought that this method may be used to provide a greater understanding of the mechanisms underlying the links between mental stress and the development of cardiovascular disease.

2.9 Clinical Use

In addition to the research studies described here, this real-time PCMR sequence is used in the clinical environment at ICH to measure flow in subjects with an irregular heart rate. Previously flow could not be measured in these subjects as conventional methods of measuring blood flow, using cardiac gating, fail. Figure 2.27 shows an example of flow data acquired using the real-time spiral PCMR sequence, in a patient with an irregular heart rate.

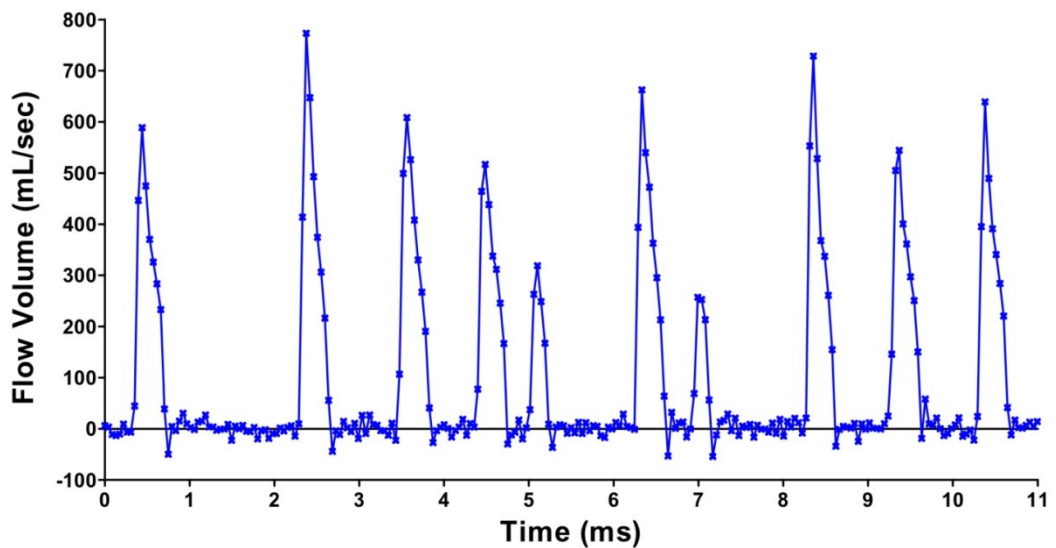


Figure 2.27: Flow curve measured using the real-time PCMR sequence, in a subject with an irregular heart rate

CHAPTER 3

Split-Acquisition Flow Measurements

3.1 Introduction

The fundamental problem with PCMR is the need to acquire two phase images to produce a single PC flow image. This limits the available spatial or temporal resolution, which is particularly problematic for real-time imaging. In children with congenital heart disease, high resolution imaging is necessary to ensure accuracy at higher heart rates and in smaller vessels. Thus, real-time imaging is not commonly used in this population. Although the real-time PCMR sequence developed in chapter 2 has a high temporal resolution, the low spatial resolution makes this sequence unsuitable for imaging small vessels. Nevertheless, fast, free breathing acquisitions are still desirable for children as they could significantly improve patient compliance and diagnostic effectiveness.

Reference-less PCMR sequences that use a single flow-encoded data set to measure flow, have been previously investigated (see section 3.2.1). In these studies, background phase offsets are predicted by fitting a low order model through the phase of static tissue surrounding the vessel of interest. Unfortunately, these methods do not perform well for intra-thoracic vessels due to the lack of stationary, surrounding tissue.

In this study, an alternative split-acquisition real-time CINE approach is considered (see section 3.3.1). Flow-encoded and flow-compensated data are acquired continuously at high temporal resolution in separate short blocks. By comparing magnitude images, the closest flow-compensated frame in the cardio-respiratory cycle is determined for each flow-encoded frame. These matched flow-compensated frames are used to subtract out background phase offsets from the flow-encoded phase data. Thus, the data is acquired in real-time but with the background phase correction originating from a different heart beat. This effectively doubles the frame rate compared to conventional interleaved real-time PCMR, allowing either higher temporal or spatial resolution.

3.1.1 Aims

The aims of this study were to;

- Develop a split-acquisition spiral SENSE PCMR sequence
- Develop a fast and accurate matching algorithm
- Validate the split-acquisition flow sequence in-vivo
- Demonstrate the utility of the split-acquisition flow sequence in a paediatric population

3.1.2 Personal Contribution

To fulfil the above aims I have:

- Designed and developed a split-acquisition sequence (see section 3.3.1) developed in the Siemens, IDEA environment. This is based on the undersampled spiral SENSE sequence developed in chapter 2
- Optimised the sequence parameters (see section 3.4)
- Designed a matching algorithm (see section 3.3.2) which was subsequently developed in the Siemens, ICE environment (also prototyped in MATLAB)
- Performed validation of the matching technique (see section 3.6)
- Assessed image quality of the split-acquisition technique, by quantification of signal-to-noise ratio (SNR), velocity-to-noise ratio (VNR) and edge sharpness (see section 3.7). These measures were calculated using plug-ins developed for OsiriX (see section 3.3.3)
- Performed in-vivo validation of the sequence, in an adult population (see section 3.8)
- Showed the utility of the sequence in a paediatric population (see section 3.9)

The results from this work have been published by J. Steeden, D. Atkinson, A. Taylor and V. Muthurangu, in *Magnetic Resonance In Medicine*, 2010, **64**(6), entitled; “Split-Acquisition Real-time CINE Phase-Contrast MR Flow Measurements” (109) (see Appendix 4).

3.2 Literature Review

In this section, literature on the following areas will be discussed:

- Reference-less flow measurements
- Splitting the acquisition of flow data
- Matching MR images

3.2.1 Reference-less Flow Measurements

Previous studies have investigated the use of reference-less flow imaging. These studies acquire just flow-encoded data and then predict the background phase offsets. This allows a doubling in the achievable temporal resolution.

In 1999, Man, et al. (110) described the use of a spiral sequence for non-subtractive flow measurements. By assuming that the background phase varies slowly in space, these offsets are predicted from the flow-encoded data itself.

In this method a fourth-order polynomial is fitted separately to the real and imaginary parts of the flow-encoded data (in areas of sufficient SNR). The resulting phase is assumed to be the global trend of the phase offset, and is subtracted from the flow-encoded phase image. A 2D median filter (with approximately twice the size of the vessel of interest) was then applied separately to the normalized real and imaginary parts of the resultant image. This filter is used to prevent phase caused by flowing blood, from affecting the background phase estimate. The resulting phase from the median filter is used as an additional background phase correction to the polynomial phase-corrected image.

Man, et al. showed this non-subtractive technique to have a good correlation with a standard PCMR sequence and the *bucket and stopwatch* method in a steady flow phantom (average velocity errors: ± 1.7 cm/s and ± 2.5 cm/s, respectively). Flow was also measured in one volunteer, where the average discrepancy in velocities was found to be up to ± 6 cm/sec.

The method by Man, et al. was shown to have a reduced accuracy in velocity measurements and increased artefacts compared to a conventional PCMR sequence. Additionally, this non-subtractive method is not suitable for measuring bulk flow in the heart chambers, or in vessels which are surrounded by air.

An extension of this work was carried out in 2009 by Nielson, et al. (111) who used a balanced steady-state free-precession (SSFP), flow-encoded, Cartesian sequence (with $TE = TR/2$) to perform reference-less PCMR imaging. Nielson, et al. manually selected stationary tissue in close proximity to the vessel of interest (VOI). A low order polynomial was then fitted through these pixels and this was subsequently subtracted from the phase of the flow-encoded images, as seen in Figure 3.1;

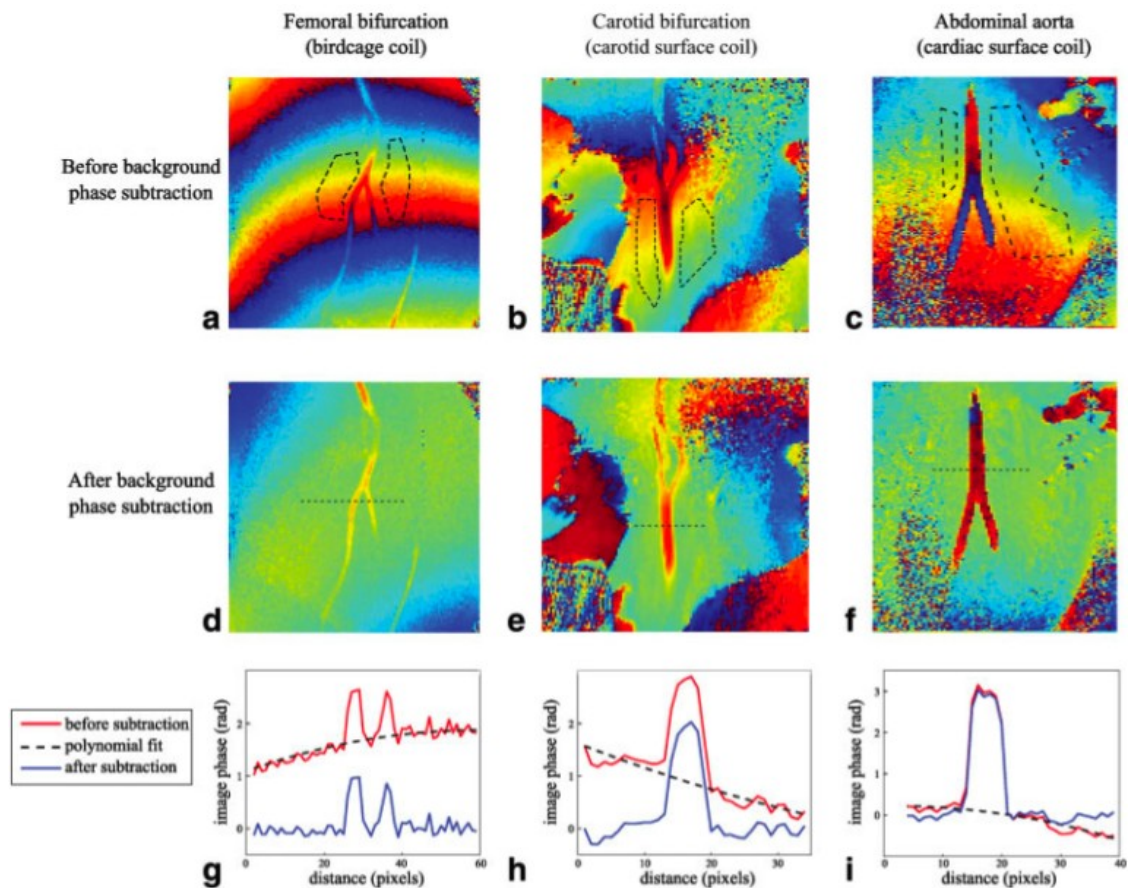


Figure 3.1: From Nielson, et al. (111). Top row shows manually drawn ROI's through the smooth background phase offsets. These images were corrected using a 2nd order polynomial fit (middle and bottom row)

Using the mean-squared error as a measure of goodness-of-fit, in two subjects it was observed that a 3rd or lower order polynomial fit could be used to adequately approximate the background phase.

Nielson, et al. demonstrated the possibility of predicting phase offsets from static regions close to the vessel of interest, to enable accurate flow quantification. The proposed technique requires manual segmentation of stationary tissue for every measurement – this is not feasible in clinical practise as it is very time consuming. This technique is also not possible where there is no or little stationary tissue near the vessel, e.g. in cardiac flow.

Both of these studies have demonstrated the possibility of acquiring just flow-encoded data and predicted the background phase offsets from stationary tissue. Unfortunately, these techniques have been demonstrated on a very limited number of volunteers, and little validation of either technique is shown. Neither of these techniques are suitable in areas where the vessel is surrounded by air, as there is no static tissue for phase reference. As we are interested in measuring flow in the aorta, which is surrounded by the lungs and non-static tissue, neither the techniques by Man, et al. or Nielsen, et al. could be used.

We wish to develop a technique which allows an effective doubling in temporal resolution, as achieved in reference-less flow measurements, however which is suitable to measure flow in the aorta. We wish to make our technique fully automated, unlike Nielson, et al. to make it clinically useful.

3.2.2 Splitting the Acquisition of Flow Data

A few studies have investigated splitting the acquisition of different flow data over multiple cardiac cycles.

In 1994, Gatehouse, et al. (7) measured flow volumes using an ECG-triggered, single shot, spiral sequence. In this study the flow-compensated data was acquired in one heart-beat and the flow-encoded data acquired in the successive heart-beat. The

resulting phase-contrast data was formed by temporal matching of the flow-compensated and flow-encoded data. This approach allows an effective doubling of temporal resolution, compared to standard phase-contrast imaging.

Gatehouse, et al. measured flow using this technique in the descending aorta of normal volunteers, using the sequence parameters shown in Table 3.1;

Sequence Parameters	
TE/TR	6/50 ms
Spiral interleaves	1
Flip angle	45°
FOV	350 mm
Matrix	64×64
Slice thickness	10 mm
Effective Temporal resolution	50 ms (20 frames/sec)
Spatial resolution	5.5 mm

Table 3.1: Sequence parameters used by Gatehouse, et al. (7)

Lower velocities were measured using this sequence compared to a standard PCMR sequence. This was thought to be due to the low spatial resolution of the spiral sequence, as the large voxels cause a greater partial volume effect and also make the area measurement unreliable.

Similarly, Nayak, et al. (112) studied the possibility of acquiring different flow-encoding directions over multiple heart-beats. Continuous “triggered” real-time data was acquired, where the flow-encoding direction was modified in response to a detected R-wave. The spiral PCMR sequence, with sliding window reconstruction, by Nayak, et al. (64) described in section 2.2.1.1, was used to acquire data in one healthy volunteer. By acquiring data over three RR-intervals (breath-hold of 4 sec), flow was measured in three directions.

Additionally, Nayak, et al. (112) measured flow in six parallel slices by acquiring data (in a single flow-encoding direction) over six RR-intervals (breath-hold of 7 sec), showing how this technique could be used for multi-slice coverage. The accuracy of these techniques was not demonstrated.

These studies by Gatehouse, et al. (7) and Nayak, et al. (112) demonstrate that it is possible to acquire phase-contrast data over multiple heart-beats, and retrospectively combine the data to obtain flow measurements. However, validation of these techniques is limited. Both studies used cardiac gating to trigger the start of a new flow-encoding. We do not wish to use cardiac gating, as this is susceptible to inaccurate R-wave detection, and is not feasible for subjects with irregular heart-beats. Additionally by removing the need for ECG monitoring, we are in keeping with a philosophy of a more simple MRI (113).

3.2.3 Matching MR images

When considering how best to match flow-compensated and flow-encoded data from different cardiac cycles, we wished for a simple, fast and accurate method. When performing catheter tracking using MRI, a thick slab is dynamically imaged and a baseline image subtracted. The baseline image is used to highlight the movement of devices and must be reacquired if any motion occurs, if scan geometry changes or if other parameters are changed.

A modified catheter tracking technique was developed by Bakker, et al. (114) where a set of dynamic reference images were acquired, instead of a single baseline image. The most suitable reference image was selected automatically for each acquired image, and used for subtraction. This method is called *adaptive subtraction*. Bakker, et al. selected the most suitable reference image, as the frame with the minimum least square error with the acquired image pixels.

This technique was validated in-vitro and in-vivo, where it was observed that the adaptive subtraction method was not sensitive to motion (of the phantom in-vitro, or respiratory motion in-vivo) or modified scan parameters, whereas with a conventional baseline subtraction, the images remained severely degraded by artefacts.

This study showed that *adaptive subtraction* can be used in-vivo to accurately track catheters, by matching images from different RR-intervals. This matching method is very simple, and hence matching can be performed rapidly with very little computational delay.

3.2.4 Summary

From the literature review it can be seen that:

- Previous studies have investigated using reference-less PCMR techniques, where just flow-encoded data is acquired and background phase offsets are predicted from stationary tissue. Unfortunately these techniques do not work well where there is little stationary tissue near to the vessel of interest
- Previous studies have investigated splitting the different encoding gradients for PCMR over multiple RR-intervals. These studies use cardiac gating, and match the flow data according to their temporal position
- In catheter tracking, an adaptive subtraction technique has been developed to successfully match images from different subsets of data

3.3 Development

In this study we investigated the possibility of splitting the acquisition of flow-compensated and flow-encoded data, and retrospectively matching these images to remove background phase offsets. Data was acquired using the real-time spiral SENSE sequence developed in chapter 2. However, an alternative acquisition scheme and an accurate matching technique, were developed.

3.3.1 Split-acquisition Scheme

Accurate phase subtraction relies on correct spatial alignment (matching in the cardio-respiratory cycle) of flow-compensated and flow-encoded data. The proposed split-acquisition strategy relies on the fact that the cardiac and respiratory cycles have different frequencies. Thus, data from adjacent RR-intervals is likely to be in similar positions in the respiratory cycle. This means that flow-compensated and flow-encoded data can be acquired continuously in consecutive short blocks and still be matched in the cardio-respiratory cycle.

As it is necessary to capture one whole cardiac cycle in each block, each block must be longer than one RR-interval. However, to ensure adjacent blocks are in a similar position in the respiratory cycle, each block must be as short as possible. Therefore, in this study the split-acquisition sequence was divided into three blocks of two seconds each (compensated – encoded – compensated), as seen in Figure 3.2;

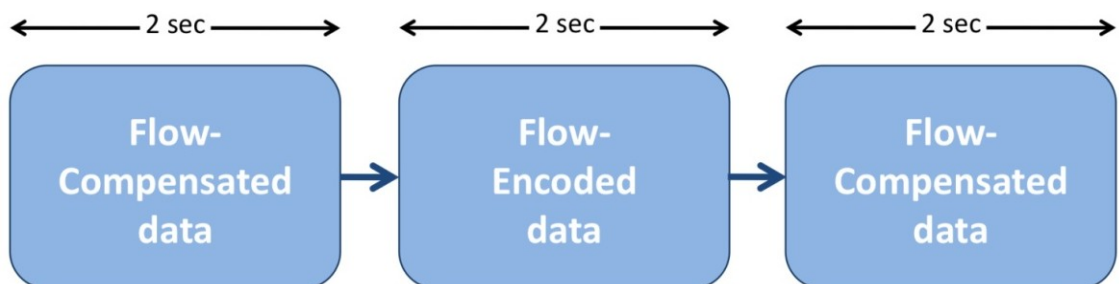


Figure 3.2: Acquisition of flow data for split-acquisition technique

Two flow-compensated blocks were used to increase the likelihood of at least one flow-compensated measurement being acquired at a similar point in the respiratory cycle to each flow-encoded measurement.

3.3.2 Matching Technique

Precise matching of flow-compensated and flow-encoded data is necessary to ensure accurate flow measurements. In this study we propose to use a variation of the adaptive subtraction technique used by Bakker, et al. (114) (section 3.2.3), to retrospectively match the flow-compensated and flow-encoded data.

In this study we are interested in accurate quantification of flow in the aorta. It is therefore important that the flow-encoded and selected flow-compensated images align well in the vessel of interest. By planning the scan position so that the vessel of interest was in the centre of the resultant images, it was possible to apply an adapted 2D Tukey window (as described in section 2.3.2.1) to all magnitude images before matching, to attenuate signal at the edge of the image. This weights the matching more heavily on the vessel of interest. The optimal filter parameters were found to be; flat top radius = FOV/6, transition width = FOV/8. The effect of this Tukey filter can be seen in Figure 3.3;

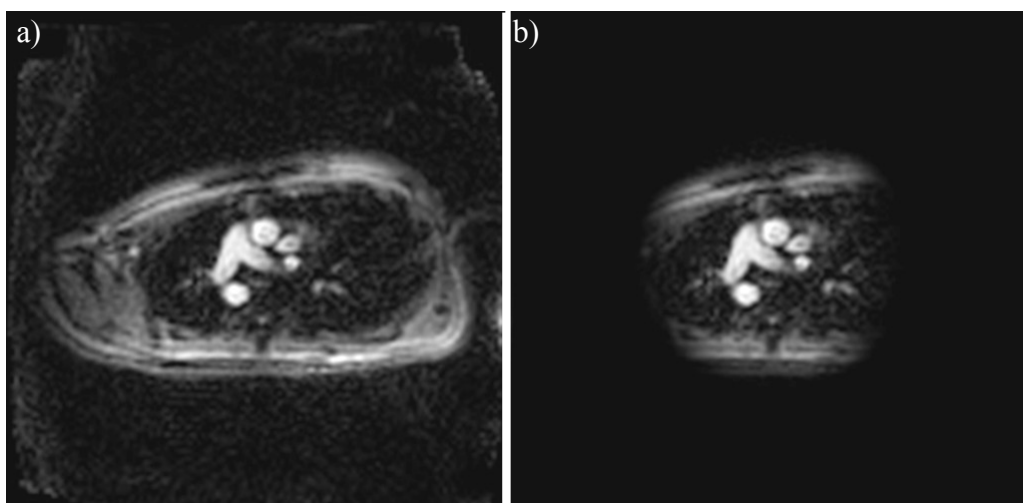


Figure 3.3: Effect of the Tukey filter on the magnitude images. a) Magnitude image before Tukey filter, b) Windowed magnitude image after Tukey Filter

Each windowed flow-encoded frame was then matched to a windowed flow-compensated frame from either of the two blocks, using the following scheme (also see Figure 3.4);

- Pixel-wise subtraction of the flow-encoded frame (windowed magnitude reconstruction) from every flow-compensated frame (windowed magnitude reconstruction, from both blocks) to produce a set of difference images
- A matching error metric (ϵ) was calculated by summing all of the absolute pixel values in each difference image
- Identification of the ‘matched’ flow-compensated frame that is associated with the lowest ϵ value
- Phase subtraction of the flow-encoded frame with its matched flow-compensated frame to remove background phase offsets and produce the final PC image

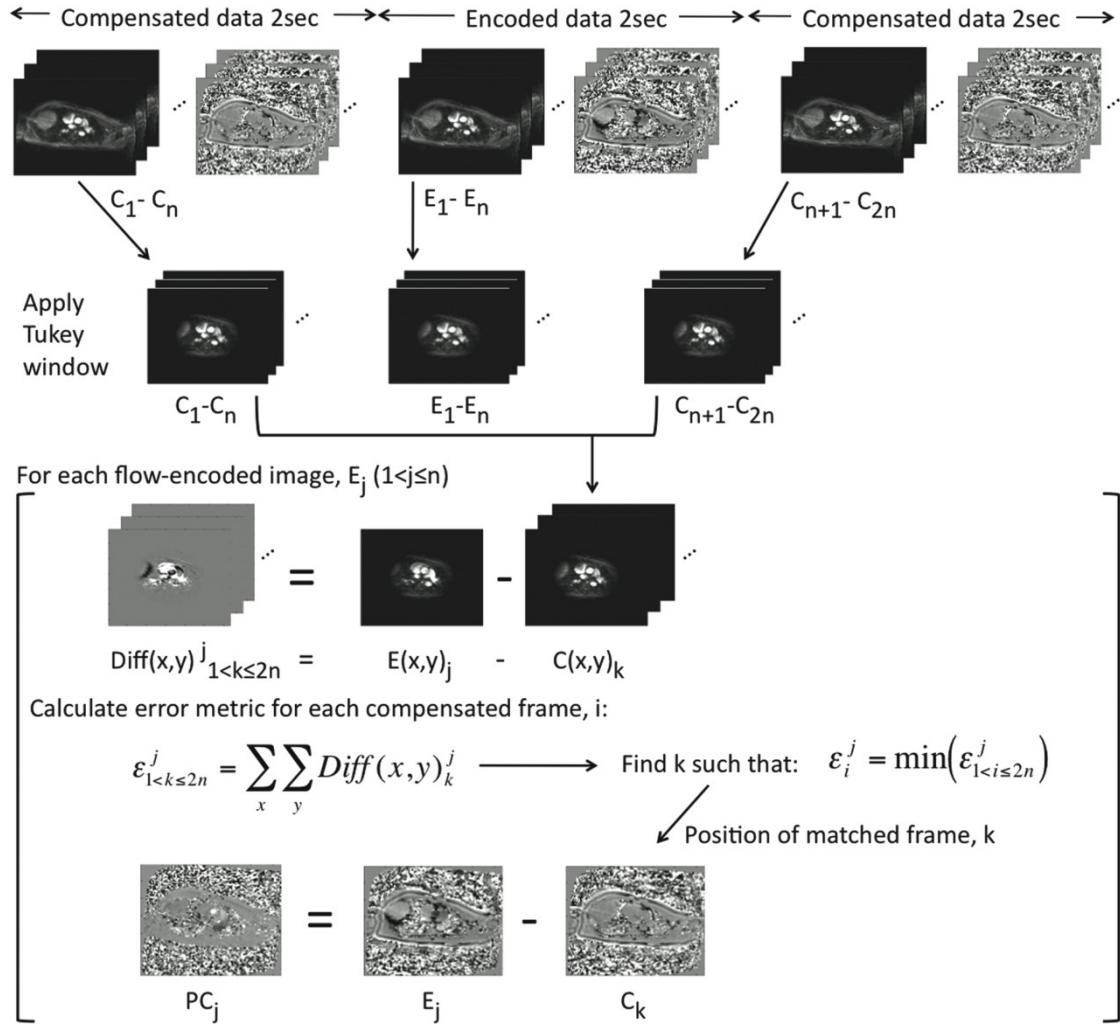


Figure 3.4: Figure from (109). Pipeline of data acquisition and reconstruction for the proposed split-acquisition real-time CINE PCMR technique

3.3.3 Development of Image Quality Assessment Tools

We wished to quantify the image quality of the resultant split-acquisition sequence. Parallel imaging is known to affect the SNR by;

$$SNR_{SENSE} = \frac{SNR_{NORMAL}}{g\sqrt{R}} \quad \text{Equation 3.1}$$

where SNR_{NORMAL} is the SNR achieved in a non-acceleration acquisition and g is the *geometry factor* which determines how independent the coils are (14).

In this study image quality was assessed using measures of SNR, VNR and edge sharpness – this allowed us to assess the effect of matching data from different RR-intervals on the resultant image quality. True quantification of SNR and VNR in images acquired using non-Cartesian parallel imaging is non-trivial due to the uneven distribution of noise (87, 115). Therefore in this study estimated SNR and estimated VNR were calculated.

3.3.3.1 Calculation of Estimated SNR

Noise in the signal intensity (σ_S) was estimated from a ROI manually drawn in approximately stationary tissue as close to the vessel of interest as possible (note: this ROI is only used for the SNR and VNR calculations and not for background correction). For each pixel within the ROI, the standard deviation of the magnitude data was calculated over all measurements. The estimated signal noise, σ_S , was calculated as the average standard deviation over all pixels. The estimate of SNR was then calculated by dividing the mean pixel intensity inside the vessel of interest (during peak systole) by the estimated signal noise.

3.3.3.2 Calculation of Estimated VNR

Similarly, an estimate of VNR was calculated by dividing the mean velocity inside the vessel of interest (during peak systole) by an estimate of velocity noise (σ_V). The estimated velocity noise was calculated from the same ROI in stationary tissue as used above. For each pixel within the ROI, the standard deviation of the phase data was calculated over all measurements and averaged over all pixels to provide an estimated velocity noise, σ_V . This is the same method as used by Nielsen, et al. (111).

3.3.3.3 OsiriX Plug-in Implementation

The calculation of estimated SNR and estimated VNR was implemented as a plug-in for OsiriX. In this plug-in;

- An average magnitude image is formed from all phase-contrast magnitude frames
- The user manually segments an area of stationary tissue near to the vessel of interest in the average image (see Figure 3.5a). This ROI is copied to all phase-contrast magnitude frames
- The user manually segments the vessel of interest in the average image (see Figure 3.5b). The semi-automated segmentation described in section 2.7 is used to propagate this ROI through all phase-contrast magnitude frames
- The user opens the corresponding phase series, and the ROI's are automatically copied from the magnitude images to the phase images
- The frame with maximum flow in the vessel of interest is found (this can be changed by user from the UI) and the SNR and VNR are calculated for this frame (as described above) and output to the UI (see Figure 3.5c)

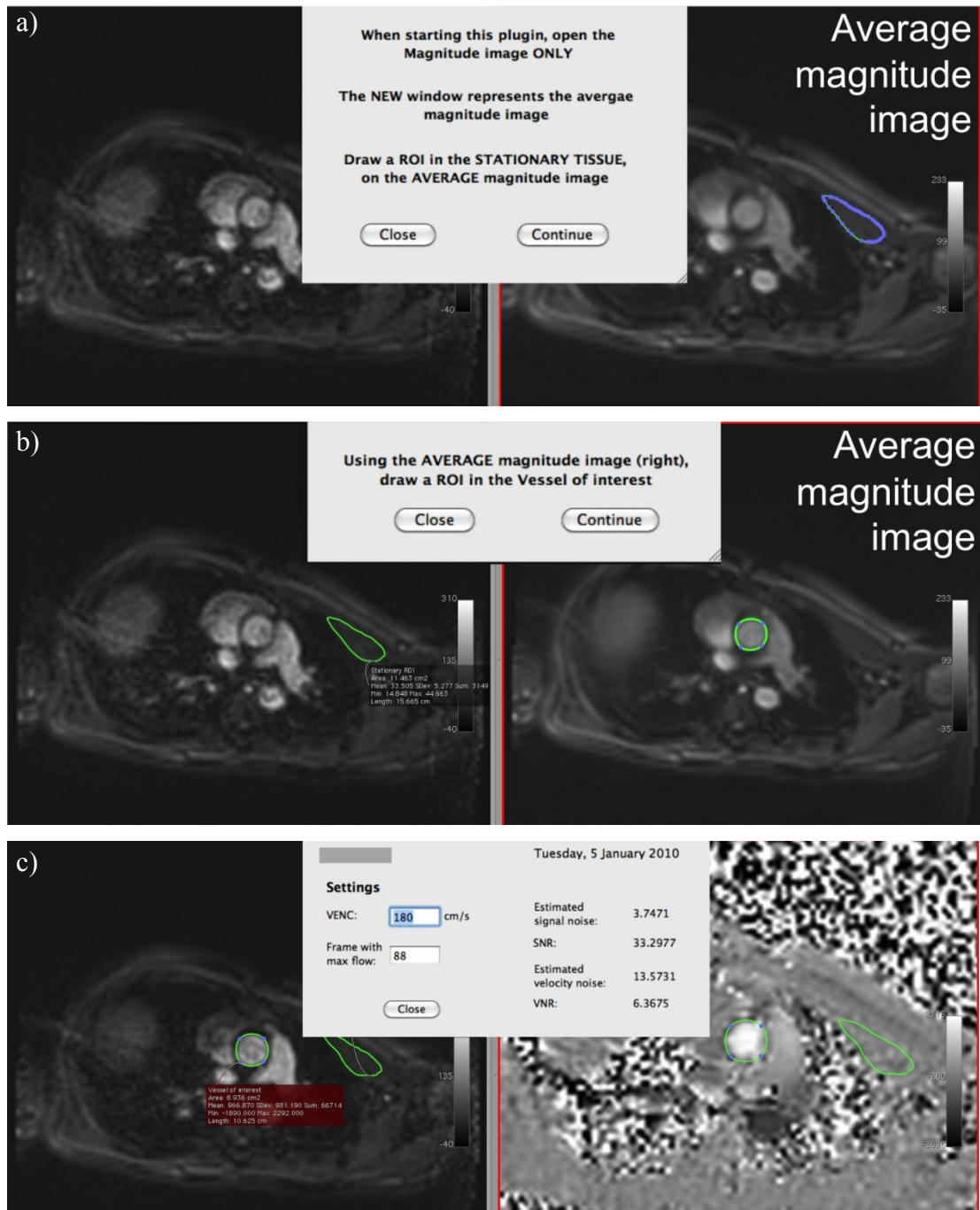


Figure 3.5: OsiriX plug-in developed for calculation of estimated SNR and VNR. a) First a ROI drawn in stationary tissue in an average magnitude image. b) The stationary ROI is copied to all magnitude frames (left). A ROI is then drawn in the vessel of interest in the average magnitude image. c) The semi-automatic segmentation tool is used to propagate the segmentation of the vessel through all magnitude frames. Estimated SNR and VNR are calculated in the frame with maximum flow (as indicated on the UI)

3.3.3.4 Calculation of Edge Sharpness

A quantitative edge sharpness measure was calculated by measuring the maximum relative gradient of pixel intensities across the border of the vessel of interest, as previously been carried out by Muthurangu, et al. (87). In this measure, sharp edges in the images are represented by a high gradient of the pixel intensities. To prevent noise providing artificially high gradients, the pixel intensities were fitted to a fifth-order polynomial prior to differentiation (87).

A plug-in was implemented for OsiriX, where the user draws a line over the border of the vessel in the frame during peak systole (as seen in Figure 3.6). The pixel values at 1 mm intervals along this line are found, and a 5th order polynomial fit is made to the data. The original pixel intensities and the fitted pixel intensities are plotted (in red and black, respectively) in the top graph on the plug-in (see Figure 3.6) allowing the user to assess how well the polynomial fit has worked.

The relative gradient of pixel intensities was calculated by differentiation of the polynomial data, and dividing the result by the pixel intensities – this is plotted on the bottom graph of the plug-in (see Figure 3.6). Edge sharpness is taken to be the maximum gradient of the pixel intensities along the ROI.

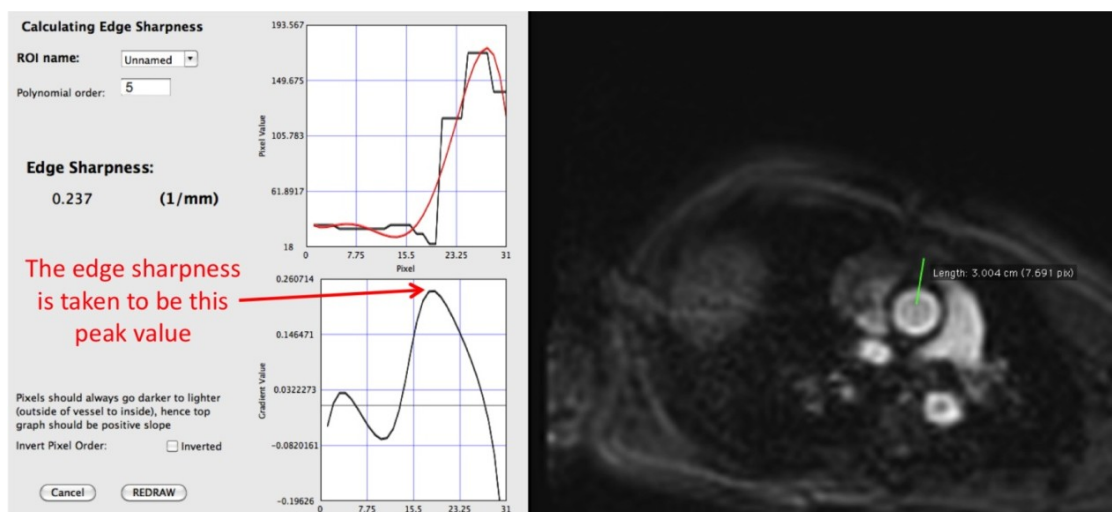


Figure 3.6: OsiriX plug-in used to calculate edge sharpness

3.4 Optimisation of Sequence Parameters

In this study we wished to demonstrate the effective doubling in temporal resolution achieved using a split-acquisition technique, and also the ability to achieve increased spatial resolution.

To demonstrate the effective doubling in temporal resolution, a high temporal resolution (HTR) split-acquisition sequence was developed and compared to the standard interleaved real-time sequence developed in chapter 2. These two sequences were run with the same scan parameters, including a 128 matrix (giving a spatial resolution of 3.9×3.9 mm, with a FOV of 500 mm). After optimisation the split-acquisition sequence achieved a temporal resolution of 22 ms, and the standard real-time sequence achieved a temporal resolution of 44 ms (using 12 spiral interleaves accelerated by a factor of 4 – see Table 3.2 for all imaging parameters).

To demonstrate the ability to increase the spatial resolution whilst still maintaining a high temporal resolution, a high spatial resolution (HSR) split-acquisition sequence was also tested. This sequence used a 192 matrix. It was found that 24 spiral interleaves accelerated by a factor of 4 gave the best compromise between image quality and adequate temporal resolution. With these settings a split-acquisition sequence with a spatial resolution of 2.6×2.6 mm (and a temporal resolution of 38 ms) was achieved (see Table 3.2 for all imaging parameters).

The resulting image quality from the two split-acquisition sequences in a resolution phantom, can be seen in Figure 3.7.

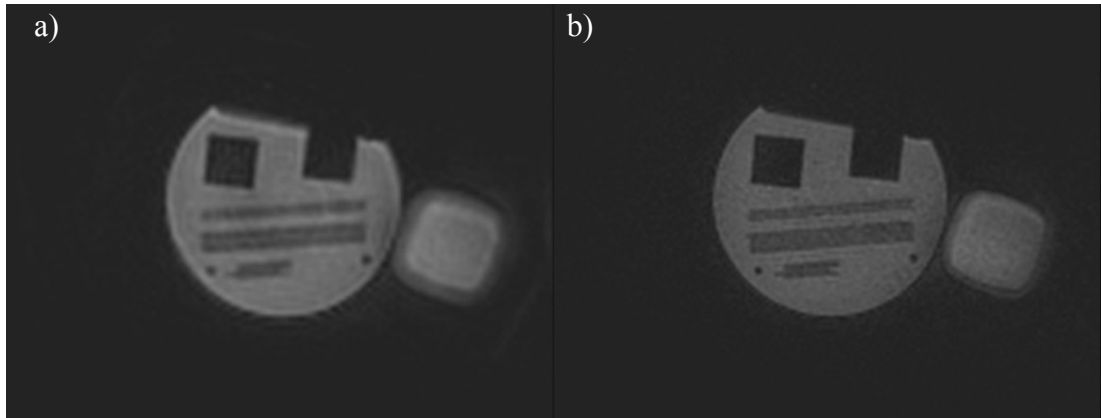


Figure 3.7: Examples of image quality in a resolution phantom (circular object on left of image), with a bottle of oil (square object on right of image) from the optimised split-acquisition sequences, a) HTR sequence, b) HSR sequence

3.4.1 In-vitro Validation

To assess the accuracy of the split-acquisition sequences, an experiment was carried out using the pulsatile flow pump described in section 2.4. The developed split-acquisition sequences were observed to be accurate when compared to a reference standard PCMR gated sequence and the standard real-time sequence (developed in chapter 2), as seen in Figure 3.8.

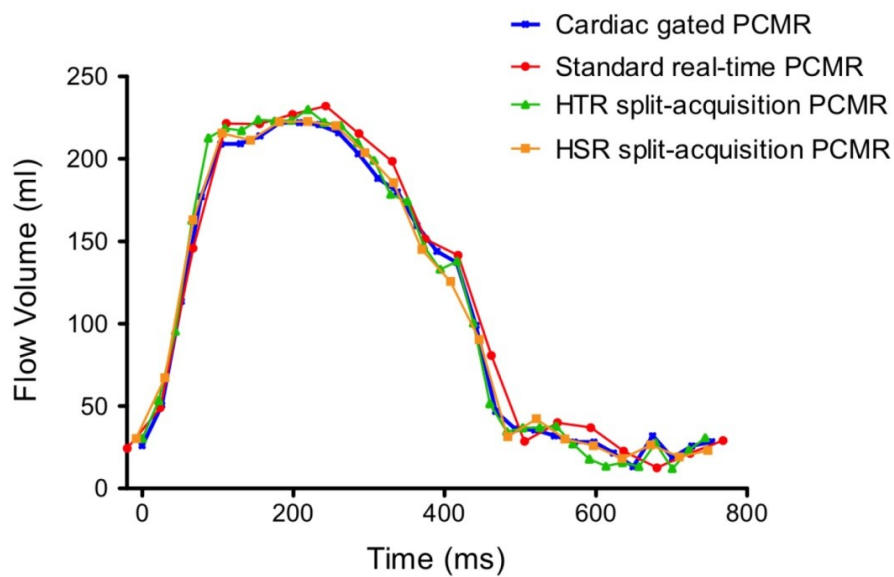


Figure 3.8: Comparison of flow profiles from the pulsatile flow pump between the four sequences tested

For the data shown in Figure 3.8 a good agreement was found in stroke volumes (reference gated PCMR sequence; 86.6 mL/cycle, standard real-time PCMR sequence; 91.9 mL/cycle, HTR split-acquisition sequence; 87.4 mL/cycle, HSR split-acquisition sequence; 87.7 mL/cycle). However in the flow pump there is very little motion, therefore it is not possible to assess the accuracy of the matching algorithm using the pump. Therefore, it was necessary to perform all validation of the matching technique in-vivo.

3.5 Adult Protocol

The adult population consisted of 15 healthy volunteers (7 male, 8 female: median age 39.8: range 25.2-57.9 years), and 5 patients with congenital heart disease (1 male, 4 female: median age 23.4: range 15.2-37.7 years). Additionally the split-acquisition method was tested on a single adult volunteer with an irregular heart rate.

Exclusion criteria were;

- i) Aortic regurgitation
- ii) Aortic surgery
- iii) Contraindications for MR such as MR-incompatible implants
- iv) Pregnancy

The local research ethics committee approved the study and written consent was obtained from all volunteers and patients.

All imaging was performed at rest, during free-breathing using two three-element spine coils and two three-element body-matrix coils. The SENSE reconstruction algorithm and matching of data was performed online in the Siemens reconstruction environment. The imaging plane for aortic flow assessment was located in the ascending aorta as it passes the bifurcation of the pulmonary arteries.

Flow was measured using four sequences:

- i) Cardiac gated PCMR
- ii) Interleaved spiral real-time PCMR
- iii) Split-acquisition real-time CINE PCMR with a high temporal resolution; 22 ms (spatial resolution; 3.9×3.9 mm)
- iv) Split-acquisition real-time CINE PCMR with a high spatial resolution; 2.6×2.6 mm (temporal resolution; 38 ms)

3.5.1 Cardiac Gated PCMR

Cardiac gated PCMR was performed using a retrospectively-gated, velocity-encoded, Cartesian, gradient echo sequence (parameters shown in Table 3.2). Similarly to chapter 2, flow measurements made using this sequence were considered to be the reference standard.

3.5.2 Interleaved Spiral Real-time PCMR

Interleaved spiral real-time (*standard real-time*) PCMR was performed using the sequence developed in chapter 2 (parameters shown in Table 3.2). In this sequence the flow-compensated and flow-encoded data were interleaved in their acquisition. Magnitude and phase images for the un-combined flow-compensated and flow-encoded data were output, along with the combined PC data. Six seconds of real-time data were acquired in order to perform the ‘accuracy of matching’ experiment detailed below (section 3.6).

3.5.3 Split-acquisition Real-time CINE PCMR

Split-acquisition real-time CINE PCMR was carried out using the same sequence as the standard real-time PCMR sequence, except that flow-compensated and flow-encoded data were split into separate blocks, as described in section 3.3.1. Two split-acquisition real-time CINE flow assessments were carried out; one with a higher temporal resolution, and the second with a higher spatial resolution (parameters shown in Table 3.2).

	Cardiac Gated PCMR	Standard real-time PCMR	HTR split-acquisition PCMR	HSR split-acquisition PCMR
TE/TR	2.7/7.0 ms	1.9/7.3 ms	1.9/7.3 ms	1.9/6.3 ms
Spiral Readouts	-	12	12	24
Acceleration factor	-	4	4	4
Matrix Size	256×192	128×128	128×128	192×192
FOV	~320 mm	500 mm	500 mm	500 mm
Rectangular FOV	75%	100%	100%	100%
Slice Thickness	6 mm	6 mm	6 mm	6 mm
Flip Angle	30°	25°	25°	25°
Pixel bandwidth	390 Hz/pixel	1860 Hz/pixel	1860 Hz/pixel	1860 Hz/pixel
VENC	180 cm/s	180 cm/s	180 cm/s	180 cm/s
NSAs	3	-	-	-
Total Scan Duration	~2.5 mins	6 sec	6 sec	6 sec
Voxel Size	1.3×1.3 mm	3.9×3.9 mm	3.9×3.9 mm	2.6×2.6 mm
Temporal resolution	30 ms	44 ms	22 ms	38 ms
	(~33 frames/sec)	(~23 frames/sec)	(~45 frames/sec)	(~26 frames/sec)

Table 3.2: Sequence Parameters for all four sequences tested, in adult study

3.5.4 Experiments

Three experiments were carried out within the adult study;

- i) To assess the accuracy of the matching technique
- ii) To compare image quality between the sequences
- iii) To validate the split-acquisition technique

3.5.5 Data Analysis

All images were processed using in-house plug-ins for the open-source software OsiriX. For each aortic stroke volume measurement, the aorta was manually segmented (by J.A.S) using the modulus images. The plug-in described in section 2.3.6.1 was used for calculation of flow volumes from the split-acquisition data.

All results are expressed as the mean \pm standard deviation, where the data is combined for the adult volunteers and patients. Bland-Altman analysis was performed to give measurements of agreement with the cardiac gated flow sequence (116). Additionally, the correlation coefficients were calculated. Comparison of means was performed by using repeated measures ANOVA (analysis of variance) tests with Bonferroni correction for multiple comparisons. All statistical analysis was performed using GraphPad Prism.

3.6 Accuracy of Matching

The purpose of the *accuracy of matching* experiments was to test the assertion that data from adjacent blocks could be matched with sufficient precision to accurately calculate flow.

3.6.1 ‘Simulated Split-acquisition’ Reconstruction

We were able to assess the accuracy of the matching technique described in section 3.3.2, by reconstructing the standard real-time PCMR data in two ways;

- ‘Conventional’ reconstruction
- ‘Simulated split-acquisition’ reconstruction

The ‘conventional’ reconstruction used the interleaved flow-encoded and flow-compensated images for subtraction and production of the final phase image. For the ‘simulated split-acquisition’ reconstruction, the real-time PCMR data was divided into three blocks (of two seconds each). Only the flow-compensated data was used from the first and third blocks, while only flow-encoded data was used from the second block. The ‘simulated split-acquisition’ data then underwent the matching process described in section 3.3.2. Flow measurements from the same data using the two reconstruction methods were compared for all adult subjects.

In addition, this ‘simulated split-acquisition’ reconstruction experiment was carried out on one volunteer with an irregular heart rate in order to assess the accuracy of the split-acquisition technique in this population.

3.6.1.1 Results

Mean aortic stroke volumes assessed using the ‘conventional’ reconstruction method and the ‘simulated split-acquisition’ reconstruction method were 94.6 ± 21.8 mL/cycle vs. 95.0 ± 21.9 mL/cycle ($r = 0.996$, $p < 0.0001$) respectively. Bland-Altman assessment found a bias of 0.5 mL/cycle with limits of agreement of -3.3 to 4.3 mL/cycle (Figure 3.9);

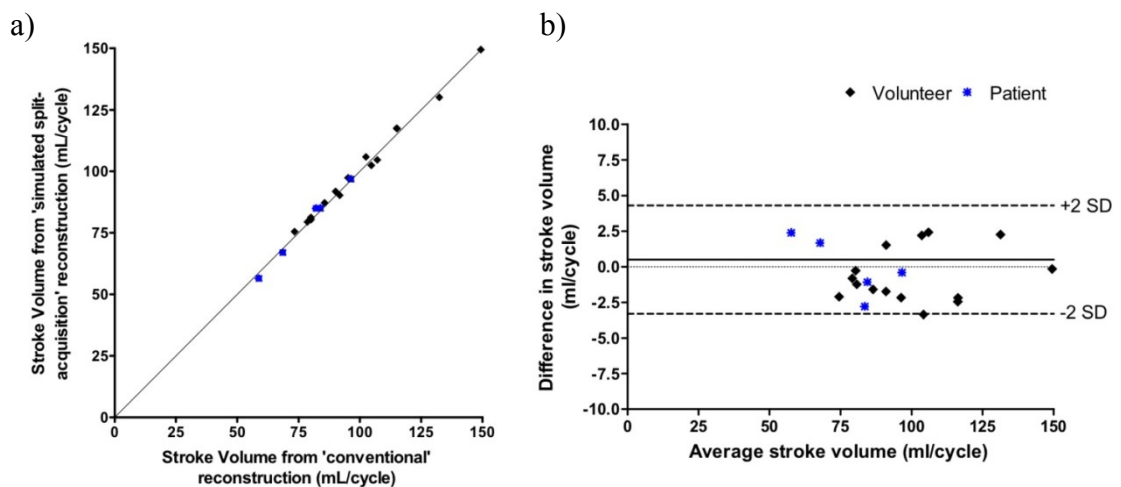


Figure 3.9: Comparison of ‘conventional’ and ‘simulated split-acquisition’ reconstructions of the same in-vivo data. a) Correlation of flow measured from both reconstruction techniques. b) Bland-Altman plot of the difference in flow measured using both reconstruction techniques

Comparable flow profiles obtained were obtained for all subjects, using the two reconstruction methods, as seen in Figure 3.10 for one patient.

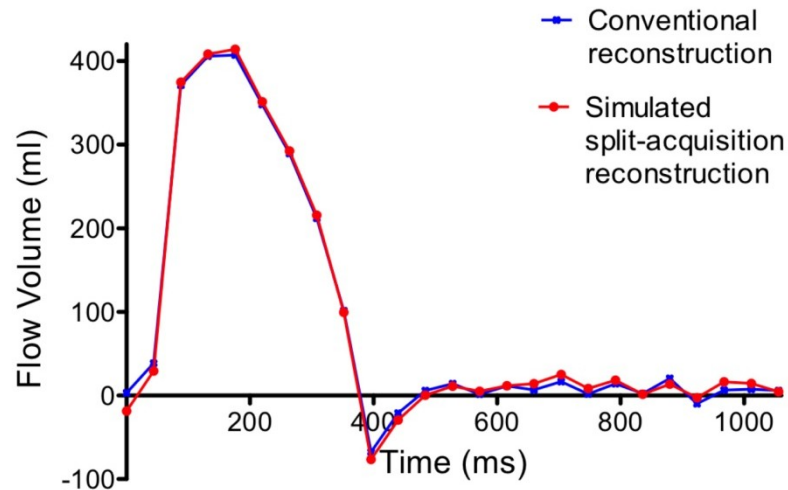


Figure 3.10: Figure from (109). Comparison of flow profiles from one interleaved real-time PCMR adult patient data set, reconstructed using the ‘conventional’ and ‘simulated split-acquisition’ reconstruction methods

In one patient with an irregular heart rate, a good agreement in flow profiles between the ‘conventional’ reconstruction method and the ‘simulated split-acquisition’ reconstruction method was also found;

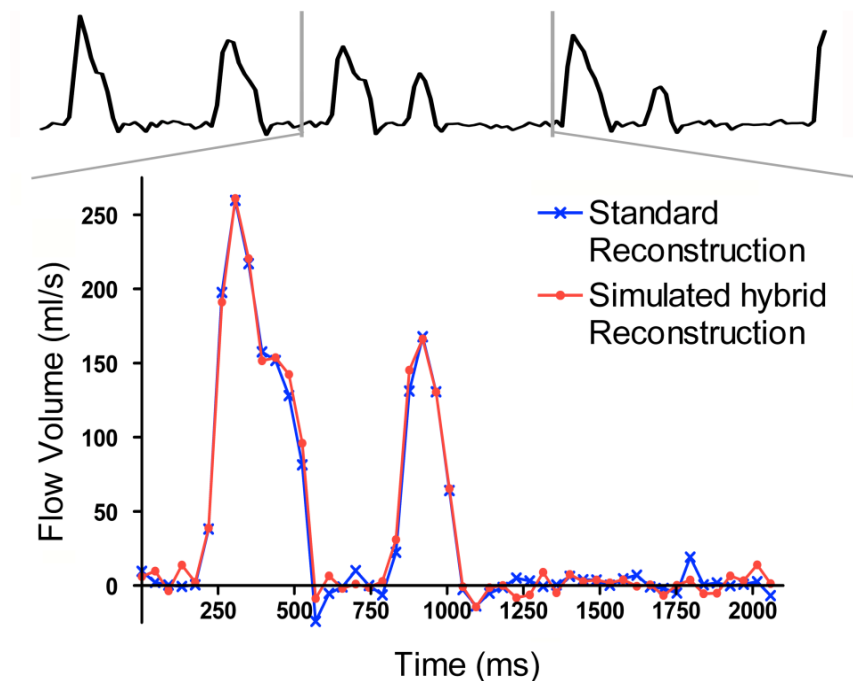


Figure 3.11: Comparison of flow profiles from one patient with an irregular heart rate. Top: flow throughout the 6 seconds of interleaved real-time PCMR data (calculated from standard reconstruction). Bottom: Flow profiles as calculated from ‘conventional’ and ‘simulated split-acquisition’ reconstruction methods

From the two reconstructed cardiac cycles shown in Figure 3.11, a good agreement in stroke volume was found between the ‘conventional’ reconstruction method and the ‘simulated split-acquisition’ reconstruction method; cycle 1: 53.1 mL vs. 54.9 mL, cycle 2: 23.2 mL vs. 23.9 mL, respectively.

3.6.2 Importance of Matching

The importance of accurately matching flow-compensated and flow-encoded data was also assessed. The ‘simulated split-acquisition’ flow-encoded frame with maximum flow was found and reconstructed using every ‘simulated split-acquisition’ flow-compensated frame (from the simulated split-acquisition experiment above, section 3.6.1). The resulting flow volumes were compared to the ‘conventional’ reconstruction for this frame. For each resulting frame the flow error and matching error metric were calculated, giving an indication of the effect of mismatching on the accuracy of the flow assessment.

A further experiment was carried out using this data to demonstrate the need for two flow-compensated blocks; before and after the flow-encoded data. The flow-compensated frame with the minimum matching error metric was found from each block and the flow errors compared. Because these two frames should be in similar position in the cardiac cycle, any differences in flow are thought to be attributed to respiratory cycle mismatching.

3.6.2.1 Results

Figure 3.12 shows the matching error metric calculated between a single flow-encoded frame (during peak systole), and all flow-compensated frames (from both blocks), for one subject. It can be seen that the matching metric has a periodicity, which is equivalent to the heart rate.

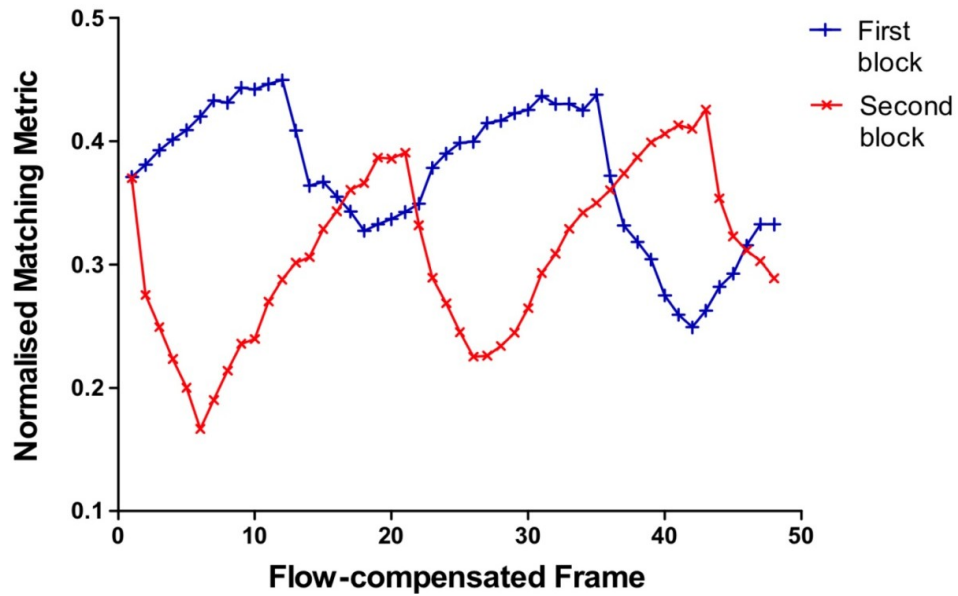


Figure 3.12: Matching error between a single flow-encoded frame and all flow-compensated frames from both blocks

Figure 3.13 shows the relationship between the matching error and the flow error (%) from a single flow-encoded frame as reconstructed with all 96 ‘simulated split-acquisition’ flow-compensated frames, from all adult subjects. It can be seen that a small matching metric leads to a small flow error, and mismatching of frames can lead to high flow errors (up to 80 %);

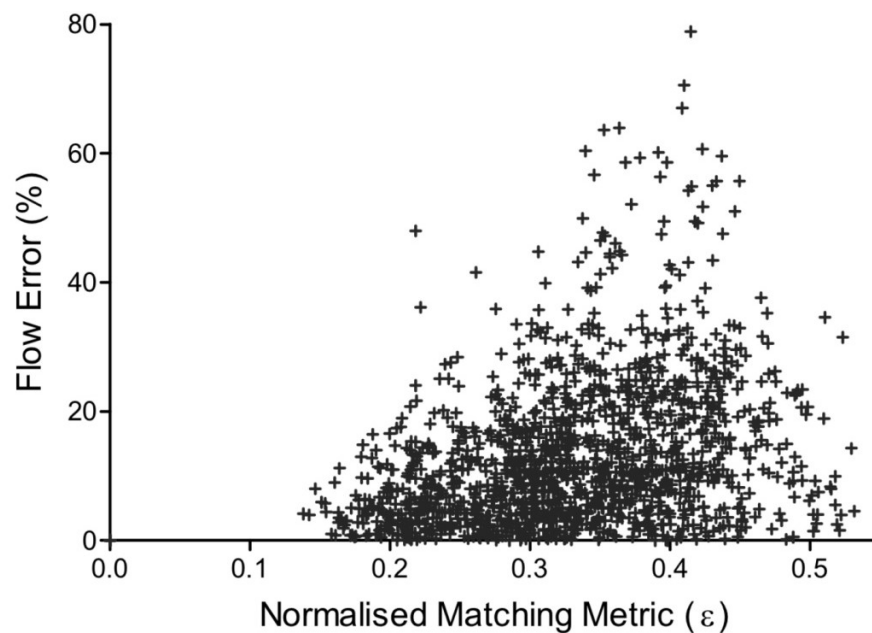


Figure 3.13: Correlation between normalized matching metric and flow error in all adult subjects

The importance of using two blocks of flow-compensated data was demonstrated by assessing flow error from the flow-compensated frame with the minimum matching metric from each ‘simulated split-acquisition’ block. For example, for the data shown in Figure 3.12, the lowest matching metric from the first flow-compensated block was found in the 42nd frame (matching error: 0.249, flow error: 14.1 %), and from the second flow-compensated block was found in the 6th frame (matching error: 0.167, flow error: 1.9 %). Of these two frames, the one with the lower matching metric gave a lower average flow error, over all adult subjects of 16.1 mL/cycle. In eight subjects, the minimum matching metric was found from the first block and in the remaining twelve subjects from the second block.

3.7 Image Quality

Image quality was assessed using measures of SNR, VNR and edge sharpness during peak systole, using the OsiriX plug-ins described in section 3.3.3.

Figure 3.14 shows examples of the image quality from all four tested sequences. No residual aliasing artefacts were seen over the vessel of interest, in any standard real-time PCMR images or split-acquisition PCMR images. Some image blurring was observed (see Figure 3.14) and this was attributed to the sensitivity of the spiral trajectories to off-resonance effects and small k-space trajectory errors.

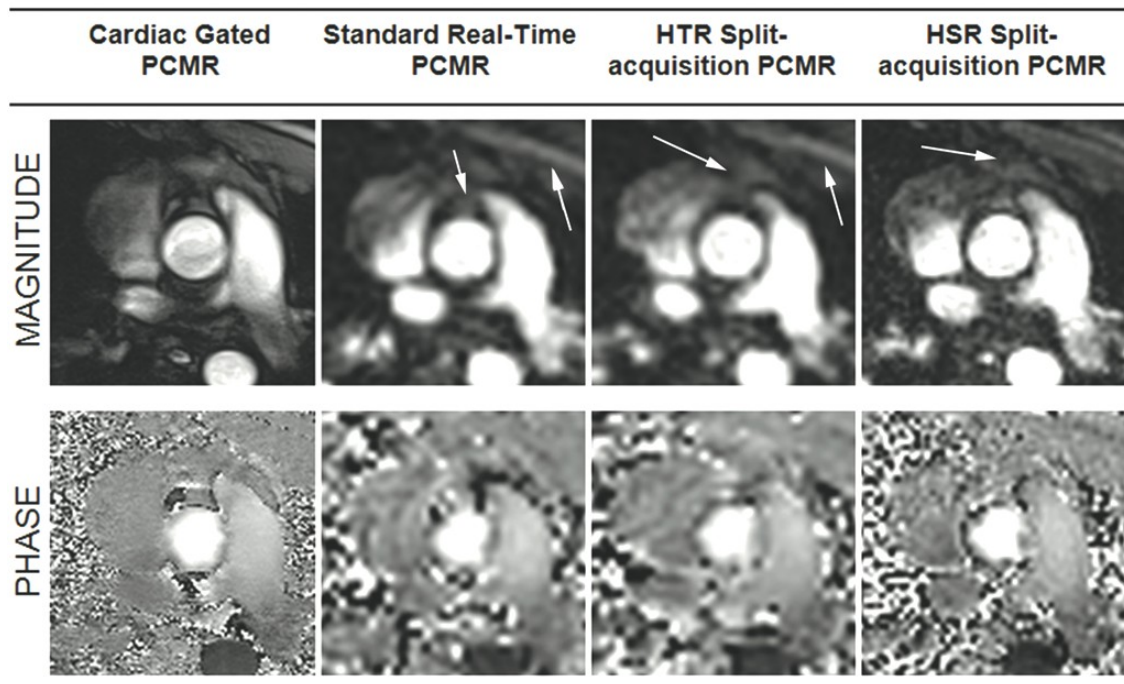


Figure 3.14: Figure from (109). Comparison of image quality from the sequences. Arrows indicate image blurring

Quantitative image quality metrics can be seen in Table 3.3. The cardiac gated PCMR images had the highest estimated SNR, compared to both standard and split-acquisition real-time CINE PCMR data. The HSR split-acquisition images had the lowest estimated SNR and VNR. Estimated velocity noise and VNR were not significantly different in the other three sequences.

Edge sharpness was significantly greater in the cardiac gated PCMR images compared to all of the real-time images (Table 3.3). However, the cardiac gated sequence had the highest standard deviation over all adults. The standard real-time and HTR split-acquisition images had very similar edge sharpness measures. The HSR split-acquisition images had slightly higher edge sharpness than the other real-time images, although this was not found to be statistically significant. A visual improvement in the edge sharpness for this HSR proposed sequence can be seen in Figure 3.14, making segmentation of the images easier.

	Cardiac Gated PCMR	Standard real-time PCMR	HTR split-acquisition PCMR	HSR split-acquisition PCMR
Estimated signal variation: σ_S	4.5 ± 1.1	$5.6 \pm 1.2^*$	$6.0 \pm 1.6^*$	$6.3 \pm 1.1^*$
σ_S / σ_S^{PC}	1	1.3 ± 0.4	1.4 ± 0.5	1.5 ± 0.5
Estimated SNR	50.3 ± 16.1	$34.5 \pm 10.9^*$	$32.5 \pm 10.9^*$	$28.8 \pm 8.1^*$
Estimated velocity variation: σ_V (cm/s)	5.8 ± 1.9	5.5 ± 2.1	5.2 ± 1.8	$7.3 \pm 2.0^{*\dagger}$
σ_V / σ_V^{PC}	1	0.96 ± 0.16	0.92 ± 0.22	1.31 ± 0.24
Estimated VNR	14.9 ± 9.0	15.7 ± 9.0	16.3 ± 11.0	$11.2 \pm 5.1^{*\dagger}$
Edge Sharpness (mm^{-1})	0.97 ± 0.50	$0.43 \pm 0.21^*$	$0.46 \pm 0.21^*$	$0.58 \pm 0.26^*$

* Values are significantly different from cardiac gated PCMR ($p < 0.05$)

† Values are significantly different from standard real-time PCMR ($p < 0.05$)

Table 3.3: Estimated SNR, VNR and edge sharpness measures for all four sequences

3.8 In-vivo Validation

The split-acquisition sequences were validated in-vivo in all adult subjects, by calculating the aortic stroke volume for each of the four sequences described in section 3.4.1. A good agreement in flow profiles was found for all subjects, as seen in Figure 3.15 for one volunteer;

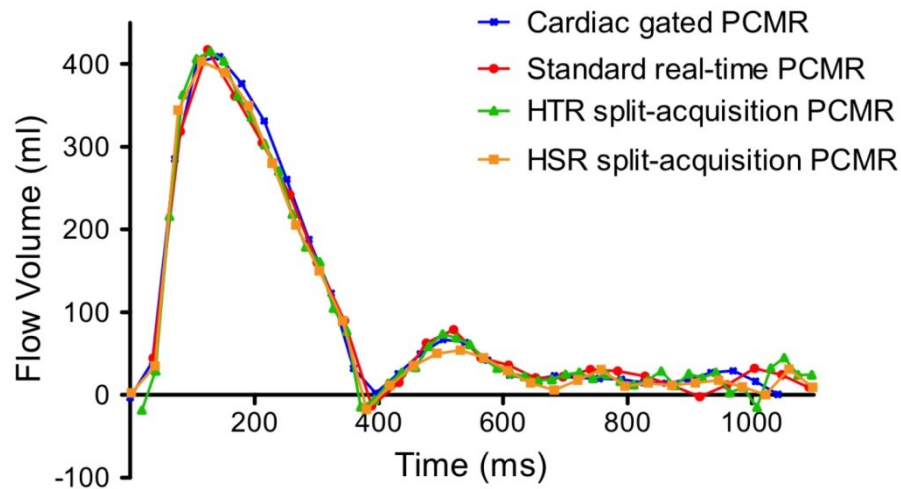


Figure 3.15: Figure from (109). Comparison of flow profiles from all four sequences in one adult volunteer

The stroke volumes calculated from each of the real-time sequences were compared to those from the gold-standard cardiac gated flow sequence and Bland-Altman assessment was carried out. The results can be found in Table 3.4, and Figure 3.16.

	Cardiac Gated PCMR	Standard real-time PCMR	HTR split- acquisition PCMR	HSR split- acquisition PCMR
Stroke Volume (mL)	95.2 ± 20.0	96.2 ± 20.7	95.6 ± 20.1	95.5 ± 20.4
Bias* (mL)	-	1.0	0.4	0.3
Limits of agreement* (mL)	-	-2.2 to 4.1	-3.9 to 4.7	-3.2 to 3.7
Correlation coefficient* (r)	-	0.998	0.994	0.997

*Calculated with cardiac gated PCMR sequence

Table 3.4: Flow volumes for all four sequences tested, in the adult population

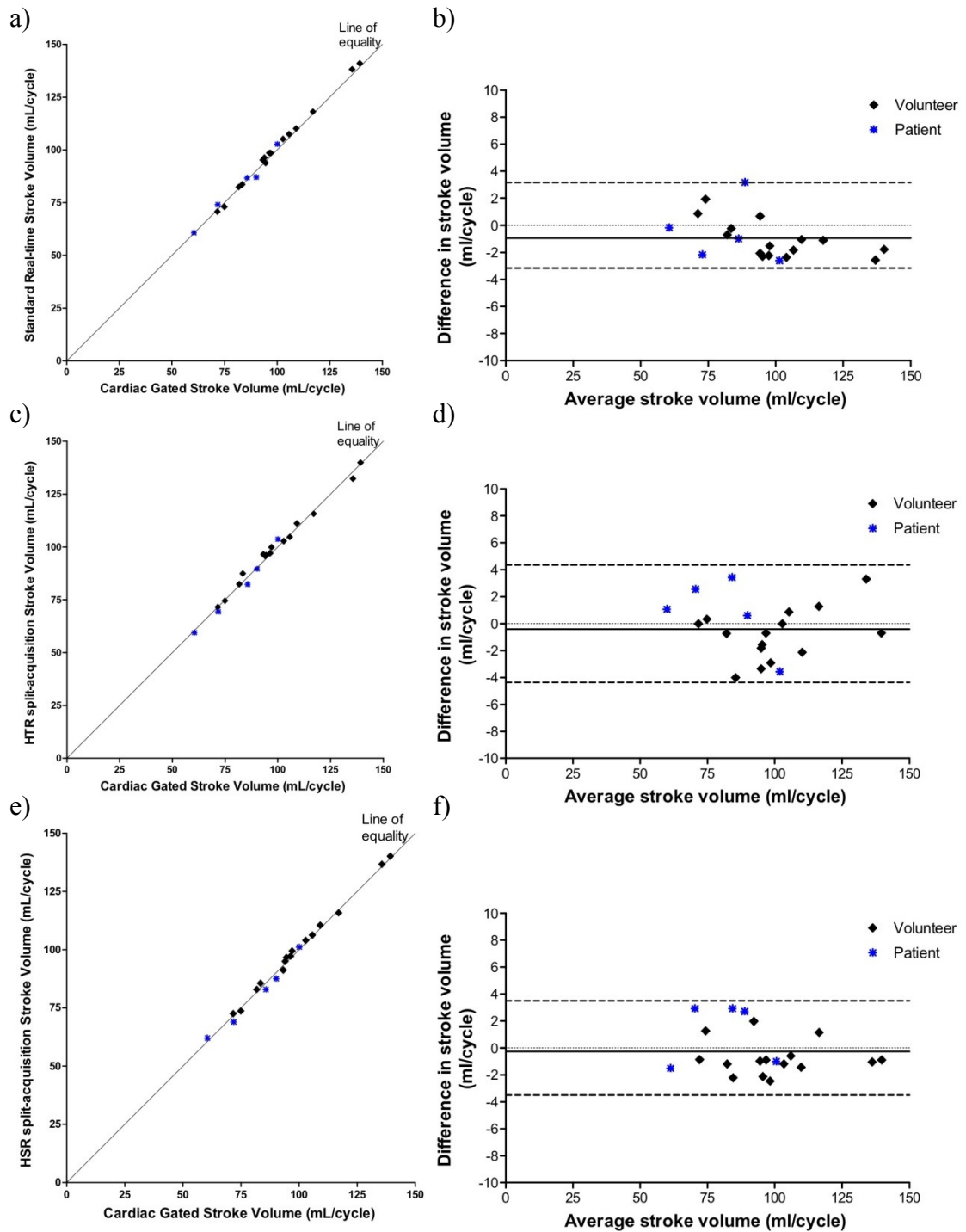


Figure 3.16: Correlation (left) and Bland-Altman analysis (right) of stroke volumes in adult population calculated from: a)-b) cardiac gated PCMR vs. standard real-time PCMR, c)-d) cardiac gated PCMR vs. HTR split-acquisition PCMR, e)-f) cardiac gated PCMR vs. HSR split-acquisition PCMR

An excellent agreement in stroke volumes between all sequences was found, with no statistical differences between any of the sequences. A slight overestimation was found in all real-time sequences, however this was not a clinically significant difference. The average heart rate for all adults was 69 beats per minute.

3.9 Paediatric Utility

To demonstrate the need for higher spatial and temporal resolution in the paediatric population, aortic stroke volumes were compared between;

- i) Cardiac gated PCMR
- ii) Standard real-time PCMR
- iii) Split-acquisition PCMR with a high spatial resolution; $\sim 1.9 \times 1.9$ mm (temporal resolution; ~ 43 ms)

The sequences have been described in section 3.4. The sequence parameters can be assumed to be the same as in Table 3.2, unless otherwise stated below;

	Cardiac Gated PCMR	Standard real-time PCMR	HSR split-acquisition PCMR
TE/TR	$\sim 2.5/7.0$ ms	$2.1/\sim 7.7$ ms	$2.1/\sim 7.1$ ms
FOV	~ 250 mm	~ 350 mm	~ 350 mm
VENC	~ 210 cm/s	~ 210 cm/s	~ 210 cm/s
Total Scan Duration	~ 2.5 mins	6 sec	6 sec
Spatial resolution	$\sim 1.0 \times 1.0 \times 5.0$ mm	$\sim 2.8 \times 2.8 \times 5.0$ mm	$\sim 1.9 \times 1.9 \times 5.0$ mm
Temporal resolution	~ 32 ms (~ 31 frames/sec)	~ 46 ms (~ 22 frames/sec)	~ 43 ms (~ 23 frames/sec)

Table 3.5: Sequence Parameters for all three sequences tested, in the paediatric study

The paediatric population consisted of 6 patients with congenital heart disease (3 male: 3 female, median age: 4.8 years, range: 0.2-8.3 years). Aortic stroke volumes were calculated for all three sequences and Bland-Altman analysis was performed to give measurements of agreement with the cardiac gated flow sequence.

3.9.1 Paediatric Results

The average stroke volumes and Bland-Altman assessment from the paediatric study can be seen in Table 3.6 and Figure 3.17;

	Cardiac Gated PCMR	Standard real-time PCMR	HSR split- acquisition PCMR
Stroke Volume (mL)	20.6 ± 7.6	24.3 ± 9.2 [†]	20.8 ± 7.8
Bias* (mL)	-	3.7	0.3
Limits of agreement* (mL)	-	-0.2 to 7.6	-2.1 to 2.7
Correlation coefficient* (r)	-	0.990	0.995

* Calculated with cardiac gated PCMR sequence

[†] Value is significantly different from cardiac gated PCMR (p<0.05)

Table 3.6: Flow volumes for all three sequences tested, in the paediatric population

There was excellent agreement in stroke volumes between the gold-standard cardiac gated PCMR sequence and the split-acquisition real-time CINE PCMR sequence, with no statistical differences between these two sequences. However, the standard real-time sequence overestimated the stroke volume when compared to the cardiac gated PCMR sequence. The average heart rate for all children was 87 beats per minute.

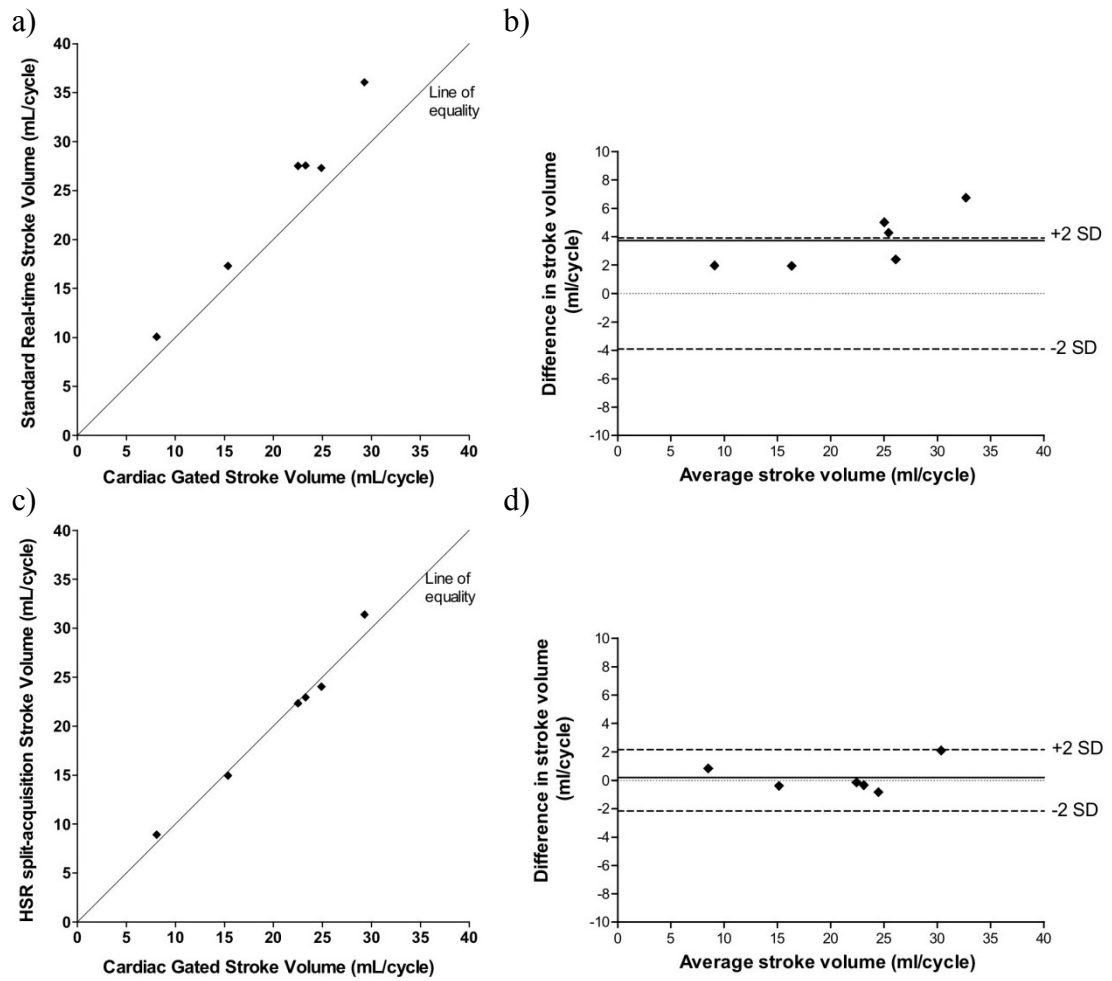


Figure 3.17: Correlation (left) and Bland-Altman analysis (right) of stroke volumes in paediatric population, calculated from: a)-b) cardiac gated PCMR vs. standard real-time PCMR, c)-d) cardiac gated PCMR vs. HSR split-acquisition PCMR

3.10 Discussion

We have demonstrated the feasibility and accuracy of a novel split-acquisition real-time CINE PCMR sequence. Unlike standard real-time PCMR, flow-compensated and flow-encoded data are acquired in separate short blocks and retrospectively matched in the cardio-respiratory cycle. The resulting sequence has the benefit of an effective doubling of the temporal resolution or an increase in the spatial resolution when compared to standard interleaved, real-time PCMR.

3.10.1 Accuracy of Matching

Accurate PCMR assessment relies on cardio-respiratory matching of flow-encoded and compensated data. The reliability of matching was assessed in an adult population by comparing both ‘conventional’ and ‘simulated split-acquisition’ reconstructions of the same real-time PCMR data. The excellent agreement in stroke volumes and flow curves, supports the assumption that it is possible to remove background phase offsets using matched data acquired in separate blocks. The importance of matching was further demonstrated by calculating the flow error when frames were purposefully not matched. Errors of up to 80 % were seen if the wrong frame was used for phase subtraction.

Although matching in the cardiac cycle could be performed using an ECG signal (7, 112, 117), image subtraction allows matching in both the cardiac and respiratory cycles in one step (114). This is not only more efficient but also obviates the need for ECG monitoring (113). Alternatively, data from different blocks could be matched using image-based navigators along with motion correction, which has previously been demonstrated in retrospectively enhanced real-time imaging (118).

In one patient with an irregular heart rate the ‘conventional’ and ‘simulated split-acquisition’ reconstructions of the same real-time PCMR data also showed good agreement in stroke volumes and flow profiles. This suggests that the split-acquisition method could be used successfully in subjects with an irregular heart rate.

3.10.2 Image Quality

Real-time imaging often trades image quality for speed of acquisition (119). It was observed that in adults the real-time sequences all had significantly lower estimated SNR and edge sharpness than the cardiac gated sequence. Nevertheless, the estimated VNR in adults was not significantly different ($p > 0.05$) between the HTR split-acquisition sequence and cardiac gated sequence. The similar SNR, VNR and edge sharpness between the standard real-time and HTR split-acquisition images in adults suggests that image quality is not seriously affected by matching data from different RR-intervals. The lower SNR and VNR seen in the HSR split-acquisition images was to be expected, given the smaller pixel dimensions.

3.10.3 Adult In-vivo Validation

In adults, there was good agreement between stroke volumes measured using the four different sequences. Importantly, this was true in patients as well as volunteers, suggesting that matching also works in subjects with less regular respiratory patterns. In gated PCMR, variations in stroke volume from breathing are averaged out; however, when analyzing the real-time stroke volumes, a single flow cycle was chosen for comparison. This may explain some of the differences in flow volumes found between the real-time techniques and the gated technique.

3.10.4 Paediatric Utility

In children, standard real-time PCMR was found to overestimate stroke volume, probably due to inadequate spatial resolution. However, there was excellent agreement between the cardiac gated PCMR sequence and the split-acquisition real-time CINE sequence that had a higher spatial resolution.

3.10.5 Advantages of Split-acquisition PCMR

Currently, cardiac gated PCMR is considered the reference standard method of measuring flow in-vivo. It has been validated in numerous studies (57, 59, 90, 92, 93) and due to the high spatial and temporal resolution it is accurate in the paediatric population. However, it is time consuming as it is usually acquired with several signal averages to compensate for respiratory motion. Breath-hold, cardiac gated PCMR is commonly used, however for adequate spatial and temporal resolution the breath-hold time is long. This is problematic when imaging children with congenital heart disease, as they are often unable to perform long breath holds.

Another approach is real-time PCMR, which can be acquired during free breathing in a relatively short length of time. However, as shown in this study, the lower spatial and temporal resolution of standard real-time imaging reduces its accuracy in the paediatric population. The split-acquisition PCMR technique described has all the benefits of standard real-time PCMR, but with improved spatial or temporal resolution. Thus, the split-acquisition technique is accurate even in children and it may be of particular use in the assessment of paediatric heart disease.

3.10.6 Limitations

This study has shown that split-acquisition real-time CINE PCMR technique is accurate in a population of 15 volunteers and 11 patients (5 adult and 6 children). Further work is needed to validate this technique in a larger patient population. In particular the split-acquisition sequence needs to be tested in patients with irregular breathing patterns. Irregular patterns might make it more difficult to match data from different blocks in cardio-respiratory space and may reduce the accuracy of the technique. The split-acquisition technique was demonstrated to be accurate in the *accuracy of matching* experiment in one adult with an irregular heart rate. However this needs to be performed in larger population with this condition, to confirm the accuracy of the technique.

In this initial feasibility study, the split-acquisition technique was only tested in the aorta, as flow quantification has been well validated using MRI in this vessel. One advantage of this technique over other real-time techniques may be its ability to measure flow in smaller vessels, as a higher spatial resolution can be achieved. Further work is required to test this technique in other smaller vessels.

In the future, it may be advantageous to interleave many blocks of flow-compensated and flow-encoded data. This was not carried out in this study due to the long reconstruction times, of approximately 5 minutes per measurement. The matching algorithm was found to only take ~2 % of the reconstruction time, with the non-Cartesian parallel imaging reconstruction taking ~90 % of the total reconstruction time. These long reconstruction times are a drawback, as although the data is acquired in real-time, the images cannot be viewed in real-time. Reconstruction times could be improved by the use of newer multi-processor graphics cards (100, 120), which are well suited to complex iterative reconstruction (see section 5.2.2). This may also allow more complex matching techniques to be carried out, which may involve image registration

3.10.7 Conclusion

In conclusion, we have demonstrated the accuracy and reliability of a novel split-acquisition phase-contrast MR technique in both adults and children. The technique divides the acquisition of flow-compensated and flow-encoded data into separate blocks, and performs automatic matching of this data in cardio-respiratory space. This allows an increase in the temporal or spatial resolution of real-time phase-contrast MR. Split-acquisition PCMR opens up the possibility of real-time scanning of smaller vessels, in patients with higher heart rates, which will be useful in the assessment of congenital heart disease.

CHAPTER 4

Rapid Gated Flow Measurements

4.1 Introduction

Cardiac gated PCMR is a proven method of measuring blood flow in the clinical environment (56-58). It is particularly useful in patients with congenital heart disease (121), where flow assessment often guides clinical decision-making. As we have seen, PCMR is intrinsically slow because each line in k-space must be acquired twice (with different velocity-encodings) in order to perform background phase subtraction. Unfortunately, this prolongs acquisition time and prevents high spatio-temporal resolution cardiac gated PCMR from being performed in a breath-hold within the clinical environment.

We have shown in chapter 2, that it is possible to achieve real-time PCMR with the use of efficient spiral trajectories, combined with parallel imaging techniques. Unfortunately, real-time PCMR comes at the cost of low spatio-temporal resolution and is not well suited to the paediatric population. The split-acquisition technique described in chapter 3, is able to achieve higher spatio-temporal resolution than the real-time technique, however the resolution is still inferior to that desired in the clinical environment for small vessels or in subjects with high heart rates.

Due to the long breath-hold times of high spatio-temporal resolution gated PCMR, multiple signal averages are often used to compensate for respiratory motion in the clinical environment. This results in scan times of approximately 2 minutes and thus in congenital heart disease where flow is often measured in multiple vessels, complete flow assessment can take up to 10 minutes. If spatio-temporal resolution is lowered, gated PCMR can be performed in a breath-hold (96). However, in children with congenital heart disease, high resolution is necessary to assess smaller vessels at higher heart rates. Furthermore, the breath-hold times are often too long (> 15 seconds) for children or sick adults. Thus, in the congenital population there is a need for a high spatio-temporal resolution gated PCMR sequence that can be performed within a short breath-hold.

4.1.1 Aims

The aims of this study were to;

- Develop high spatial and temporal resolution PCMR imaging, using a prospectively-triggered, spiral PCMR sequence accelerated with SENSE, which can be performed in a short breath-hold
- Demonstrate the technique in a population of children and adults with congenital heart disease
- Compare the accuracy of the prospectively-triggered, spiral PCMR sequence against a breath-hold retrospectively-gated Cartesian PCMR sequence

4.1.2 Personal Contribution

To fulfil the above aims I have:

- Designed and developed a prospectively-triggered, spiral PCMR sequence (see section 4.3) in the Siemens, IDEA environment. This is based on the undersampled spiral SENSE sequence developed in chapter 2
- Automated the sequence user interface to allow ease of use (see section 4.3.3)
- Optimised the sequence parameters (see section 4.4)
- Developed an OsiriX plug-in to calculate flow volumes from the prospectively-triggered, spiral PCMR sequence (see section 4.3.4)
- Developed an OsiriX plug-in to correct for residual background phase offsets (see section 4.3.7)
- Performed in-vitro validation of the prospectively-triggered, spiral PCMR sequence (see section 4.5)
- Adapted the SNR and edge sharpness plug-ins for OsiriX (from section 3.3.3), to allow more accurate measures of image quality for this study (see section 4.3.5 and 4.3.6)
- Assessed image quality of the prospectively-triggered, spiral PCMR technique, by quantification of SNR, VNR and edge sharpness (see section 4.8)

- Performed in-vivo validation of the sequence in multiple vessels, in a population of adults and children with congenital heart disease (see section 4.7)
- Assessed intra- and inter-observer variability of the sequence (see section 4.7)

The results from this work are currently in press in *Radiology*, by J. Steeden, D. Atkinson, M. Hansen, A. Taylor and V. Muthurangu entitled; “Rapid Flow Assessment of Congenital Heart Disease Using High Spatio-Temporal Gated Spiral Phase Contrast MR”, (122) (see Appendix 5).

4.2 Literature Review

In this section previous studies which have performed rapid, gated flow measurements with the use of a SENSE reconstruction algorithm are discussed.

Beerbaum, et al. (119, 123) investigated flow measurements using a retrospectively-cardiac gated, Cartesian PCMR sequence, undersampled using SENSE factors of 1 (fully sampled, used as the reference), 2 and 3. They measured flow in the ascending aorta (Q_S) and pulmonary artery (Q_P) in a paediatric population (123) and an adult population (119), to allow quantification of Q_P/Q_S ratio during free breathing.

In the first study by Beerbaum, et al. (123), 22 paediatric patients (mean age: 7.2 ± 6.2 years) with cardiac left-to-right shunt were enrolled. The sequence parameters used are shown in Table 4.1;

	SENSE $\times 1$	SENSE $\times 2$	SENSE $\times 3$
TE/TR	6.5/15.0 ms	6.5/15.0 ms	6.5/15.0 ms
Flip angle	30°	30°	30°
FOV	300	380	380
Rectangular FOV	70 %	100 %	100 %
NSA	2	1	1
VENC	200 cm/s	200 cm/s	200 cm/s
Temporal resolution	30 ms	30 ms	30 ms
Spatial resolution	2.3 \times 3.1 \times 6.0 mm	2.3 \times 3.1 \times 6.0 mm	2.3 \times 3.1 \times 6.0 mm
Scan time	1:37 mins	0:27 mins	0:19 mins
Relative scan time*	-	28 %	19 %

*Percentage of scan time compared to SENSE $\times 1$ (reference) sequence

Table 4.1: Sequence parameters used by Beerbaum, et al. (123) in paediatric study

Beerbaum, et al. demonstrated a good correlation in velocities measured in a pulsatile flow pump between the *bucket and stopwatch* method and both the SENSE $\times 2$ ($r = 0.999$) and SENSE $\times 3$ ($r = 0.999$). In-vivo, a negligible difference was found in the stroke volumes ($\pm 1\%$) and the Q_P/Q_S ratio ($\pm 2\%$), between the reference PCMR sequence and the undersampled sequences in the paediatric population. SENSE $\times 3$ was found to give slightly more variability than SENSE $\times 2$ (Q_P/Q_S limits of agreement: 124 % to 82 %, and 112 % to 86 %, respectively). Figure 4.1, compares the aortic stroke volumes calculated from the reference (SENSE $\times 1$) sequence with those calculated from the SENSE $\times 2$ sequence;

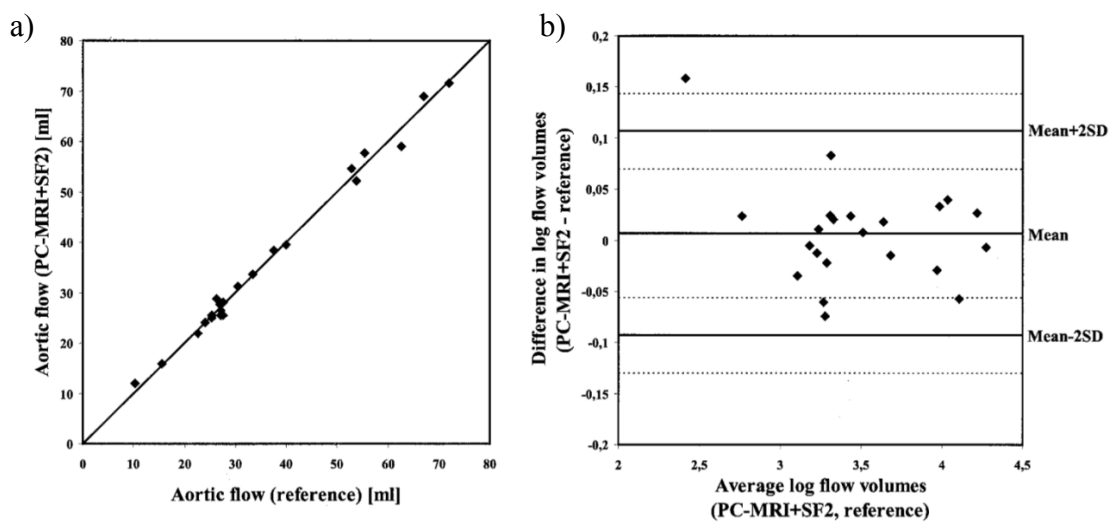


Figure 4.1: From paediatric study by Beerbaum, et al. (123). Comparison of stroke volumes in the aorta for the reference sequence vs. SENSE $\times 2$ sequence; a) Correlation between the two sequences b) Bland-Altman analysis (data log-transformed)

In the second study (119), 13 healthy adults (mean age: 33.0 ± 7.4 years) underwent the same imaging protocol. The sequence parameters were the same as Table 4.1, except an 80 % rectangular FOV was used for all sequences, with average scan times of 2:17 minutes for the reference sequence, 36 seconds for SENSE $\times 2$ and 25 seconds for SENSE $\times 3$.

In this study Beerbaum, et al. (119) demonstrated a good agreement in the Q_P/Q_S ratio in healthy adults, measured by the reference PC sequence (1.03 ± 0.07), SENSE $\times 2$ (1.05 ± 0.13) and SENSE $\times 3$ (1.08 ± 0.11). Negligible differences (between -3 % to 4 %) were found between the reference PC sequence and the undersampled sequences, in terms of stroke volumes in the pulmonary artery and aorta, and the Q_P/Q_S ratio.

Figure 4.2 shows a comparison of the pulmonary artery stroke volumes from the reference sequence and SENSE $\times 2$, as found by Beerbaum, et al. (119);

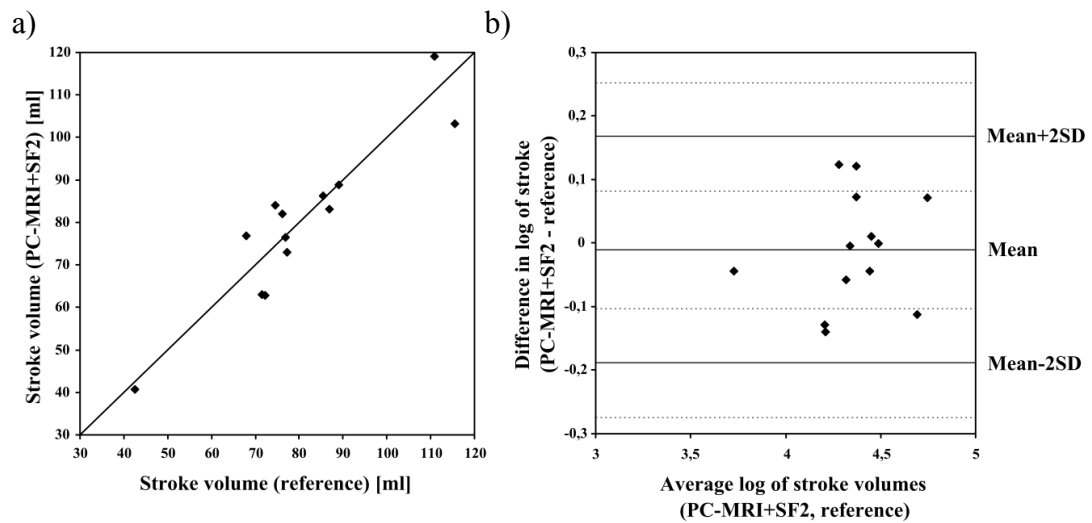


Figure 4.2: From adult study by Beerbaum, et al. (119). Comparison of stroke volumes in the pulmonary artery for a reference sequence vs. SENSE $\times 2$ sequence; a) Correlation between the two sequences b) Bland-Altman analysis (data log-transformed)

In both the paediatric study and the adult study by Beerbaum, et al. the spatial resolution achieved was 2.3×3.1 mm, with a temporal resolution of 30 ms. However, even with a SENSE factor of 3 the scan duration was ~ 20 seconds, therefore in these studies all data was acquired during free-breathing. Neither of these studies performed any correction for respiratory motion in the undersampled sequences, and only one signal average was used.

A similar study was carried out by Prakash, et al. (124). They achieved higher spatial resolution imaging than Beerbaum, et al. by the use of a smaller FOV, and a larger matrix. Flow volumes were compared from a retrospectively-gated Cartesian PCMR sequence, with a SENSE factors of 1 (reference) and 2. All data was acquired during free-breathing. The sequence parameters used are shown in Table 4.2.

Sequence parameters	
TE/TR	3.1/7.5 ms
Flip angle	20°
FOV	240-350
Matrix	256×160
NSA	2
Views per segment	2
Temporal resolution	30 ms
Spatial resolution	0.94 to 2.2 mm
Scan time	~1:58 mins (with SENSE ×1) ~0:59 mins (with SENSE ×2)

Table 4.2: Sequence parameters used by Prakash, et al. (124)

Flow was measured in 33 subjects (mean age: 24 years), in the ascending aorta (N = 33) and the pulmonary artery (N = 24). A close correlation in flow measurements was found between the two sequences in the aorta ($r = 0.965$, mean difference = 0.08 ± 0.3 L/min or 1.0 ± 6.7 %) and in the pulmonary artery ($r = 0.965$, mean difference = 0.09 ± 0.4 L/min or 1.7 ± 7.0 %), as shown in Figure 4.3.

Using a SENSE factor of 2, Prakash, et al. (124) were able to perform high spatio-temporal resolution imaging during free-breathing with 2 NSAs, in a scan time of 59 ± 19 seconds. They demonstrated the accuracy of this sequence in-vitro and in-vivo.

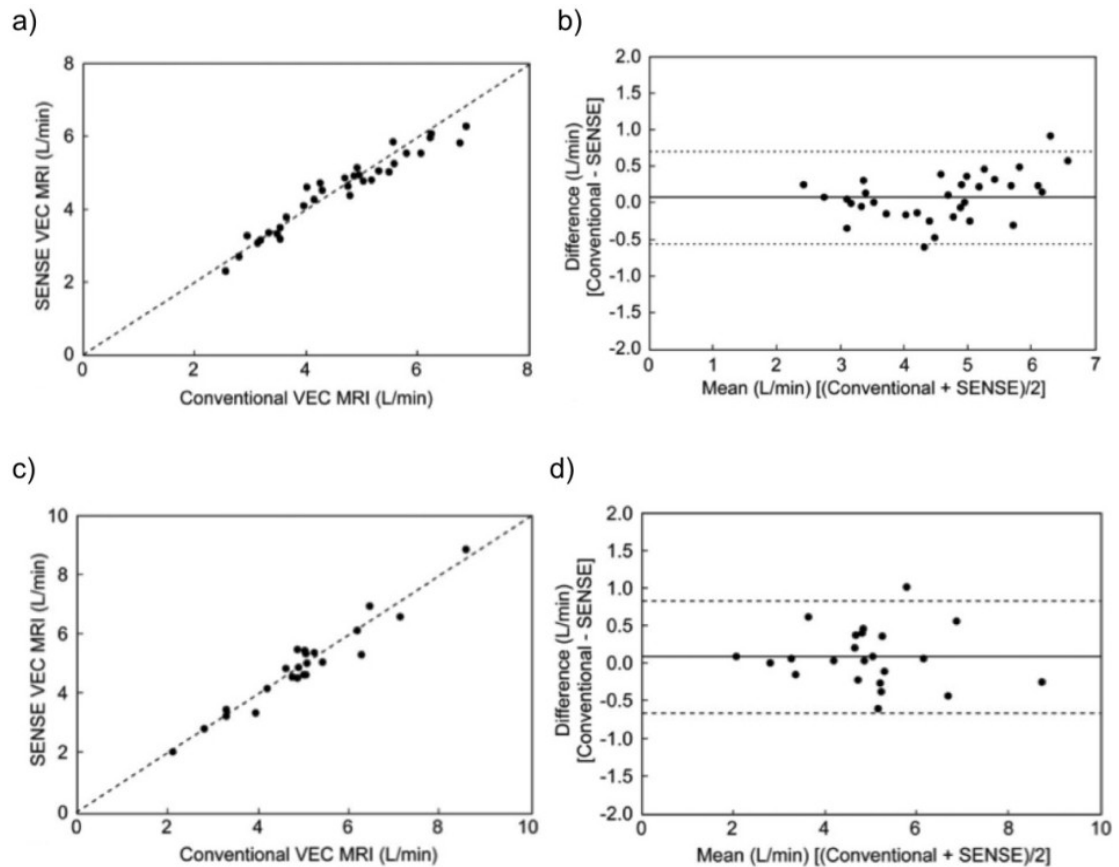


Figure 4.3: From Prakash, et al. (124). Correlation (left) and Bland-Altman analysis (right) between conventional PCMR sequence (SENSE $\times 1$) and SENSE $\times 2$ sequence, as found in a)-b) the aorta, c)-d) the pulmonary artery

Another study by Lew, et al. (125) was able to greatly reduce scan times compared to Beerbaum, et al. and Prakash, et al. allowing the possibility of breath-hold PCMR measurements. A retrospectively-gated, segmented fast gradient echo, Cartesian sequence, accelerated with SENSE factors 1, 2 and 3, was investigated. Stroke volumes were compared from the three sequences in 17 children (average age: 11.8 ± 9.6 years) in the aorta ($N = 17$) and pulmonary artery ($N = 16$) during a breath-hold. The sequence parameters are shown in Table 4.3.

Sequence parameters	
TE/TR	~2/~4 ms
Flip angle	15-30°
Matrix	256×160
Slice thickness	5-7 mm
Views per segment	1-6
Scan time	20-30 sec (with SENSE ×1) 12-20 sec (with SENSE ×2) 7-10 sec (with SENSE ×3)

Table 4.3: Sequence parameters used by Lew, et al. (125)

Lew, et al. showed a good correlation in the aortic stroke volume, the pulmonary artery stroke volume and the Q_P/Q_S ratio, between the un-accelerated sequence and accelerated sequences. The correlation coefficient was > 0.962 in all cases. For the flow volumes the maximum bias, as found by Bland Altman analysis was 0.12 L/min, with limits of agreement < 0.8 L/min.

Although image quality is not discussed in the paper, the example images are very noisy and the residual aliasing is not completely removed, see Figure 4.4;

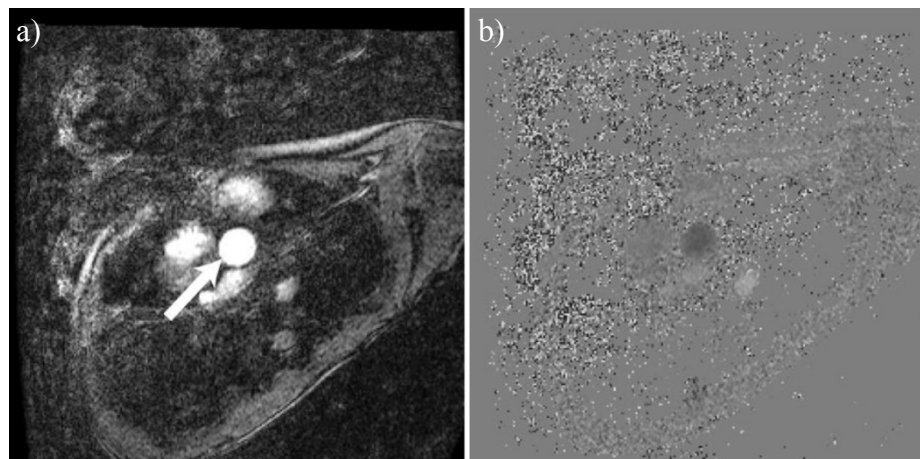


Figure 4.4: From Lew, et al. (125). Resultant image quality from a SENSE×3 sequence; a) magnitude, b) phase. A lot of noise is observed in these images, which Lew, et al. believe comes from noise in the coil sensitivity maps

Although Lew, et al. are able to achieve short breath-hold PCMR scans, which are shown to be accurate in a small number of children, Figure 4.4 shows the resultant image quality to be poor. No details are given as to the temporal or spatial resolution achieved in this study.

All of the studies described, use Cartesian sequences along with SENSE reconstruction algorithms. It is thought that spiral trajectories may be advantageous for flow imaging, due to the very short TE. Additionally, all of these studies required a calibration scan at the beginning of the examination to calculate the coil sensitivities (~ 1 minute scan by Beerbaum, et al. (119, 123) and ~ 15 seconds for Lew, et al. (125)). This increases the examination time and makes the sensitivity maps susceptible to motion, which may occur during the scan. Lew, et al. (125) observed very noisy images when using a SENSE factor of 3, which they believe was due to noisy sensitivity maps. We do not wish to perform a separate calibration scan, however will calculate high SNR sensitivity maps from the data itself (in the same way as performed in sections 2 and 3).

The studies described here only demonstrate the accuracy of the sequences in the aorta and pulmonary artery. We hope to demonstrate the accuracy of a gated spiral sequence in the aorta, pulmonary artery and in the left and right pulmonary branches. Additionally, the studies performed by Beerbaum, et al. (119, 123) and Prakash, et al. (124) are unable to reduce the scan times sufficiently to allow breath-hold imaging. Therefore in these studies all data was acquired during free breathing (scan duration > 19 seconds). We wish to reduce the scan duration further than achieved by Lew, et al. (125), to < 7 seconds to enable an achievable breath-hold even for children and sick adults.

4.2.1 Summary

From the literature review it can be seen that:

- Previous studies have combined gated Cartesian trajectories with SENSE to achieve high resolution PCMR sequences
- These have demonstrated the accuracy of SENSE PCMR in the aorta and pulmonary artery
- Only Lew, et al. (125) were able to reduce the scan times enough to achieve breath-hold imaging
- All of the studies use a calibration scan to calculate the sensitivity maps

4.3 Development

In this study we wished to develop a high spatio-temporal resolution PCMR sequence, with the use of a prospectively-triggered spiral sequence, undersampled using SENSE. The sequence and reconstruction algorithm are based on those developed in chapter 2.

4.3.1 Cardiac Triggering

To develop a prospectively-triggered sequence, the physiological (*'physio'*) tab on the UI was enabled, as seen in Figure 4.5. This allowed us to access the ECG trigger data within the sequence;

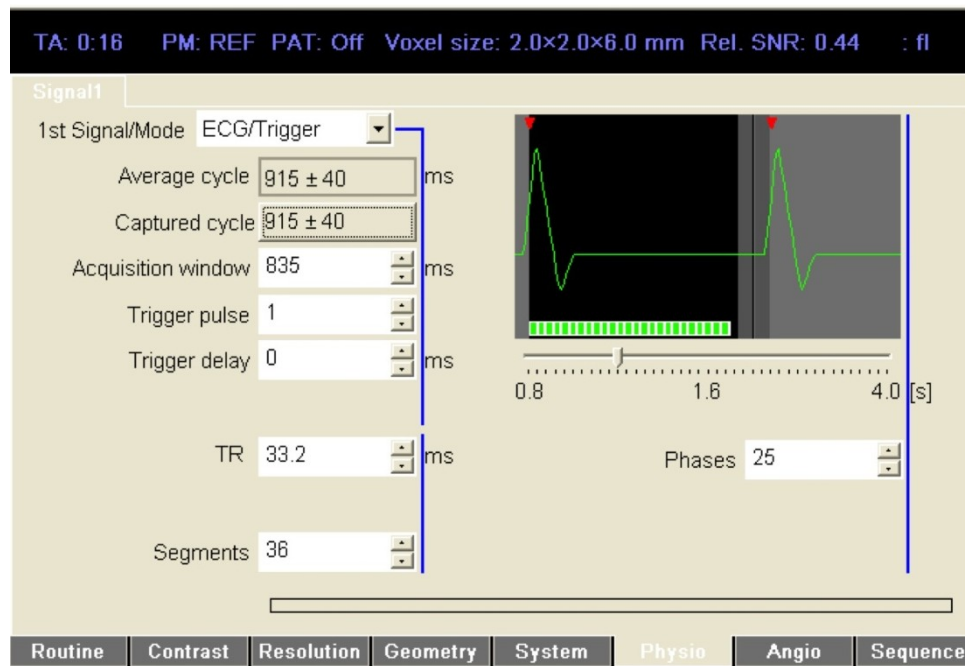


Figure 4.5: The physiological tab was enabled on the UI

In prospectively-triggered sequences (as described in section 1.5.2), it is necessary to leave a trigger window at the end of each RR-interval where the pulse sequence waits for a valid trigger. In this study the available acquisition window was calculated as the average heart rate, minus two times the standard deviation of the heart rate.

As the temporal resolution of the sequence is known (displayed on the UI as ‘TR’), it is possible to calculate the maximum number of cardiac phases we are able to capture within the acquisition window. The number of cardiac phases is calculated as the acquisition window divided by temporal resolution, rounded down to the nearest integer number.

In cardiac gated sequences (as described in section 1.5.2), the detection of an R-wave causes a change in the line that is acquired (37). For spiral imaging the detection of an R-wave, causes a change in the current spiral interleave being acquired. Therefore, if we required 10 spiral interleaves we would need to acquire data over 10 RR-intervals. To reduce the scan time it is possible to segment k-space, where more than one spiral interleave is acquired per RR-interval (in an interleaved fashion). Segmenting k-space therefore affects the temporal resolution of the sequence. For example, by acquiring two spiral interleaves per RR-interval we only need to acquire data in half the total number of RR-intervals, however the temporal resolution is also halved.

4.3.2 Stimulated Echo’s

When acquiring more than one spiral interleave per RR-interval (i.e. segmenting k-space), a hashing artefact was observed in the first few resultant images, as seen in Figure 4.6.

The sequence used to acquire the data in Figure 4.6, has a total of 20 spiral interleaves, with 2 interleaves acquired per RR-interval. No parallel imaging was used to acquire these images. The circular hashing pattern observed in Figure 4.6 in the water phantom, is symmetric about the centre of the image, and is made up of concentric circles in groups of 10. The hashing pattern is not seen in the magnitude images of the oil or the butter. It was observed that by increasing the TR or decreasing the flip angle, this artefact was reduced.

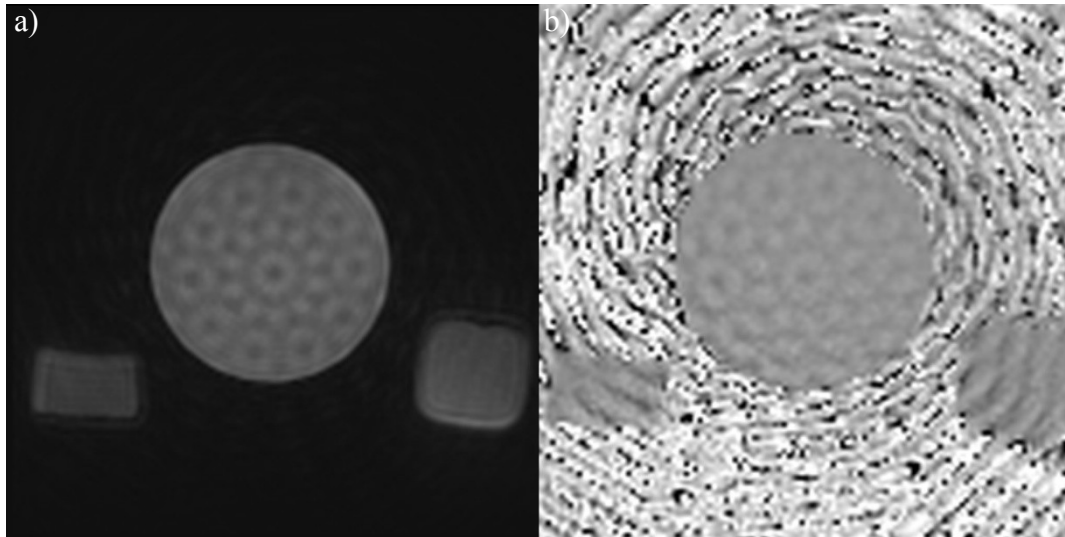


Figure 4.6: Hashing artefact observed when acquiring more than one spiral interleave per RR-interval, in a) Magnitude image, and b) Phase image. The large circular object is a water phantom, and the two smaller objects are oil (right) and butter (left)

These observations suggest that the artefact is caused by a stimulated echo from the first spiral readout, which causes signal during the second spiral readout in each RR-interval. By increasing the TR the transverse magnetization from the first spiral interleave decays, before the second RF-pulse is played out. By decreasing the flip angle the transverse magnetization caused by each RF-pulse is lower, therefore there is less residual transverse magnetization at the end of the TR. This theory is backed up by the fact that the hashing is not observed in the fat phantom, which has a shorter T_1 than water, therefore relaxes faster. Peter Gatehouse deserves special thanks for help getting to the bottom of the cause of this artefact.

In the sequence used to acquire the data in Figure 4.6, a gradient spoiler was applied on the z -axis at the end of each TR. No rewinder gradients were applied on the x - or y -axis. Gradient spoilers are not effective at spoiling transverse steady state magnetization unless the area of the gradient varies from TR to TR (36). When the area of these spoiler gradients varies from TR to TR, the spoiling is not uniform over the FOV, as shown by Bernstein, et al. (36) in Figure 4.7.

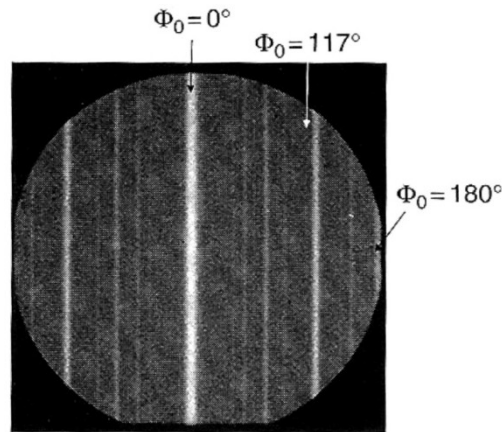


Figure 4.7: From Bernstein, et al. (36). Gradient echo image of a uniform spherical phantom, with no phase-encoding rewriter gradient (i.e. the phase encode gradient is used as a spoiler). The striped pattern demonstrates the spatially non-uniform spoiling caused as the phase-encode gradients produce spatially varying fields

The striped pattern shown in Figure 4.7 is from a Cartesian sequence with variable spoiler gradients in each TR. This striped pattern is similar to the hashing pattern seen in Figure 4.6, from our spiral sequence. In the spiral sequence because the x and y gradients are not rewound, the gradient spoiling at the end of each interleave is variable. This causes spatially non-uniform spoiling, resulting in the circular aliasing pattern.

A better solution to spoiling transverse magnetization, is to perform *RF-spoiling* (126). RF-spoiling was also carried out in the sequence used to acquire the data in Figure 4.6, however the total phase accumulated (due to gradients) in each TR must be the same to ensure spatially-independent RF-spoiling (126). Therefore, it was necessary to rephase the signal in the k_x and k_y dimensions at the end of each readout. The resulting sequence diagram can be seen in Figure 4.8. These rewriter gradients were found to completely remove the aliasing pattern in the resulting images.

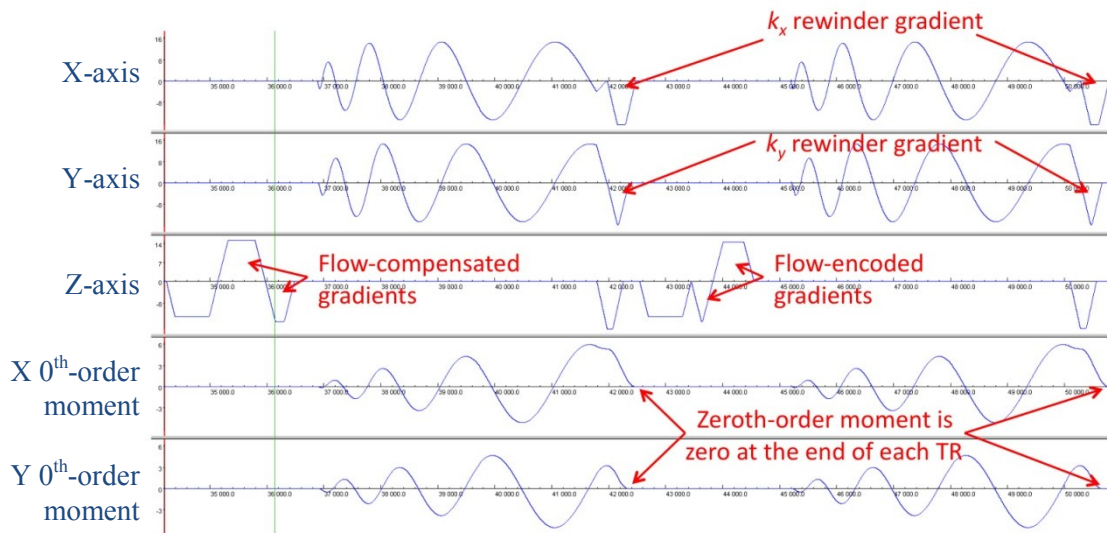


Figure 4.8: Sequence diagram of resultant sequence, showing rewriter gradients after all spiral gradients, which null the zeroth-order moments of all gradients on the x and y axes

This hashing artefact had not been observed in the previous studies, as in both chapters 2 and 3 a large number of dummy pulses were applied at the beginning of the sequence. This means that these stimulated echoes had reached a steady state before the acquisition of data. In the triggered sequence, the trigger window means that the first few frames within any RR-interval are never in a steady state. It was observed that using an additional RR-interval at the beginning of the triggered sequence, which contained dummy pulses, reduced steady state artefacts in the first cardiac phase.

4.3.3 Automating the UI

In order for the triggered sequence to be as easy to use as possible, it was necessary to automate many of the dependent parameters on the UI. For example, the TE and TR should always be minimized to allow the highest temporal resolution. However, when changing some parameters (e.g. when decreasing the bandwidth) it is necessary to increase the TR from its current value, therefore the temporal resolution decreases and the number cardiac phases must be reduced.

These dependent parameters mean that without automating the UI, it is not possible to decrease the bandwidth on the UI without first reducing the number of cardiac phases, and increasing the TR. Once the bandwidth has been set to the required value, the user would then have to minimize the TR, and maximize the number of cardiac phases to allow the highest temporal resolution to be achieved.

Solve-handlers were written to automatically handle these dependent parameters – these ensure the TE and TR are minimized and the number of cardiac phases is maximised after any of the following parameters are changed;

- Bandwidth
- Total number of spiral interleaves
- Number of interleaves acquired per RR-interval
- VENC
- Slice thickness
- FOV
- ‘Capture cycle’ button is pressed (to capture the current average RR-interval and standard deviation of the RR-interval)

Solver handlers were also written to;

- Automatically decrease the bandwidth when the FOV is reduced, if the current bandwidth is not achievable (due to maximum gradient strength restrictions). This also optimises the TR, and number of cardiac phases for the new bandwidth
- Automatically decrease the bandwidth when the matrix size is increased, if the current bandwidth is not achievable (due to maximum gradient strength restrictions). This also optimises the TR, and number of cardiac phases for the new bandwidth
- Automatically put the coils in triple combine mode when SENSE is on, and automatically put coils in combined mode when SENSE is off
- Automatically calculate the acquisition window when the ‘capture cycle’ button is pressed, and optimise the number of cardiac phases achievable within the new acquisition window

4.3.4 Analysis of Flow Data

In chapters 2 and 3, flow volumes were calculated by integrating the flow curve for one cardiac cycle to a 1 ms temporal resolution by Fourier interpolation (see section 2.3.6.1). In this study Fourier interpolation cannot be used as the data points are not evenly distributed, due to the need for a trigger window at the very end of diastole. In this study it was found that on average ~ 80 ms at the very end of diastole was not sampled, as seen in Figure 4.9;

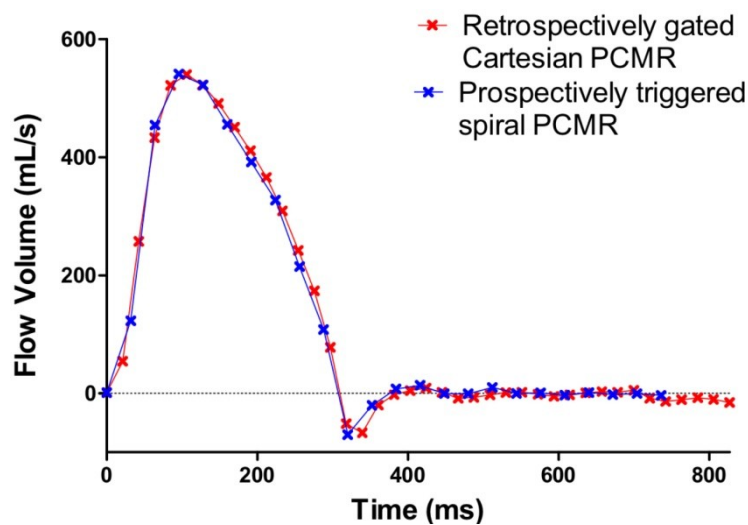


Figure 4.9: Example of a normal flow profile (plotted with linear interpolation) from a retrospectively-gated PCMR sequence, and the prospectively-triggered spiral PCMR sequence. It can be seen that, for this subject, the last 90 ms at the end of diastole is not captured by the prospectively-triggered sequence

It was found that smooth and accurate interpolation between the acquired points could be achieved using a shape preserving piecewise cubic Hermite interpolating polynomial (127) (called '*pchip*' in MATLAB), as seen in Figure 4.10.

From Figure 4.9 it can be seen that missing out the very end of diastole is not important in subjects with normal flow profiles, however is important in patients with regurgitant flow during diastole, as seen in Figure 4.10. Therefore, the missing flow data was predicted by performing a linear interpolation between the last calculated point and the first point, so that the flow profile filled the entire RR-interval (as stored during the acquisition of data from the ECG data), as seen in Figure 4.10.

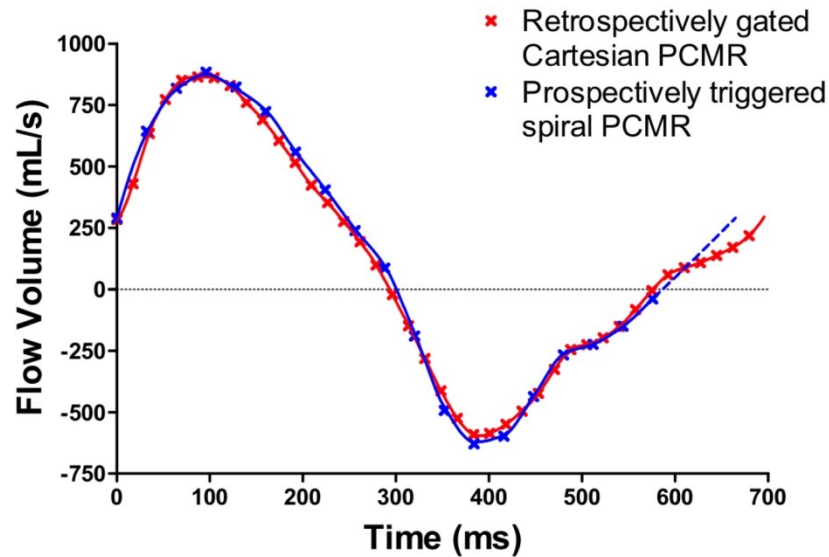


Figure 4.10: Abnormal flow profile, with regurgitant flow during diastole. A cubic interpolation is performed between the acquired data points, and a linear interpolation is used between the last and first points, to ensure the flow profile filled the entire RR-interval

The cubic interpolation (between the acquired points) and the linear interpolation (to ensure the data fills the entire RR-interval) were implemented within a plug-in for OsiriX, as shown in Figure 4.11. The top graph of the plug-in (see Figure 4.11) shows the acquired data points plotted in black (displayed with a linear interpolation) – the corresponding flow volumes are shown in the first column (on the right hand side). The interpolated data is also plotted on the top graph in green and the corresponding flow volumes shown in the second column. This allows the user see the effect of the interpolation – therefore if the interpolation is deemed to be incorrect, the un-interpolated results can still be used. In this study all stroke volumes were calculated from the interpolated flow curves.

For the normal flow curve shown in Figure 4.11, despite the large trigger window (of 167 ms) the stroke volumes calculated with and without interpolation vary by only 0.4 mL/cycle, indicating the accuracy of the cubic interpolation method. This also demonstrates that the linear interpolation does not affect normal stroke volumes, as expected.

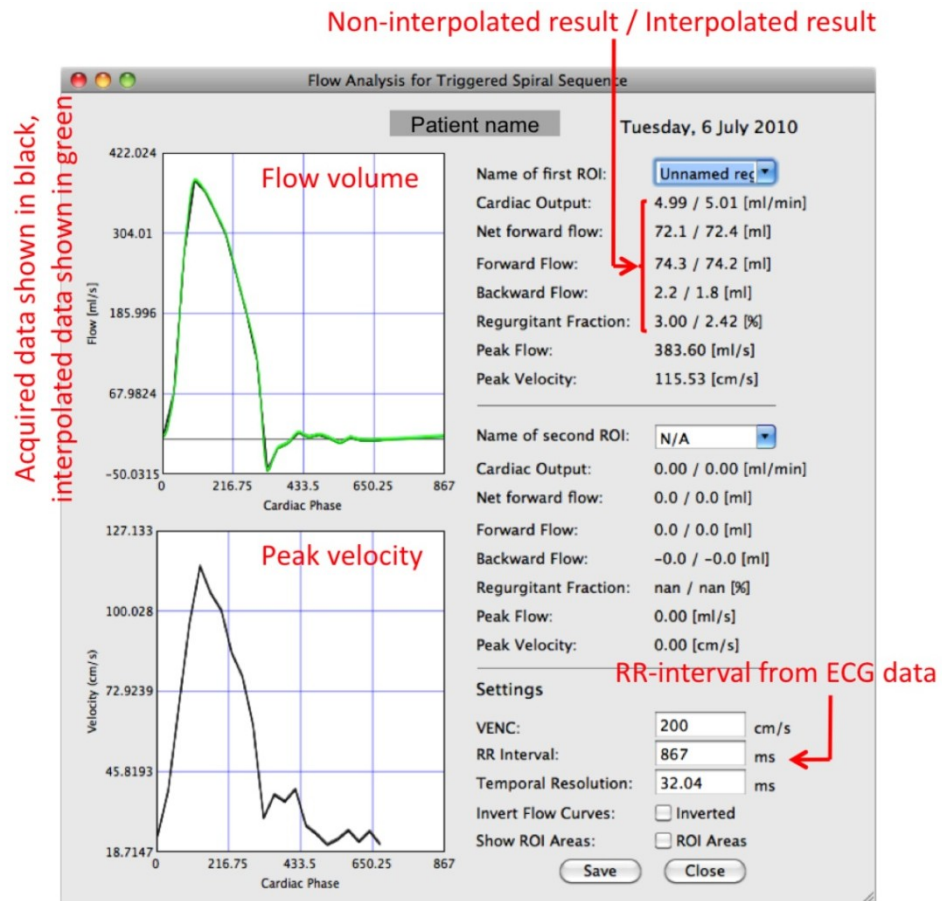


Figure 4.11: OsiriX plug-in developed to analyse flow from the prospectively-triggered PCMR sequence. In this subject 22 cardiac phases are captured, meaning the last acquired point is at time 673 ms. As the RR-interval is 867 ms, data for the remaining 167 ms was predicted using linear interpolation

4.3.5 SNR measurements

SNR and VNR measurements were performed in a similar way to that described in section 3.3.3. However, the trigger-window in a prospectively-triggered sequence disturbs the steady state of the sequence, leading to increased signal intensity in the first few cardiac phases – this is known as the *lightning* artefact (37). Therefore, in this study it was necessary to adapt the SNR calculation to take account of this signal intensity variation.

The signal intensity in the prospectively-triggered spiral PCMR sequence was found to decay exponentially. It was therefore necessary to correct for this exponential signal decay, before calculating the estimated signal noise, σ_S . The exponential signal decay was calculated as follows;

- The average signal intensity (I_A) within the stationary ROI (see section 3.3.3) was calculated for each cardiac phase
- The minimum value of I_A across all cardiac phases was found (I_{A_min}), and subtracted from all values of I_A
- The natural log of the offset average intensity values was calculated, and the y-crossing and slope of the resulting line were found
- The exponential fitted curve was calculated, for each cardiac phase, x , as:

$$fitted_curve(x) = [exp(y_crossing) \cdot exp(gradient \cdot x)] + I_{A_min}$$

The corrected signal intensities were calculated by subtracting the fitted exponential value (for the current cardiac phase) from each pixel value in the corresponding image (and adding I_{A_min}). This was implemented in OsiriX. The result of the exponential signal intensity correction is plotted in the plug-in, as seen in Figure 4.12;

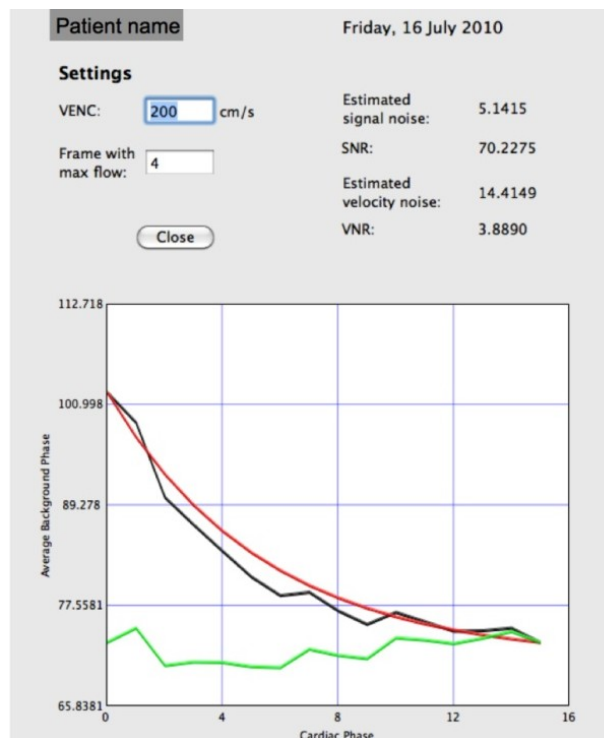


Figure 4.12: Plug-in for SNR quantification, showing the average signal intensity in the stationary ROI (I_A) in the black line, the exponential fitted curve in red, and the corrected signal intensity in green, for a prospectively-triggered spiral PCMR data set

The estimated signal noise and estimated SNR were calculated from the corrected signal intensities (during peak systole), as described in chapter 3. The VNR was calculated in exactly the same way as described in chapter 3.

To allow a fair comparison, SNR was calculated in the same way for all sequences used in this study. Figure 4.13 shows SNR measurements from a retrospectively-gated standard Cartesian sequence and a prospectively-triggered spiral sequence, in the same patient. It can be seen from Figure 4.13 that the exponential fit does not affect the signal intensity in the retrospectively-gated sequence, however does a good job of correcting the exponential decay in the prospectively-gated sequence;

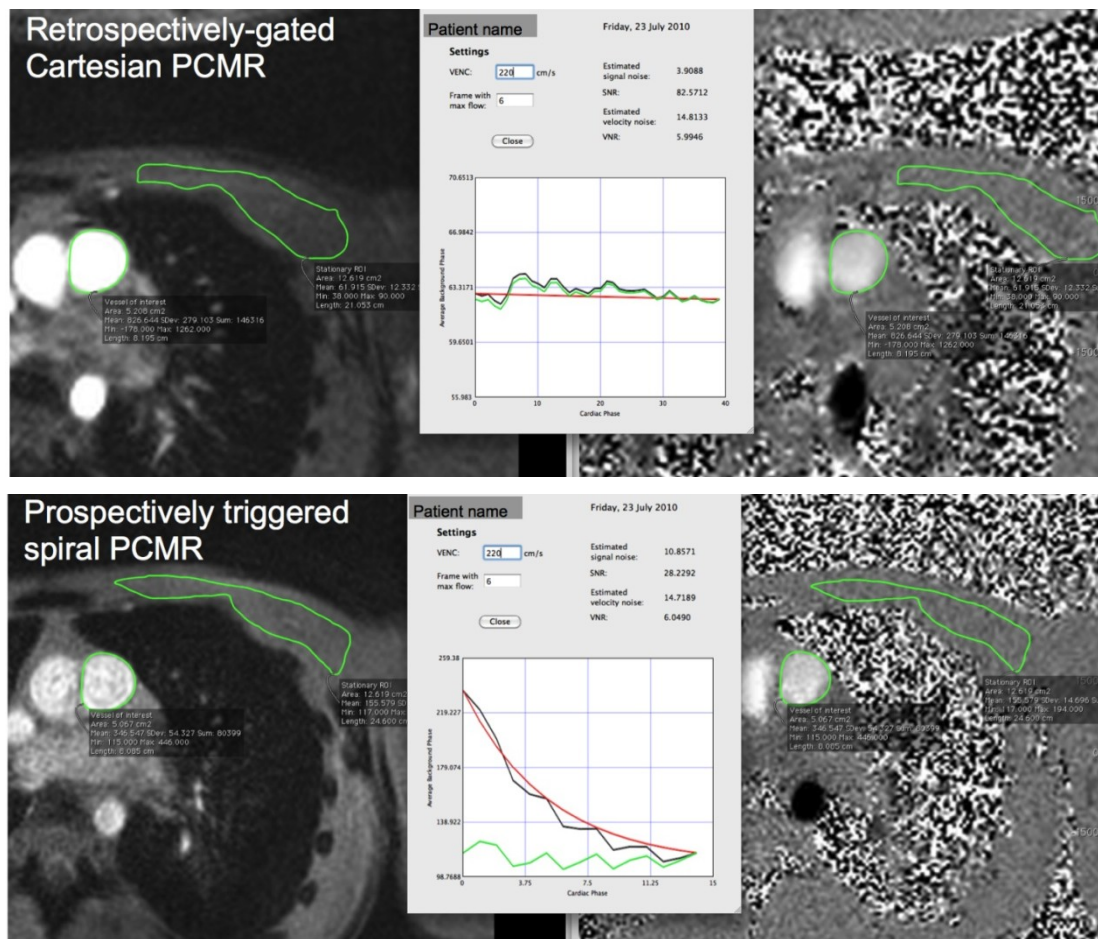


Figure 4.13: SNR measurements with exponential curve fitting from; top) retrospectively-gated Cartesian PCMR sequence, bottom) prospectively-triggered spiral PCMR sequence

4.3.6 Edge sharpness

In this study we wished to quantify edge sharpness, similarly to that carried out in section 3.3.3.4. In the previous study a fifth-order polynomial was fitted to the pixel intensities, to prevent noise providing artificially high gradients (representing sharp edges), see section 3.3.3.4. In this study it was observed that the fifth-order polynomial fit was prone to oscillations caused by noise, which provided artificially high gradients (see Figure 4.14a). This is likely to be because in chapter 3, edge sharpness was only quantified in the aorta, where the edge sharpness was assessed over the border between the aorta and one of the surrounding chambers of the heart. In this study edge sharpness was quantified in the aorta, main pulmonary artery, and pulmonary branches. In the main pulmonary artery, and pulmonary branches edge sharpness was generally quantified over the border between the vessel and the surrounding lung, i.e. noise pixels, leading to artificially high gradients.

It was observed that by filtering the pixel intensities using a Savitzky–Golay filter (128), the edge sharpness algorithm more accurately detected the edge of the vessels in this study, as seen in Figure 4.14.

A Savitzky–Golay filter smoothes data, removing the noise without removing the high frequency components. It works by dividing the data into small windows and performing a polynomial fit on the data within the window (the size of the window and the degree of the polynomial fit are specified by the user from the UI in OsiriX, see Figure 4.14b). For the middle position within the window, the smoothed value is taken to be value at the centre position of the calculated polynomial. The window is stepped through all of the data points, to smooth the data in this way.

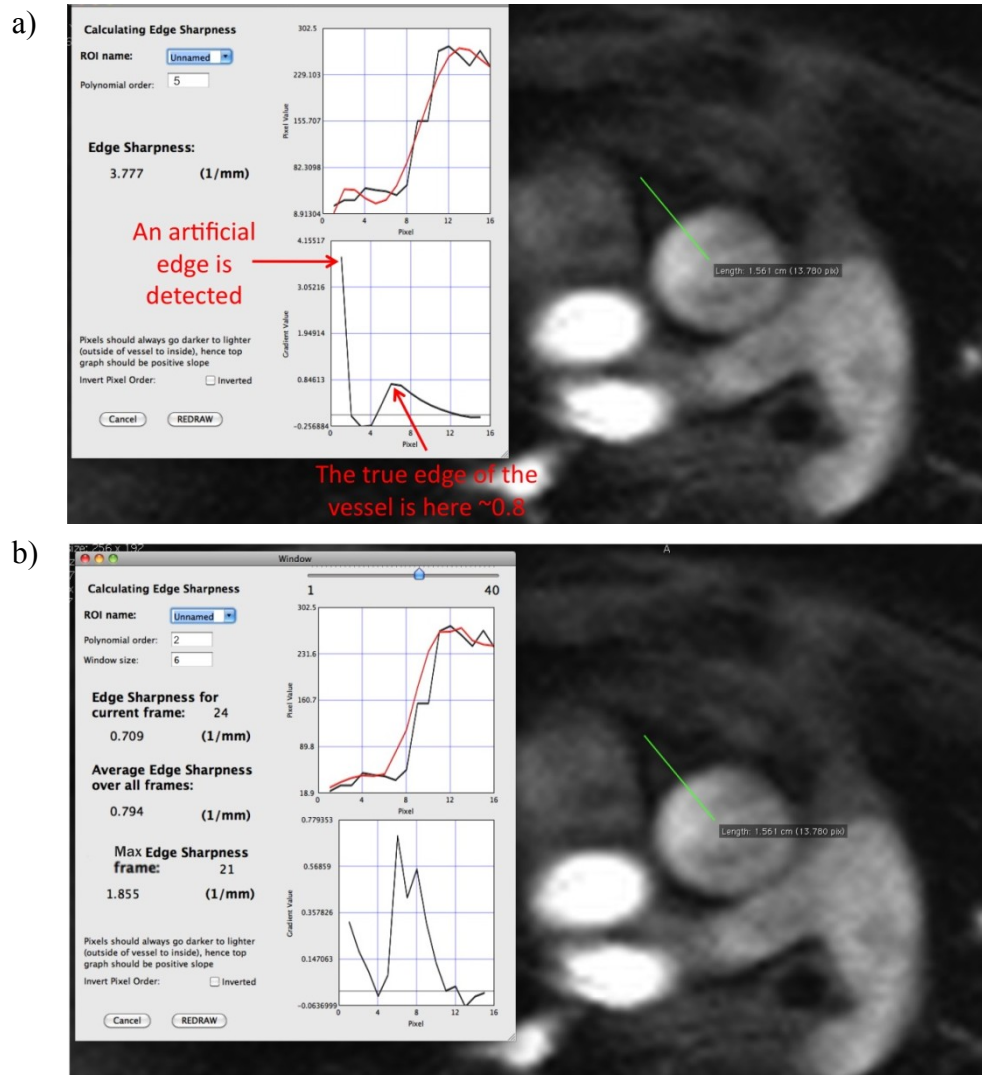


Figure 4.14: Example of edge sharpness calculation for one data set, using; a) fifth-order polynomial fit, b) Savitzky–Golay filter. It can be seen that polynomial fit detects an artificial edge. The Savitzky–Golay filter detects the vessel border correctly

In this application a window size of 6, with a polynomial fit of degree 2, was found to optimally smooth out noise but not smooth out the steep transition at vessel border. These parameters were used for all vessels in this study.

In chapter 3 the edge sharpness was only quantified in one frame during peak systole, however in this study we decided to use an average edge sharpness measure over all frames.

4.3.7 Residual Background Phase Correction

In section 2.3.4 residual background phase offsets (after phase subtraction) were observed to be negligible using a ramp-up time of 10 μs , with a TE delay of 400 μs . However, in this study using the same ramp-up time and TE delay, residual phase offsets were observed (after phase subtraction and Maxwell correction) predominantly when performing PCMR imaging in the pulmonary artery. These additional phase offsets were not observed in chapters 2 or 3 because PCMR was only carried out in the aorta. This may be because the slice position tends to be more angulated when imaging the pulmonary artery, or because the pulmonary artery is further from the isocentre of the magnet.

As described in section 1.6.4, it is possible to predict these background offsets using a similar principle to Walker, et al. (52). This principle uses the assumption that the phase offsets vary smoothly in space. The offsets can therefore be predicted by fitting a surface through the phase of stationary pixels (40, 47, 52).

In this study, the residual phase was observed to be of a low polynomial order and did not change significantly between different cardiac phases. It was observed that these background phase offsets could be accurately predicted by fitting a quadratic surface ($Ax^2+By^2+Cxy+Dx+Ey+F$), through the phase of stationary pixels. The surface was calculated using a Cholesky decomposition algorithm.

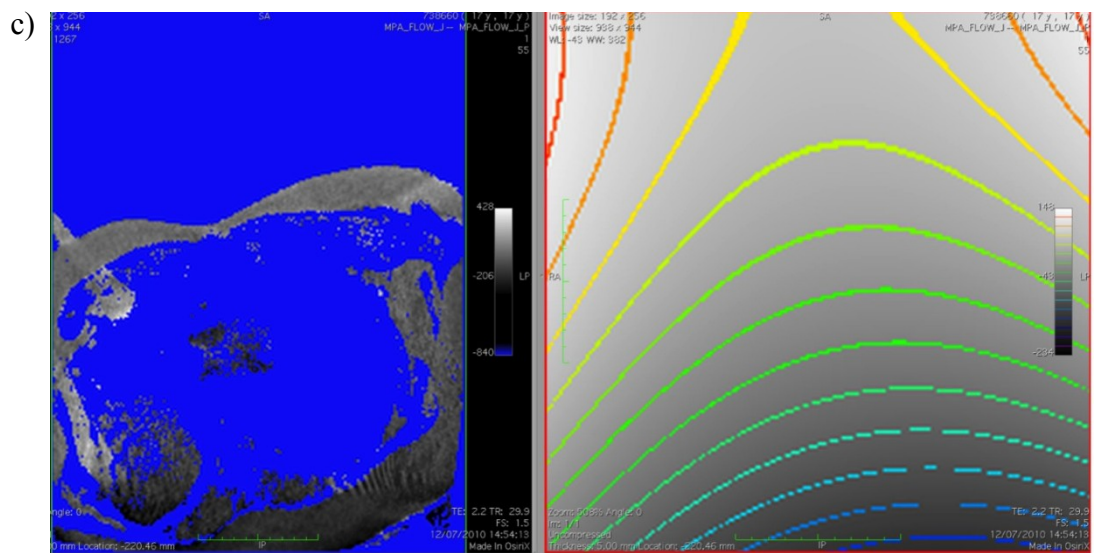
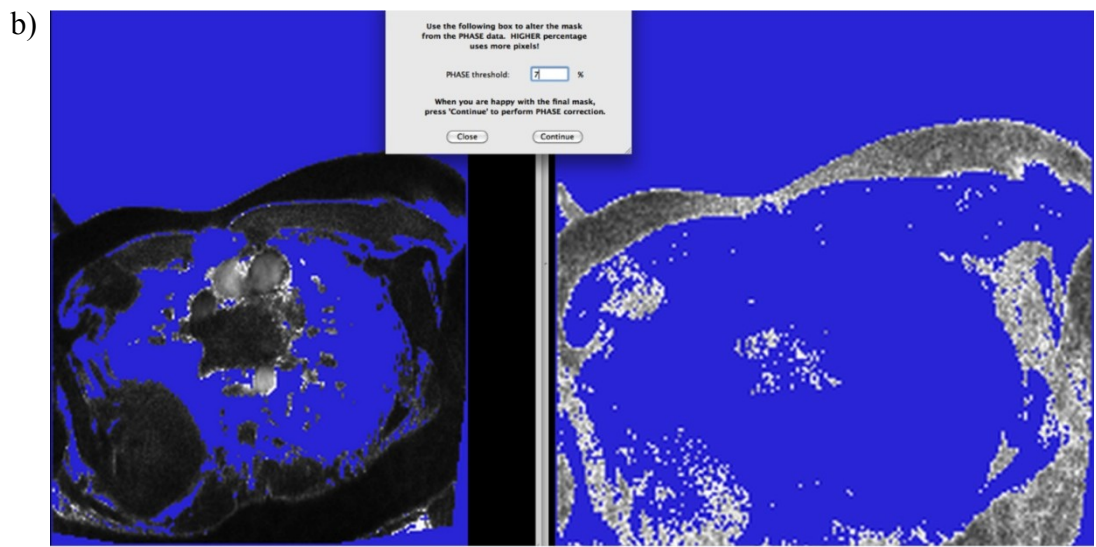
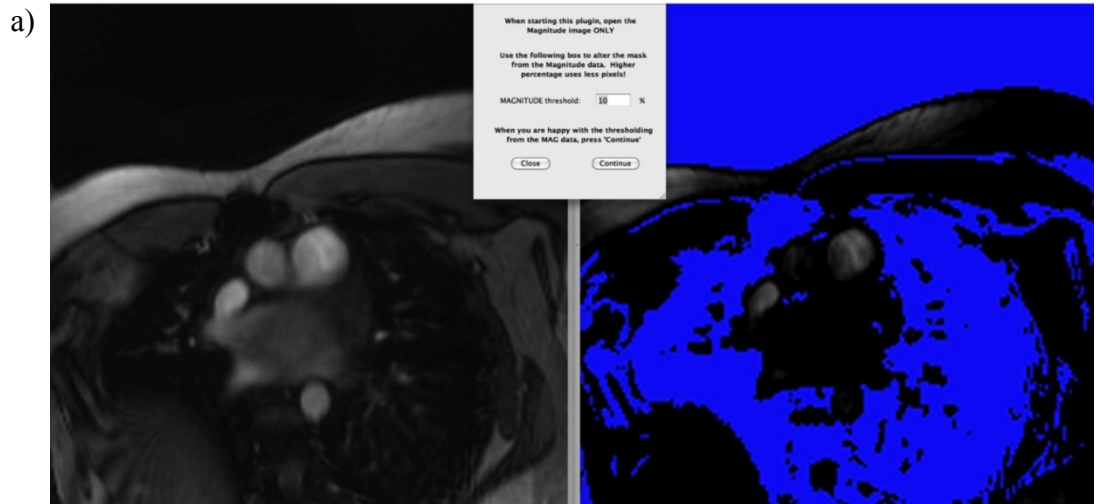
In this study background phase correction was implemented in OsiriX (after prototyping in MATLAB). The stationary tissue was identified in two steps;

1. From the pixel intensity in an average magnitude image (over all cardiac phases). This allowed detection of pixels containing tissue
2. From the standard deviation of each pixel in the phase images (through all cardiac phases). This allowed determination of stationary tissue

In OsiriX, an average magnitude image was first calculated and displayed in a new window (see Figure 4.15a). A mask ($\text{mask}_{\text{MAGNITUDE}}$) was formed using only pixels with values that were greater than a defined threshold (see Figure 4.15a). The default threshold was 10 % of the maximum pixel value in the average magnitude image, however the percentage could be altered from the UI, as seen in Figure 4.15a.

Once the pixels containing tissue had correctly been identified, the stationary tissue was identified from the phase images. Firstly, the standard deviation of each pixel (in the phase images) was calculated through all cardiac phases. This standard deviation image was then masked using the $\text{mask}_{\text{MAGNITUDE}}$ (see Figure 4.15b). The final mask ($\text{mask}_{\text{FINAL}}$) was then formed using pixel values in the masked standard deviation image, which were smaller than a defined threshold (see Figure 4.15b). The default threshold was 7 % of VENC, however the percentage could be altered from the UI, as seen in Figure 4.15b.

An average phase image was finally formed over all cardiac phases, and the final mask applied (see Figure 4.15c). The quadratic surface was calculated from the non-zero pixel values, using a Cholesky decomposition (see Figure 4.15c). This surface was subtracted from all phase images, to correct for background phase offsets (see Figure 4.15d). The flow analysis plug-in was then automatically opened to show the effect of the phase correction on the calculated flow volumes (see Figure 4.15e).



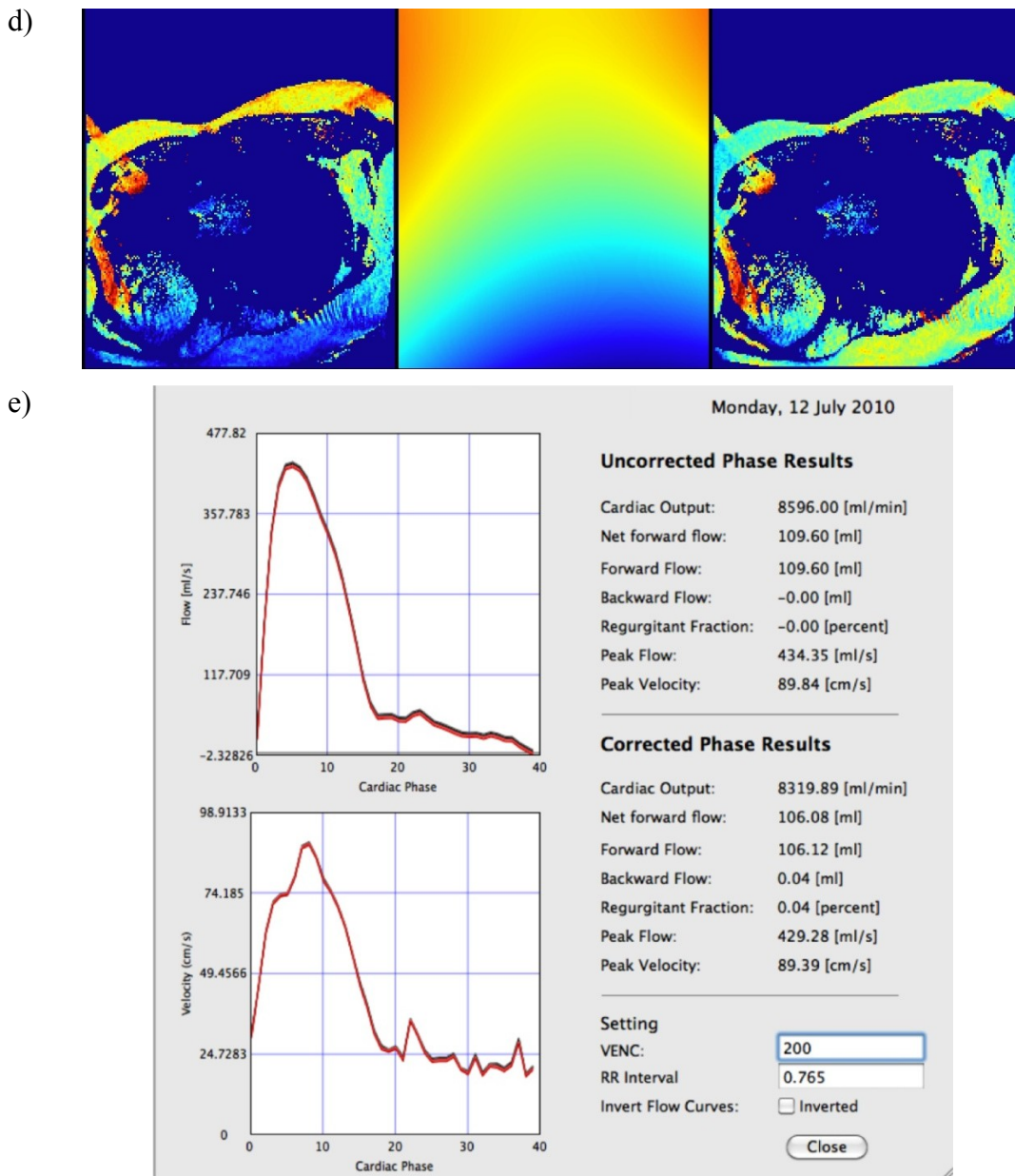


Figure 4.15: Phase correction plug-in as implemented in OsiriX. a) An average magnitude image is formed (left). Using the threshold from the UI, the mask_{MAGNITUDE} is formed (right). Blue pixels show pixels not in the mask. b) The standard deviation of the phase data through all cardiac phases is calculated, and masked using the mask_{MAGNITUDE} (left). Using the threshold from the UI the mask_{FINAL} is formed (right). c) An average phase image is formed and masked with the mask_{FINAL} (left). The pixel values remaining in this image are used to calculate the quadratic correction surface (right). d) The quadratic surface is subtracted from all phase images to correct for offsets. Left; uncorrected average phase image, middle; quadratic surface, right; corrected average phase image. e) Flow analysis is carried out for the uncorrected and corrected phase series, plotted in black and red, respectively

For the subject shown in Figure 4.15, a separate scan was performed on a stationary phantom using identical imaging parameters, immediately after the subject's examination (seen in Figure 4.16a). The phase offset from the stationary phantom and from the quadratic surface were compared in the same ROI as the vessel, as seen in Figure 4.16. This method of phase correction was described in section 1.6.4).

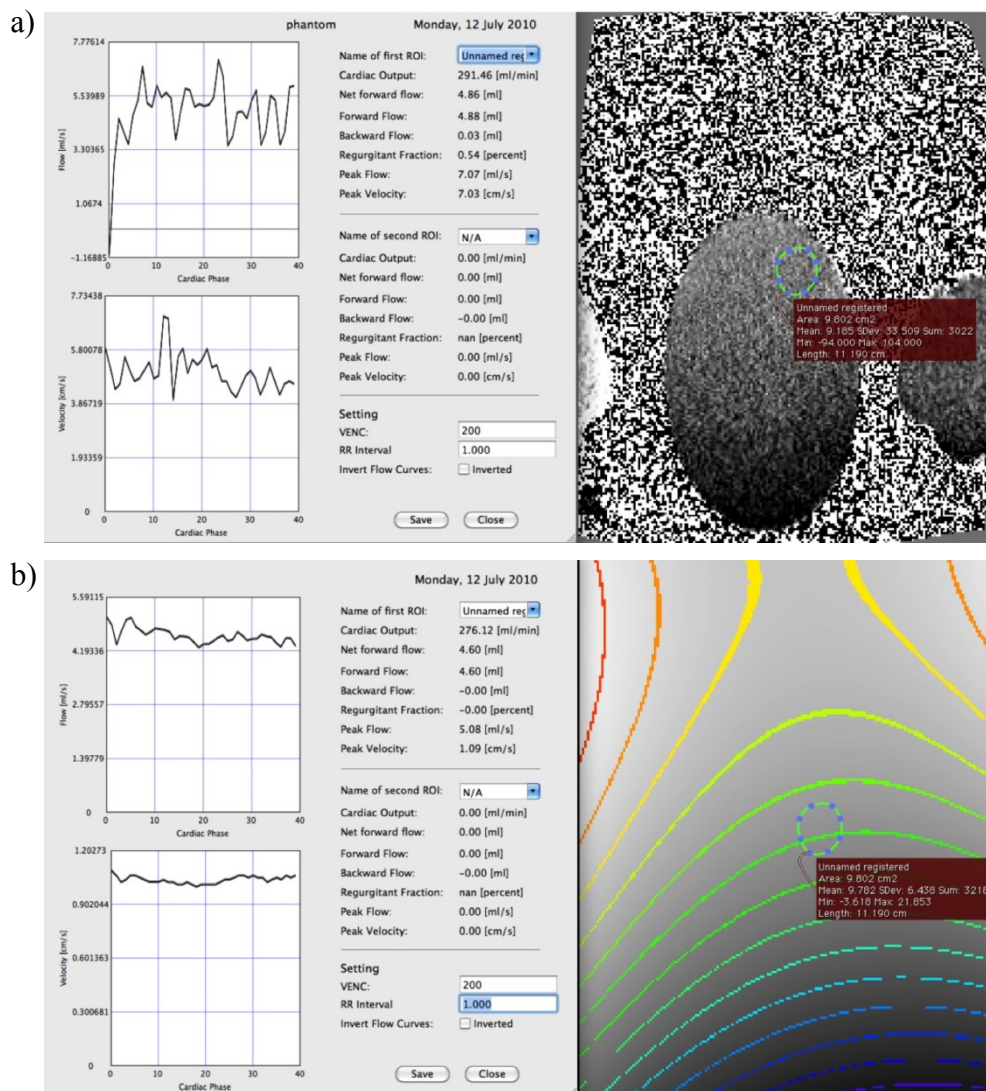


Figure 4.16: Phase offsets observed in a stationary water phantom, with identical imaging parameters to those used in the subject from Figure 4.15. The flow volume plug-in was used to calculate the average flow offset caused by the phase offsets (left)

From Figure 4.16 it can be seen that the average background phase offset calculated from the stationary phantom resulted in an average flow volume offset of 4.86 mL/s, and from the quadratic surface was 4.60 mL/s.

This method of calculating a surface through stationary pixels, can be used on any PCMR sequence. Note, that in Figure 4.15 and Figure 4.16 the phase offsets were assessed from the retrospectively-gated Cartesian PCMR sequence. Figure 4.17 shows an example of the background phase correction used for the prospectively-triggered spiral PCMR sequence in a subject with more severe background phase offsets;

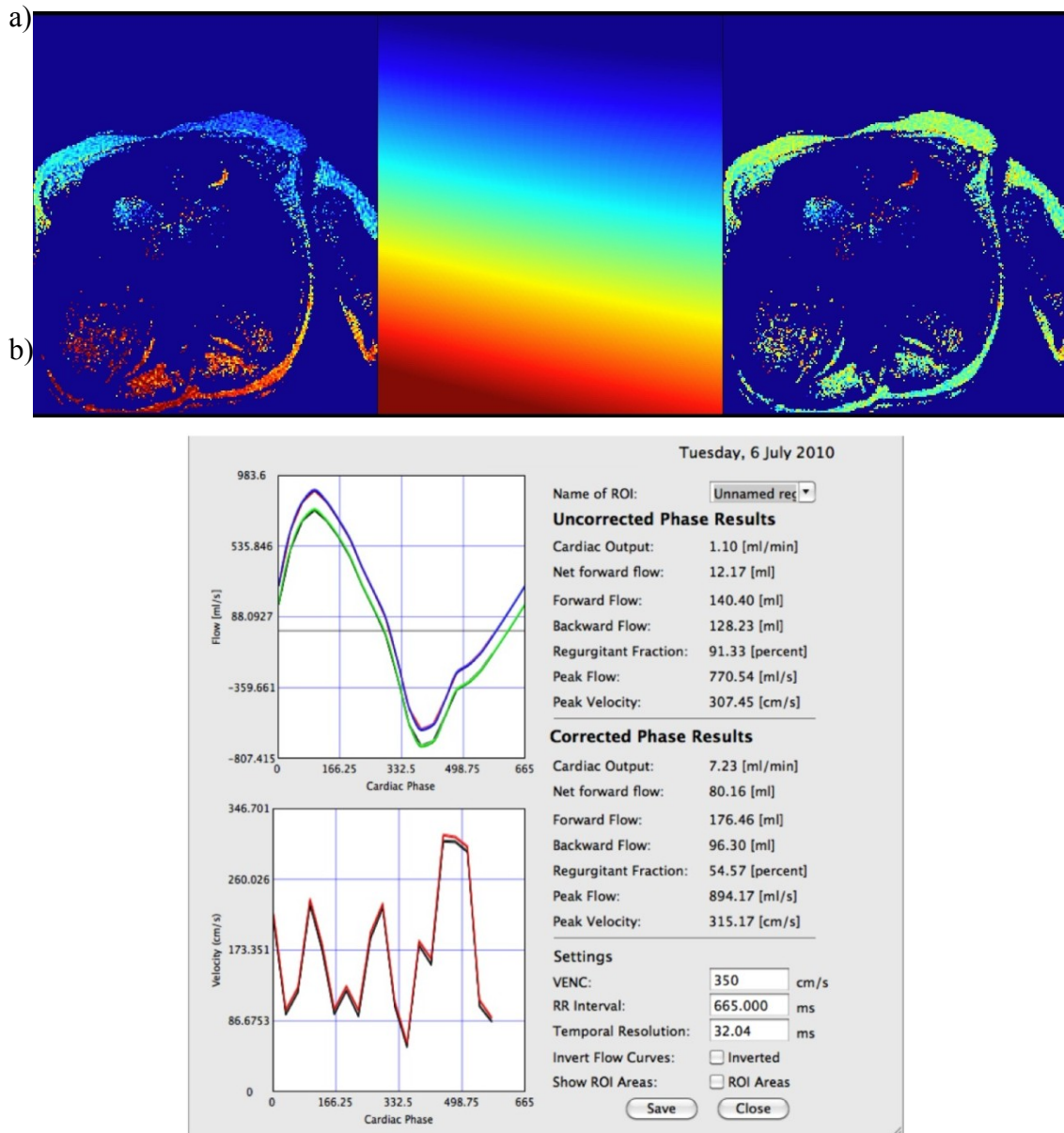


Figure 4.17: Background phase correction for a prospectively-triggered spiral sequence. a) Calculation of quadratic surface, left; average phase image with final mask, middle; quadratic correction surface, right; average phase image with background phase correction. b) Flow analysis for the uncorrected and corrected phase series, plotted in green and blue, respectively

For the subject shown in Figure 4.17, it can be seen that the uncorrected net flow was 12.17 mL/cycle, and the corrected net flow was 80.16 mL/cycle. The net flow for the retrospectively-gated Cartesian PCMR sequence was 81.22 mL/cycle, indicating that the background phase correction does a good job of correcting the stroke volume.

It was important that this background phase correction plug-in did not artificially add phase to images where no background phase offsets were present. Figure 4.18 shows an example of flow volume calculations with and without background phase correction, in a subject where no background phase offsets were present. The uncorrected and corrected stroke volumes differ by only 0.5 mL/cycle;

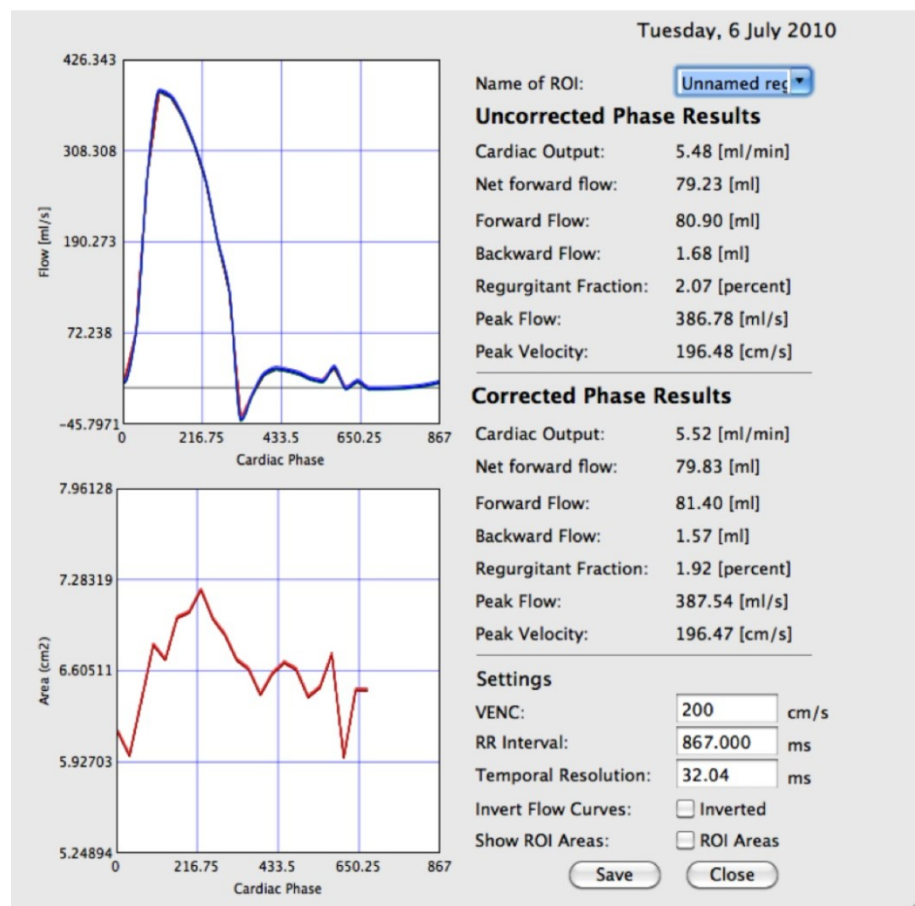


Figure 4.18: Flow analysis for the uncorrected and corrected phase series for a subject with no background phase offsets. It can be seen that the background phase correction has not added artificial phase to the data

Background phase offsets were only observed in a few patients.

4.3.8 Recording Physiological Data

Using the ECG monitor and the respiratory bellows, we were able to record the physiological data during the acquisition of data for all sequences used in this study. This was implemented within the sequence IDEA code. Data was logged from the start of the first dummy pulse, to the end of the last readout. The ECG and respiratory data were written into text files, and processed in MATLAB.

Figure 4.19 shows an example physiological data set acquired for one subject during the prospectively-triggered spiral PCMR sequence;

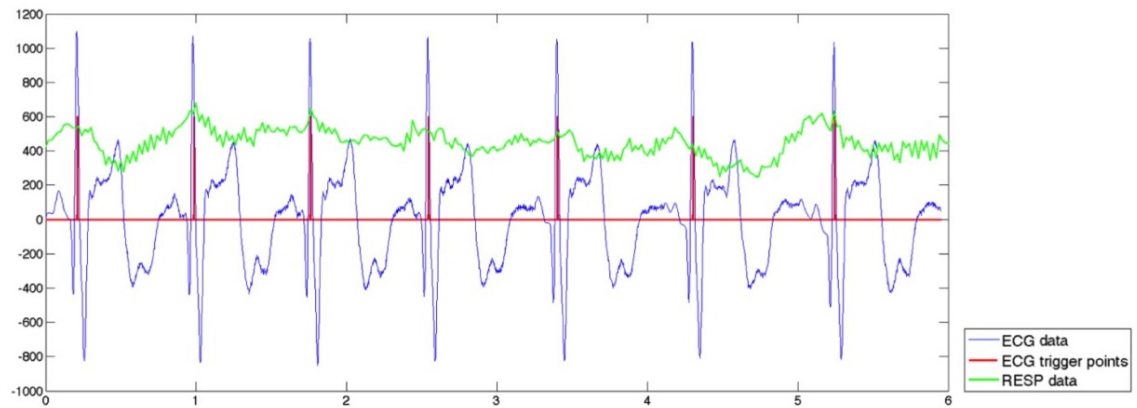


Figure 4.19: Example of physiological data acquired for one subject during the prospectively-triggered spiral PCMR sequence. It can be seen that the sequence correctly triggers at the R-wave in each heart-beat. The respiratory data shows little variation over the 6 second scan

Unfortunately we were not able to quantitatively compare the physiological data between subjects as the data was internally scaled, before being written to the files.

4.4 Optimisation of Sequence Parameters

In this study we wished to acquire high temporal and high spatial resolution images within a short breath-hold. We hoped to achieve a spatio-temporal resolution similar to that of the free breathing, retrospectively-gated sequence used clinically at ICH; ~ 30 ms temporal resolution and ~ 1.25 mm spatial resolution. We wished to reduce the scan duration further than achieved by Lew, et al. (125), to < 7 seconds to enable the breath-hold to be achievable even by children and sick adults.

With these specifications we were able to optimise the triggered spiral PCMR sequence. To achieve a high spatial resolution we needed to use a 256 matrix. It was observed that with the use of > 30 spiral interleaves, less image blurring was observed. However, the higher the total number of spiral interleaves, the more RR-intervals needed to acquire data.

With the use of 36 spiral interleaves, a TR of ~ 8 ms was achieved. This gives a temporal resolution of ~ 16 ms (for both flow-compensated and flow-encoded readouts), when acquiring just one interleave per RR-interval. Therefore, a temporal resolution of ~ 32 ms could be achieved by acquiring two spiral interleaves per RR-interval. In this case, 18 RR-intervals were needed to acquire all spiral interleaves with no SENSE acceleration. Using a SENSE factor of 3, allowed all data to be acquired within 6 RR-intervals (plus one RR-interval for the dummy pulses), resulting in a scan time of ~ 7 seconds (for an RR-interval of 1000ms). These parameters were observed to give the optimal trade-off between temporal resolution and total scan time, whilst maintaining good image quality.

4.4.1 Interleave Ordering

In order to calculate the sensitivity maps from the data itself (in the same way as chapters 2 and 3), it was necessary to rotate the spiral interleaves in each cardiac phase. Therefore, by combining the data from three consecutive cardiac phases, we were able to compute a fully sampled data set with 36 spiral interleaves.

The resulting data acquisition scheme can be seen in Figure 4.20;

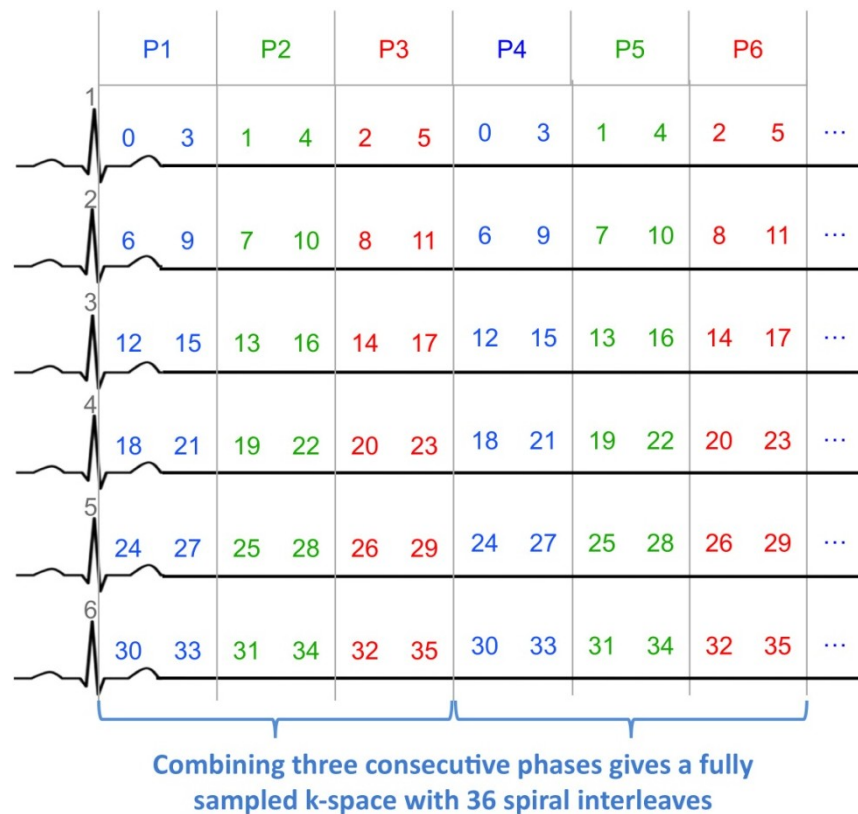


Figure 4.20: The optimised sequence uses a total of 36 spiral interleaves, with 2 interleaves acquired in each RR-interval, undersampled by a factor of 3. The sampling pattern is rotated in each cardiac phase (P, indicated along the top). In total 6 RR-intervals are required to collect all of the data (indicated in gray along the left). The coloured numbers in the boxes, represent which spiral interleaves were acquired – for each spiral interleave the flow-compensated data was acquired first, followed by the flow-encoded data

All data was reconstructed online using the iterative SENSE algorithm developed in chapter 2. The coil-sensitivity information was calculated from the time-averaged (flow-compensated) data from each coil, divided by the sum-of-squares of the time-averaged coil data, in the same way as chapter 2.

4.5 In-vitro Validation

To validate the prospectively-triggered spiral PCMR sequence, an experiment was carried out using the pulsatile flow pump described in section 2.4. The output from the pump was varied from 1.8-4.8 L/min, by changing the stroke volume (30-60 mL/cycle) and the pump rate (55-75 bpm). Flow was quantified at 10 different output volumes.

4.5.1 In-vitro protocol

PCMR images were acquired using a standard, retrospectively-gated Cartesian sequence and the prospectively-triggered spiral PCMR sequence, at the mid-point of the phantom with a transverse imaging plane. The flow volumes measured from the standard, retrospectively-gated Cartesian sequence were assumed to be the true flow volumes. Two three-element spine coils (below the phantom) and two three-element body-matrix coils (above the phantom) were used for imaging. The sequences parameters are shown in Table 4.4.

4.5.2 Image Analysis

All images were processed in OsiriX. Flow images were segmented using the semi-automatic segmentation propagation plug-in described in section 2.7 (by J.A.S. using the modulus images). The pump output was measured.

Results are expressed as the mean \pm standard deviation. Measurements of agreement between the standard flow sequence and the real-time flow sequence were performed using Bland-Altman analysis, as well as calculation of correlation coefficients. All statistical analysis was performed using GraphPad Prism.

	Retrospectively-gated Cartesian PCMR	Prospectively-triggered spiral PCMR
TE/TR	2.7/7.0 ms	2.3/5.2 ms
GRAPPA (ACL)	2 (24)	-
Spiral readouts	-	36
SENSE factor	-	3
Readouts per RR	2	2
Flip angle	30°	25°
FOV	240×320	375×375
Rectangular FOV	75 %	-
Asymmetric echo	77 %	-
Matrix	192×256	256×256
Pixel Bandwidth	391 Hz/pixel	1395 Hz/pixel
VENC	100 cm/s	100 cm/s
NSA	1	1
Temporal resolution	25.3 ms	30.9 ms
Spatial resolution	1.3×1.3×6.0 mm	1.5×1.5×6.0 mm
Scan Time	~50 seconds (54 RR-intervals)	~5 seconds (6 RR-intervals)

Table 4.4: Sequence parameters in-vitro, for retrospectively-gated Cartesian sequence and prospectively-triggered spiral sequence

4.5.3 In-vitro Results

For each experiment the pump output was calculated using both of the sequences. There was good agreement between the retrospectively-gated Cartesian PCMR sequence and the prospectively-triggered spiral PCMR sequence, throughout the cycle as seen in Figure 4.21.

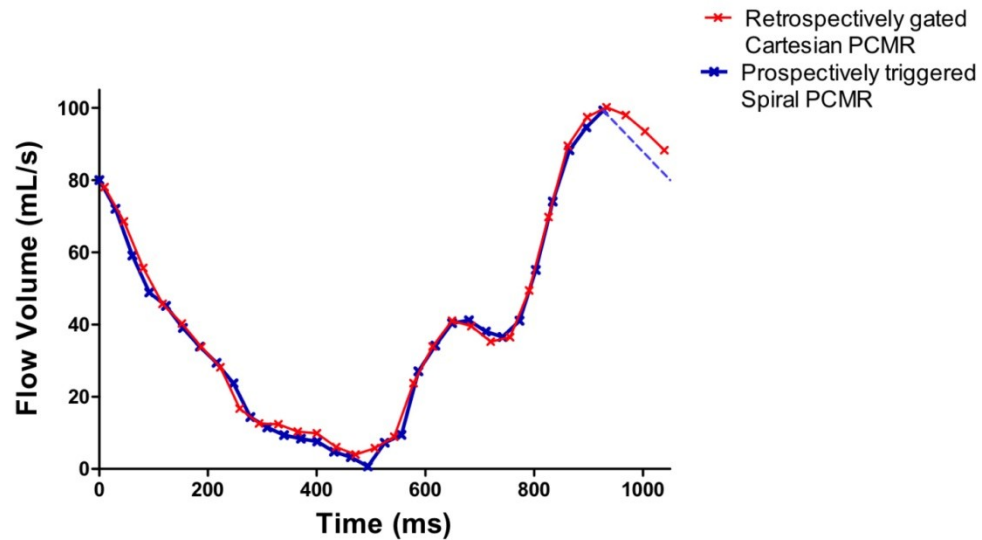


Figure 4.21: Comparison of flow profiles in-vitro

From Figure 4.21 it can be seen that the flow pump triggers during peak systole, therefore the need for a trigger window means that data is not acquired during peak flow. The dashed line at the very end of the RR-interval shows the linear interpolation between the last point and the first point to ensure the prospectively-triggered data fills the entire RR-interval (as described in section 4.3.4).

However, a good agreement was found between the pump output calculated from the retrospectively-gated Cartesian PCMR sequence and prospectively-triggered spiral PCMR sequence (3.24 ± 0.90 L/min vs. 3.15 ± 0.88 L/min, respectively). Bland-Altman analysis of the pump output found the bias was -0.10 L/min, with limits of agreement from -0.29 to 0.09 L/min (as seen in Figure 4.22). The correlation coefficient was 0.994 ($p < 0.005$).

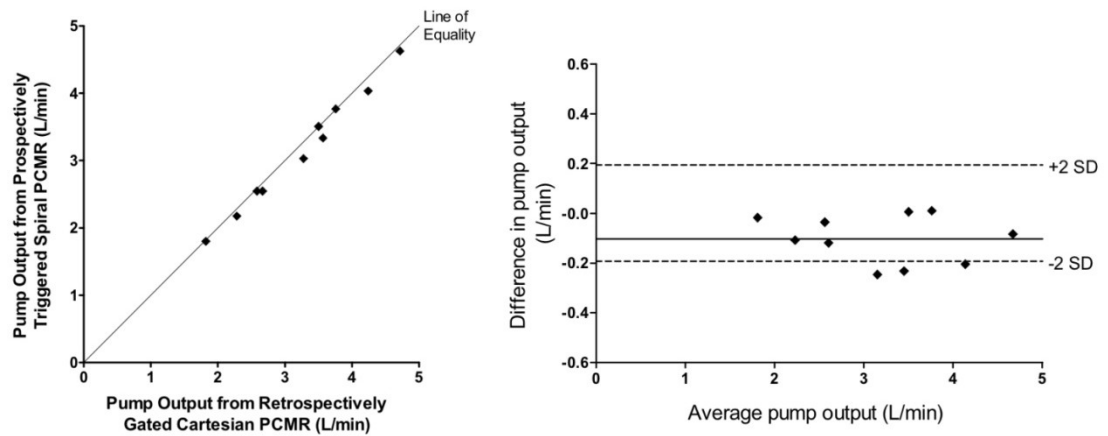


Figure 4.22: Comparison of pump output in-vitro between retrospectively-gated Cartesian sequence and prospectively-triggered spiral sequence. a) Correlation of flow measured from both techniques. b) Bland-Altman plot of the difference in flow measured using both techniques

The prospectively-triggered spiral PCMR sequence is thought to underestimate the pump output compared to the retrospectively-gated Cartesian sequence because the pump is triggered during peak systole. This means that the trigger window always occurs when there is maximum flow, and the linear interpolation does not completely account for the true flow as seen in Figure 4.21.

4.6 In-vivo Protocol

The prospectively-triggered spiral PCMR sequence was validated in-vivo by comparing image quality and flow volumes measured using:

- a) Breath-hold spiral SENSE PCMR
- b) Standard breath-hold PCMR
- c) Reference free-breathing PCMR

4.6.1 Patient population

In July and August 2010, 40 consecutive children and adults (22 male: 18 female) referred for cardiac MR imaging, were enrolled in this study. The median age was 21.4 ± 13.8 years (range: 3.0 to 61.3 years, 17 of whom were less than 16 years old).

Their diagnoses were;

- Repaired tetralogy of Fallot/ pulmonary atresia with ventricular septal defect – 15
- Coarctation of the Aorta – 7
- Cardiomyopathy exam – 6
- Pulmonary stenosis – 4
- Transposition of the great arteries repair – 2
- Atrial septal defect - 2, dilated aortic root – 2
- Left pulmonary artery stenosis – 1
- Bicuspid aortic valve – 1

Of these, 5 children were imaged whilst under general anaesthetic. The sample size was chosen to detect a mean difference in stroke volumes of 2 mL with a statistical power of 80 % and a p-value of .05 (means and standard deviation assumed from values found by Sakuma, et al. (96) between CO measurements made during free breathing and small lung volume breath-holding; 6.09 ± 0.49 L/min vs. 5.87 ± 0.53 L/min, respectively). This analysis was performed using open-source

software (G*power 3; University of Dusseldorf, Dusseldorf, Germany) (129) which gave an estimated sample size of 36 (which was increased to 40 for this study).

Inclusion criteria were:

- a) Clinical referral for cardiac MR imaging

Exclusion criteria were:

- a) Contraindications for MR such as MR-incompatible implants
- b) Pregnancy
- c) Irregular heart rate

The local research ethics committee approved the study and written consent was obtained from all subjects/guardians.

4.6.2 MR protocol

Imaging was performed on a 1.5 T MR scanner using two spine coils and one body-matrix coil (giving a total of 12 coil elements). A vector ECG system was used for cardiac gating.

All patients underwent a standard clinical cardiac MR examination for diagnostic purposes. Flow imaging was performed in the following vessels as per clinical need, with stented vessels excluded:

- Ascending aorta, AAO (N = 40, including 4 with regurgitation)
- Main pulmonary artery, MPA (N = 38, including 12 with regurgitation)
- Right pulmonary artery, RPA (N = 22, including 10 with regurgitation)
- Left pulmonary artery, LPA (N = 24, including 14 with regurgitation)

Flow assessment was performed in each vessel using the three sequences described below (parameters shown in Table 4.5), before moving to the next vessel.

4.6.2.1 Reference Free-breathing Sequence

The reference standard was a retrospectively-gated, free-breathing, Cartesian, gradient echo PCMR sequence (provided by the manufacturer). Respiratory motion was compensated by the acquisition of three NSA's. This sequence had high spatial and temporal resolution (Table 4.5) and is well-validated in-vitro and in-vivo (57, 93, 130-132). Therefore in this study the flow volumes measured from this sequence are assumed to be the true flow volumes.

4.6.2.2 Standard Breath-hold Sequence

The standard breath-hold sequence was a retrospectively-gated, Cartesian PCMR sequence (provided by the manufacturer). This sequence was the same as the free-breathing flow sequence described above. However, in order to acquire the data within a breath-hold, spatio-temporal resolution was lowered (Table 4.5).

4.6.2.3 Spiral SENSE Breath-hold Sequence

The spiral sequence was a prospectively-triggered, segmented PCMR sequence, described in section 4.3.

The FOV was not optimized for children, as this would have resulted in a reduction in temporal resolution in the spiral sequence. This is because to reduce the FOV, we must go further out in k-space. Due to limitations in the gradient strength, it is not possible to traverse this outer part of k-space at the sampling bandwidth used in Table 4.5. Therefore a reduction in FOV, results in a reduction in bandwidth for spiral imaging, causing a decrease in the temporal resolution.

	Reference Free- Breathing PCMR	Standard Breath-hold PCMR	Spiral Breath-hold PCMR
TE/TR	~2.2 / 7.0 ms	~2.2 / 7.0 ms	2.1 / 8.0 ms
Spiral Readouts	-	-	36
Acceleration factor	2 (GRAPPA)	2 (GRAPPA)	3 (SENSE)
Matrix Size	256 × 192	192 × 113	256 × 256
FOV	200 - 400 mm	290 - 400 mm	400 mm
Rectangular FOV	75%	66%	100%
Readouts per segment	3	4	2
Slice Thickness	5 mm	5 mm	5mm
Flip Angle	30°	30°	25°
Pixel bandwidth	543 Hz/pixel	543 Hz/pixel	1220 Hz/pixel
VENC	180 - 400 cm/s	180 - 400 cm/s	180 - 400 cm/s
NSAs	3	1	1
Total Scan Duration	44 - 144 s	11 - 24 s	3 - 8 s
Voxel Size	~ 0.8 – 1.5 mm	~ 1.5 – 2.1 mm	1.6 mm
Temporal resolution	~ 30.0 ms (~33 frames/sec)	~ 40.0 ms (~25 frames/sec)	32.0 ms (31 frames/sec)

Table 4.5: Imaging parameters

4.6.3 Image Analysis

All images were processed in OsiriX by J.A.S. Flow images were segmented using the semi-automatic segmentation propagation plug-in described in section 2.7 (using the modulus images). For each flow measurement the stroke volume (net forward flow) and regurgitation fraction were calculated. Additionally, where flow was measured in both the MPA and AAO (N = 38) the Q_P/Q_S ratio was calculated, and where flow was measured in both the pulmonary branch vessels (N = 20) the RPA/LPA ratio was calculated.

In 10 randomly selected patients, the AAO flow data was reanalyzed for all three sequences (J.A.S. – 3 years experience) to determine intra-observer variability. This data was also analyzed by a second operator (V.M. – 8 years experience), to determine inter-observer variability.

4.6.4 Statistical analysis

All statistical analysis was performed using GraphPad Prism. The results were combined for all subjects, and were expressed as the mean \pm standard deviation. Comparison of means was performed by using repeated-measures ANOVA tests, with Bonferroni correction for multiple comparisons. A p-value of less than .05 indicated a significant difference. Bland-Altman analysis was performed to give measures of agreement with the free-breathing PCMR sequence (116). Additionally, the correlation coefficients were calculated.

4.7 In-vivo Results

The average heart rate was 76 ± 12 bpm (range: 50 to 111 bpm). For the reference free-breathing sequence, data was acquired over 108 heart-beats, which was 91 ± 17 seconds (range: 44 to 144 seconds). In the standard breath-hold sequence, data was acquired over 18 heart-beats, which was 16 ± 3 seconds (range: 11 to 24 seconds). For the spiral breath-hold sequence, data was acquired over 7 heart-beats, which was 5 ± 1 seconds (range: 3 to 8 seconds).

4.7.1 Physiological Data

Although it was not possible to perform any quantitative analysis of the physiological data, due to internal scaling of the data prior to being recoded (see section 4.3.8), it was observed that some subjects found the breath-hold time for the standard breath-hold sequence too long. This can be seen in Figure 4.23, where subjects 1 and 2 both completed the first half of the breath-hold well, but breathe throughout the second half of the sequence. Figure 4.23 shows that these subjects were able to complete the much shorter breath-hold for the spiral SENSE breath-hold sequence successfully.

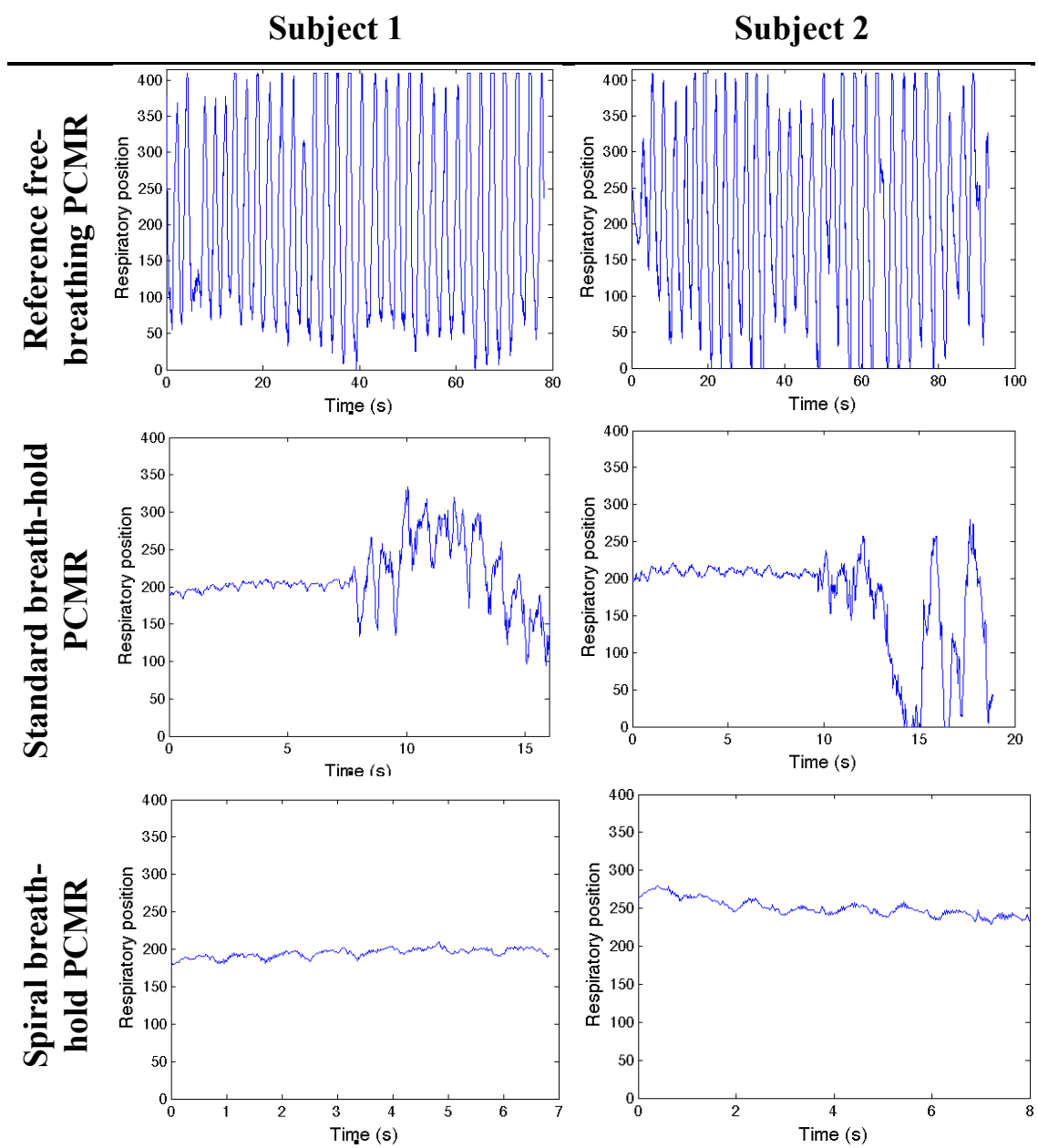


Figure 4.23: Respiratory data recorded from two subjects, for all three sequences. These subjects were able to complete the short breath-hold for the spiral sequence, however were only able to complete about half of the breath-hold for the standard breath-hold sequence. Note: different time axis.

4.7.2 Functional Assessment

A good agreement was seen throughout the cardiac cycle for all sequences, in all vessels, as can be seen for one subject in Figure 4.24;

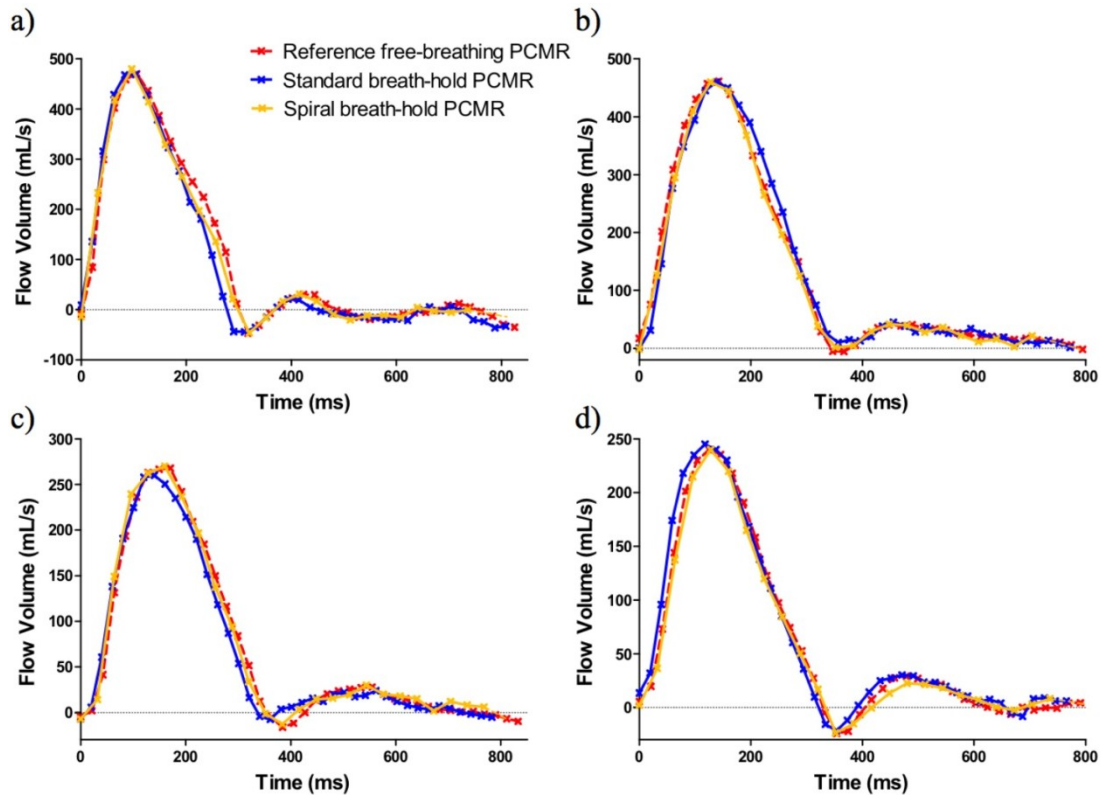


Figure 4.24: Comparison of flow profiles from all three sequences for one patient, for; a) AAO, b) MPA, c) RPA, d) LPA

Combining all vessels ($N = 124$), there were no statistical differences in mean stroke volume calculated from the reference free-breathing sequence (60.3 ± 27.3 mL/cycle), the standard breath-hold sequence (59.8 ± 27.6 mL/cycle) and the spiral breath-hold sequence (59.5 ± 27.1 mL/cycle). Bland-Altman analyses comparing the breath-hold sequences to the reference free-breathing sequence are shown in Figure 4.25.

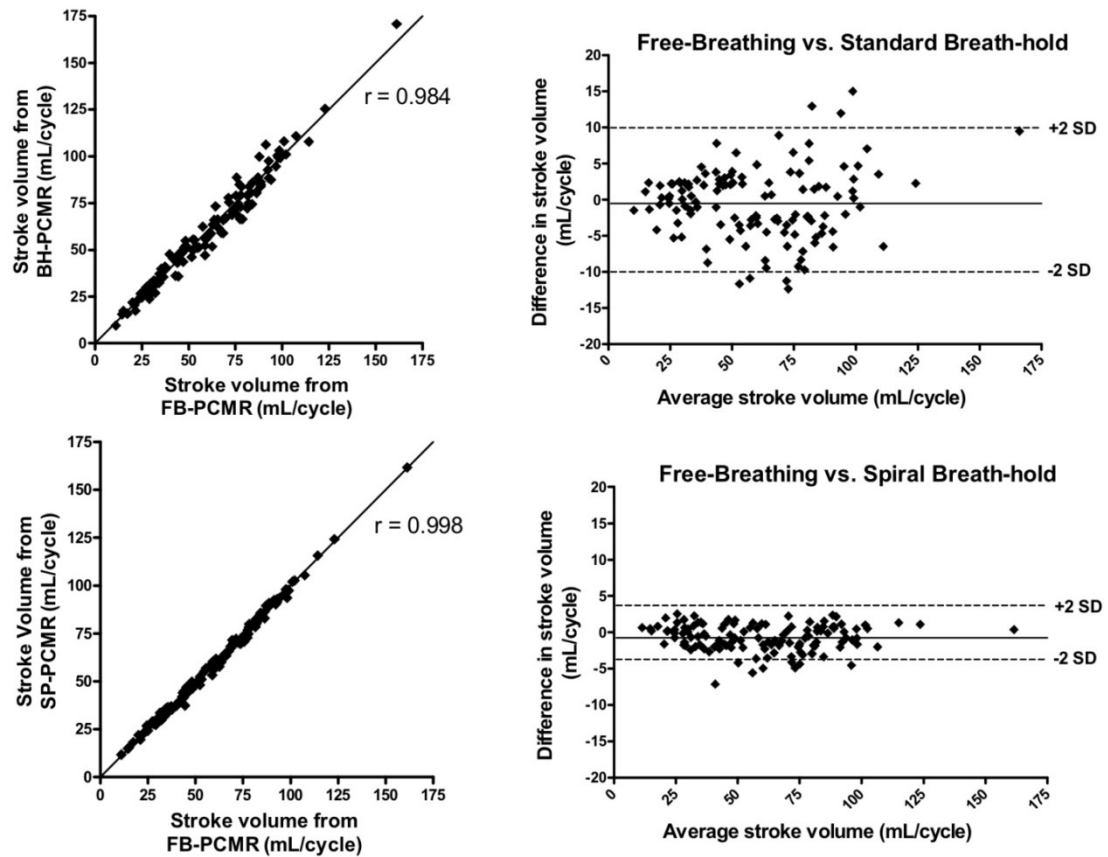


Figure 4.25: Comparisons of stroke volumes in all vessels between reference free-breathing PCMR (FB-PCMR) and standard breath-hold PCMR (BH-PCMR) (top), and between free-breathing PCMR and spiral breath-hold PCMR (SP-PCMR) (bottom). Scatter plots shown on the left and associated Bland-Altman analysis shown on the right

There was no clinically significant bias between the reference free-breathing sequence and either breath-hold sequence (spiral breath-hold: -0.7 mL/cycle, standard breath-hold: -0.5 mL/cycle). However, the limits of agreement were smaller and the correlation better for the spiral breath-hold sequence compared to the standard breath-hold sequence (-4.4 to 2.9 mL/cycle vs. -10.3 to 9.3 mL/cycle, $r = 0.984$ vs. $r = 0.998$, respectively).

Separate mean stroke volumes, Bland-Altman analysis and correlations for the AAO, MPA and branch pulmonary arteries are shown in Table 4.6 and Figure 4.26.

	Free- Breathing PCMR	Standard Breath-hold PCMR	Spiral Breath-hold PCMR
AORTA			
Stroke Volume (mL)	68.6 ± 19.6	67.3 ± 19.6	67.7 ± 19.9
Bias* (mL)	-	-1.3	-0.9
Limits of agreement* (mL)	-	-11.1 to 8.5	-4.6 to 2.8
Correlation coefficient* (r)	-	0.968	0.996
MPA			
Stroke Volume (mL)	76.6 ± 27.6	76.2 ± 29.1	75.9 ± 27.7
Bias* (mL)	-	-0.5	-0.8
Limits of agreement* (mL)	-	-13.1 to 12.1	-4.4 to 2.8
Correlation coefficient* (r)	-	0.976	0.998
PULMONARY BRANCHES			
Stroke Volume (mL)	39.5 ± 18.5	39.7 ± 19.2	38.9 ± 18.1
Bias* (mL)	-	0.2	-0.6
Limits of agreement* (mL)	-	-6.5 to 6.8	-4.2 to 3.1
Correlation coefficient* (r)	-	0.985	0.995

* Compared to free-breathing PCMR sequence

Table 4.6: Comparison of stroke volumes calculated from the three sequences

There were no statistically significant differences in stroke volumes calculated between any of the sequences. Bland-Altman analysis found only a small bias in stroke volume between the free-breathing and both the breath-hold sequences. For all vessels, the limits of agreement were smaller and the correlation was greater for spiral breath-hold acquisition, compared to the standard breath-hold acquisition.

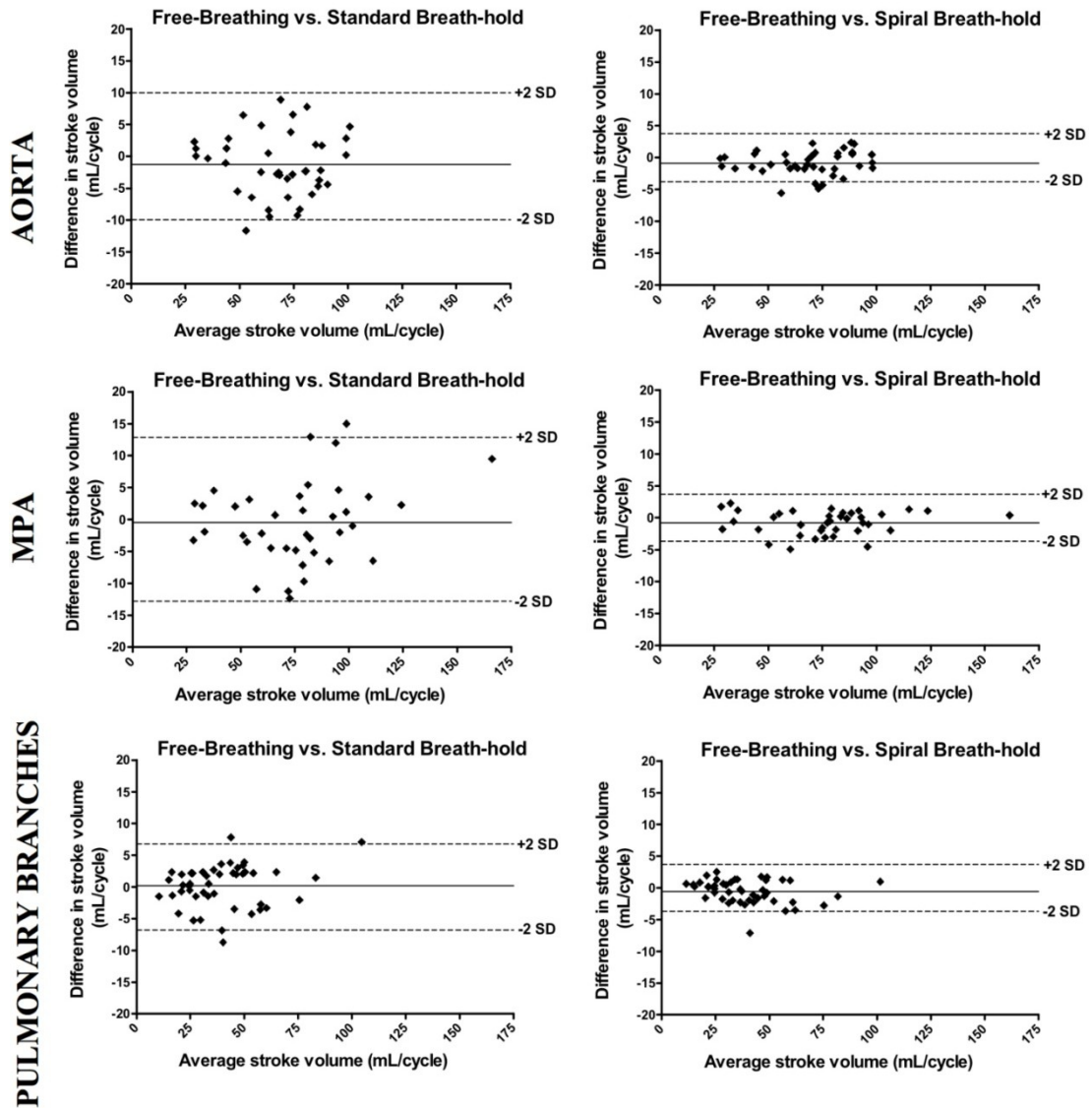


Figure 4.26: Bland-Altman analysis comparing stroke volumes in the aorta, MPA and pulmonary branches between reference free-breathing and standard breath-hold PCMR (left), and between free-breathing PCMR and spiral breath-hold PCMR (right)

Regurgitant flow was found in 40 vessels (see Table 4.7 and Figure 4.27). For free-breathing vs. standard breath-hold PCMR there was no significant difference in regurgitation. However, a small but statistically significant difference was found between the free-breathing and spiral breath-hold PCMR sequences. Despite this, the correlation coefficient was found to be higher and limits of agreement to be lower with the spiral breath-hold acquisition, compared to the standard breath-hold acquisition.

	Free- Breathing PCMR	Standard Breath-hold PCMR	Spiral Breath-hold PCMR
REGURGITATION (N=40)			
Regurgitation fraction (%)	31.1 ± 14.7	30.0 ± 15.0	29.1 ± 14.2 [†]
Range (%)	11.16 to 60.8	6.4 to 60.4	8.6 to 55.7
Bias* (%)	-	-1.1	-2.0
Limits of agreement* (%)	-	-8.2 to 5.9	-6.8 to 2.8
Correlation coefficient* (r)	-	0.971	0.986

* Compared to free-breathing PCMR sequence

[†] Value is significantly different from free-breathing PCMR ($p < 0.05$)

Table 4.7: Comparison of regurgitation fraction calculated from the three sequences

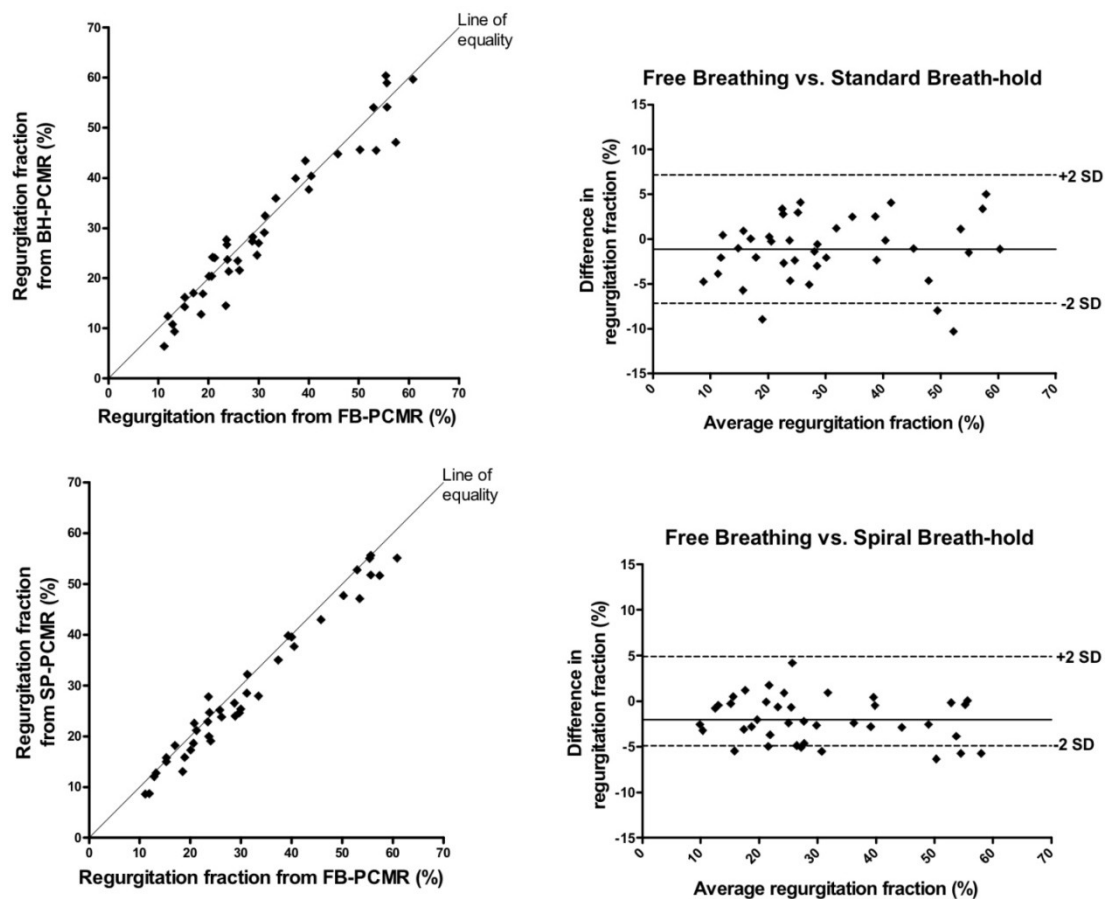


Figure 4.27: Comparisons of stroke volumes in all vessels between reference free-breathing PCMR (FB-PCMR) and standard breath-hold PCMR (BH-PCMR) (top), and between free-breathing PCMR and spiral breath-hold PCMR (SP-PCMR) (bottom). Scatter plots shown on the left and associated Bland-Altman analysis shown on the right

Q_P/Q_S and RPA/LPA ratios were calculated where possible (see Table 4.8, Figure 4.28 and Figure 4.29). No significant differences were found between any of the sequences. Bland-Altman analysis found a slightly lower bias, and smaller limits of agreement with the spiral breath-hold acquisition compared to the standard breath-hold acquisition.

	Free-Breathing PCMR	Standard Breath-hold PCMR	Spiral Breath-hold PCMR
Q_P/Q_S (N=38)			
Q_P/Q_S ratio	1.13 ± 0.29	1.15 ± 0.34	1.14 ± 0.30
Range	0.81 to 2.64	0.78 to 2.92	0.83 to 2.73
Bias*	-	0.018	0.006
Limits of agreement*	-	-0.23 to 0.27	-0.08 to 0.10
Correlation coefficient* (r)	-	0.933	0.989
RPA/LPA (N=20)			
RPA/LPA ratio	1.44 ± 0.59	1.42 ± 0.65	1.39 ± 0.53
Range	0.55 to 2.78	0.44 to 2.62	0.54 to 2.70
Bias*	-	-0.049	-0.050
Limits of agreement*	-	-0.32 to 0.21	-0.22 to 0.12
Correlation coefficient* (r)	-	0.973	0.991

* Compared to free-breathing PCMR sequence

Table 4.8: Comparison of Q_P/Q_S and RPA/LPA ratios calculated from the three sequences

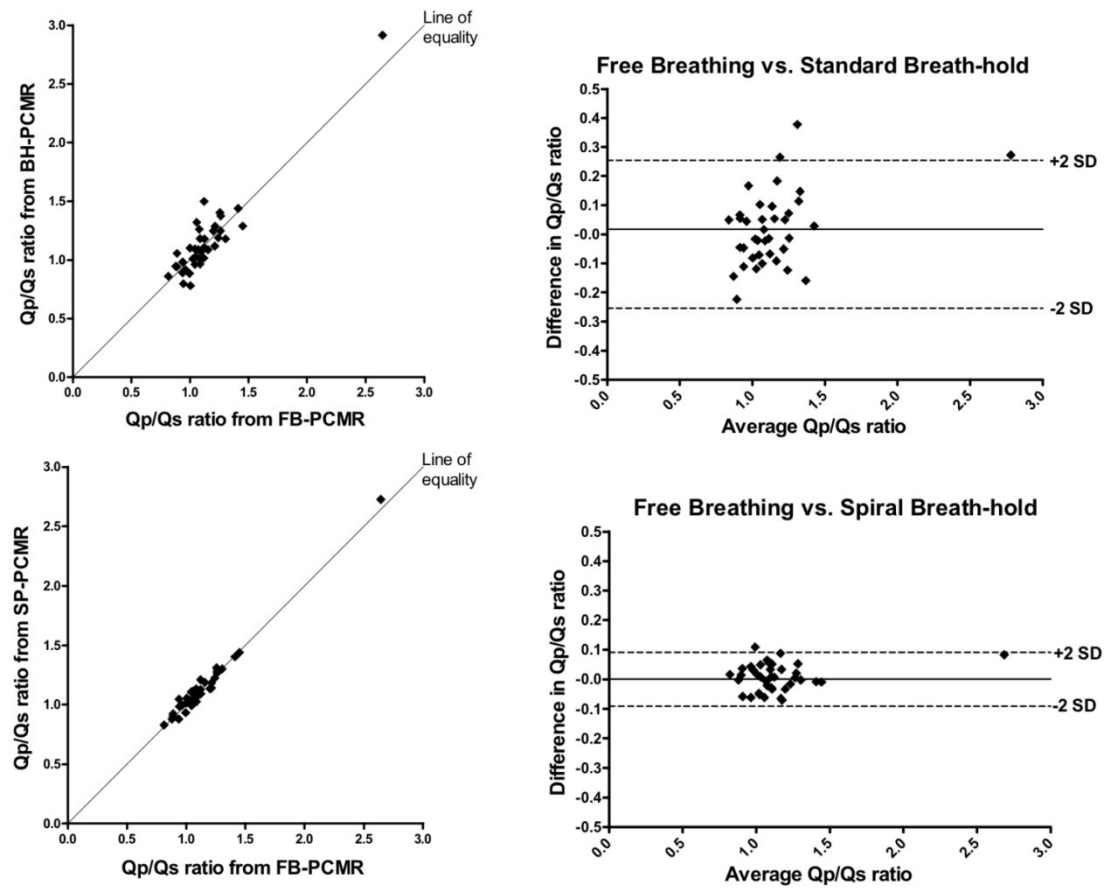


Figure 4.28: Comparisons of Q_p/Q_s ratio in all vessels between reference free-breathing PCMR (FB-PCMR) and standard breath-hold PCMR (BH-PCMR) (top), and between free-breathing PCMR and spiral breath-hold PCMR (SP-PCMR) (bottom). Scatter plots shown on the left and associated Bland-Altman analysis shown on the right

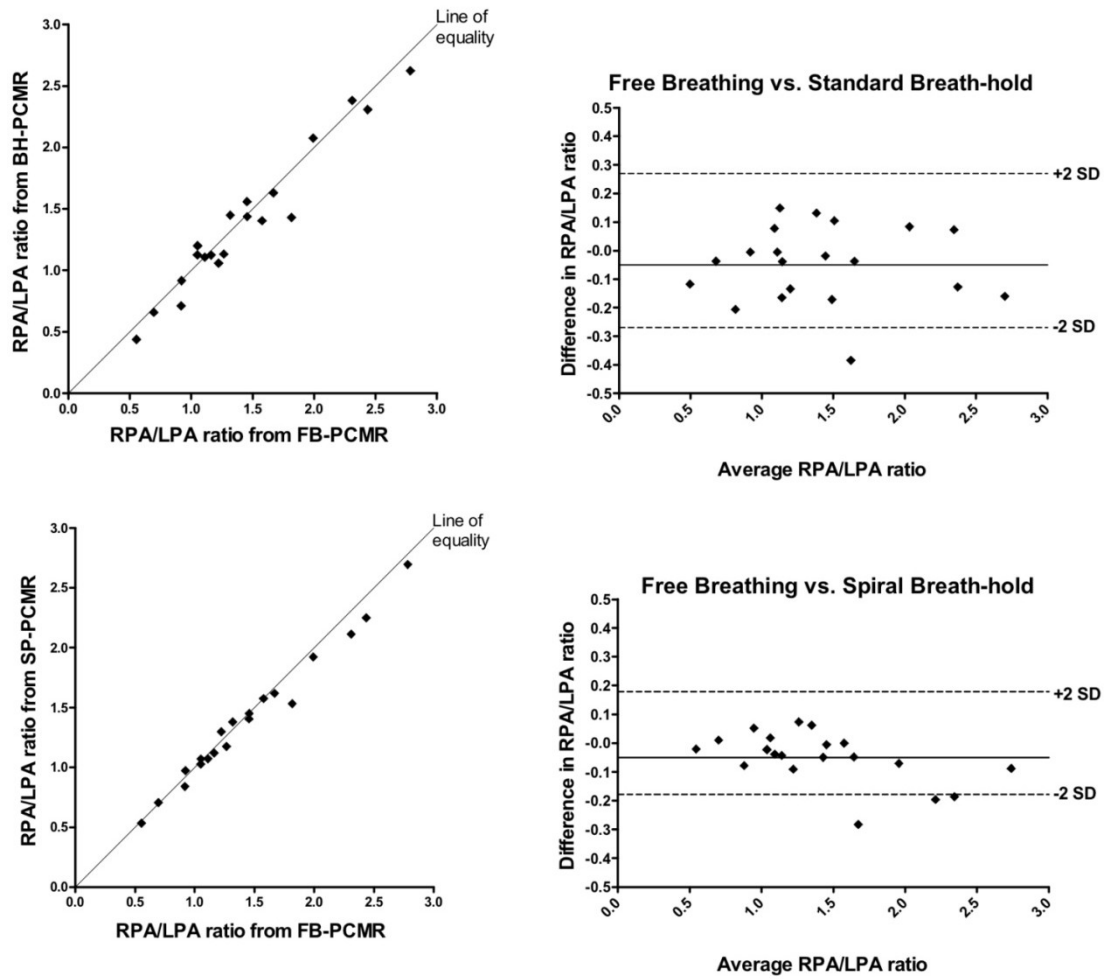


Figure 4.29: Comparisons of *RPA/LPA* ratio in all vessels between reference free-breathing PCMR (FB-PCMR) and standard breath-hold PCMR (BH-PCMR) (top), and between free-breathing PCMR and spiral breath-hold PCMR (SP-PCMR) (bottom). Scatter plots shown on the left and associated Bland-Altman analysis shown on the right.

For 10 randomly selected subjects, the AAO data from all three sequences was re-evaluated by the same observer (J.A.S.). The mean difference in stroke volumes from the free-breathing sequence was $0.5 \pm 1.2\%$ (range: -1.1 to 2.9 %, $p = 0.25$), for the standard breath-hold sequence was $0.9 \pm 2.4\%$ (range: -3.6 to 5.6 %, $p = 0.20$) and for the spiral breath-hold was $-0.3 \pm 1.2\%$ (range: -2.6 to 1.6 %, $p = 0.22$), as seen in Figure 4.30. There were no statistically significant differences between the repeated measures for any of the sequences.

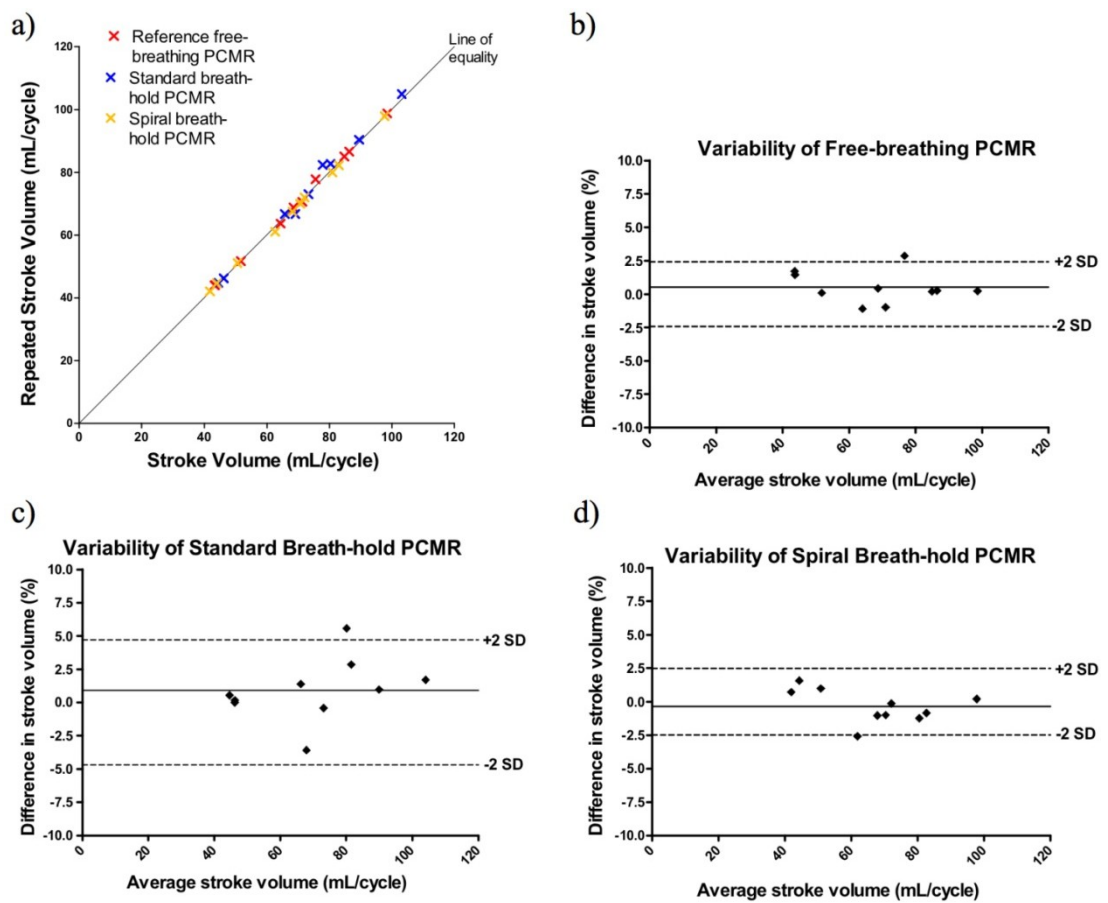


Figure 4.30: Comparisons of intra-observer variability between the three sequences. a) Scatter plot for all three sequences, as well as Bland-Altman analysis for b) reference free-breathing sequence, c) standard breath-hold sequence, and d) spiral breath-hold sequence

These 10 AAO data sets were also independently reviewed by a second observer (V.M.), to assess inter-observer variability. The mean difference in stroke volumes from the free-breathing sequence was $0.1 \pm 1.5\%$ (range: -2.5 to 3.4 %, $p = 0.75$), for the standard breath-hold sequence was $0.7 \pm 2.3\%$ (range: -3.9 to 3.6 %, $p = 0.40$) and for the spiral breath-hold was $-0.5 \pm 1.5\%$ (range: -2.7 to 2.5 %, $p = 0.21$), as seen in Figure 4.31. There were no statistically significant differences between the repeated measures for any of the sequences.

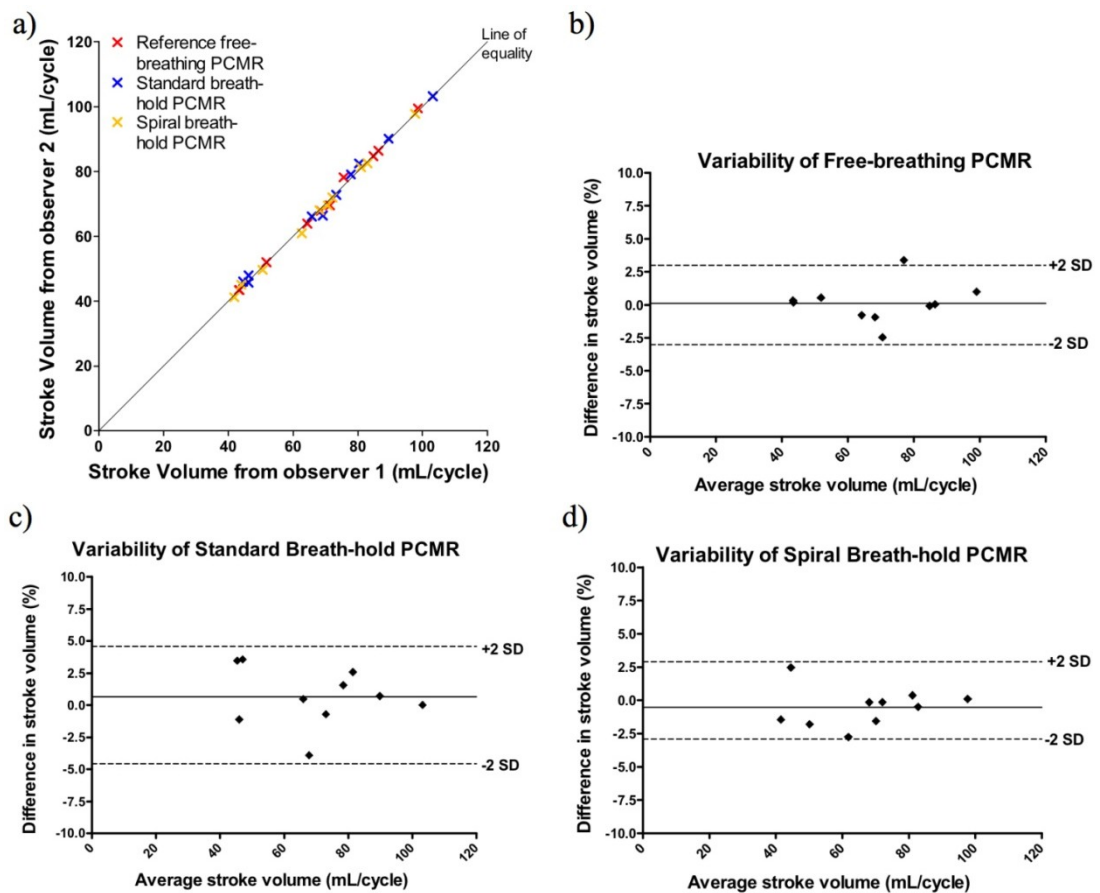


Figure 4.31: Comparisons of inter-observer variability between the three sequences. a) Scatter plot for all three sequences, as well as Bland-Altman analysis for b) reference free-breathing sequence, c) standard breath-hold sequence, and d) spiral breath-hold sequence

4.8 Image Quality

Image quality was assessed for all three sequences using measures of SNR, VNR and edge sharpness, as described in section 4.3.5 and 4.3.6. Figure 4.32 shows examples of the image quality from all three tested sequences in the AAO, MPA, RPA and LPA. Quantitative image quality metrics can be seen in Table 4.9;

	Free- Breathing PCMR	Standard Breath-hold PCMR	Spiral Breath-hold PCMR
Estimated signal variation: σ_S	5.4 ± 1.4	$5.9 \pm 1.5^\dagger$	$8.6 \pm 2.2^{\dagger\ddagger}$
$\sigma_S / \sigma_{S \text{ Free-breathing}}$	-	1.1 ± 0.3	1.7 ± 0.6
Estimated SNR	45.6 ± 14.9	$41.7 \pm 14.2^\dagger$	$31.9 \pm 11.6^{\dagger\ddagger}$
Estimated velocity variation: σ_V (cm/s)	17.6 ± 9.1	$19.5 \pm 10.5^\dagger$	$19.7 \pm 7.7^\dagger$
$\sigma_V / \sigma_{V \text{ Free-breathing}}$	-	1.1 ± 0.4	1.2 ± 0.4
Estimated VNR	8.4 ± 4.8	$7.4 \pm 3.9^\dagger$	$6.7 \pm 3.1^{\dagger\ddagger}$
Edge Sharpness (mm^{-1})	0.78 ± 0.36	0.74 ± 0.34	0.78 ± 0.35

[†] Value is significantly different from free-breathing PCMR ($p < 0.05$)

[‡] Value is significantly different from standard breath-hold PCMR ($p < 0.05$)

Table 4.9: Image Quality - estimated SNR, VNR and edge sharpness measures for all sequences

The free-breathing PCMR images had the highest estimated SNR and VNR compared to both of the breath-hold PCMR sequences ($p < 0.05$). The spiral breath-hold PCMR images had the lowest estimated SNR and VNR compared to the free-breathing and standard breath-hold PCMR images ($p < 0.05$).

Edge sharpness was not significantly different between any of the sequences (Table 4.9). However, the free-breathing PCMR images and the spiral breath-hold PCMR images had the same average edge sharpness, whereas the edge sharpness was slightly lower in the standard breath-hold PCMR images.

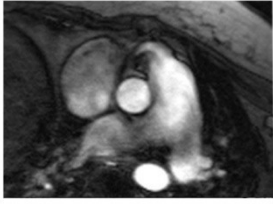
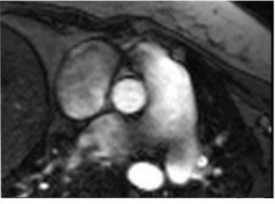

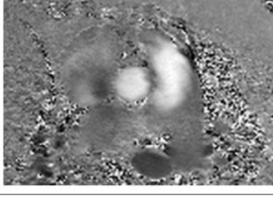
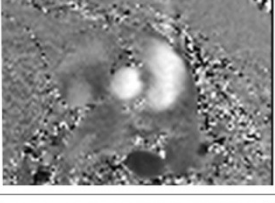
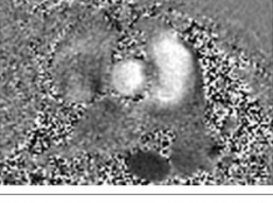
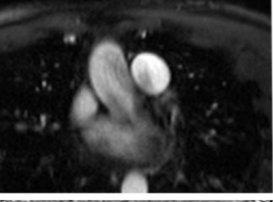
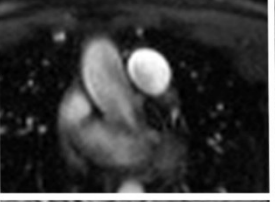
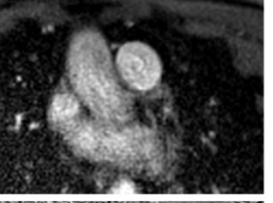
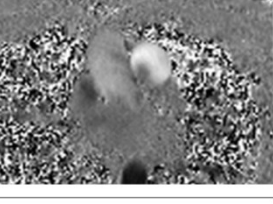
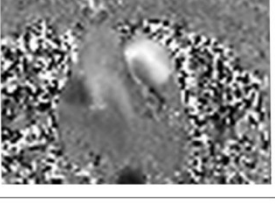
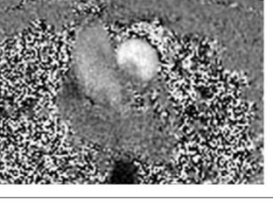
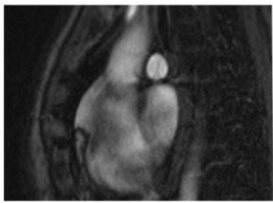
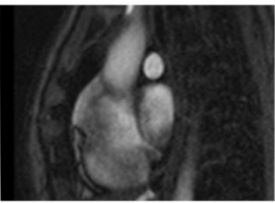
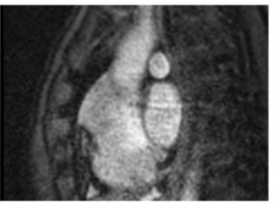
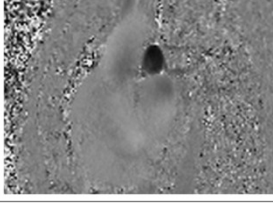
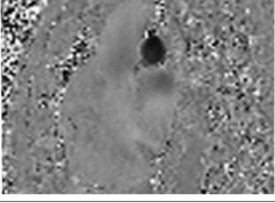
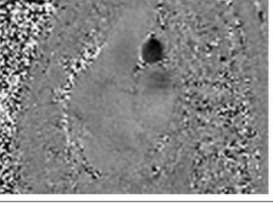
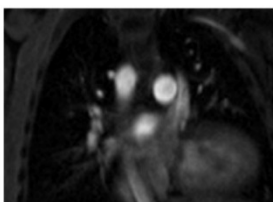
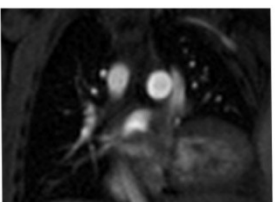
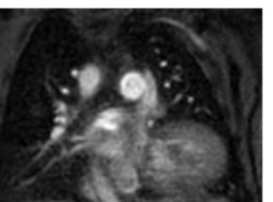
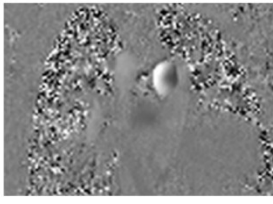
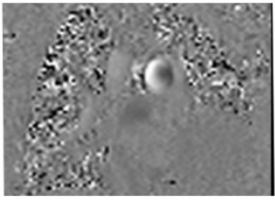
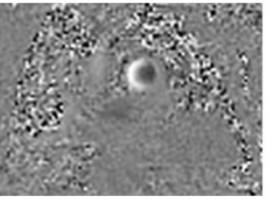
	Free-Breathing PCMR	Standard Breath-hold PCMR	Spiral Breath-hold PCMR
AAO Magnitude			
AAO Phase			
MPA Magnitude			
MPA Phase			
RPA Magnitude			
RPA Phase			
LPA Magnitude			
LPA Phase			

Figure 4.32: Examples of image quality from the three sequences

4.9 Discussion

We have demonstrated that it is possible to use a prospectively-triggered, undersampled spiral PCMR sequence with a SENSE reconstruction algorithm to accurately and reliably measure flow within a short breath-hold (3-8 seconds). Currently the reference standard method of measuring flow in patients with congenital heart disease is high spatio-temporal resolution, free-breathing, cardiac gated PCMR. Unfortunately, due to multiple signal averaging, each flow assessment can take more than 2 minutes to perform. Thus in congenital cardiac MR, where between 4 and 8 separate flow assessments are necessary, flow imaging can take a significant proportion of the total scan time. The spiral breath-hold sequence used in this study should be able to reduce the total duration of flow imaging from an average of 10 minutes, to less than 1 minute. This would lead to a marked reduction in total scan time and has implications for patient throughput and compliance for congenital cardiac MR scanning.

4.9.1 Spiral SENSE PCMR

Achieving high spatio-temporal resolution PCMR in a short breath-hold requires efficient filling of k-space. In this study, spiral trajectories were used to significantly speed up acquisition time. Imaging was further accelerated with non-Cartesian SENSE. The resultant sequence had a breath-hold time of ~5 seconds, compared to ~16 seconds for a standard Cartesian breath-hold PCMR sequence. Furthermore, unlike the standard breath-hold sequence, spatio-temporal resolution was not compromised in order to achieve the short breath-hold. This makes this spiral sequence extremely useful in both children and sick adults who are unable to perform long breath-holds (as demonstrated in Figure 4.23). There are some disadvantages to spiral trajectories and parallel imaging, including off resonance effects and trajectory errors, as well as reduced signal-to-noise. However, these were not seen to affect the accuracy of the spiral PCMR sequence in this study.

4.9.2 Comparison of sequences

For stroke volumes, Q_P/Q_S and RPA/LPA ratios, there was an excellent agreement between the spiral breath-hold sequence and the reference free-breathing sequence. Furthermore, the spiral breath-hold sequence was found to be superior to the standard breath-hold sequence in terms of limits of agreement and correlation. This is most likely to be due to the higher temporal and spatial resolution of the spiral breath-hold sequence. It may also be attributed to the shorter breath-hold times, which may prevent residual breathing, as well as limiting heart rate variability during the scan. In addition the intra-observer and inter-observer variability seen in the spiral breath-hold PCMR sequence was good.

There was however, a small, but statistically significant difference in the regurgitation fractions calculated from the free-breathing PCMR sequence and the spiral breath-hold sequence. This was probably due to the interpolation of the flow curve at the very end of diastole in the prospectively-triggered spiral sequence. However, it should be noted that the difference in regurgitant fraction was on average only 2 % and this would not be considered clinically important.

4.9.3 Image quality

The edge sharpness of the spiral breath-hold sequence was found to be similar to the free-breathing sequence, and higher than the standard breath-hold sequence. This is most likely due to the lower spatial resolution of the standard breath-hold PCMR sequence. The good edge sharpness of the spiral breath-hold sequence may have benefits in terms of either manual or automatic segmentation of the vessels compared to standard breath-hold sequences. However, the spiral breath-hold sequence had a lower estimated SNR and VNR than the free-breathing and standard breath-hold sequences. This is due to:

- i) Higher acceleration factor used compared to the other two sequences
- ii) Much higher bandwidth used compared to the other two sequences
- iii) No signal averages (unlike the free-breathing PCMR sequence)
- iv) Higher spatial resolution compared to the standard breath-hold sequence

4.9.4 Limitations

The main limitation of using an undersampled spiral trajectory is the need for a large FOV, in order to prevent wrapping of signal and ensure accurate reconstruction of the undersampled data. As we do not use a selective excitation, it is necessary for the FOV to be larger than the object being scanned. In the future, the FOV could be reduced by the use of improved coil configurations, or RF-shielding of the arms and torso (see section 5.2.1). Additionally, a spatially-selective RF-pulse, or saturation bands could be used, however these would increase the scan time, or reduce the temporal resolution (see section 5.2.1).

As seen from the image quality analysis, the spiral breath-hold PCMR sequence has a significantly lower SNR and VNR than the standard breath-hold PCMR sequence, or the free-breathing sequence. Although this is a limitation of the sequence it did not affect the accuracy of the stroke volume measurements made in this study.

4.9.5 Conclusion

Currently, MR flow assessment can take more than 10 minutes in patients with congenital heart disease. Thus it often represents almost 25 % of total scan time. Using the spiral breath-hold sequence validated in this study, all flow imaging could be performed in less than 1 minute. This would significantly reduce total scan time without compromising the accuracy of the flow assessment. The benefits of this would be twofold. Firstly, in the paediatric population a shorter total scan time would be less demanding on the patients and improve compliance. Secondly, shorter scan times should improve patient throughput. Therefore, we believe that this sequence has significant benefits in congenital CMR.

CHAPTER 5

Conclusions and Future Work

5.1 Summary

The present work has focussed on the development of fast and accurate methods of measuring blood flow, using undersampled spiral SENSE PCMR.

Chapter 2 presented a real-time spiral PCMR sequence, which was used to measure flow during the continuation of exercise, using an up-down ergometer. The flow data was combined with simultaneous blood pressure measurements to allow quantification of vascular resistance and compliance during exercise, in a population of 20 healthy volunteers. This technique was shown to successfully measure the hemodynamic response to exercise using MRI for the first time.

The sequence presented in chapter 2 was able to achieve a high temporal resolution of 40.4 ms, however the low spatial resolution (of 3.9x3.9 mm) means that this sequence is not suitable for quantification of flow volumes in small vessels or in children. To achieve higher spatial resolution imaging, during free-breathing, chapter 3 presented a split-acquisition PCMR technique. In this study the acquisition of flow-compensated and flow-encoded data was split into short blocks. By comparing magnitude images, the closest flow-compensated frame in the cardio-respiratory cycle was determined for each flow-encoded frame, allowing higher temporal or spatial resolution compared to conventional interleaved real-time PCMR. This technique was shown to be accurate in a population of 15 healthy adults, and 5 adult patients. Additionally, in 6 paediatric patients it was found that this split-acquisition sequence was more accurate than conventional interleaved real-time PCMR, due to the higher spatial resolution achieved.

Although the split-acquisition PCMR sequence (presented in chapter 3) was able to achieve a higher spatial resolution than the real-time PCMR sequence (presented in chapter 2), the resolution was still inferior to that desired clinically in patients with congenital heart disease. Chapter 4 therefore presented a high spatio-temporal resolution, prospectively triggered (interleaved) PCMR sequence. This sequence was demonstrated to accurately and reliably measure flow within a short breath-hold, in a population of 40 patients with congenital heart disease. This sequence allowed

comparable resolution to the clinical reference free-breathing, Cartesian PCMR sequence, however in ~ 5 seconds compared to ~ 90 seconds. The prospectively triggered spiral breath-hold sequence was shown to be accurate in terms of stroke volumes, Q_P/Q_S and RPA/LPA ratios. A small, but statistically significance difference was found in terms of regurgitation fraction calculated from the sequence, although this was not clinically significant. This sequence is now being widely used at ICH, leading to a marked reduction in total scan time. This has implications for patient throughput and compliance for congenital cardiac MR scanning.

5.2 Future Work

The studies described in this work all use undersampled spiral trajectories, with an iterative conjugate gradient SENSE algorithm. In all of these studies the main limitations were:

- The use of a large FOV, which was necessary to prevent wrapping of signal and ensure accurate reconstruction of the undersampled spiral data
- Long reconstruction times, due to the complex, iterative conjugate gradient algorithm used

Thus, future work could be directed towards addressing these limitations.

Additionally, future developments related to the studies described in this work include:

- 4D flow measurements
- Fourier velocity encoding (FVE)
- Fourier acceleration encoding (FAE)

5.2.1 Reducing the FOV

In the studies described in this work, the FOV was always > 400 mm in adults (and > 350 mm in children). This was necessary to ensure that the arms of the subjects were included in the FOV, therefore preventing ambiguity between aliasing caused by undersampling of data and aliasing caused by wrapping of signal.

The FOV could be reduced by the use of:

- Improved coil configurations
- RF-shielding of the arms and torso
- Spatially-selective RF-pulses
- Saturation bands

5.2.1.1 Improved Coil Configurations

Improved coil configurations may allow a reduction in the FOV, as smaller coils cannot ‘see’ as far as large coils (133). Therefore it is possible that by using specialist coils containing an array of smaller coils, the arms will not be ‘seen’ by the coils allowing a reduction in the FOV. The use of more coil elements may also improve the parallel imaging reconstruction algorithm or may allow higher acceleration factors to be achieved. However, the use of more coil elements would increase the reconstruction time.

5.2.1.2 RF-Shielding

RF-shielding of the arms and torso offers a very simple way to reduce the FOV. RF shields work by absorbing the RF signal, so that spins within the shield are not excited. *Accusorb* (134) offer advanced flexible RF absorbers, which are shaped to fit around the arms and torso, as seen in Figure 5.1;



Figure 5.1: From (134). Accusorb shields for the arms (left) and the torso (right)

We have carried out some preliminary experiments with these *Accusorb* RF shields over the arms of the subject. For the exercise study described in chapter 2, the shields allowed a reduction in FOV from 500 mm to 400 mm in adult subjects. This allowed an increase in the spatial resolution (from 3.9×3.9 mm to 3.1×3.1 mm), as well as greatly improving the image quality, as seen in Figure 5.2.

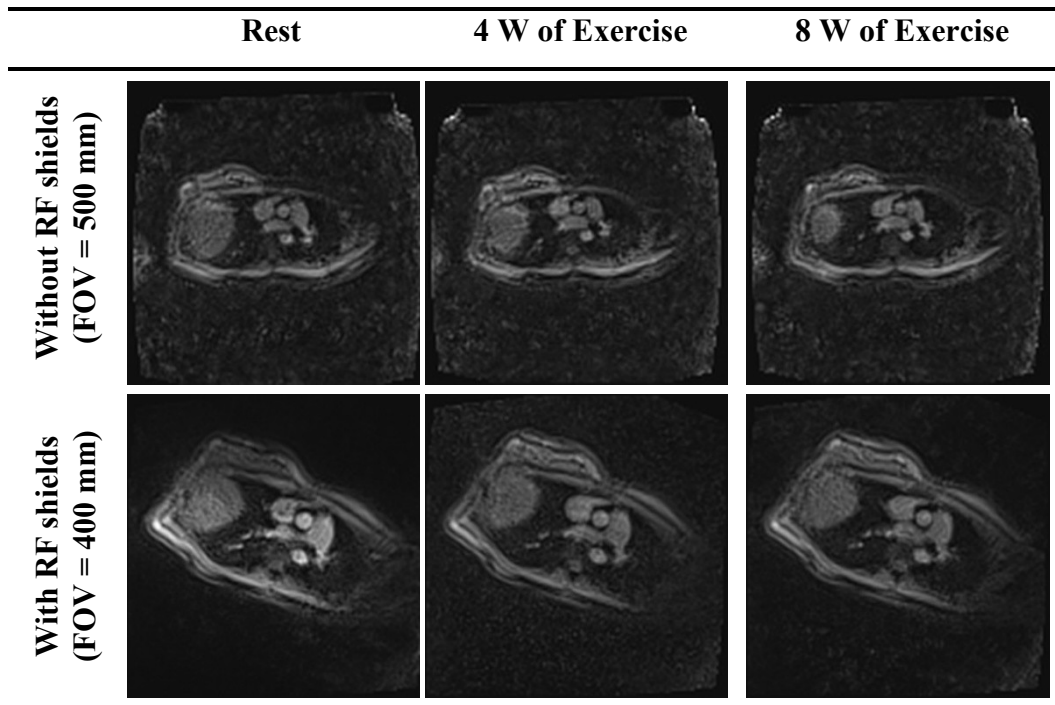


Figure 5.2: Effect of *Accusorb* RF arm shields in the same subject, from the real-time PCMR sequence described in chapter 2, at rest and during exercise

5.2.1.3 Spatially-selective RF-pulses

Spatially-selective RF-pulses could be used to only excite the tissue around the vessel of interest, allow significant reductions in the FOV. 2D spatially-selective RF-pulses are achieved by playing out appropriate gradients on two independent gradient axes, simultaneously with the RF waveform (135). Often the gradient waveforms used resemble the time-reversed spiral trajectories, described in this work.

Additionally, a spectral-spatial RF-pulse could be used (136), which would excite magnetization in a specified location and with a specified spectral content. This would allow one chemical species (e.g. water) to be excited, while leaving others virtually unaffected (e.g. lipids). This may be advantageous in spiral imaging due to the sensitivity of spiral trajectories to off-resonance effects. The biggest disadvantage of using selective RF-pulses is their long duration, which would conversely decrease the temporal resolution. For example, the study by Nayak, et al. (64) described in section 2.2.1.1 used a water-selective spectral-spatial excitation pulse which had a duration of 7 ms, compared to the non-selective RF-pulse with duration 600 μ s used in this work.

5.2.1.4 Saturation bands

Saturation bands could also be used to reduce the FOV by attenuating signal from spins outside the FOV. Saturation bands are created by applying 90° spatially selective RF-pulses over the desired area(s), prior to the excitation pulse (137). These saturation pulses are followed by large dephasing gradients to create maximal phase dispersion across the saturated band. This results in minimal transverse magnetization in the saturation band during the subsequent readout, allowing a smaller FOV to be imaged without wrap. Saturation pulses are typically played out in every TR. Like selective RF-pulses, the use of saturation bands would decrease the resultant temporal resolution.

5.2.2 Speeding up the Reconstruction

The largest limitation found in all of the studies described in this work, were the long reconstruction times. These long reconstruction times mean that although the data is acquired rapidly, the user had to wait before the images could be viewed (~5 minutes in chapters 2 and 3, and ~30 seconds in chapter 4). This greatly limits the use of these sequences, as it is not clinically feasible to wait more than a few seconds for the images to reconstruct. Reconstruction times could be improved by the use of newer multi-processor graphics cards, which are well suited to complex iterative reconstructions.

Previous studies have shown the use of graphics cards (GPU's) for the speedup of complex reconstruction algorithms. Hansen, et al. (120) used a GPU to perform fast Cartesian SENSE and k-t SENSE reconstructions. The SENSE inversion step was shown to be up to 146 times faster on a GPU compared to a CPU. However, the total speedup achieved between a CPU reconstruction and a GPU reconstruction was in the order of 20.

Sørensen, et al. (100) have shown the use of GPU's for non-equispaced fast Fourier transform (NFFT). In this paper the NFFT was used for reconstruction of radial and spiral MRI data. For the NFFT algorithm the GPU implementation was found to be up to 85 times faster than a CPU implementation. However, the overall speedup in reconstruction time was in the order of 20.

Additionally, Sørensen, et al. have shown the use of GPUs for the reconstruction of real-time radial SENSE data in cardiac imaging, and real-time radial k-t SENSE data in speech imaging (138). The GPU NFFT gridding was found to be accurate compared to a CPU based NDFT (non-equispaced discrete Fourier transform): mean error; 0.0024 vs. 0.0022, respectively. The overall acceleration factor achieved using the GPU implementation was between 10-12, compared to the CPU reconstruction.

If an overall speed-up between 10-fold and 20-fold could be achieved for the studies described in this work, the reconstruction times for chapters 2 and 3 could be reduced from 5 minutes to ~15-30 seconds. This would make these techniques clinically useable.

At ICH, Grzegorz Kowalik has already developed a fully integrated platform within the MRI environment, to send raw data to a networked GPU. The complex reconstruction of MR data can be performed on the GPU and fed back to the scanner. At the moment this is used for T2 IDEAL (iterative decomposition of water and fat with echo asymmetry and least-squares estimation) (139), however we hope that in the near future an iterative CG SENSE algorithm can be implemented for a GPU reconstruction of undersampled spiral data.

5.2.3 4D Flow Measurements

Time-resolved 3D PCMR imaging using three-directional velocity encoding (known as *4D PCMR*), allows quantification of flow in any imaging plane, in addition to the visualization of complex flow patterns (140). However, 4D PCMR is rarely used in the clinical setting due to long acquisition times (141). As we have shown in this work, the use of efficient trajectories in addition to parallel imaging can greatly reduce the scan times in 2D PCMR. It may be possible to use efficient spiral trajectories, along with parallel imaging to greatly reduce the acquisition times for 4D PCMR.

Preliminary work has been carried out to develop a 4D PCMR sequence from the prospectively triggered spiral sequence described in chapter 4. A 3D volume is imaged using a slab-selective RF-excitation (to limit wrap in the z -direction) and an additional phase encode gradient is used on the z -axis to encode slice information (see Figure 5.3). The x and y gradients remain the same as described previously. Additionally, in each cardiac phase a flow-compensated readout plus the three flow-encoded readouts (one for each direction) were repeatedly acquired, as seen in Figure 5.3;

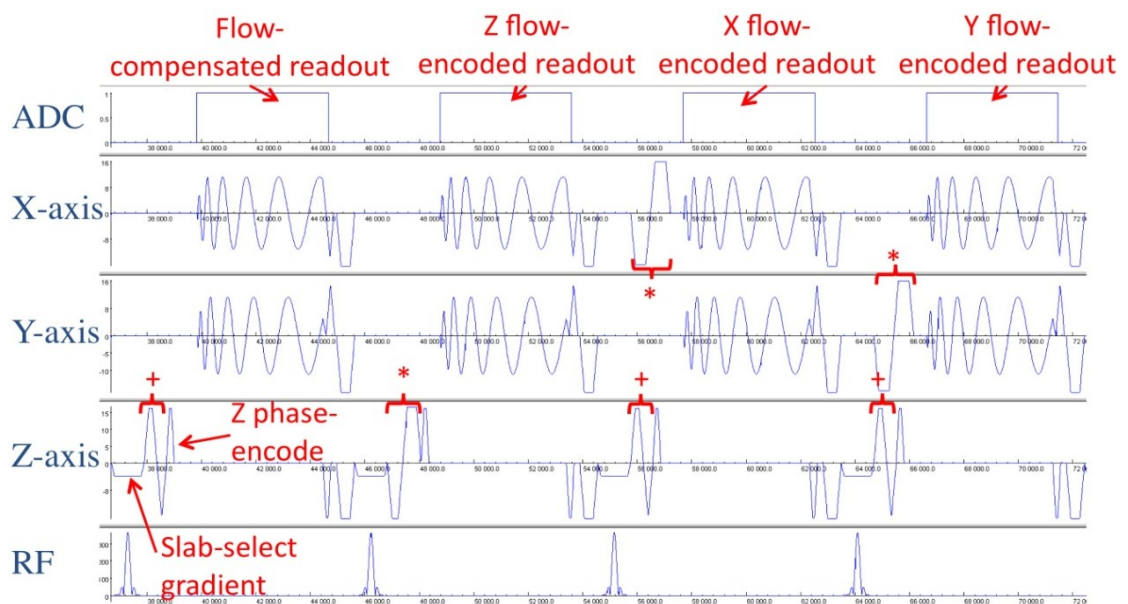


Figure 5.3: Sequence diagram for spiral 4D PCMR sequence. + indicates flow-compensated gradients, * indicates flow-encoding gradients

The sequence parameters used in these preliminary experiments were;

Sequence Parameters	
TE/TR	2.6/9.85 ms
Spiral interleaves	16
SENSE	4
Flip angle	25°
FOV	500×500×180 mm
Matrix	192×192
VENC	180 cm/sec
Temporal resolution	39.4 ms (~25 frames/sec)
Spatial resolution	2.6×2.6×5 mm

Table 5.1: Sequence parameters used for 4D PCMR sequence

Imaging was performed in the transverse plane, with 36, 5 mm thick slices. Two body coils and 2 spine coils were used (giving a total of 12 elements). Data was acquired during free-breathing, with 2 signal averages to reduce respiratory motion. In total data was acquired over 288 RR-intervals, giving a scan time of ~4 minutes.

The sampling pattern was rotated for each cardiac phase so that four consecutive cardiac phases comprised a fully-sampled k-space with 16 spiral readouts. The undersampled data was reconstructed online using an iterative SENSE algorithm (with a 3D reconstruction kernel). Coil sensitivity information was calculated for each slice, from the time-average of each coil (over all flow-compensated phases), divided by the sum-of-squares of the time-averaged coil data (for the respective slice). The reconstruction time was ~20 minutes.

There was a good agreement in stroke volumes measured in the descending Aorta between the 4D PCMR sequence and a standard 2D PCMR sequence, (51.5 ml/cycle vs. 53.2 ml/cycle), as seen in Figure 5.4.

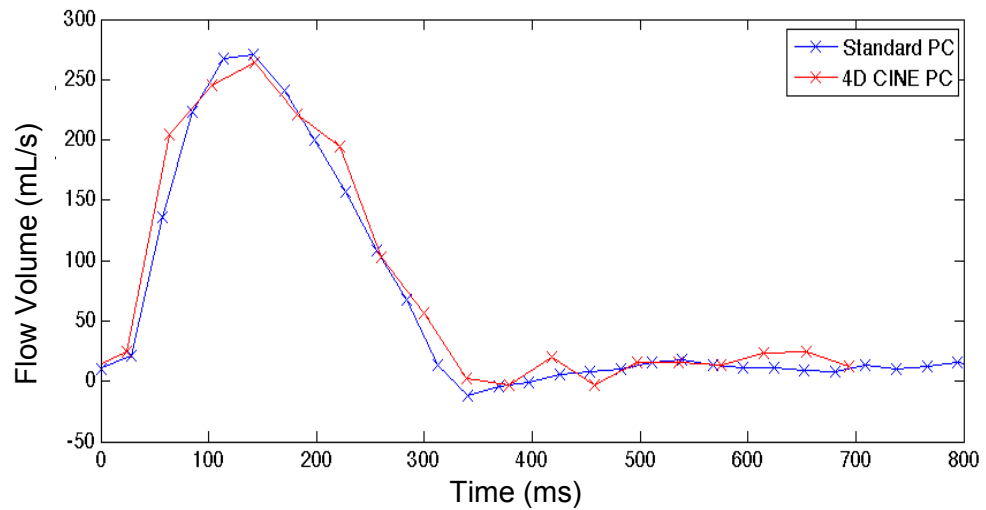


Figure 5.4: Comparison of flow profiles between standard PCMR and the 4D CINE PCMR sequence

Particle tracking was also performed in MATLAB, as shown in Figure 5.5;

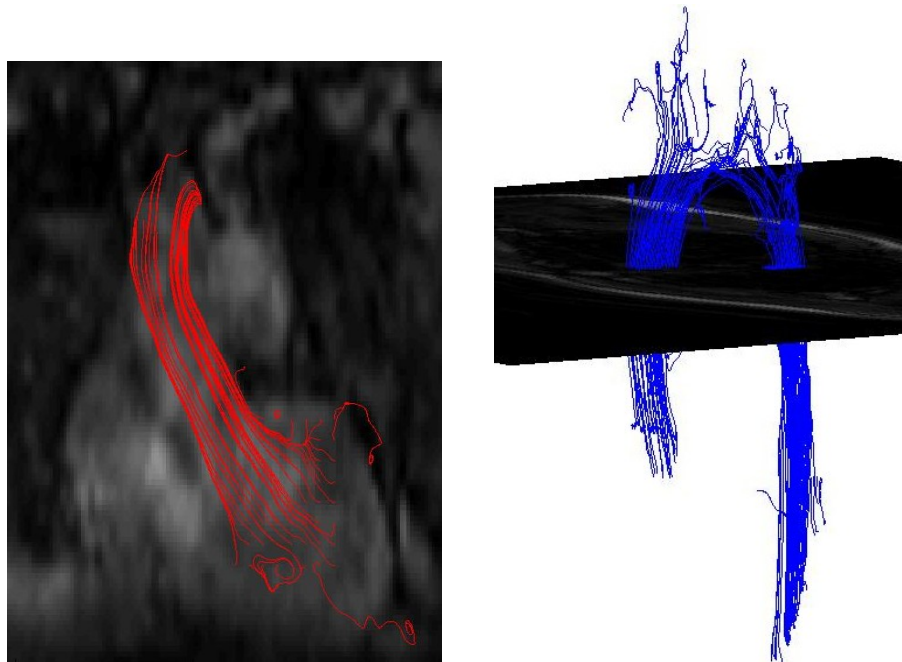


Figure 5.5: Streamlines from the 4D PCMR sequence performed in MATLAB. a) Streamlines seeded in the left ventricle, showing path through aorta, b) Streamlines seeded in the ascending and descending aorta, showing the aortic arch

By combining spiral readouts with 2D SENSE we were able to achieve high spatio-temporal resolution 4D PCMR, within a reasonable scan time. In this initial work no respiratory gating was used, nevertheless flow volumes and streamlines appear valid.

Further work is ongoing to implement respiratory navigation. Additionally acceleration in the slice direction may allow isotropic spatial resolution to be achieved without increasing the scan time.

5.2.4 Fourier Velocity Encoding and Fourier Acceleration Encoding

Standard PCMR averages blood velocity within each pixel and therefore tends to underestimate peak velocities. An alternative MR approach is Fourier Velocity Encoding (FVE), which acquires multiple phase contrast data sets with different velocity sensitivities. From this, a velocity spectrum and peak blood velocity can be reconstructed for each image pixel (39, 142, 143). Unfortunately FVE is not commonly used due to long acquisition times. With the use of undersampled spiral trajectories it may be possible to reduce the acquisition times of FVE, making this technique clinically useful.

Peak velocities measured using FVE could be used to calculate pressure using the modified Bernoulli equation (144). Measuring blood pressure gradients is vital in the evaluation of patients with valvular heart disease and vessel stenosis. These diseases are becoming more common as the population ages, with > 50% of over 75 year olds having valvular heart disease.

The ‘gold standard’ method of measuring pressure gradients is invasive catheterization, however this is not practical as part of routine clinical management. Normally Doppler ultrasound measurements are used to calculate peak velocities however Doppler is limited by the restricted viewing angles and the penetration depth. Quantification of velocities using MRI is free from the restrictions of ultra-sound. Thus FVE MRI may represent a more robust, non-invasive method of measuring pressure drops.

Although FVE provides accurate measures of peak velocity, calculation of pressure gradients is still susceptible to the significant assumptions of the Bernoulli equation. A better approach would be to measure blood acceleration and use it as an input to the Navier-Stokes equation for the calculation of pressures (145). Acceleration could be computed from temporal and spatial derivatives of velocity, but this is subject to noise and requires multiple velocity measures for finite differencing (146).

A more accurate pressure calculation could be obtained from direct measures of acceleration, which is possible with MRI by using an extension of the phase contrast method (147). However, similar to phase contrast velocity MRI, this method would only provide average blood acceleration within each pixel. To measure peak acceleration, Fourier Acceleration Encoding (FAE) may be used (148), where multiple data sets with different acceleration encodings are acquired (146, 149).

To provide accurate pressure calculations from MRI data, future work may include:

- The development of a FVE sequence (with ~ 16 velocity sensitivities)
- The development of acceleration encoded PCMR sequence
- The development of a FAE sequence (with ~ 16 acceleration sensitivities)

To make these sequences clinically useful the acquisition times must be relatively short. This could be achieved using undersampled spiral trajectories, as described in this work. Validation of these sequences would be carried out in-vitro and in-vivo. Additionally the accuracy of pressure calculations from PCMR, FVE, acceleration PCMR, FAE and Doppler could be compared to invasive catheter manometers.

5.3 Conclusion

This thesis has investigated the use of novel acquisition strategies and reconstruction algorithms for PCMR. These studies have provided benefits to the research and clinical environment. For example, the real-time sequence in chapter 2 provides a novel method of researching the hemodynamic response to physical and mental stress using MRI. Additionally this real-time sequence can be used in the clinical environment in subjects with irregular heart-beats where conventional gated sequences fail.

The prospectively triggered sequence described in chapter 4 has had the largest clinical impact, providing high spatio-temporal resolution PCMR imaging in a short breath-hold. This allows a significant reduction in total scan time, improving patient compliance and increasing throughput. It is hoped that future work could continue to bring additional benefits to the clinical environment.

References

1. F. Bloch, Nuclear induction. *Physical review*, 1946. **70**(7-8): p. 460.
2. E.M. Purcell, H.C. Torrey, and R.V. Pound, Resonance Absorption by Nuclear Magnetic Moments in a Solid. *Physical review*, 1946. **69**(1-2): p. 37.
3. P.C. Lauterbur, Image Formation by Induced Local Interactions: Examples Employing Nuclear Magnetic Resonance. *Nature*, 1973. **242**(5394): p. 190.
4. K.T. Block and J. Frahm, Spiral imaging: A critical appraisal. *Journal of Magnetic Resonance Imaging*, 2005. **21**(6): p. 657.
5. G.H. Glover, Simple analytic spiral K-space algorithm. *Magnetic Resonance in Medicine*, 1999. **42**(2): p. 412.
6. C.H. Meyer, B.S. Hu, D.G. Nishimura, and A. Macovski, Fast Spiral Coronary Artery Imaging. *Magnetic Resonance in Medicine*, 1992. **28**(2): p. 202.
7. P.D. Gatehouse, D.N. Firmin, S. Collins, and D.B. Longmore, Real time blood flow imaging by spiral scan phase velocity mapping. *Magnetic Resonance in Medicine*, 1994. **31**(5): p. 504.
8. K.F. King, T. K. F. Foo, and C.R. Crawford, Optimized gradient waveforms for spiral scanning. *Magnetic Resonance in Medicine*, 1995. **34**(2): p. 156.
9. P. Boernert, H. Schomberg, B. Aldefeld, and J. Groen, Improvements in spiral MR imaging. *Magma*, 1999. **9**(1-2): p. 29.
10. J.D. O'Sullivan, A Fast Sinc Function Gridding Algorithm for Fourier Inversion in Computer Tomography. *Medical Imaging, IEEE Transactions on*, 1985. **4**(4): p. 200.
11. H. Schomberg and J. Timmer, The gridding method for image reconstruction by Fourier transformation. *Medical Imaging, IEEE Transactions on*, 1995. **14**(3): p. 596.
12. J.I. Jackson, C.H. Meyer, D.G. Nishimura, and A. Macovski, Selection of a convolution function for Fourier inversion using gridding [computerised

- tomography application]. *Medical Imaging, IEEE Transactions on*, 1991. **10(3)**: p. 473.
13. K.P. Pruessmann, M.k. Weiger, P. Bornert, and P. Boesiger, *Advances in sensitivity encoding with arbitrary k-space trajectories*. *Magnetic Resonance in Medicine*, 2001. **46(4)**: p. 638.
 14. K.P. Pruessmann, M. Weiger, M.B. Scheidegger, and P. Boesiger, *SENSE: Sensitivity encoding for fast MRI*. *Magnetic Resonance in Medicine*, 1999. **42(5)**: p. 952.
 15. J. Tsao, P. Boesiger, and K.P. Pruessmann, *k-t BLAST and k-t SENSE: Dynamic MRI with high frame rate exploiting spatiotemporal correlations*. *Magnetic Resonance in Medicine*, 2003. **50(5)**: p. 1031.
 16. P. Kellman, F.H. Epstein, and E.R. McVeigh, *Adaptive sensitivity encoding incorporating temporal filtering (TSENSE)*. *Magnetic Resonance in Medicine*, 2001. **45(5)**: p. 846.
 17. D.K. Sodickson and W.J. Manning, *Simultaneous acquisition of spatial harmonics (SMASH): Fast imaging with radiofrequency coil arrays*. *Magnetic Resonance in Medicine*, 1997. **38(4)**: p. 591.
 18. M.A. Griswold, P.M. Jakob, R.M. Heidemann, M. Nittka, V. Jellus, J. Wang, B. Kiefer, and A. Haase, *Generalized autocalibrating partially parallel acquisitions (GRAPPA)*. *Magnetic Resonance in Medicine*, 2002. **47(6)**: p. 1202.
 19. F. Huang, J. Akao, S. Vijayakumar, G.R. Duensing, and M. Limkeman, *k-t GRAPPA: A k-space implementation for dynamic MRI with high reduction factor*. *Magnetic Resonance in Medicine*, 2005. **54(5)**: p. 1172.
 20. M.A. Griswold, F. Breuer, M. Blaimer, S. Kannengiesser, R.M. Heidemann, M. Mueller, M. Nittka, V. Jellus, B. Kiefer, and P.M. Jakob, *Autocalibrated coil sensitivity estimation for parallel imaging*. *NMR in Biomedicine*, 2006. **19(3)**: p. 316.
 21. C.A. McKenzie, E.N. Yeh, M.A. Ohliger, M.D. Price, and D.K. Sodickson, *Self-calibrating parallel imaging with automatic coil sensitivity extraction*. *Magnetic Resonance in Medicine*, 2002. **47(3)**: p. 529.
 22. Y. Qian, Z. Zhang, V.A. Stenger, and Y. Wang, *Self-calibrated spiral SENSE*. *Magnetic Resonance in Medicine*, 2004. **52(3)**: p. 688.

23. K. Heberleins and X. Hu, *Auto-calibrated parallel spiral imaging*. *Magnetic Resonance in Medicine*, 2006. **55**(3): p. 619.
24. B. Madore, G.H. Glover, and N.J. Pelc, *Unaliasing by Fourier-encoding the overlaps using the temporal dimension (UNFOLD), applied to cardiac imaging and fMRI*. *Magnetic Resonance in Medicine*, 1999. **42**(5): p. 813.
25. J. Shewchuk, *Conjugate gradient without the agonizing pain*. 1994, Carnegie Mellon University: Pittsburgh.
26. M.T. Heath, *Scientific Computing: An Introductory Survey*. Second ed. 2002: McGraw-Hill.
27. M. Bydder, J.E. Perthen, and J. Du, *Optimization of sensitivity encoding with arbitrary k-space trajectories*. *Magnetic Resonance Imaging*, 2007. **25**(8): p. 1123.
28. P.C. Hansen, *Rank-deficient and discrete ill-posed problems: numerical aspects of linear inversion*. 1998: Society for Industrial Mathematics.
29. L. Ying, D. Xu, and Z.P. Liang. *On Tikhonov regularization for image reconstruction in parallel MRI*. in *Engineering in Medicine and Biology Society, 2004. IEMBS '04. 26th Annual International Conference of the IEEE*. 2004.
30. K. King, *SENSE image quality improvement using matrix regularization*. *Proceedings of the 9th Annual Meeting of ISMRM, Glasgow, Scotland, 2001*: p. 1771.
31. F.H. Lin, K.K. Kwong, J.W. Belliveau, and L.L. Wald, *Parallel imaging reconstruction using automatic regularization*. *Magnetic Resonance in Medicine*, 2004. **51**(3): p. 559.
32. J. Tsao, K. Pruessmann, and P. Boesiger, *Feedback Regularization for SENSE Reconstruction* *Proceedings of the 10th Annual Meeting of ISMRM*, 2002. : p. 739.
33. D. Rosenfeld, *New approach to gridding using regularization and estimation theory*. *Magnetic Resonance in Medicine*, 2002. **48**(1): p. 193.
34. H. Eggers and P. Boesiger, *Improved Preconditioning for the Non-Cartesian SENSE Reconstruction with Regularization*. *Proceedings of the 11th Annual Meeting of ISMRM, Kyoto, 2004*: p. 2409.

35. D. Firmin, J. Keegan, P. Gatehouse, P. Jhooti, and Y. Guang Zhong. *Flow and motion: implications on cardiac MR. in Medical Imaging and Augmented Reality, 2001. Proceedings. International Workshop on. 2001.*
36. M.A. Bernstein, K.F. King, and X.J. Zhou, *Handbook of MRI Pulse Sequences. 2004: Elsevier Academic Press.*
37. G.W. Lenz, E.M. Haacke, and R.D. White, *Retrospective cardiac gating: A review of technical aspects and future directions. Magnetic Resonance Imaging, 1989. 7(5): p. 445.*
38. J.L. Duerk and O.P. Simonetti, *Review of MRI gradient waveform design methods with application in the study of motion. Concepts in Magnetic Resonance, 1993. 5(2): p. 105.*
39. P.R. Moran, *A flow velocity zeugmatographic interlace for NMR imaging in humans. Magnetic Resonance Imaging, 1982. 1(4): p. 197.*
40. G. Greil, T. Geva, S.E. Maier, and A.J. Powell, *Effect of acquisition parameters on the accuracy of velocity encoded cine magnetic resonance imaging blood flow measurements. Journal of Magnetic Resonance Imaging, 2002. 15(1): p. 47.*
41. C. Tang, D. Blatter, D., and D. Parker, L. , *Accuracy of phase-contrast flow measurements in the presence of partial-volume effects. Journal of Magnetic Resonance Imaging, 1993. 3(2): p. 377.*
42. M.A. Bernstein, X.J. Zhou, J.A. Polzin, K.F. King, A. Ganin, N.J. Pelc, and G.H. Glover, *Concomitant gradient terms in phase contrast MR: Analysis and correction. Magnetic Resonance in Medicine, 1998. 39(2): p. 300.*
43. K. King, F., A. Ganin, X.J. Zhou, and M.A. Bernstein, *Concomitant gradient field effects in spiral scans. Magnetic Resonance in Medicine, 1999. 41(1): p. 103.*
44. A. Chernobelsky, O. Shubayev, C.R. Comeau, and S.D. Wolff, *Baseline Correction of Phase Contrast Images Improves Quantification of Blood Flow in the Great Vessels. Journal of cardiovascular magnetic resonance, 2007. 9(4): p. 681.*
45. T. Miller, A. Landes, and A. Moran, *Improved accuracy in flow mapping of congenital heart disease using stationary phantom technique. Journal of cardiovascular magnetic resonance, 2009. 11(1): p. 52.*

46. A. Caprihan, S.A. Altobelli, and E. Benitez-Read, *Flow-velocity imaging from linear regression of phase images with techniques for reducing eddy-current effects. Journal of Magnetic Resonance*, 1990. **90**(1): p. 71.
47. J.-W. Lankhaar, M.B.M. Hofman, J.T. Marcus, J.J.M. Zwanenburg, T.J.C. Faes, and A. Vonk-Noordegraaf, *Correction of phase offset errors in main pulmonary artery flow quantification. Journal of Magnetic Resonance Imaging*, 2005. **22**(1): p. 73.
48. P. Gatehouse, M. Rolf, M. Graves, M. Hofman, J. Totman, B. Werner, R. Quest, Y. Liu, J. von Spiczak, M. Dieringer, D. Firmin, A. van Rossum, M. Lombardi, J. Schwitter, J. Schulz-Menger, and P. Kilner, *Flow measurement by cardiovascular magnetic resonance: a multi-centre multi-vendor study of background phase offset errors that can compromise the accuracy of derived regurgitant or shunt flow measurements. Journal of cardiovascular magnetic resonance*, 2010. **12**(1): p. 5.
49. J. Lotz, C. Meier, A. Leppert, and M. Galanski, *Cardiovascular Flow Measurement with Phase-Contrast MR Imaging: A Basic Facts and Implementation. RadioGraphics*, 2002. **22**(3): p. 651.
50. J. Keegan, D. Firmin, P. Gatehouse, and D. Longmore, *The application of breath hold phase velocity mapping techniques to the measurement of coronary artery blood flow velocity: Phantom data and initial in vivo results. Magnetic Resonance in Medicine*, 1994. **31**(5): p. 526.
51. B. Holland, B. Printz, and W. Lai, *Baseline correction of phase-contrast images in congenital cardiovascular magnetic resonance. Journal of cardiovascular magnetic resonance*, 2010. **12**(1): p. 11.
52. P.G. Walker, G.B. Cranney, M.B. Scheidegger, W. Gena, G.M. Pohost, and A.P. Yoganathan, *Semiautomated method for noise reduction and background phase error correction in MR phase velocity data. Journal of Magnetic Resonance Imaging*, 1993. **3**(3): p. 521.
53. Z. Chang and Q.-S. Xiang, *Nonlinear phase correction with an extended statistical algorithm. Medical Imaging, IEEE Transactions on*, 2005. **24**(6): p. 791.
54. E.H. Hardy, J.r. Hoferer, D. Mertens, and G. Kasper, *Automated phase correction via maximization of the real signal. Magnetic Resonance Imaging*, 2009. **27**(3): p. 393.

55. J.P. Singh, M.G. Larson, T.A. Manolio, C.J. O'Donnell, M. Lauer, J.C. Evans, and D. Levy, *Blood Pressure Response During Treadmill Testing as a Risk Factor for New-Onset Hypertension : The Framingham Heart Study*. *Circulation*, 1999. **99**(14): p. 1831.
56. D.N. Firmin, G.L. Nayler, R.H. Klipstein, S.R. Underwood, R.S.O. Rees, and D.B. Longmore, *In Vivo Validation of MR Velocity Imaging*. *Journal of Computer Assisted Tomography*, 1987. **11**(5): p. 751.
57. P. Beerbaum, H. Korperich, P. Barth, H. Esdorn, J. Gieseke, and H. Meyer, *Noninvasive Quantification of Left-to-Right Shunt in Pediatric Patients : Phase-Contrast Cine Magnetic Resonance Imaging Compared With Invasive Oximetry*. *Circulation*, 2001. **103**(20): p. 2476.
58. A.C. Van Rossum, F.C. Visser, K.H. Peels, J. Valk, and J.P. Roos, *An in vivo validation of quantitative blood flow imaging in arteries and veins using magnetic resonance phase-shift techniques*. *European Heart Journal*, 1991. **12**(2): p. 117.
59. W.G. Hundley, R.A. Lange, G.D. Clarke, B.M. Meshack, J. Payne, C. Landau, R. McColl, D.E. Sayad, D.L. Willett, J.E. Willard, L.D. Hillis, and R.M. Peshock, *Assessment of Coronary Arterial Flow and Flow Reserve in Humans With Magnetic Resonance Imaging*. *Circulation*, 1996. **93**(8): p. 1502.
60. B. Beleslin, M. Ostojic, J. Stepanovic, A. Djordjevic-Dikic, S. Stojkovic, M. Nedeljkovic, G. Stankovic, Z. Petrasinovic, L. Gojkovic, and Z. Vasiljevic-Pokrajcic, *Stress echocardiography in the detection of myocardial ischemia. Head- to-head comparison of exercise, dobutamine, and dipyridamole tests*. *Circulation*, 1994. **90**(3): p. 1168.
61. P.S. Nandi and D.H. Spodick, *Recovery from exercise at varying work loads. Time course of responses of heart rate and systolic intervals*. *Br. Heart J.*, 1977. **39**(9): p. 958.
62. B. Hargreaves. <http://mrsrl.stanford.edu/~brian/vdspiral/>. 2001.
63. J.A. Steeden, D. Atkinson, A.M. Taylor, and V. Muthurangu, *Assessing vascular response to exercise using a combination of real-time spiral phase contrast MR and noninvasive blood pressure measurements*. *Journal of Magnetic Resonance Imaging*, 2010. **31**(4): p. 997.
64. K.S. Nayak, J.M. Pauly, A.B. Kerr, B.S. Hu, and D.G. Nishimura, *Real-time color flow MRI*. *Magnetic Resonance in Medicine*, 2000. **43**(2): p. 251.

65. C. Klein, S. Schalla, B. Schnackenburg, A. Bornstedt, E. Fleck, and E. Nagel, *Magnetic resonance flow measurements in real time: Comparison with a standard gradient-echo technique. Journal of Magnetic Resonance Imaging*, 2001. **14**(3): p. 306.
66. H. Korperich, J. Gieseke, P. Barth, R. Hoogeveen, H. Esdorn, A. Peterschroder, H. Meyer, and P. Beerbaum, *Flow Volume and Shunt Quantification in Pediatric Congenital Heart Disease by Real-Time Magnetic Resonance Velocity Mapping: A Validation Study. Circulation*, 2004. **109**(16): p. 1987.
67. K.P. Pruessmann, M. Weiger, and P. Boesiger, *Sensitivity encoded cardiac MRI. Journal of cardiovascular magnetic resonance*, 2001. **3**(1): p. 1.
68. R. Nezafat, P. Kellman, A. Derbyshire, and E. McVeigh, R. , *Real-time blood flow imaging using autocalibrated spiral sensitivity encoding. Magnetic Resonance in Medicine*, 2005. **54**(6): p. 1557.
69. R. Nezafat, P. Kellman, J.A. Derbyshire, and E.R. McVeigh, *Real Time High Spatial-Temporal Resolution Flow Imaging with Spiral MRI using Auto-Calibrated SENSE. Engineering in Medicine and Biology Society, 2004. IEMBS '04. 26th Annual International Conference of the IEEE, 2004. 1: p. 1914.*
70. D.S. Dymond, C. Foster, R.P. Grenier, J. Carpenter, and D.H. Schmidt, *Peak exercise and immediate postexercise imaging for the detection of left ventricular functional abnormalities in coronary artery disease. The American Journal of Cardiology*, 1984. **53**(11): p. 1532.
71. H. Hecht, L. DeBord, N. Sotomayor, R. Shaw, R. Dunlap, and C. Ryan, *Supine bicycle stress echocardiography: peak exercise imaging is superior to postexercise imaging. Journal of the American Society of Echocardiography*, 1993. **6**(3): p. 265.
72. R.H. Mohiaddin, P.D. Gatehouse, and D.N. Firmin, *Exercise-related changes in aortic flow measured with spiral echo-planar MR velocity mapping. Journal of Magnetic Resonance Imaging*, 1995. **5**(2): p. 159.
73. E.M. Pedersen, S. Kozerke, S. Ringgaard, M.B. Scheidegger, and P. Boesiger, *Quantitative abdominal aortic flow measurements at controlled levels of ergometer exercise. Magnetic Resonance Imaging*, 1999. **17**(4): p. 489.

74. E.M. Pedersen, E.V. Stenbog, T. Frund, K. Houliind, O. Kromann, K.E. Srensen, K. Emmertsen, and V.E. Hjortdal, *Flow during exercise in the total cavopulmonary connection measured by magnetic resonance velocity mapping. Heart*, 2002. **87**(6): p. 554.
75. M. Jekic, E. Foster, M. Ballinger, S. Raman, and O. Simonetti, *Cardiac function and myocardial perfusion immediately following maximal treadmill exercise inside the MRI room. Journal of cardiovascular magnetic resonance*, 2008. **10**(1): p. 3.
76. C.A. Taylor, C.P. Cheng, L.A. Espinosa, B.T. Tang, D. Parker, and R.J. Herfkens, *In Vivo Quantification of Blood Flow and Wall Shear Stress in the Human Abdominal Aorta During Lower Limb Exercise. Annals of biomedical engineering*, 2002. **30**(3): p. 402.
77. C.P. Cheng, D.F. Schwandt, E.L. Topp, J.H. Anderson, R.J. Herfkens, and C.A. Taylor, *Dynamic exercise imaging with an MR-compatible stationary cycle within the general electric open magnet. Magnetic Resonance in Medicine*, 2003. **49**(3): p. 581.
78. C.P. Cheng, R.J. Herfkens, A.L. Lightner, C.A. Taylor, and J.A. Feinstein, *Blood flow conditions in the proximal pulmonary arteries and vena cavae: healthy children during upright cycling exercise. Am J Physiol Heart Circ Physiol*, 2004. **287**(2): p. H921.
79. C.P. Cheng, R.J. Herfkens, C.A. Taylor, and J.A. Feinstein, *Proximal pulmonary artery blood flow characteristics in healthy subjects measured in an upright posture using MRI: The effects of exercise and age. Journal of Magnetic Resonance Imaging*, 2005. **21**(6): p. 752.
80. A.S. Tenforde, C.P. Cheng, G.Y. Suh, R.J. Herfkens, R.L. Dalman, and C.A. Taylor, *Quantifying in vivo hemodynamic response to exercise in patients with intermittent claudication and abdominal aortic aneurysms using cine phase-contrast MRI. Journal of magnetic Resonance Imaging*, 2010. **31**(2): p. 425.
81. V.E. Hjortdal, K. Emmertsen, E. Stenbog, T. Frund, M.R. Schmidt, O. Kromann, K. Sorensen, and E.M. Pedersen, *Effects of Exercise and Respiration on Blood Flow in Total Cavopulmonary Connection: A Real-Time Magnetic Resonance Flow Study. Circulation*, 2003. **108**(10): p. 1227.
82. L.M. Pedersen, T.A.L. Pedersen, E.M. Pedersen, H. Hojmyr, K. Emmertsen, and V.E. Hjortdal, *Blood flow measured by magnetic resonance imaging at*

- rest and exercise after surgical bypass of aortic arch obstruction. Eur J Cardiothorac Surg, 2010. 37(3): p. 658.*
83. P. Gatehouse, J. Keegan, L. Crowe, S. Masood, R. Mohiaddin, K.-F. Kreitner, and D. Firmin, *Applications of phase-contrast flow and velocity imaging in cardiovascular MRI. European Radiology, 2005. 15(10): p. 2172.*
84. A.A.W. Roest, P. Kunz, H.J. Lamb, W.A. Helbing, E.E. van der Wall, and A.d. Roos, *Biventricular response to supine physical exercise in young adults assessed with ultrafast magnetic resonance imaging. The American Journal of Cardiology, 2001. 87(5): p. 601.*
85. A.A.W. Roest, W.A. Helbing, P. Kunz, J.G. van den Aardweg, H.J. Lamb, H.W. Vliegen, E.E. van der Wall, and A. de Roos, *Exercise MR Imaging in the Assessment of Pulmonary Regurgitation and Biventricular Function in Patients after Tetralogy of Fallot Repair. Radiology, 2002. 223(1): p. 204.*
86. P. Lurz, V. Muthurangu, S. Schievano, J. Nordmeyer, P. Bonhoeffer, A.M. Taylor, and M.S. Hansen, *Feasibility and Reproducibility of Biventricular Volumetric Assessment of Cardiac Function During Exercise Using Real-Time Radial k-t SENSE Magnetic Resonance Imaging. Journal of Magnetic Resonance Imaging, 2009. 29: p. 1062.*
87. V. Muthurangu, P. Lurz, J. Critchely, J. Deanfield, A. Taylor, and M.S. Hansen, *Real-time Assessment of Right and Left Ventricular Volumes and Function in Patients with Congenital Heart Disease by Using High Spatiotemporal Resolution Radial k-t SENSE. Radiology, 2008. 248(3): p. 782.*
88. P. Segers, S. Brimiouille, N. Stergiopoulos, N. Westerhof, R. Naeije, M. Maggiorini, and P. Verdonck, *Pulmonary arterial compliance in dogs and pigs: the three-element windkessel model revisited. Am J Physiol Heart Circ Physiol, 1999. 277(2): p. 725.*
89. Z. Liu, K.P. Brin, and F.C. Yin, *Estimation of total arterial compliance: an improved method and evaluation of current methods. Am J Physiol Heart Circ Physiol, 1986. 251(3): p. 588.*
90. V. Muthurangu, A. Taylor, R. Andriantsimiavona, S. Hegde, M.E. Miquel, R. Tulloh, E. Baker, D.L.G. Hill, and R.S. Razavi, *Novel Method of Quantifying Pulmonary Vascular Resistance by Use of Simultaneous Invasive Pressure Monitoring and Phase-Contrast Magnetic Resonance Flow. Circulation, 2004. 110: p. 826.*

91. V. Muthurangu, D. Atkinson, M. Sermesant, M.E. Miquel, S. Hegde, R. Johnson, R. Andriantsimiavona, A.M. Taylor, E. Baker, R. Tulloh, D. Hill, and R.S. Razavi, *Measurement of total pulmonary arterial compliance using invasive pressure monitoring and MR flow quantification during MR-guided cardiac catheterization. AJP - Heart and Circulatory Physiology* 2005. **289**: p. 1301.
92. V.S. Lee, C.E. Spritzer, B.A. Carroll, L.G. Pool, M.A. Bernstein, S.K. Heinle, and J.R. MacFall, *Flow quantification using fast cine phase-contrast MR imaging, conventional cine phase-contrast MR imaging, and Doppler sonography: in vitro and in vivo validation. Am. J. Roentgenol.*, 1997. **169**(4): p. 1125.
93. A.J. Evans, F. Iwai, T.A. Grist, H.D. Sostman, L.W. Hedlund, C.E. Spritzer, R. Negro-vilar, C.A. Beam, and N.J. Pelc, *Magnetic Resonance Imaging of Blood Flow with a Phase Subtraction Technique: In Vitro and In Vivo Validation. Investigative Radiology*, 1993. **28**(2): p. 109.
94. M.F. Wilson, B.H. Sung, G.A. Pincomb, and W.R. Lovallo, *Exaggerated pressure response to exercise in men at risk for systemic hypertension. The American Journal of Cardiology*, 1990. **66**(7): p. 731.
95. E. Raaijmakers, T.J.C. Faes, R.J.P.M. Scholten, H.G. Goovaerts, and R.M. Heethaar, *A meta-analysis of three decades of validating thoracic impedance cardiography. Critical Care Medicine*, 1999. **27**(6): p. 1203.
96. H. Sakuma, N. Kawada, H. Kubo, Y. Nishide, K. Takano, N. Kato, and K. Takeda, *Effect of breath holding on blood flow measurement using fast velocity encoded cine MRI. Magnetic Resonance in Medicine*, 2001. **45**(2): p. 346.
97. M.H. Frick and T. Somer, *Base-line effects on response of stroke volume to leg exercise in the supine position. J Appl Physiol*, 1964. **19**(4): p. 639.
98. Y. Ichihara, J. Ohno, M. Suzuki, T. Anno, M. Ugino, and K. Nagata, *Blunt circulatory response to exercise in coronary high-risk subjects among apparently healthy Japanese. Circulation journal: A official journal of the Japanese Circulation Society*, 2004. **68**(4): p. 286.
99. M.S. Hansen, C. Baltes, J. Tsao, S. Kozerke, K.P. Pruessmann, and H. Eggers, *k-t BLAST reconstruction from non-Cartesian k-t space sampling. Magnetic Resonance in Medicine*, 2006. **55**(1): p. 85.

100. T.S. Sorensen, T. Schaeffter, K.O. Noe, and M.S. Hansen, *Accelerating the Nonequispaced Fast Fourier Transform on Commodity Graphics Hardware. Medical Imaging, IEEE Transactions on*, 2008. **27**(4): p. 538.
101. D.J. Burkart, J.P. Felmlee, C.D. Johnson, R.L. Wolf, A.L. Weaver, and R.L. Ehman, *Cine phase-contrast MR flow measurements: improved precision using an automated method of vessel detection. J. Comput Assist Tomogr*, 1994. **18**: p. 469.
102. A. Lalande, P.K. van Kien, N. Salvé, D.B. Salem, L. Legrand, P.M. Walker, J.E. Wolf, and F. Brunotte, *Automatic determination of aortic compliance with cine-magnetic resonance imaging: an application of fuzzy logic theory. Invest Radiol*, 2002. **37**(685-691): p. 685.
103. S. Kozerke, R. Botnar, S. Oyre, M.B. Scheidegger, E.M. Pedersen, and P. Boesiger, *Automatic vessel segmentation using active contours in cine phase contrast flow measurements. Journal of magnetic Resonance imaging*, 1999. **10**: p. 41.
104. S. Oyre, S. Ringgaard, S. Kozerke, W.P. Paaske, M.B. Scheidegger, P. Boesiger, and E.M. Pedersen, *Quantitation of circumferential subpixel vessel wall position and wall shear stress by multiple sectorized three-dimensional paraboloid modeling of velocity encoded cine MR. Magnetic Resonance in Medicine*, 1998. **40**: p. 645.
105. F. Odille, J. Steeden, V. Muthurangu, and D. Atkinson, *Automatic Segmentation Propagation of the Aorta in Real-Time Phase Contrast MRI using Nonrigid Registration. Journal of Magnetic Resonance Imaging*, 2010. **In press**.
106. L.R. Dice, *Measures of the amount of ecologic association between species. Ecology*, 1945. **26**: p. 297.
107. A. Jones, J. Steeden, J. Pruessner, A. Taylor, A. Deanfield, and V. Muthurangu, *Detailed Assessment of The Hemodynamic Response to Psychosocial Stress using Real-Time MRI. Journal of Magnetic Resonance Imaging*, 2010. **In Press**.
108. K. Dedovic, R. Renwick, N.K. Mahani, V. Engert, S.J. Lupien, and J.C. Pruessner, *The Montreal Imaging Stress Task: using functional imaging to investigate the effects of perceiving and processing psychosocial stress in the human brain. J Psychiatry Neurosci*, 2005. **30**(5): p. 319.

109. J.A. Steeden, D. Atkinson, A.M. Taylor, and V. Muthurangu, *Split-Acquisition Real-time CINE Phase-Contrast MR Flow Measurements Magnetic Resonance in Medicine*, 2010. **64**(6): p. 1664.
110. L.-C. Man, J.M. Pauly, D.G. Nishimura, and A. Macovski, *Nonsubtractive spiral phase contrast velocity imaging. Magnetic Resonance in Medicine*, 1999. **42**(4): p. 704.
111. J.-F. Nielsen and K.S. Nayak, *Referenceless phase velocity mapping using balanced SSFP. Magnetic Resonance in Medicine*, 2009. **61**(5): p. 1096.
112. K.S. Nayak and B.S. Hu, *Triggered real-time MRI and cardiac applications. Magnetic Resonance in Medicine*, 2003. **49**(1): p. 188.
113. A.C. Larson, R.D. White, G. Laub, E.R. McVeigh, D. Li, and O.P. Simonetti, *Self-gated cardiac cine MRI. Magnetic Resonance in Medicine*, 2004. **51**(1): p. 93.
114. C.J. Bakker, J.H. Seppenwoolde, L.W. Bartels, and R. van der Weide, *Adaptive subtraction as an aid in MR-guided placement of catheters and guidewires. Journal of Magnetic Resonance Imaging*, 2004. **20**(3): p. 470.
115. O. Dietrich, J.G. Raya, S.B. Reeder, M.F. Reiser, and S.O. Schoenberg, *Measurement of signal-to-noise ratios in MR images: Influence of multichannel coils, parallel imaging, and reconstruction filters. Journal of Magnetic Resonance Imaging*, 2007. **26**(2): p. 375.
116. J.M. Bland and D.G. Altman, *Statistical methods for assessing agreement between two methods of clinical measurement. Lancet*, 1986. **i**: p. 307.
117. P. Lanzer, E. Botvinick, N. Schiller, L. Crooks, M. Arakawa, L. Kaufman, P. Davis, R. Herfkens, M. Lipton, and C. Higgins, *Cardiac imaging using gated magnetic resonance. Radiology*, 1984. **150**(1): p. 121.
118. P. Kellman, C. Ched'hotel, C.H. Lorenz, C. Mancini, A.E. Arai, and E.R. McVeigh, *Fully automatic, retrospective enhancement of real-time acquired cardiac cine MR images using image-based navigators and respiratory motion-corrected averaging. Magnetic Resonance in Medicine*, 2008. **59**(4): p. 771.
119. P. Beerbaum, H. Körperich, J. Gieseke, P. Barth, M. Peuster, and H. Meyer, *Blood flow quantification in adults by phase-contrast MRI combined with SENSE--a validation study. Journal of cardiovascular magnetic resonance*, 2005. **7**(2): p. 361.

120. M.S. Hansen, D. Atkinson, and T.S. Sorensen, *Cartesian SENSE and k-t SENSE reconstruction using commodity graphics hardware. Magnetic Resonance in Medicine*, 2008. **59**(3): p. 463.
121. S. Rees, D. Firmin, R. Mohiaddin, R. Underwood, and D. Longmore, *Application of flow measurements by magnetic resonance velocity mapping to congenital heart disease. The American Journal of Cardiology*, 1989. **64**(14): p. 953.
122. J.A. Steeden, D. Atkinson, A.M. Taylor, and V. Muthurangu, *Rapid Flow Assessment of Congenital Heart Disease Using High Spatio-Temporal Gated Spiral Phase Contrast MR. Radiology*, 2010. **In Press**.
123. P. Beerbaum, H. Korperich, J. Gieseke, P. Barth, M. Peuster, and H. Meyer, *Rapid Left-to-Right Shunt Quantification in Children by Phase-Contrast Magnetic Resonance Imaging Combined With Sensitivity Encoding (SENSE). Circulation*, 2003. **108**(11): p. 1355.
124. A. Prakash, R. Garg, E.N. Marcus, G. Reynolds, T. Geva, and A.J. Powell, *Faster flow quantification using sensitivity encoding for velocity-encoded cine magnetic resonance imaging: In vitro and in vivo validation. Journal of Magnetic Resonance Imaging*, 2006. **24**(3): p. 676.
125. C.D. Lew, M.T. Alley, R. Bammer, D.M. Spielman, and F.P. Chan, *Peak Velocity and Flow Quantification Validation for Sensitivity-Encoded Phase-Contrast MR Imaging. Academic Radiology*, 2007. **14**(3): p. 258.
126. Y. Zur, M.L. Wood, and L.J. Neuringer, *Spoiling of transverse magnetization in steady-state sequences. Magnetic Resonance in Medicine*, 1991. **21**(2): p. 251.
127. C. Molar, *Interpolation, in Numerical Computing with MATLAB*. 2004, SIAM.
128. A. Savitzky and M.J.E. Golay, *Smoothing and Differentiation of Data by Simplified Least Squares Procedures. Analytical Chemistry*, 1964. **36**(8): p. 1627.
129. F. Faul, E. Erdfelder, A.-G. Lang, and A. Buchner, *G*power 3: A flexible statistical power analysis program for the social, behavioral, and biomedical sciences. Behavior Research Methods*, 2007. **39**(2): p. 175.
130. A.J. Powell, S.E. Maier, T. Chung, and T. Geva, *Phase-Velocity Cine Magnetic Resonance Imaging Measurement of Pulsatile Blood Flow in*

- Children and Young Adults: In Vitro and In Vivo Validation. Pediatric Cardiology*, 2000. **21**(2): p. 104.
131. R. Frayne, D.A. Steinman, B.K. Rutt, and C.R. Ethier, Accuracy of MR phase contrast velocity measurements for unsteady flow. *Journal of Magnetic Resonance Imaging*, 1995. **5**(4): p. 428.
132. D. Meier, S. Maier, and P. Bösiger, Quantitative flow measurements on phantoms and on blood vessels with MR. *Magnetic Resonance in Medicine*, 1988. **8**(1): p. 25.
133. M.A. Ohliger and D.K. Sodickson, An introduction to coil array design for parallel MRI. *NMR in Biomedicine*, 2006. **19**(3): p. 300.
134. Accusorb. <http://www.magmedix.com/default.htm>. 2006.
135. P. Börnert and B. Aldefeld, On spatially selective RF excitation and its analogy with spiral MR image acquisition. *Magnetic Resonance Materials in Physics, Biology and Medicine*, 1998. **7**(3): p. 166.
136. C.H. Meyer, J.M. Pauly, A. Macovskiand, and D.G. Nishimura, Simultaneous spatial and spectral selective excitation. *Magnetic Resonance in Medicine*, 1990. **15**(2): p. 287.
137. J.P. Felmlee and R.L. Ehman, Spatial presaturation: a method for suppressing flow artifacts and improving depiction of vascular anatomy in MR imaging. *Radiology*, 1987. **164**(2): p. 559.
138. T.S. Sorensen, D. Atkinson, T. Schaeffter, and M.S. Hansen, Real-Time Reconstruction of Sensitivity Encoded Radial Magnetic Resonance Imaging Using a Graphics Processing Unit. *Medical Imaging, IEEE Transactions on*, 2009. **28**(12): p. 1974.
139. H. Yu, C.A. McKenzie, A. Shimakawa, A.T. Vu, A.C.S. Brau, P.J. Beatty, A.R. Pineda, J.H. Brittain, and S.B. Reeder, Multiecho reconstruction for simultaneous water-fat decomposition and T2* estimation. *JOURNAL OF MAGNETIC RESONANCE IMAGING*, 2007. **26**(4): p. 1153.
140. M. Markl, F.P. Chan, M.T. Alley, K.L. Wedding, M.T. Draney, C.J. Elkins, D.W. Parker, R. Wicker, C.A. Taylor, R.J. Herfkens, and N.J. Pelc, Time-resolved three-dimensional phase-contrast MRI. *Journal of Magnetic Resonance Imaging*, 2003. **17**(4): p. 499.

141. D.N. Firmin, P.D. Gatehouse, J.P. Konrad, G.Z. Yang, P.J. Kilner, and D.B. Longmore. *Rapid 7-dimensional imaging of pulsatile flow. in Computers in Cardiology 1993, Proceedings. 1993.*
142. J. Carvalho, J. Nielsen, and K. Nayak, *Validation of the spiral Fourier velocity encoding method. Journal of cardiovascular magnetic resonance, 2008. 10(Suppl 1): p. A403.*
143. C. Baltes, M.S. Hansen, J. Tsao, S. Kozerke, R. Rezavi, E.M. Pedersen, and P. Boesiger, *Determination of Peak Velocity in Stenotic Areas: Echocardiography versus kt SENSE Accelerated MR Fourier Velocity Encoding. Radiology, 2007. 246(1): p. 249.*
144. N.B. Wood, *Aspects of Fluid Dynamics Applied to the Larger Arteries. Journal of Theoretical Biology, 1999. 199(2): p. 137.*
145. J.-P. Tasu, O. Jolivet, and J. Bittoun, *From flow to pressure: estimation of pressure gradient and derivative by MR acceleration mapping. Magnetic Resonance Materials in Physics, Biology and Medicine, 2000. 11(1): p. 55.*
146. F. Balleux-Buyens, O. Jolivet, J. Bittoun, and A. Hermet, *Velocity encoding versus acceleration encoding for pressure gradient estimation in MR haemodynamic studies. Physics in Medicine and Biology, 2006. 51(19): p. 4747.*
147. J.-P. Tasu, O. Jolivet, E. Mousseaux, A. Delouche, B. Diebold, and J. Bittoun, *Acceleration mapping by fourier acceleration-encoding: in vitro study and initial results in the great thoracic vessels. Magnetic Resonance in Medicine, 1997. 38(1): p. 110.*
148. J. Bittoun, O. Jolivet, A. Herment, E. Itti, E. Durand, E. Mousseaux, and J.P. Tasu, *Multidimensional MR mapping of multiple components of velocity and acceleration by fourier phase encoding with a small number of encoding steps. Magnetic Resonance in Medicine, 2000. 44(5): p. 723.*
149. J.-P. Tasu, E. Mousseaux, P. Colin, M.S. Slama, O. Jolivet, and J. Bittoun, *Estimation of left ventricular performance through temporal pressure variations measured by MR velocity and acceleration mappings. Journal of Magnetic Resonance Imaging, 2002. 16(3): p. 246.*

APPENDIX 1

J.A. Steeden, D. Atkinson, A.M. Taylor, and V. Muthurangu

Assessing vascular response to exercise using a combination of real-time spiral phase contrast MR and noninvasive blood pressure measurements

Journal of Magnetic Resonance Imaging, 2010. 31(4): p. 997.

Technical Note

Assessing Vascular Response To Exercise Using a Combination of Real-Time Spiral Phase Contrast MR and Noninvasive Blood Pressure Measurements

Jennifer A. Steeden, MEng,^{1,2} David Atkinson, PhD,¹ Andrew M. Taylor, MD,² and Vivek Muthurangu, MD^{2*}

Purpose: To measure the hemodynamic response to exercise using real-time velocity mapping magnetic resonance imaging (MRI), incorporating a high temporal resolution spiral phase contrast (PC) sequence accelerated with sensitivity encoding (SENSE).

Materials and Methods: Twenty healthy adults underwent MRI at rest and during supine exercise at two different exercise levels. Flow volumes were assessed in the ascending aorta using a spiral SENSE real-time PC sequence. The sequence was validated at rest against a vendor supplied gated PC sequence, and also at rest and during exercise against left ventricular volumes assessed using a radial *k-t* SENSE real-time sequence. Combining the measured flow volumes with simultaneous oscillometric blood pressure measurements, enabled the noninvasive calculations of systemic vascular resistance (SVR) and arterial compliance (C).

Results: Measured flow volumes correlated very well between the sequences at rest and during exercise. Cardiac output (CO) and heart rate were found to significantly increase during exercise, while SVR and C were found to decrease significantly.

Conclusion: Hemodynamic response to exercise can be accurately quantified using a high temporal resolution spiral SENSE real-time flow imaging. This may allow early detection of hypertension and a greater understanding of the early changes in this condition.

Key Words: cardiovascular imaging; exercise; real-time imaging

J. Magn. Reson. Imaging 2010;31:997–1003.
© 2010 Wiley-Liss, Inc.

EXERCISE IS A powerful stimulator of the cardiovascular system and can be used to unmask subtle changes in early hypertensive disease (1). Routinely, only blood pressure (BP) and heart rate response are measured during exercise (1). These are not sensitive markers of early vascular dysfunction and thus the full potential of exercise stress testing is not achieved. It would be advantageous if systemic vascular resistance (R) and total arterial compliance (C) were also measured during exercise. This requires assessment of aortic flow in addition to blood pressure.

Magnetic resonance (MR) imaging is a proven method of velocity mapping at rest, allowing accurate measurement of arterial flow (2). In the pulmonary vasculature, MR phase contrast (PC) measurements have been combined with invasive pressure measurements to calculate vascular resistance and compliance (3,4). However, these studies used cardiac gated sequences that are difficult to perform during exercise. Previous exercise studies that used cardiac gated sequences required suspension of exercise during imaging (5,6). This is nonphysiological and makes ramped exercise protocols difficult to perform. A better approach may be to use real-time MR flow imaging (7). Real-time MR is less susceptible to motion (caused either by exercising or breathing) and can be performed without cardiac gating, making it more suited to imaging during exercise. However, real-time imaging may come at the cost of low temporal resolution, which may affect accuracy at the high heart rates present during exercise (8).

The high temporal resolution required for real-time imaging during exercise can be achieved through efficient *k*-space filling. For instance, spiral trajectories are appealing as they efficiently fill a large portion of *k*-space after each excitation. In addition, they also have a very short effective echo time (TE), which is optimal for flow imaging (9). Further improvements in temporal resolution can be achieved by undersampling *k*-space and then reconstructing using an iterative sensitivity encoding (SENSE) algorithm (10).

The aims of this study were to (i) Validate an in-house real-time spiral SENSE flow sequence in a phantom and in vivo, (ii) Demonstrate feasibility of

¹Centre for Medical Image Computing, UCL Department of Medical Physics & Bioengineering, London, United Kingdom.

²Centre for Cardiovascular MR, UCL Institute of Child Health, London, United Kingdom.

Contract grant sponsor: UK EPSRC.

*Address reprint requests to: V.M., Cardiovascular Unit, Great Ormond Street Hospital, Great Ormond St., London WC1N 3JH, UK. E-mail: v.muthurangu@ich.ucl.ac.uk

Received August 25, 2009; Accepted January 6, 2010.

DOI 10.1002/jmri.22105

Published online in Wiley InterScience (www.interscience.wiley.com).

using this sequence to measure cardiac output during exercise, and (iii) Combine this with noninvasive pressure measurements to calculate resistance and compliance.

METHODS

Study Population

Twenty healthy volunteers (9 male; 11 female) were recruited for this study between May and July 2009. The median age was 27.6 (range, 21.9–49.2 years). Exclusion criteria were (i) cardiovascular disease (assessed by clinical history), (ii) illness that prevented exercise (i.e., joint disease), (iii) contraindications for MR such as MR-incompatible implants, or pregnancy. The local research ethics committee approved the study and written consent was obtained from all volunteers.

MR Protocol

All imaging was performed on a 1.5 Tesla (T) MR scanner (Avanto, Siemens Medical Solutions, Erlangen, Germany) using two six-element body-matrix coils. The imaging protocol at rest and at two exercise levels is shown in Figure 1.

Standard Flow Assessment

Standard aortic flow quantification at rest was performed using a retrospectively-gated, velocity-encoded gradient echo sequence (field of view [FOV], ~320 mm; rectangular FOV, 75%; matrix, 256 × 192; voxel size, 1.25 × 1.25 × 7 mm; echo time/repetition time [TE/TR], 3.2/27.1 ms; flip angle, 30°, pixel; bandwidth [BW], 390 Hz/pixel; NSA, 3; VENC, 180 cm/s; scan time, ~2.5 min; temporal resolution, 30 ms). The imaging plane was located in the ascending aorta, as it passes the bifurcation of the pulmonary arteries. The scan was performed during free breathing. This sequence has been well validated in many previous studies against the gold-standard stop-watch cylinder method of measuring flow (3). Therefore, in this study the flow volumes measured from this sequence are assumed to be the true flow volumes.

Real-Time Flow Assessment

Real-time flow quantification was performed using a uniform density spiral PC sequence with eight interleaves, undersampled by a factor of four (FOV: 500 mm, matrix: 128 × 128, voxel size: 3.9 × 3.9 × 7 mm, TR/TE: 1.8/10.1 ms, flip angle: 15°, pixel BW: 1775 Hz/pixel, VENC: 200 cm/s, interleaves: 8, SENSE acceleration factor: 4, temporal resolution: 40.4 ms). For each scan, 152 consecutive frames were acquired. The sampling pattern was rotated for each frame so that four consecutive frames comprised a fully sampled *k*-space with eight interleaves. This undersampled data was reconstructed online using an iterative SENSE algorithm. All coil sensitivity and regularization information required for the reconstruction process was calculated from the sum-of-squares of

the coil data over all time frames. Reconstruction for each scan took 5 minutes. Maxwell correction was performed to remove the effects of concomitant gradients, originating from the flow encoding gradients (11). To minimize residual phase offsets in the images, automatic phase correction was carried out by fitting a quadratic surface through the stationary tissue. Stationary tissue was identified by the intensity of the pixels in the magnitude image and also by the standard deviation of the pixels in the phase image.

Real-Time Volume Assessment

Ventricular volumes were assessed using a real-time radial *k-t* SENSE sequence (FOV: ~380 mm, matrix: 128 × 128, voxel size: 3.0 × 3.0 × 10 mm, TR/TE: 1.2/2.5 ms, flip angle: 38°, pixel BW: 1500 Hz/pixel, radial spokes: 128, *k-t* SENSE acceleration factor: 8, scan time: ~30 s, temporal resolution: ~35.5 ms). Eleven to thirteen contiguous slices were acquired in the short axis to ensure coverage of the ventricle. Real-time data for each slice was acquired for 1.5 s and the slice was then automatically moved down the ventricle. Image acquisition was performed during free breathing. This sequence has previously been validated at rest (12) and during exercise (8).

Flow Pump Validation

A validation experiment was carried out using a pulsatile flow pump (Harvard Medical Systems) connected to a distensible rubber tubing vessel phantom. The output from the pump was varied from 2.8 to 6.8 l/min, by changing the stroke volume and the pump rate per minute. Images were acquired using the standard flow sequence and the real-time flow sequence at the mid-point of the phantom. The standard flow sequence was gated from an external square wave signal generated by the flow pump. The data underwent the same reconstruction and preprocessing as the *in vivo* experiments. The flow volumes from the two sequences were calculated as described below.

In Vivo Validation

At rest flow rate values from the real-time spiral SENSE sequence were compared with those from the standard flow sequence. At rest and during exercise, aortic flow volumes from the real-time MR flow sequence were compared with left ventricular stroke volumes from real-time *k-t* SENSE volume measurements.

Vascular Response To Exercise

Exercise was performed with an MR-compatible ergometer (MR cardiac ergometer Up/Down, Lode, Groningen, Netherlands). The participants were placed supine in the MR scanner, with their feet strapped into the peddles and the upper leg strapped to supports of the ergometer, before the scan. Exercise

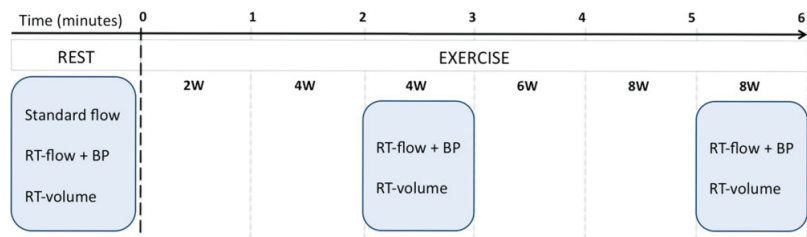


Figure 1. The time line of the MRI protocol at rest and during each exercise level.

consisted of an up- and downward motion of the pedals. This type of exercise is designed to minimize motion artifacts as motion is restricted to the lower legs. Exercise intensity was increased incrementally during the scan (Fig. 1). All exercise data was acquired during free breathing and in the course of exercise. Brachial artery systolic, mean, and diastolic blood pressure was measured with a cuff based oscillometric device (Datex Ohmeda, Finland) during acquisition of all real-time flow data (Fig. 1).

Image Analysis

All images were processed using in-house plug-ins for the open-source software Osirix (the Osirix Foundation, Geneva, Switzerland). Measurement of ventricular stroke volume was performed as previously described (8,12). Flow images were manually segmented (using the modulus images) and stroke volume and cardiac output were measured. Resistance (measured in mmHg/L/min, also known as WU) was calculated by dividing the mean blood pressure by cardiac output. Compliance was calculated using an optimization of the two-element windkessel model as previously described (5,13). Briefly MR flow data and R are used as inputs to a windkessel model. A series of modeled pressure curves (P) were then generated using values of C between 0.1 and 5.0 mL/mmHg in increments of 0.01. Compliance was taken to be the value that produced the best match with the actual pulse pressure as seen in Figure 2.

Statistical Analysis

All results are expressed as the mean \pm standard deviation (SD). Measurements of agreement between the standard flow sequence and the real-time flow sequence, and also between the real-time *k-t* ventricular volume sequence and the real-time flow sequence, were performed using Bland-Altman analysis, as well as calculation of correlation coefficients. Two-tailed Student's *t*-tests were used to compare the hemodynamic responses at different exercise levels. All statistical analysis was performed using GraphPad Prism (GraphPad Software Inc., San Diego, CA).

RESULTS

Image Quality

Small residual aliasing artifacts were visible in all real-time spiral flow images. Motion artifacts due to

free breathing and continuation of exercise were not significant between images acquired at rest and at 8W of continuous exercise. This is due to the very high temporal resolution achieved and because there is limited motion in the torso during the up-down exercise performed. Additionally, some image blurring was observed and this is attributed to the sensitivity of spiral trajectories to off-resonance effects and small *k*-space trajectory errors. Figure 3 shows examples of the image quality from the real-time flow at rest and during exercise.

Phantom Validation

There was good agreement between the standard gated flow sequence and the real-time spiral flow sequence. Bland-Altman analysis of the pump output found the bias was -0.08 l/min, with limits of agreement from -0.34 to 0.18 l/min. The correlation coefficient was 0.995 ($P < 0.005$). Bland-Altman analysis of the stroke volume from the pump found the bias was -0.77 ml, with limits of agreement from -4.8 to 3.2 ml. The correlation coefficient was 0.99 ($P < 0.005$).

In Vivo Validation

At rest, there was good agreement in stroke volumes between the standard flow sequence and the real-time flow sequence (Fig. 4) with a bias of -0.58 ml/cycle and limits of agreement from -4.71 to 3.56 ml/cycle. The correlation coefficient was 0.994 ($P < 0.005$). Validation during rest and exercise was also performed by comparing aortic stroke volume (measured using the real-time spiral SENSE sequence) and LV stroke volume (measured using the real-time radial *k-t* SENSE sequence). At rest, Bland-Altman assessment found a bias of -2.04 ml/cycle and limits of agreement from -8.29 to 4.21 ml/cycle. The correlation coefficient between the two data sets was 0.988 ($P < 0.005$). During exercise at 8W, Bland-Altman assessment found a bias of 0.83 ml/cycle, with limits of agreement from -4.18 to 5.84 ml/cycle and a correlation coefficient of 0.984 ($P < 0.005$). Bland-Altman assessment of the combined rest and 8W data found a bias of -0.57 ml/cycle and limits of agreement from -6.83 to 5.69 ml/cycle.

Vascular Hemodynamics During Exercise

All participants successfully completed the exercise protocol. Blood pressure and MR flow data were

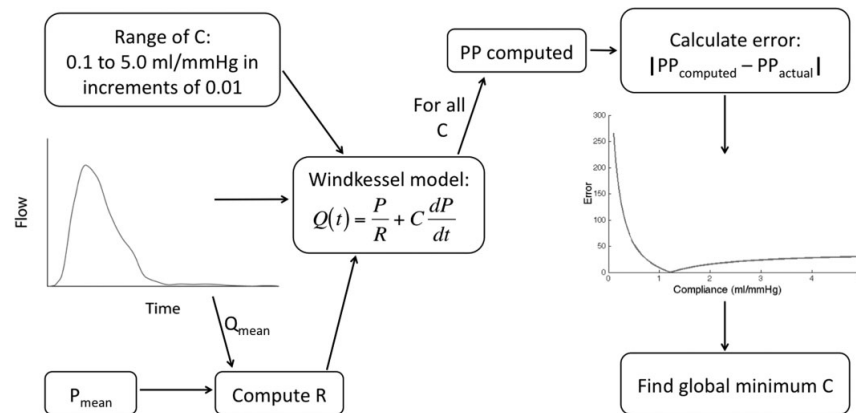


Figure 2. Diagram to show calculation of compliance.

measured successfully on all subjects at rest, and at 4W and 8W of exercise. This data was then used to calculate R and C successfully in all subjects at rest and during exercise. Figure 5 shows the average measured responses to exercise, which demonstrates the expected behavior (14). Heart rate, cardiac output, and systolic and mean blood pressure increased significantly between rest and 4W (Table 1). Conversely, R and C decreased significantly between rest and 4W (Table 1). Between 4W and 8W heart rate, cardiac output and R changed significantly. There was no change in stroke volume or diastolic blood pressure during either stage of exercise.

DISCUSSION

The main findings of this study were as follows: (i) real-time spiral SENSE MR flow is an accurate method of measuring aortic flow at rest and during exercise, and (ii) MR flow data can be successfully combined with simultaneous blood pressure measurements to quantify hemodynamic responses to exercise in healthy volunteers. Exercise may be used to unmask early signs of vascular disease in at risk groups. The ability to noninvasively measure vascular resistance and compliance further improves the sensitivity of exercise testing. Thus, this technique may allow the identification of at-risk individuals (3,4).

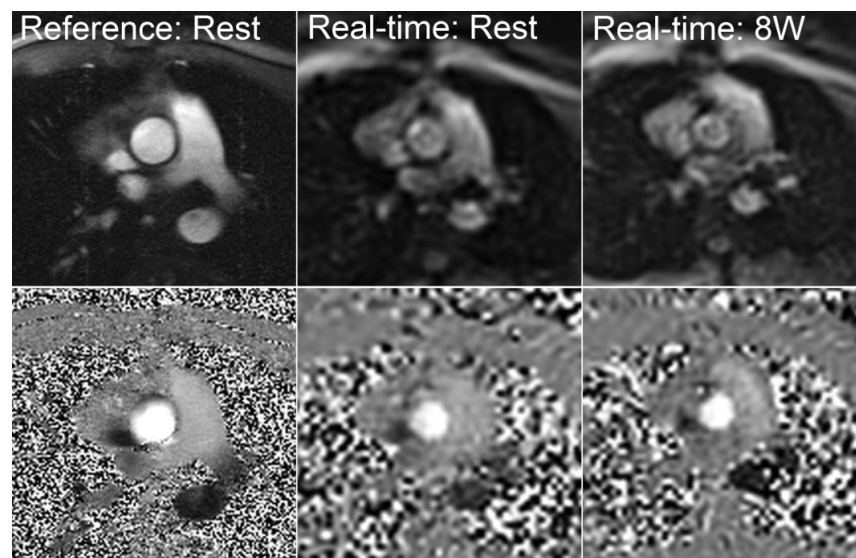


Figure 3. Magnitude (top) and phase (bottom) images from reference gated flow sequence at rest (a), real-time flow sequence at rest (b), and real-time flow sequence during exercise at 8W (c).

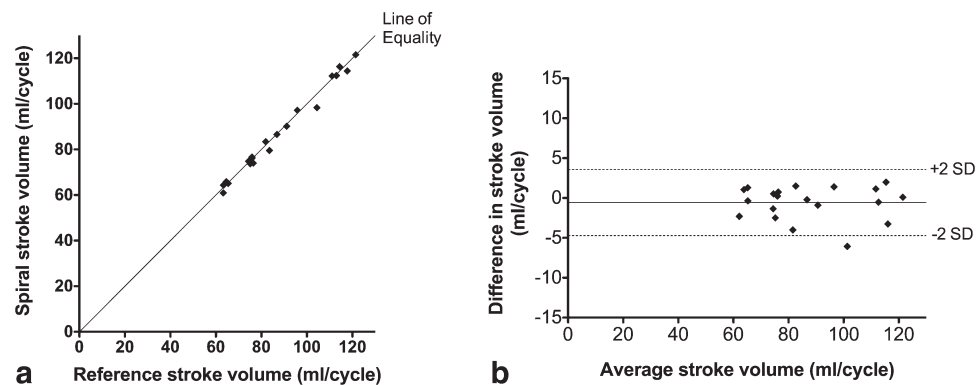


Figure 4. Comparison of aortic flow volumes at rest calculated from the reference gated flow sequence and the real-time spiral flow sequence. **a:** Correlation of flow measured from both techniques. **b:** Bland-Altman plot of the difference in flow measured using both techniques. Bias (solid line) equals mean difference between techniques. Limits of agreement (dashed lines) correspond to two standard deviations of differences between techniques.

Impedance cardiography offers an alternative method of measuring flow in real-time, however, it is often unreliable and is not as accurate as MRI.

Gated flow sequences are not reliable during exercise due to excessive motion. A more robust solution is real-time imaging (8,15). However, real-time sequences generally have a lower temporal resolution than gated sequences. This is problematic for exercise studies due to the high heart rates arising during physical stress. In this study adequate temporal resolution was

achieved in three ways. First, spatial resolution was sacrificed, requiring less coverage of k -space and thus allowing quicker filling of k -space. Second, a spiral trajectory was used, which allowed more efficient filling of k -space (16). Lastly, k -space was undersampled and reconstructed using a sensitivity encoding algorithm (10). The resultant images have a low spatial resolution with an improved high temporal resolution, and minimal residual aliasing. Increased breathing during exercise caused little visual difference in image quality

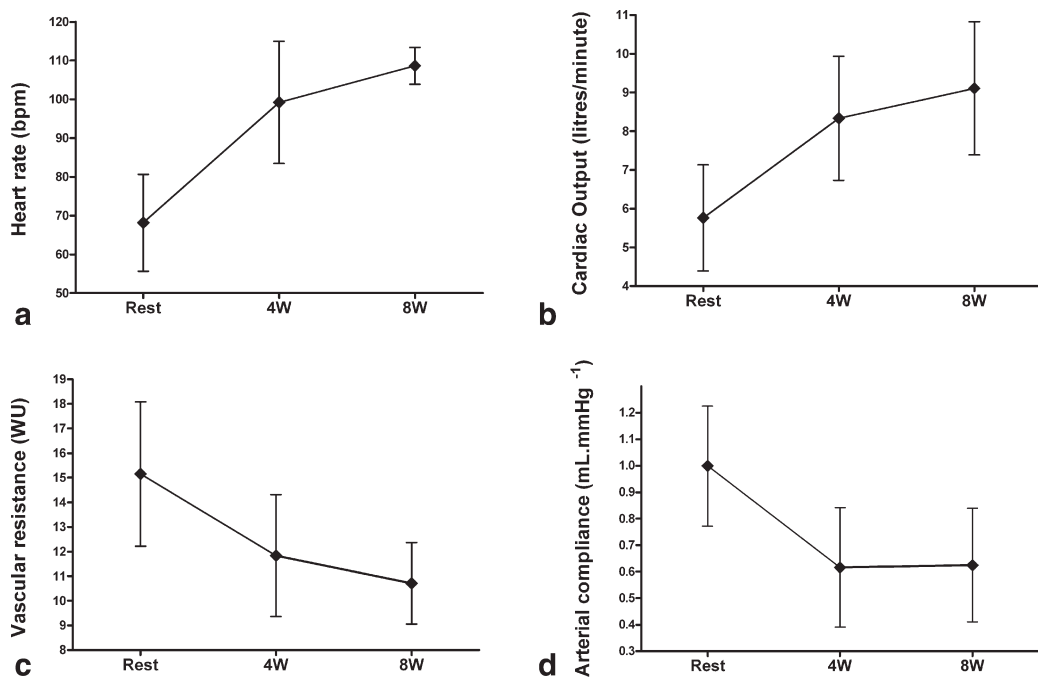


Figure 5. Measured responses to exercise. All points are mean values, and SD is shown with error bars. Effect of exercise on heart rate (a), cardiac output (b), systemic vascular resistance (c), and arterial compliance (d), showing expected behavior.

Table 1
Response to Exercise

	Rest ^a	4W ^a	8W ^a	P ^b (0W-4W)	P ^b (4W-8W)	P ^b (0W-8W)
Heart rate (bpm)	68.2 (12.5)	99.2 (15.8)	108.6 (21.2)	<.001	<.001	<.001
Stroke volume (mL·cycle ⁻¹)	87.2 (19.5)	85.1 (16.2)	85.2 (13.6)	.30	.97	.41
Cardiac output (L·min ⁻¹)	5.8 (1.4)	8.3 (1.6)	9.1 (1.7)	<.001	0.002	<.001
Systolic BP (mmHg)	112.5 (10.4)	137.2 (15.2)	134.6 (21.0)	<.001	.50	<.001
Diastolic BP (mmHg)	64.8 (6.0)	66.3 (12.3)	64.3 (13.1)	.54	.46	.85
Mean BP (mmHg)	83.9 (6.8)	95.5 (9.4)	95.3 (8.9)	<.001	.91	<.001
Vascular resistance (WU)	15.2 (2.9)	11.8 (2.5)	10.7 (1.7)	<.001	.007	<.001
Arterial compliance (mL·mmHg ⁻¹)	1.00 (0.23)	0.62 (0.23)	0.63 (0.21)	<.001	.80	<.001

^aMean from all volunteers (SD).

^bPaired t-test.

between scans acquired at rest and in exercise due to the high temporal resolution achieved. However, breathing is known to affect the stroke volume (17). In the standard flow sequence, variations in stroke volume from breathing are averaged out, however, when analyzing the real-time stroke volumes, a single flow cycle was chosen for comparison. This may explain some of the differences in flow volumes found between the two techniques.

Despite compromising the spatial resolution and using an undersampled non-Cartesian trajectory, there was good agreement with the reference flow sequence and the real-time ventricular volumes. Thus, this sequence is a robust method for assessing aortic flow during exercise.

The hemodynamic responses to exercise were calculated. Using the real-time flow sequence, we were able to demonstrate an increase in cardiac output at 4W and 8W, driven by an increase in heart rate rather than stroke volume. It has previously been observed that, in raised leg supine exercise at a low intensity level, increased cardiac output was driven by heart rate rather than stroke volume (18). The low exercise levels undertaken may explain why stroke volume did not significantly change, compared with previous supine exercise studies which have used higher exercise levels including 7.5W, 15.0W, and 22.5W (8). Nevertheless, we were able to elicit a fall in R and C in this normal population. To our knowledge, this is the first time R and C have been quantified using MR during exercise. Previously, R and C have been assessed in the pulmonary vasculature by combining MR flow data at rest and simultaneous blood pressure measurements (3,4). We have extended these well-validated techniques to the systemic vasculature during exercise. It has been hypothesized that a lower than normal fall in R in response to exercise is an indicator of early vascular disease (14,19). An excessive drop in C during exercise may also predispose patients to vascular disease. Further work is required to demonstrate abnormal vascular responses in a patient population using this technique.

There were some limitations of this study. Vascular response was only measured during mild, supine exercise. Increasing the exercise intensity may increase the sensitivity to subtle vascular abnormalities. Unfortunately, as exercise intensity increases it may become more difficult to accurately measure

blood pressure noninvasively. However, it should be noted that we were able to elicit a response during mild exercise. The other limitations of this technique are low spatial resolution and long reconstruction times. Spatial resolution could be increased by the use of a smaller FOV, which here was set high to include the arms. This could be achieved by the use of selective excitations (which would conversely decrease temporal resolution) or RF shielding of the arms. Alternative reconstruction algorithms, which take advantage of spatiotemporal correlations (e.g., kt-SENSE (20)), may allow an increase in matrix size without a large temporal penalty. Reconstruction times could be improved by the use of newer multi-processor graphics cards (21), which are well suited to complex iterative reconstruction.

In conclusion, we have shown that it is possible to measure the hemodynamic response to exercise using a combination of real-time MR flow and simultaneous blood pressure measurements.

ACKNOWLEDGMENTS

We thank Rod Jones, Wendy Norman, Joseph Panzer, and Philipp Lurz for their support.

REFERENCES

1. Singh JP, Larson MG, Manolio TA, et al. Blood pressure response during treadmill testing as a risk factor for new-onset hypertension: the Framingham Heart Study. *Circulation* 1999;99:1831-1836.
2. Hundley WG, Lange RA, Clarke GD, et al. Assessment of coronary arterial flow and flow reserve in humans with magnetic resonance imaging. *Circulation* 1996;93:1502-1508.
3. Muthurangu V, Taylor A, Andriantsimiavona R, et al. Novel method of quantifying pulmonary vascular resistance by use of simultaneous invasive pressure monitoring and phase-contrast magnetic resonance flow. *Circulation* 2004;110:826-834.
4. Muthurangu V, Atkinson D, Sermesant M, et al. Measurement of total pulmonary arterial compliance using invasive pressure monitoring and MR flow quantification during MR-guided cardiac catheterization. *Am J Physiol Heart Circ Physiol* 2005;289:H1301-H1306.
5. Pedersen EM, Kozerke S, Ringgaard S, Scheidegger MB, Boesiger P. Quantitative abdominal aortic flow measurements at controlled levels of ergometer exercise. *Magn Reson Imaging* 1999;17:489-494.
6. Roest AA, Helbing WA, Kunz P, et al. Exercise MR imaging in the assessment of pulmonary regurgitation and biventricular function in patients after tetralogy of fallot repair. *Radiology* 2002;223:204-211.

7. Pedersen EM, Stenbog EV, Frund T, et al. Flow during exercise in the total cavopulmonary connection measured by magnetic resonance velocity mapping. *Heart* 2002;87:554-558.
8. Lurz P, Muthurangu V, Schievano S, et al. Feasibility and reproducibility of biventricular volumetric assessment of cardiac function during exercise using real-time radial k-t SENSE magnetic resonance imaging. *J Magn Reson Imaging* 2009;29:1062-1070.
9. Gatehouse PD, Firmin DN, Collins S, Longmore DB. Real time blood flow imaging by spiral scan phase velocity mapping. *Magn Reson Med* 1994;31:504-512.
10. Pruessmann KP, Weiger M, Bornert P, Boesiger P. Advances in sensitivity encoding with arbitrary k-space trajectories. *Magn Reson Med* 2001;46:638-651.
11. Bernstein MA, Zhou XJ, Polzin JA, et al. Concomitant gradient terms in phase contrast MR: analysis and correction. *Magn Reson Med* 1998;39:300-308.
12. Muthurangu V, Lurz P, Critchely J, Deanfield J, Taylor A, Hansen MS. Real-time assessment of right and left ventricular volumes and function in patients with congenital heart disease by using high spatiotemporal resolution radial k-t SENSE. *Radiology* 2008;248:782-791.
13. Stergiopoulos N, Meister J, Westerhof N. Simple and accurate way for estimating total and segmental arterial compliance: the pulse pressure method. *Ann Biomed Eng* 1994;22:392.
14. Wilson MF, Sung BH, Pincomb GA, Lovallo WR. Exaggerated pressure response to exercise in men at risk for systemic hypertension. *Am J Cardiol* 1990;66:731-736.
15. Hjortdal VE, Emmertsen K, Stenbog E, et al. Effects of exercise and respiration on blood flow in total cavopulmonary connection: a real-time magnetic resonance flow study. *Circulation* 2003;108:1227-1231.
16. Park J, Santos JM, Hargreaves B, et al. Rapid measurement of renal artery blood flow with ungated spiral phase-contrast MRI. *J Magn Reson Imaging* 2005;21:590-595.
17. Sakuma H, Kawada N, Kubo H, et al. Effect of breath holding on blood flow measurement using fast velocity encoded cine MRI. *Magn Reson Med* 2001;45:346-348.
18. Frick MH, Somer T. Base-line effects on response of stroke volume to leg exercise in the supine position. *J Appl Physiol* 1964;19:639-643.
19. Ichihara Y, Ohno J, Suzuki M, Anno T, Uchino M, Nagata K. Blunt circulatory response to exercise in coronary high-risk subjects among apparently healthy Japanese. *Circulation* 2004;68:286-293.
20. Hansen MS, Baltes C, Tsao J, Kozerke S, Pruessmann KP, Eggers H. k-t BLAST reconstruction from non-Cartesian k-t space sampling. *Magn Reson Med* 2006;55:85-91.
21. Sorensen TS, Schaeffter T, Noe KO, Hansen MS. Accelerating the nonequispaced fast fourier transform on commodity graphics hardware. *IEEE Trans Med Imaging* 2008;27:538-547.

APPENDIX 2

F. Odille, J. Steeden, V. Muthurangu, and D. Atkinson

*Automatic Segmentation Propagation of the Aorta in Real-Time Phase
Contrast MRI using Nonrigid Registration*

Journal of Magnetic Resonance Imaging, 2010. In press.

Technical Note

Automatic Segmentation Propagation of the Aorta in Real-Time Phase Contrast MRI Using Nonrigid Registration

Freddy Odille, PhD,¹ Jennifer A. Steeden, MEng,^{1,2} Vivek Muthurangu, MD,² and David Atkinson, PhD^{1*}

Purpose: To assess the use of a nonrigid registration technique for semi-automatic segmentation of the aorta from real-time velocity mapping MRI.

Materials and Methods: Real-time phase contrast images were acquired to measure flow and stroke volumes in 10 subjects, during free breathing, at rest, and during exercise. A nonrigid registration algorithm was developed to propagate a manually drawn region of interest in the aorta from one frame to all other frames of the real-time sequence (148 images). Thus the technique provided a semi-automatic segmentation over the whole sequence of images. The accuracy was assessed by comparison with manual segmentations in terms of Dice overlap measures and stroke volumes (SV).

Results: Semi-automatic segmentations were comparable to manual ones (Dice score of 0.89 ± 0.04). Inter-observer reproducibility was similar for manual and semi-automatic segmentations (Dice score of 0.90 ± 0.04 in both cases, the difference was not significant). SV measurements also showed good agreement between manual and semi-automatic segmentations (correlation coefficient $r > 0.94$), and the differences were not statistically significant.

Conclusion: Although real-time phase contrast images have compromised image quality, a fast and robust segmentation of the aorta was possible using the registration-based technique.

Key Words: flow; phase contrast; segmentation; nonrigid registration

J. Magn. Reson. Imaging 2010;00:000–000.
© 2010 Wiley-Liss, Inc.

VELOCITY MAPPING IN great vessels can be achieved by phase contrast MRI (PC MRI) (1). This technique is commonly used to assess cardiac function parameters such as cardiac output, flow, or stroke volume (2,3).

Real-time velocity mapping is becoming possible thanks to recent advances including parallel imaging and non-Cartesian k -space trajectories (4). The benefits of real-time imaging are that it can be performed during free breathing and during exercise. However, in real-time imaging, there is a compromise between speed and image quality. The lower spatial resolution and signal-to-noise ratio, as well as the misalignments from frame to frame due to free breathing, make the postprocessing more challenging. Nevertheless, computer-assisted segmentation tools are desirable as high temporal resolution real-time MR can generate a large number of frames in a few cardiac cycles.

Semi-automated segmentation of vessels has been described in the past for high resolution (non-real-time) gated PC MRI sequences. Existing methods are based on adaptive thresholding (5,6), graph searching (7), or active contours (8–10). In the case of small vessels, model-based approaches have also been proposed that consist of fitting a paraboloid to the velocity profile in the vessel (11,12). Methods that use the phase information as in Alperin and Lee (6) to classify pixels with similar velocity profiles do not apply in the present application as movement of the vessel and other structures occur, thereby mixing velocity information from pixels belonging to different regions. The performance of these methods relies on a good choice of various parameters. In particular for active contours, these parameters include the initialization of the contour, the trade-off between internal and external energy of the contours, elasticity and rigidity weights, and other preprocessing steps. Transferring these approaches to real-time images is challenging. For instance, initializing the contour with limited user intervention can be difficult for real-time images as large misalignments can occur between frames. One possible solution would be to first register the images to correct for gross misalignment and, therefore, allow easy and automatic initialization of the contour.

¹Centre for Medical Image Computing, UCL Department of Medical Physics and Bioengineering, United Kingdom.

²Centre for Cardiovascular MR, UCL Institute of Child Health, London, United Kingdom.

Contract grant sponsor: UK EPSRC.

*Address reprint requests to: D.A., Room 2.04, Malet Place Engineering Building, University College London, London WC1E 6BT UK. E-mail: d.atkinson@ucl.ac.uk

Received July 15, 2010; Accepted September 15, 2010.

DOI 10.1002/jmri.22402

View this article online at wileyonlinelibrary.com.

Because image registration may be necessary for segmenting real-time free-breathing sequences, we propose an alternative segmentation strategy, based exclusively on an accurate, fully deformable (nonrigid) registration. The registration provides displacement fields that describe motion between each frame of the temporal series and a chosen reference frame. If a contour is drawn manually in the reference frame, it will be automatically propagated to other frames, resulting in a fast segmentation of the whole real-time sequence of images.

The purpose of this study is to describe a registration-based segmentation technique and to evaluate its performance in real-time PC MRI sequences at rest and during exercise. This was done by comparing the automatically propagated contours to manual segmentations by two observers.

METHODS

Study Population

Ten healthy volunteers were recruited for this study (6 males, 4 females). The mean age was 28.6 years (range: 21.9–40.8 years). Exclusion criteria were (i) cardiovascular disease (assessed by clinical history), (ii) illness that prevented exercise (i.e., joint disease), and (iii) contraindication for MR such as MR-incompatible implants or pregnancy. The local research ethics committee approved the study, and written informed consent was obtained from all volunteers.

MRI Protocol

Real-time phase contrast data were acquired on a Siemens 1.5 Tesla (T) Avanto scanner (Erlangen, Germany), using a flow-encoded spiral sequence described by Steeden et al (4). This sequence has been previously validated against a standard retrospectively gated PC MRI sequence in terms of flow measurements, in a phantom and in volunteers. The imaging plane was located in the ascending aorta as it passes the bifurcation of the pulmonary arteries. The same parameters as in Steeden et al (4) were used. In particular, the spiral trajectory was undersampled by a factor of 4, resulting in a spatial resolution of $3.9 \times 3.9 \text{ mm}^2$ and a temporal resolution of 40.4 ms/frame. The velocity encoding (VENC) was 200 cm/s.

Data were acquired at rest and during physical stress. All sequences were acquired during free breathing. Exercise was performed with an MR-compatible ergometer (MR cardiac ergometer Up/Down, Lode, Groningen, Netherlands). The subjects were placed supine in the scanner. The pedaling exercise consisted of an up- and downward motion of the pedals. Thus motion was restricted to the lower legs so that imaging was possible during the course of exercise.

Nonrigid Registration

Manual segmentation of the aorta was required in one reference frame (the choice of this reference frame is

discussed later). Other frames were then registered onto the reference frame using the nonrigid registration scheme described hereafter. Only the magnitude of the complex images was used for the registration.

The registration searches for a time sequence of two-dimensional displacement fields that best match each frame onto the reference frame. This is done by minimizing a cost function defined below. Assuming the sequence contains N_t images of size $N_x \times N_y$, we denote the magnitude image intensities by a vector ρ of length $N = N_x N_y N_t$. The displacement fields in x and y are represented by N -length vectors u_x and u_y , which allow mapping the voxels from the reference image onto those of the original (unregistered) images. The transformations associated with these fields can be represented by a sparse matrix T_{u_x, u_y} operating on the image vector. T_{u_x, u_y} has the effect of interpolating image intensity values at the locations pointed by the displacement fields.

Our formulation of the registration problem aims at minimizing the following cost function with respect to u_x and u_y :

$$C(u_x, u_y) = \text{SSD}(u_x, u_y) + \lambda R(u_x, u_y), \quad [1]$$

The first term (SSD) is the sum-of-squared-differences of the sequence of magnitude images. It is used as a dissimilarity measure to quantify misregistration errors and is defined by:

$$\text{SSD}(u_x, u_y) = \|T_{u_x, u_y} \rho - \rho_{\text{ref}}\|^2, \quad [2]$$

where ρ_{ref} is an N -length vector whose entries are the intensities of the reference frame, replicated N_t times. $\|\cdot\|$ is the Euclidian norm. The second term in Eq. [1] is an additional constraint (regularization term) imposing spatial and temporal smoothness on u_x and u_y :

$$R(u_x, u_y) = \|G_{xyt} u_x\|^2 + \|G_{xyt} u_y\|^2, G_{xyt} = \begin{bmatrix} G_x \\ G_y \\ v_0 G_t \end{bmatrix}, \quad [3]$$

G_x , G_y , and G_t are $N \times N$ sparse matrices representing gradient operators computed by forward differences in dimensions x , y , and t , respectively. The scalar term v_0 (analogous to a velocity) allows tuning of the relative weight given to smoothness in space and smoothness in time. The value of v_0 should be proportional to the maximum allowed velocity of tissues and is not related to the VENC acquisition parameter, which is the velocity upper bound of blood.

Minimizing C with respect to (u_x, u_y) is a nonlinear least-squares optimization problem which we solve iteratively using a Gauss-Newton scheme (13,14). This consists of turning the nonlinear least-squares problem into a sequence of (easier) linear least-squares problems which are solved iteratively. This means that, at each iteration, the function $\text{SSD}(u_x, u_y)$ is approximated by a linearized version around the current estimate (u_x, u_y) , and we then search for an optimal refinement $(\delta u_x, \delta u_y)$. The linearized expression is referred to in the image processing literature

as the optical flow equation (15). It involves the partial derivatives of the images ρ_x and ρ_y (spatial gradients in x and y, respectively):

$$SSD(u_x + \delta u_x, u_y + \delta u_y) \approx \left\| \begin{bmatrix} \text{diag}(\rho_x) & \text{diag}(\rho_y) \end{bmatrix} \cdot \begin{bmatrix} \delta u_x \\ \delta u_y \end{bmatrix} - \rho_{res} \right\|^2, \quad (4)$$

with the residual registration error being $\rho_{res} = T_{ux,uy} \rho - \rho_{ref}$ and with $\text{diag}(\rho_x)$ and $\text{diag}(\rho_y)$ being $N \times N$ diagonal matrices, whose diagonal elements are ρ_x and ρ_y , respectively. Thus, at each iteration k , using Eqs. [1], [3], and [4], an optimal update of the solution is given by the following least-squares solution:

$$\begin{bmatrix} \delta u_x^{opt} \\ \delta u_y^{opt} \end{bmatrix} = \arg \min_{\delta u_x, \delta u_y} C \left(u_x^{(k)} + \delta u_x, u_y^{(k)} + \delta u_y \right), \quad (5)$$

i.e.,

$$\begin{bmatrix} \delta u_x^{opt} \\ \delta u_y^{opt} \end{bmatrix} = \left(\begin{bmatrix} \text{diag}(\rho_x^2) & \text{diag}(\rho_x \rho_y) \\ \text{diag}(\rho_x \rho_y) & \text{diag}(\rho_y^2) \end{bmatrix} + \lambda \begin{bmatrix} G_{xyt}^T G_{xyt} & 0 \\ 0 & G_{xyt}^T G_{xyt} \end{bmatrix} \right)^\dagger \begin{bmatrix} \text{diag}(\rho_x) \rho_{res} \\ \text{diag}(\rho_y) \rho_{res} \end{bmatrix} - \lambda \begin{bmatrix} G_{xyt}^T G_{xyt} u_x^{(k)} \\ G_{xyt}^T G_{xyt} u_y^{(k)} \end{bmatrix}, \quad (6)$$

where the superscripts T and \dagger denote respectively the transpose and an estimated inverse. Finally the solution is updated according to:

$$\begin{bmatrix} u_x^{(k+1)} \\ u_y^{(k+1)} \end{bmatrix} = \begin{bmatrix} u_x^{(k)} \\ u_y^{(k)} \end{bmatrix} + \begin{bmatrix} \delta u_x^{opt} \\ \delta u_y^{opt} \end{bmatrix} \quad (7)$$

Propagation of the Aortic Contours

Finally the displacement fields provided by the non-rigid registration were used to propagate the manually drawn contour from the reference frame to all other frames in the sequence. The contour is described by a closed polygon, so the propagation was done by applying displacements to every vertex of the polygon. The coordinates of the polygon vertices are generally not integer values so a linear interpolation was used to compute the actual displacement to be applied. Therefore, like the aorta, all generated contours exhibit nonrigid deformations, allowing flow measures to be computed in the same manner as with manual segmentations.

Implementation Details

A rectangular ROI of size $9 \times 9 \text{ cm}^2$ was automatically selected around the manually drawn reference contour. The registration was limited to this box to save computation time. The size of the box must be such that the vessel is always contained in the box. A histogram matching was applied to all images of the time

series before running the registration. This is to make the algorithm less sensitive to intensity changes from inflow enhancement over time.

The registration was implemented in a multi-resolution manner, so that the displacement fields were initialized to zero at the first (coarser) scale. Three scales were used, corresponding to multi-resolution factors 1/4, 1/2, and 1. Images needed to be down-sampled to each of these resolution levels after Gaussian filtering (to avoid aliasing). Once convergence has been reached at a given resolution level, the displacement fields are interpolated to the next (finer) resolution level, and the process is repeated until convergence at the finest scale.

Linear interpolation was used to apply the transformations $T_{ux,uy}$, which means that $T_{ux,uy}$ had 4 non-zero elements per row. The matrix inversion involved in Eq. [6] was implemented in the form of a conjugate gradient system solver. Gauss-Seidel preconditioning was used to speed-up convergence of the conjugate gradient, and a tolerance of 10^{-3} was chosen as a stopping condition (this is a typical choice for the conjugate gradient). Gauss-Newton iterations were stopped once the norm of the residual registration error $|\rho_{res}|$ stopped decreasing. Finally, the following values were chosen as the regularization parameters:

$\lambda = 0.01 \times \left\| \begin{bmatrix} \text{diag}(\rho_x) \rho_{res} \\ \text{diag}(\rho_y) \rho_{res} \end{bmatrix} \right\|$, $v_0 = 20 \text{ cm/s}$. These parameters were determined empirically from one particular subject of the database with particularly large displacements. Parameters that gave a good compromise between accuracy and smoothness were chosen by visual inspection of the propagated contours (the amount of spatial and temporal smoothness is easily visualized in x-t space as in Figure 1). These parameters were then used for the whole study.

Software Integration

The registration-based segmentation was written in the C language. It was integrated into the open-source medical image processing software OsiriX (OsiriX Foundation, Geneva, Switzerland) as a plugin. The user interface allows setting various parameters (size of the rectangular box, resolution levels, and regularization parameters), although these were fixed for this study. Another in-house plugin allowed generation of flow curves and computation of stroke volumes. All segmented ROIs were exported and the statistical analysis was performed offline with Matlab (The MathWorks, Natick, MA).

Validation

Two observers performed manual (M_1 and M_2) and semi-automatic (A_1 and A_2) segmentations of the aorta in the 10 subjects (rest+exercise). Only a few cardiac cycles were manually segmented out of the 148 frames (47 frames per sequence on average). Only a few cardiac cycles were manually segmented out of the 148 frames (47 frames per sequence on average). The reasons for segmenting only part of the dataset

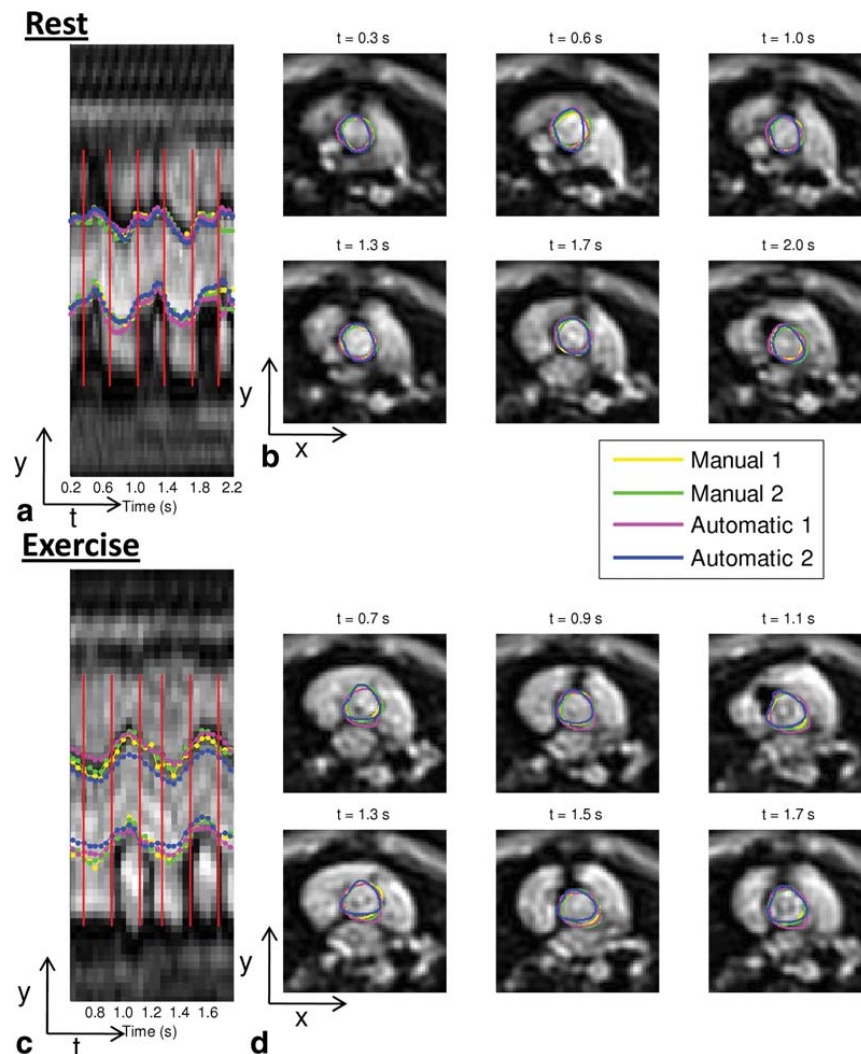


Figure 1. Example of manual and semi-automatic segmentations from two observers in a real-time PC MRI sequence. **a-d:** Data were acquired at rest (a,b) and during exercise (c,d). Segmentations are shown in a hybrid space-time view (a,c) and in various frames (c,d) chosen at times indicated by the red vertical lines. For this volunteer, Dice scores, expressed as rest/exercise values, were as follows: 0.92/0.91 (M_1 versus M_2), 0.89/0.84 (A_1 versus A_2), 0.88/0.87 (manual versus automatic, all combinations averaged).

are that (i) the manual segmentation procedure is time-consuming and (ii) the clinical parameter of interest, namely the stroke volume (SV), is computed from just one full cardiac cycle. We limited this study to SV measurements in one cardiac cycle (arbitrarily chosen in the sequence) because SV measurements from different cardiac cycles of the same subject do not provide new independent data. We validated the method at rest and during exercise when larger motion between frames may occur. In total, 930 frames were segmented. We assessed inter-observer variability for both manual and semi-automatic segmentations, and compared semi-automatic against

manual segmentations. The following criteria were used to quantify segmentation errors: (i) Dice score (16) (i.e. the intersection area divided by the mean area of the ROIs); (ii) stroke volume measurements. To quantify the “amount” of misregistration that the algorithm had to deal with, we also computed the Dice scores of ROIs propagated from frame to frame without registration (copy/paste of one manually drawn ROI). Results are expressed as mean \pm standard deviation. Statistical evaluation was performed by linear regression (correlation coefficient) and Bland-Altman analyses. Statistical significance was tested by means of Wilcoxon signed rank tests.

Table 1
Dice Overlap Measures (10 Volunteers, 930 Frames Segmented in Total)

	Manual versus automatic ^a	Manual 1 versus manual 2	Automatic 1 versus automatic 2	Manual versus unregistered ^b	Automatic versus unregistered ^c
Rest	0.886 ± 0.039	0.906 ± 0.034	0.909 ± 0.022	0.779 ± 0.110	0.804 ± 0.095
Exercise	0.886 ± 0.034	0.903 ± 0.036	0.895 ± 0.045	0.779 ± 0.096	0.806 ± 0.091

^aAverage from M₁ versus A₁, M₁ versus A₂, M₂ versus A₁, M₂ versus A₂.

^bUnregistered is a segmentation from one frame propagated to other frames without registration; Average from M₁ versus Unregistered, M₁ versus Unregistered.

^cAverage from A₁ versus Unregistered, A₁ versus Unregistered.

RESULTS

Dice Overlap Measures

Dice overlap measures are summarized in Table 1. Comparison of semi-automatic against manual segmentations resulted in Dice scores of 0.886 ± 0.039 . The reproducibility was similar for both segmentations, with mean Dice scores greater than 0.89, and similar standard deviations (0.02 to 0.04 for semi-automatic and 0.03 for manual). The difference in reproducibility was not significant ($P = 0.92$ at rest / $P = 0.43$ during exercise, when comparing the mean Dice scores obtained in $N = 10$ subjects). For comparison, an unregistered ROI resulted in much lower Dice scores and much larger standard deviations (0.779 ± 0.110 when compared with manual segmentations).

A typical example of segmentations is shown in Figure 1. Dice scores for this example were close to the averaged values shown in Table 1.

Stroke Volumes

The correlation coefficient between SV measurements, expressed as rest/exercise value, was 0.988/0.960 (M₁ versus M₂), 0.983/0.945 (A₁ versus A₂), 0.987/0.958 (manual versus semi-automatic, averaged over all combinations).

Results of the Bland-Altman analysis are presented in Table 2 and in Figure 2. The SV values obtained from manual and semi-automatic segmentation were not statistically different ($P > 0.11$ in all comparisons between manual and semi-automatic at rest or during exercise). By comparison, SV values measured from

unregistered ROIs were significantly different from both manual and semi-automated segmentations ($P < 0.01$). Inter-observer limits of agreement were slightly smaller for manual than semi-automatic segmentation, with rest/exercise values (expressed as ± 2 standard deviations) being respectively $\pm 6.6/\pm 8.2$ mL/cycle (M₁ versus M₂) and $\pm 7.9/\pm 10.1$ mL/cycle (A₁ versus A₂). However, the bias was larger for manual segmentations than for semi-automatic ones: 2.64/3.24 mL/cycle (M₁ versus M₂), 0.54/1.17 mL/cycle (A₁ versus A₂). The bias was statistically significant for manual segmentations ($P < 0.05$), but was not significant for semi-automatic segmentations.

Computation Time

The registration-based segmentation needed 10 seconds to process 148 frames (histogram matching, registration, and segmentation propagation) on an Apple MacBook Pro computer (2.8 GHz Intel Core 2 Duo processor, 4 GB RAM). For comparison, a manual segmentation of 148 frames required approximately 30 min.

DISCUSSION

In this study, we have shown that the proposed registration-based segmentation can be used to semi-automatically segment the aorta in real-time phase contrast MR images. The main advantage of this technique is that hundreds of images are able to be accurately segmented in only a few seconds, even though the images were obtained during free

Table 2
Bland-Altman Analysis of Stroke Volumes (Bias ± Standard Deviation in mL per Heart Cycle, 10 Volunteers)

	Manual versus automatic ^a	Manual 1 versus manual 2	Automatic 1 versus automatic 2	Manual versus unregistered ^b	Automatic versus unregistered ^c
Rest	0.82 ± 3.83 (P = 1.00)	2.64 ± 3.31 (P = 0.02)	0.54 ± 3.94 (P = 0.23)	13.33 ± 12.08 (P = 0.004)	14.15 ± 12.13 (P = 0.002)
	-1.36 ± 3.07 (P = 0.28)			15.97 ± 12.20 (P = 0.002)	14.69 ± 11.72 (P = 0.002)
	1.82 ± 3.11 (P = 0.11)				
Exercise	1.28 ± 3.73 (P = 0.28)	3.24 ± 4.10 (P = 0.01)	1.17 ± 5.04 (P = 0.49)	10.57 ± 9.69 (P = 0.01)	12.04 ± 8.40 (P = 0.002)
	-1.47 ± 4.52 (P = 0.23)			13.81 ± 9.18 (P = 0.002)	13.21 ± 11.25 (P = 0.01)
	-2.64 ± 5.43 (P = 0.28)				
	1.77 ± 3.35 (P = 0.11)				
	0.60 ± 3.70 (P = 0.63)				

^a Listed results include SV from M₁ versus A₁, M₁ versus A₂, M₂ versus A₁ and M₂ versus A₂.

^b Listed results include SV from M₁ versus unregistered and M₂ versus unregistered.

^c Listed results include SV from A₁ versus unregistered and A₂ versus unregistered.

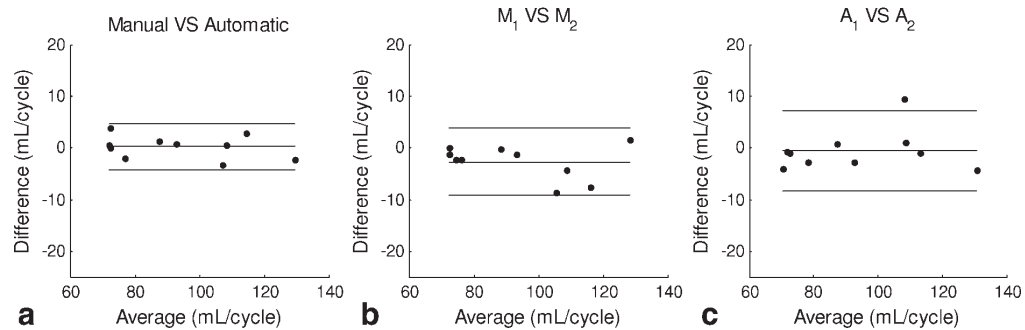
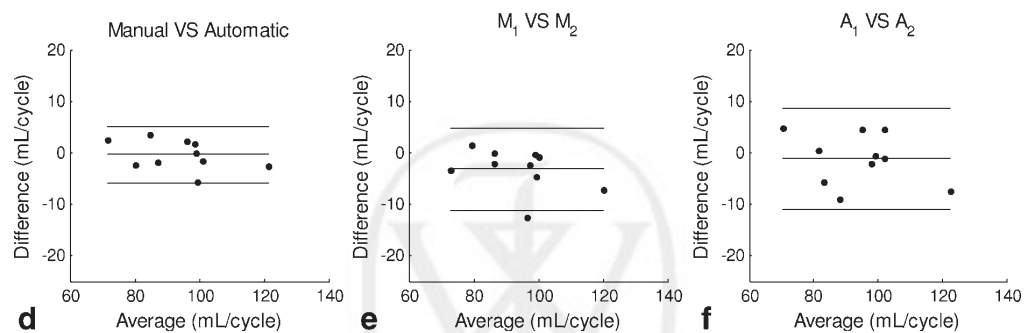
Rest**Exercise**

Figure 2. Bland-Altman analysis of the stroke volumes obtained from manual and semi-automatic segmentations (10 volunteers, segmentations from two observers). **a–f:** Data were acquired at rest (a–c) and during exercise (d–f). The graphs show comparison between manual and semi-automatic segmentations (a and d, average SV of M_1 and M_2 versus average SV of A_1 and A_2), inter-observer reproducibility of manual segmentations (b and e), and inter-observer reproducibility of semi-automatic segmentations (c and f). Plain lines indicate the bias and dashed lines indicate limits of agreement (bias \pm 1.96 standard deviation).

breathing and had relatively low spatial resolution and low signal-to-noise ratio. Because the data acquisition was in real-time, it would be desirable to also obtain flow measurements in real-time on the scanner. Here the registration was performed offline but it took only 10 s to register the aorta in a sequence of 148 images acquired in 6 s. Real-time processing should be feasible by implementing both the non-Cartesian SENSE reconstruction and the image registration on parallel architectures such as graphics processing units (GPU).

The relevance of this work is that real-time PC MRI is becoming an increasingly important tool both in the clinical and research environment. It can be used to perform pediatric cardiovascular MR without the need for general anesthetic, as well as cardiovascular MR during novel stressors such as exercise. However, although many segmentation techniques have been published for high-resolution, gated PC MRI sequences, none of these to our knowledge have been applied to real-time PC MRI. This is probably due to difficulties in transferring the segmentation schemes to low quality real-time images. With the semi-automatic method described in this study, all frames can be segmented within a matter of seconds. This is compared

with up to 30 min when segmenting the data manually.

The semi-automatic segmentations were shown to be accurate when compared with manually drawn ROIs, both in terms of Dice overlap measures and in terms of SV measures. This was true both at rest and in exercise, demonstrating that this technique works even in the presence of significant movement of the vessel in interest. The variability of the semi-automatic segmentations in terms of SV measurements was comparable to that of the manual ones (slightly higher standard deviation but lower bias). The variability of the semi-automatic segmentation is partly limited by the intrinsic variability of the manual segmentation because ROIs are propagated from a manually drawn contour. This explains why the semi-automatic method does not provide a better reproducibility. The lower bias suggests that the semi-automatic segmentation technique is less likely to suffer from systematic inter-observer error. The method seemed to be robust to regularization parameters in the sense that the same parameters were able to be used for the whole study.

Our method might either be used as it is, that is, as an alternative segmentation technique, or to complement existing segmentation techniques such as active

contours, i.e., as a preprocessing step to provide a good initial guess of the contours. Dice scores reported here are slightly lower than those reported in Herment et al (10), including those corresponding to inter-observer reproducibility of manual segmentations but this is expected due to the lower spatial resolution of our real-time sequence, resulting in less accurate delineation.

In certain situations, the registration-based method may provide suboptimal results or fail. This may occur if a "bad" reference frame is chosen from which to initialize the segmentation propagation. A "bad" reference frame is a frame which is significantly different from the other frames in the dataset, mostly due to severe through-plane motion, which would make the registration problem too difficult. However, it should be noted that in such situations, other postprocessing techniques may encounter problems as well. It is desirable for the clinician to be able to quickly visualize and potentially modify the automatically propagated contours, as is possible in this implementation. In this study, when the user was not satisfied with the segmentation, the registration was run again with a different choice of the reference frame, and no modification was performed to the contours. In this study, this only happened with one subject for which the image quality was significantly poorer, so this was not found to be a limitation. Because the registration used an SSD criterion, another possible limitation of the technique is the presence of large intensity changes over time, for example due to inflow effects. Here to minimize this effect we preprocessed the images with a histogram matching. This provided good results for this study, but histogram matching may affect matching near image gradients due to partial volume effects. The proposed technique is quite general, so it could also be applied to other segmentation propagation tasks such as the delineation of vessels in high resolution gated PC MRI or the delineation of left or right ventricular contours. The registration-based technique is expected to be particularly useful when large displacements occur due to breathing or cardiac motion for instance as this makes conventional segmentation techniques more difficult to use (e.g. initializing the contour may become challenging). Other MR images acquired in real-time are also expected to benefit from our method as they typically have low spatial resolution and low signal-to-noise ratio and exhibit various artifacts (ghosts in echo-planar imaging, gradient inhomogeneities and off-resonance artifacts in spirals, streaking artifacts in radials, etc.). Segmentation techniques such as active contours only make use of image information in a small neighborhood of the contour whereas registration makes use of information from the whole image or from a whole ROI to determine the

displacements to be applied to the contours. Therefore the registration-based technique may give acceptable results when conventional methods fail or become less robust. In conclusion, a fast and accurate registration-based technique has been developed for the semi-automated segmentation of real-time PC MRI sequences. The results were comparable to those obtained from manual segmentations. Our method allows fast processing of large series of images, which is especially suitable for studies performed during the course of exercise.

REFERENCES

1. Nayler GL, Firmin DN, Longmore DB. Blood flow imaging by cine magnetic resonance. *J Comput Assist Tomogr* 1986;10:715-722.
2. Mostbeck GH, Caputo GR, Higgins CB. MR measurement of blood flow in the cardiovascular system. *AJR Am J Roentgenol* 1992; 159:453-461.
3. Hundley WG, Lange RA, Clarke GD, et al. Assessment of coronary arterial flow and flow reserve in humans with magnetic resonance imaging. *Circulation* 1996;93:1502-1508.
4. Steeden JA, Atkinson D, Taylor AM, Muthurangu V. Assessing vascular response to exercise using a combination of real-time spiral phase contrast MR and noninvasive blood pressure measurements. *J Magn Reson Imaging* 2010;31:997-1003.
5. Burkart DJ, Felmlee JP, Johnson CD, Wolf RL, Weaver AL, Ehman RL. Cine phase-contrast MR flow measurements: improved precision using an automated method of vessel detection. *J Comput Assist Tomogr* 1994;18:469-475.
6. Alperin N, Lee SH. PUBS: pulsatility-based segmentation of lumens conducting non-steady flow. *Magn Reson Med* 2003;49: 934-944.
7. Lalonde A, van Kien PK, Salve N, et al. Automatic determination of aortic compliance with cine-magnetic resonance imaging: an application of fuzzy logic theory. *Invest Radiol* 2002;37:685-691.
8. Kozerke S, Botnar R, Oyre S, Scheidegger MB, Pedersen EM, Boesiger P. Automatic vessel segmentation using active contours in cine phase contrast flow measurements. *J Magn Reson Imaging* 1999;10:41-51.
9. Krug R, Boese JM, Schad LR. Determination of aortic compliance from magnetic resonance images using an automatic active contour model. *Phys Med Biol* 2003;48:2391-2404.
10. Herment A, Kachenoura N, Lefort M, et al. Automated segmentation of the aorta from phase contrast MR images: validation against expert tracing in healthy volunteers and in patients with a dilated aorta. *J Magn Reson Imaging* 2010;31:881-888.
11. Oyre S, Ringgaard S, Kozerke S, et al. Quantitation of circumferential subpixel vessel wall position and wall shear stress by multiple sectorized three-dimensional paraboloid modeling of velocity encoded cine MR. *Magn Reson Med* 1998;40:645-655.
12. Box FMA, Spilt A, Buchem MAV, van der Geest RJ, Reiber JHC. Automatic model-based contour detection and blood flow quantification in small vessels with velocity encoded magnetic resonance imaging. *Invest Radiol* 2003;38:567-577.
13. Modersitzki J. Numerical methods for image registration. Chapters 6 and 8. Oxford: Oxford University Press; 2004.
14. Weickert J, Bruhn A, Brox T, Papenberg N. A survey on variational optic flow methods for small displacements. In: Scherzer O, editor. *Mathematical models for registration and applications to medical imaging*. Berlin: Springer; 2006. p 103-136.
15. Horn BK, Schunck BG. Determining optical flow. *Artif Intell* 1981;17:185-203.
16. Dice LR. Measures of the amount of ecologic association between species. *Ecology* 1945;26:297-302.

APPENDIX 3

*A. Jones, J. Steeden, J. Pruessner, A. Taylor, A. Deanfield, and V. Muthurangu
Detailed Assessment of The Hemodynamic Response to Psychosocial Stress
using Real-Time MRI
Journal of Magnetic Resonance Imaging, 2010. In Press.*

Technical Note**Detailed Assessment of the Hemodynamic Response to Psychosocial Stress Using Real-Time MRI**

Alexander Jones, PhD,^{1,3*} Jennifer A. Steeden, MEng,¹ Jens C. Pruessner, PhD,² John E. Deanfield, MB,³ Andrew M. Taylor, MD,¹ and Vivek Muthurangu, MD¹

Purpose: To demonstrate that combining the Montreal Imaging Stress Task (MIST) with real-time cardiac magnetic resonance imaging (MRI) allows detailed assessment of the cardiovascular mental stress response.

Materials and Methods: In all, 22 healthy volunteers (1:1 M:F, 26–64 years) underwent MRI during rest and the MIST. Real-time spiral phase contrast MR, accelerated with sensitivity encoding (SENSE) was used to assess stroke volume (SV), and radial k-t SENSE was used to assess ventricular volumes. Simultaneous heart rate (HR) and blood pressure (BP) measures allowed calculation of cardiac output (CO), systemic vascular resistance (SVR), and arterial compliance (TAC). Endocrine responses were assessed using salivary cortisol.

Results: In response to stress, BP increased due to increased CO and reduced TAC but not increased SVR, which fell. HR, not SV, determined CO increases. Greater BP responses occurred in men due to greater CO increases and relatively higher SVR. Older participants had greater BP responses due to greater falls in TAC. Greater cortisol response was correlated with greater falls in TAC but resting cortisol and TAC were not related.

Conclusion: This new approach allows detailed, accurate assessment of stress physiology. Preliminary findings suggest stress exposes relationships, not seen at rest, of cardiovascular function with age, sex, and endocrine function.

Key Words: mental stress; real-time MR; cardiovascular; physiology; cortisol

J. Magn. Reson. Imaging 2010;000:000-000.
© 2010 Wiley-Liss, Inc.

MENTAL STRESS is a potent stimulator of the cardiovascular system and has been linked to a number of cardiovascular diseases (1–5). Characterization of the cardiovascular response to mental stress is crucial for understanding the underlying mechanisms. Traditionally, heart rate (HR) and blood pressure (BP) are the main parameters of investigation, although they do not fully describe hemodynamic responses. A comprehensive approach would include measurement of cardiac output (CO), systemic vascular resistance (SVR), total arterial compliance (TAC), and ventricular function. Very different modulation of these parameters may result in identical BP responses but with dissimilar health implications.

Cardiac magnetic resonance imaging (MRI) is the reference standard method of measuring CO and ventricular function and MR data can be combined with BP to calculate SVR and TAC (6–8). Unfortunately, standard cardiac-gated sequences have limitations that make them unsuitable for mental stress studies. These include: requirement for multiple breatholds, long acquisition times, and intolerance to nonperiodic motion. Thus, MR has not been used to assess cardiovascular responses to mental stress. However, development of high temporal resolution real-time MR sequences makes this possible. Previous studies have shown the suitability of this approach by measuring the cardiovascular response to exercise (9).

Another necessary component for this approach is a stress task suitable for an MR environment. The Montreal Imaging Stress Task (MIST) was developed for neuroimaging functional MRI studies (10). Since the MR environment is confined and allows limited interaction with participants, the MIST was designed to overcome these impediments and incorporate crucial elements required to evoke a neuroendocrine stress response (11). These are: ego-involvement (participants must engage with the task and care about the result); social evaluative threat (participants must feel that their performance will be judged by others, and that this judgment will be negative if they perform poorly); and uncontrollability (participants must feel that they have limited authority to alter the sequence of events during the task).

The principal aim of this study was to demonstrate that a combination of the MIST with real-time cardiac

¹Centre for Cardiovascular MR, UCL Institute of Child Health & Great Ormond Street Hospital for Children, London, United Kingdom.

²Douglas Institute, Department of Psychiatry, McGill University, Montreal, Quebec, Canada.

³Department of Vascular Physiology, UCL Institute of Child Health, London, United Kingdom.

Contract grant sponsor: National Institute for Health Research (UK) Specialist Biomedical Research Centre (to A.J.); National Institute for Health Research (UK) (to A.M.T.); Contract grant sponsor: BHF (to V.M.).

*Address reprint requests to: A.J., Cardiovascular Unit, Great Ormond Street Hospital, Great Ormond Street, London WC1N 3JH, UK. E-mail: alexander.jones@ich.ucl.ac.uk

Received August 4, 2010; Accepted October 20, 2010.

DOI 10.1002/jmri.22438

View this article online at wileyonlinelibrary.com.

MR was feasible to enable a detailed assessment of the cardiovascular response to mental stress. Secondary aims were to assess age and sex differences in the responses and associations with endocrine stress responses. To demonstrate broad applicability, this novel methodology was tested in a wide age range of healthy adult men and women.

MATERIALS AND METHODS

Study Population

Twenty-two healthy nonsmoking volunteers (11 men and 11 women) with a median age of 36.2 (range 25.9–63.7) years were recruited. Participants with cardiovascular disease, endocrine disorders of the hypothalamic–pituitary axes, or contraindications for MR, such as pregnancy or MR-incompatible implants, were excluded. The study was approved by the local research ethics committee and informed, written consent was obtained from all participants.

Montreal Imaging Stress Task

Mental arithmetic tasks were displayed on a computer screen (Fig. 1), visible to the participants by way of a mirror. Answers were selected from a circularly arranged set of numbers (0–9) using a fiberoptic mouse. A loud and unpleasant noise was played in response to an incorrect answer or a timeout. Pointers on a multicolored “performance” bar continuously indicated both participant performance and that of an “average performance” of a “peer group.” The three colored regions of this bar indicated poor (red), mediocre (yellow), and good (green) performance. Participants were asked to reach at least “average performance” to ensure useful data collection. They were also told that they would be scored and judged by the investigators. To increase performance pressure, a high-tempo musical track was played through headphones throughout the task.

Unknown to participants, the computer responded to correct answers by increasing the difficulty and reducing the time available for the questions, and the “average performance” was not of a peer group but was computer-generated. Thus, regardless of competence, participant performance was negatively biased such that they appeared to perform poorly in comparison to their “peer group.” During salivary cortisol collection between the two stress periods, their attention was directed to the performance indicators by the investigator and it was restated that a poor performance would not provide useful data. This ensured participant perception of their poor performance and of the possibility of negative judgment, stimulating a stress response. Importantly, upon completion of the protocol all participants were informed that their poor performance was artificial and that their data was useful.

Protocol

All imaging was performed on a 1.5 T MR scanner (Avanto, Siemens Medical Solutions, Erlangen, Ger-

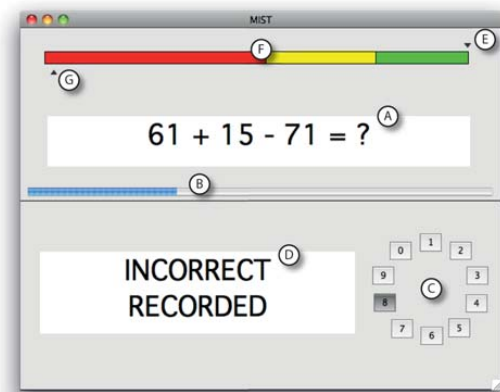


Figure 1. A screenshot of the MIST, showing (A) an example mathematical problem, (B) a blue timer bar advancing from left to right, (C) a rotary dial for selecting answers (0–9), and (D) a feedback box stating that the answer was “Incorrect.” The “peer” indicator (E) is above the colored bar (F) and in the green zone, suggesting a good performance and the participant’s own indicator (G) is below the bar in the red zone, suggesting a poor performance. Provision of a proxy of peer performance is designed to enhance social evaluative threat.

many) using two spine coils and one body-matrix coil (giving a total of 12 coil elements). This is the standard coil configuration for cardiac MRI at our institution.

The mental stress protocol was: 1) a 1-minute practice session, with no scoring, time limits, or evaluation; 2) two consecutive 5-minute stress periods with scoring, time limits, and evaluation; 3) a recovery period beginning 25 minutes after the onset of the first stress period. Participants were told to rest after the termination of the stress protocol. Oscillometric BP was measured in the nondominant arm at 1-minute intervals. MR data were acquired on six occasions: at rest, at 1 and 3 minutes into the two 5-minute stress periods, and finally during the recovery period. Each MR data acquisition lasted ≈ 30 seconds.

Real-Time Volume Assessment

Ventricular volumes were assessed using a real-time radial k-t SENSE sequence (field of view [FOV]: ≈ 380 mm, matrix: 128×128 , voxel size: $\approx 3.0 \times \approx 3.0 \times 10$ mm, TE/TR: $\approx 1.14/\approx 2.3$ msec, flip angle: 38° , pixel bandwidth [BW]: 1500 Hz/pixel, radial spokes: 128, k-t SENSE acceleration factor: 8, scan time: ≈ 1.5 seconds per slice, temporal resolution: ≈ 35.5 msec). Eleven to 13 contiguous slices were acquired in the short axis to ensure coverage of the ventricle. Image acquisition was performed during free breathing.

Real-Time Flow Assessment

Real-time flow quantification was performed through-plane in a cross-section of the ascending aorta as it

passes the bifurcation of the pulmonary arteries. A uniform density spiral PC sequence with eight interleaves, undersampled by a factor of four was used (matrix: 128×128 , voxel size: $3.9 \times 3.9 \times 6$ mm, TE/TR: 1.93/9.63 msec, flip angle: 25° , pixel BW: 1860 Hz/pixel, VENC: 180 cm/s, temporal resolution: 38.5 msec) (9). For each scan, 76 consecutive frames were acquired over 3 seconds. The sampling pattern was rotated for each frame so that four consecutive frames comprised a fully sampled k -space with eight interleaves. These undersampled data were reconstructed offline using an iterative SENSE algorithm. In order to reconstruct undersampled spiral data using iterative SENSE, the FOV must be larger than the object. In this study of adults, the FOV was set at 500 mm due to double oblique slice angulations. All coil sensitivity and regularization information required for the reconstruction process was calculated from the sum-of-squares of the coil data over all time frames.

Data Processing

All images were processed using in-house plug-ins for the open-source software OsiriX (OsiriX Foundation, Geneva, Switzerland). Measurement of ventricular volumes was performed as previously described (12,13). Flow images were manually segmented (using the modulus images) and SV and CO were measured. SVR (measured in $\text{mmHg.L}^{-1}.\text{min}^{-1}$, also known as WU) was calculated by dividing the mean blood pressure by CO. Compliance was calculated by optimization of a two-element windkessel model, as previously described (7,8). Briefly, CO, mean arterial pressure, and SVR were used as inputs to a windkessel model. Pulse pressure was calculated for a series of modeled pressure curves generated using a range of compliance values from 0.1 to 5.0 mL.mmHg^{-1} in increments of 0.01. The compliance value that gave the smallest error between the modeled pulse pressure and the true pulse pressure was taken to be the true compliance.

Salivary Cortisol

Using established protocols, six saliva samples were obtained during the course of the experiment (Salivette Cortisol, Sarstedt, Nümbrecht, Germany): just after the first rest period, and then at median delays of 5, 12, 24, and 34 minutes following the onset of the first stress period (Fig. 2). Concentration of salivary free cortisol was measured using a commercially available chemiluminescence-immuno-assay (CLIA; IBL, Hamburg, Germany).

Statistical Analysis

For all statistical tests, P -values below 0.05 were taken to be significant. Where possible, right-skewed variables were log-transformed prior to parametric testing. If transformation to normality could not be achieved, nonparametric comparisons were made using Wilcoxon rank-sum tests. Where multiple comparisons were made for time-series data, significance thresholds were Bonferroni-adjusted. For the purpose

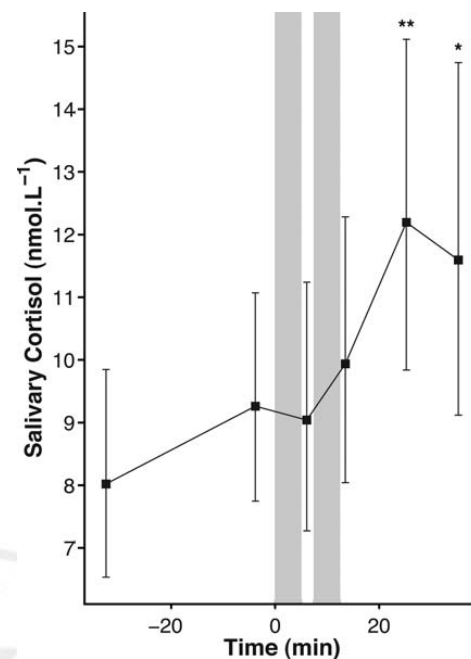


Figure 2. Geometric mean \pm 95% confidence interval (CI) salivary cortisol at rest and in response to two 5-minute periods of stress (vertical gray bars). * $P < 0.01$, ** $P < 0.002$ for pair-wise 2-sided t -test comparisons of mean values at each timepoint with initial values. P -value thresholds were Bonferroni-corrected to account for five comparisons.

of calculating cardiovascular stress responses, mean values across both stress periods were used. Pearson partial correlation was used to examine relationships of cardiovascular parameters with age and cortisol, adjusting for age and sex as necessary. Cortisol stress response (CSR) was defined as the difference between the greater of the cortisol concentrations at timepoints 5 and 6 and the lowest value at timepoints 1–3 (see Fig. 2). To account for decline throughout the day as part of diurnal rhythm, salivary cortisol measures were adjusted by removing the inverse linear relationship between time of day and log-transformed cortisol concentration ($r = -0.31$, $P = 0.0002$). End-diastolic volume (EDVi), stroke volume (SVi), cardiac output (COi), systemic vascular resistance (SVRi), and total arterial compliance (TACi) were indexed to body surface area (BSA).

RESULTS

Image quality at rest and during stress was very similar and all data was suitable for analysis. Figure 3 shows representative images from the real-time sequences.

Cardiovascular Response to MIST

Arterial BP (systolic [SAP], mean [MAP], and diastolic [DAP] arterial pressures), COi, and HR all increased in response to mental stress (all $P < .00025$). SVRi and

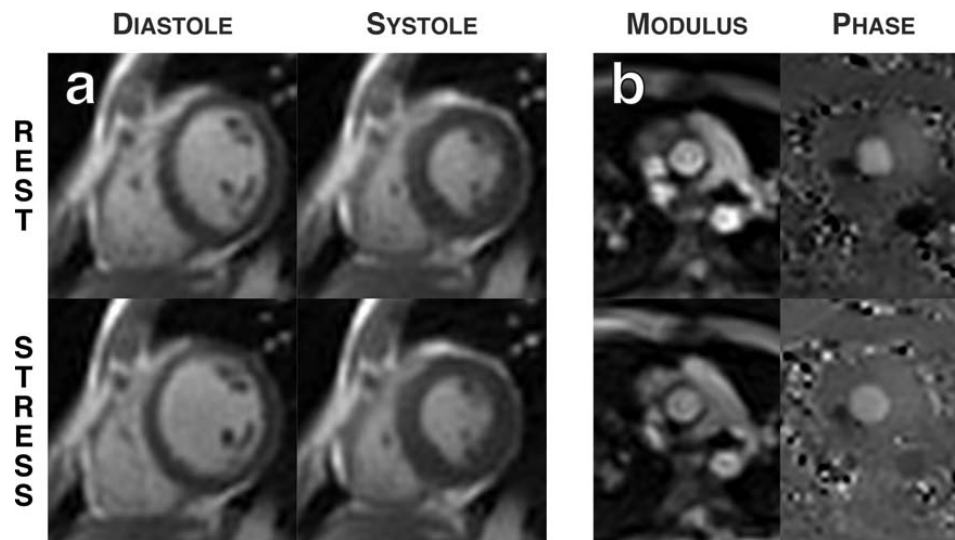


Figure 3. Examples of the (a) real-time radial k-t SENSE sequence at end diastole and end systole, and of the (b) uniform density spiral PC sequence show no appreciable evidence of an effect of stress on image quality.

TACi both fell significantly during stress (Fig. 4). Other cardiovascular parameters did not change significantly. TACi and DAP remained significantly reduced during recovery, while other parameters returned to baseline. The second stress period provoked a significant incremental response of HR, COi, SVRi, and TACi in comparison to the first (Fig. 4).

Sex and Age Differences

Men were taller (median: 182 vs. 162 cm; $P = 0.0002$) and heavier (median: 78 vs. 61 kg; $P = 0.002$) than women, but there were no sex differences in age, BMI (median: 23.6 [range: 20.2–30] in men vs. 23 [19.2–27.3] in women; $P = 0.41$) or proportion of overweight participants. At rest, men had a trend towards lower HR, significantly lower COi, and greater SVRi than women, but no difference in BP (Table 1). During mental stress and recovery, men had greater BP (SAP, MAP, and DAP), with no significant difference in COi and SVRi during stress. They had higher SVRi during recovery. However, the increase in COi in men was significantly greater than that in women when adjusted for SVRi during stress ($P = 0.02$). The other parameters did not differ by sex during rest or stress.

During stress, greater age was associated with higher SAP ($r = 0.47$, $P = 0.03$), a trend towards higher MAP ($r = 0.4$, $P = 0.07$), and lower TACi ($r = -0.45$, $P = 0.04$). During rest and recovery, these parameters did not correlate with age. Age was also correlated with DAP during recovery ($r = 0.55$, $P = 0.01$) but not significantly so during rest or stress. EDVi was inversely related to age at rest ($r = -0.56$, $P = 0.008$) and recovery ($r = -0.55$, $P = 0.009$) but not significantly so during stress ($r = -0.39$, $P = 0.08$). EF was positively correlated with age at all

times (rest: $r = 0.63$, $P = 0.002$; stress: $r = 0.5$, $P = 0.02$; recovery: $r = 0.75$, $P = 0.0001$).

Endocrine Response to MIST

The MIST provoked a CSR in all cases. Geometric mean salivary cortisol levels rose by 48%, peaked 24 minutes after stress onset, and were still raised significantly at 34 minutes (Fig. 2). Response magnitude varied widely from 0.2 to 24.1 nmol.L⁻¹. There were no age or sex differences in baseline cortisol or CSR.

There was a significant inverse association between CSR and TACi during stress ($r = -0.59$, $P = 0.006$) and recovery ($r = -0.48$, $P = 0.03$), but not rest ($r = -0.32$, $P = 0.17$). HR was strongly, positively correlated with CSR at all times (rest: $r = 0.54$, $P = 0.01$; stress: $r = 0.65$, $P = 0.002$; recovery: $r = 0.60$, $P = 0.005$). CSR was correlated inversely with EDVi at all times (rest: $r = -0.59$, $P = 0.006$; stress: $r = -0.61$, $P = 0.004$; recovery: $r = -0.54$, $P = 0.01$) and with SVi at rest ($r = -0.50$, $P = 0.02$).

DISCUSSION

The key findings in this study were: 1) It was possible to comprehensively assess the cardiovascular response to mental stress using a combination of the MIST and real-time cardiac MR; 2) The cardiovascular mental stress response differed by age and sex; 3) The MIST produces an endocrine stress response in addition to the cardiac response; 4) Endocrine and cardiovascular responses correlated.

Recent meta-analysis has shown that the weight of evidence supports an association between greater mental stress responses and poor cardiovascular outcomes (14) but many studies have failed to

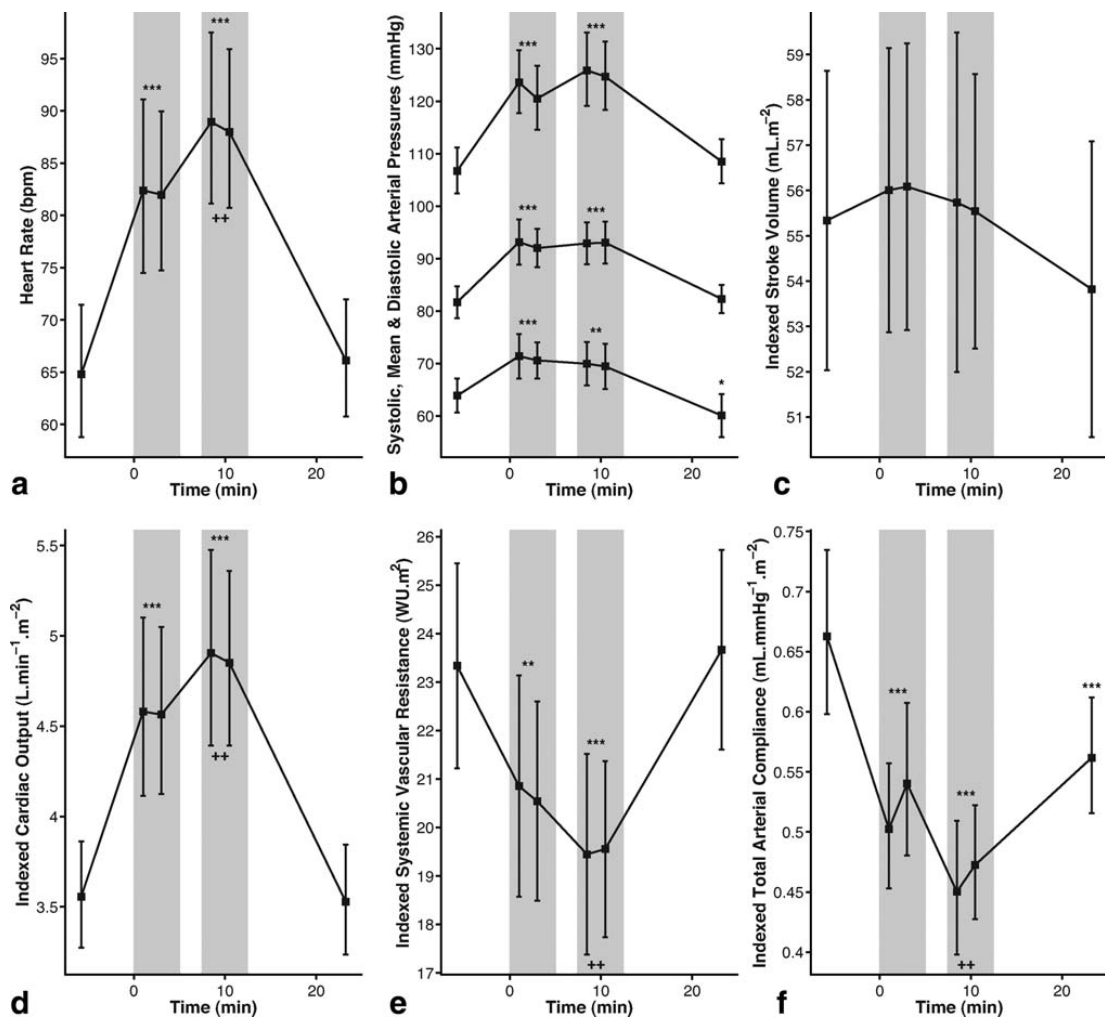


Figure 4. Mean \pm 95% CI values (geometric values for **a,d,f**, and systolic arterial pressure in **b**) at rest and in response to two 5-minute periods of stress (vertical gray bars) for (a) heart rate; (b) systolic, mean, and diastolic arterial pressure; (c) stroke volume indexed to body surface area (BSA); (d) cardiac output indexed to BSA; (e) systemic vascular resistance indexed to BSA and (f) total arterial compliance indexed to BSA. * $P < 0.0125$, ** $P < 0.0025$, *** $P < 0.00025$ for pair-wise 2-sided t -test comparisons of mean values during each stress period, or the recovery period, with those at rest. ++ $P < 0.0025$ for pair-wise 2-sided t -test comparisons of values during first and second stress periods. P -value thresholds were Bonferroni-corrected to account for four comparisons per variable.

demonstrate this, leading to controversy. Such studies have often relied on limited cardiovascular parameters (BP and HR) and unreliable mental stress paradigms. This may explain their inability to demonstrate associations between mental stress and cardiovascular risk. To improve the quality of future studies, an approach like ours, which can assess the cardiovascular response to mental stress accurately and comprehensively, is required. Such assessment should include measures of ventricular function, CO, SVR, and TAC. These measures have previously been attempted using techniques such as echocardiography (with Doppler), pulse waveform analysis, and tho-

racic impedance cardiography. However, none of these can accurately assess both the cardiac and vascular response to mental stress with the same level of accuracy as MRI. A better approach is real-time cardiac MR, a proven method of assessing the cardiovascular system. The benefits of real-time over gated MR are that: 1) it is fast, allowing frequent measurements during stress; 2) breatholding, which alters physiology, is not required; 3) it is less susceptible to the participant motion that often occurs during mental stress. Its disadvantages are that it has reduced image quality, lower spatial resolution, and poorer temporal fidelity than gated cardiac MR. However, the

Table 1
Mean (SD) Cardiovascular Measures During Rest, Stress, and Recovery

	Women (n = 11)			Men (n = 11)			P-values ^a		
	Rest	Stress ^b	Recovery	Rest	Stress ^b	Recovery	Rest	Stress	Recovery
	HR (bpm) ^c	70.3 (1.28)	90.4 (1.24)**	70.0 (1.23)	59.7 (1.17)	80.6 (1.18)***	62.4 (1.18)*	0.081	0.18
SAP (mmHg) ^c	104.3 (1.10)	118.2 (1.10)***	104.4 (1.06)	109.2 (1.10)	129.8 (1.12)***	112.8 (1.10)**	0.25	0.045	0.034
MAP (mmHg)	80.3 (7.4)	89.0 (7.6)***	79.7 (5.0)	83.1 (6.2)	96.9 (8.2)***	85.0 (6.1)	0.34	0.030	0.035
DAP (mmHg)	62.1 (8.8)	65.9 (6.5)*	56.2 (9.1)**	65.7 (5.3)	75.2 (8.5)***	64.0 (8.0)	0.26	0.0091	0.047
COi (L·min ⁻¹ ·m ⁻²) ^c	3.87 (1.20)	4.90 (1.28)**	3.75 (1.21)	3.27 (1.16)	4.56 (1.22)***	3.32 (1.21)	0.029	0.47	0.15
SVRI (WU·m ⁻²)	21.0 (3.9)	18.7 (4.5)*	21.6 (4.4)	25.7 (4.5)	21.6 (3.9)**	25.7 (4.1)	0.017	0.12	0.033
SVi (mL·m ⁻²)	55.4 (6.9)	54.6 (6.7)	54.0 (7.7)	55.3 (8.3)	56.9 (7.2)	53.6 (7.4)	0.97	0.45	0.91
EDVi (mL·m ⁻²)	69.6 (9.0)	72.0 (8.9)	73.0 (7.3)*	74.7 (12.9)	79.5 (14.7)*	73.8 (12.1)	0.30	0.16	0.85
EF (%)	80.2 (10.2)	76.4 (7.4)	74.1 (8.1)**	74.6 (7.3)	72.8 (8.6)	73.5 (9.4)	0.15	0.31	0.87
TACi (mL·mmHg ⁻¹ ·m ⁻²) ^c	0.61 (1.20)	0.46 (1.20)**	0.53 (1.20)**	0.72 (1.30)	0.53 (1.28)***	0.59 (1.22)**	0.11	0.13	0.21

^aP-values refer to 2-sided t-test comparisons between sexes.

^bMean of all four measures during stress.

^cGeometric means and SDs.

*P < 0.05.

**P < 0.01.

***P < 0.001 for within-sex 2-sided t-test comparisons with mean value at rest.

two real-time sequences used in this study have been validated successfully against reference standard gated techniques at rest (9,12). Importantly, they have also been shown to be accurate and reproducible during exercise, which produces a similar cardiovascular response to mental stress, associated with a significant increase in heart rate (9,13). Thus, we believe that these techniques are suitable for assessment of ventricular function and aortic flow during mental stress.

This study is the first demonstration of real-time cardiac MR characterization of the mental stress response. We showed that the BP response was associated with increased CO and vascular stiffening. HR rather than SV drove the increased CO. Age and sex differences in the cardiovascular stress response were analyzed in order to demonstrate the potential utility of this approach in mechanistic studies. We showed that the greater BP responses in men were due to a greater increase in COi and higher SVRI. Similarly, correlation between age and SAP during stress was partly explained by lower TACi. Such differences were not apparent at rest and highlight the importance of a stressor for unmasking important physiological mechanisms. For this reason, we believe that MR assessment of the cardiovascular response to mental stress will be useful in future prognostic and mechanistic studies.

A vital part of our approach is the use of a suitable stress test. Although existing tasks such as serial subtraction or the Stroop color-word interference task are possible in the confines of an MR scanner, they do not stimulate the cardiovascular and endocrine systems reliably (11). The MIST was specifically designed for an MR environment and contains elements designed to enhance motivation, social evaluative threat, and uncontrollability. We have shown that the MIST produces a marked cardiovascular response with a significant endocrine response in most participants. This is important because the strongest epidemiological evidence linking life stress with cardiovascular disease comes from studying life stresses that have elevated cortisol as a typical feature (15–17). Thus, the MIST offers an opportunity to examine a stress response that is known to be associated with disease.

Interestingly, endocrine responsiveness was associated with increased arterial stiffening during stress. However, cortisol and TACi were unrelated at rest, implying that cortisol does not directly control arterial compliance, although it may potentiate or prolong the vascular response. These links between the endocrine and cardiovascular system warrant further examination and importantly may only be elucidated using a stress paradigm.

In conclusion, we present a novel method for measuring the cardiovascular response to stress in a comprehensive, reliable, and accurate way. Even in this small study, we have shown associations between the cardiovascular response and participant characteristics. Thus, our method shows promise as a tool to bring greater understanding of the mechanisms underlying the links between mental stress and the development of cardiovascular disease.

ACKNOWLEDGMENTS

We thank Rod Jones, Wendy Norman, Jacob Salmon, Stuart Stagg, and Michael Hansen for valuable contributions to the study.

REFERENCES

1. Ely D, Caplea A, Dunphy G, Smith D. Physiological and neuroendocrine correlates of social position in normotensive and hypertensive rat colonies. *Acta Physiol Scand Suppl* 1997;640:92-95.
2. Mormede P. Genetic influences on the responses to psychosocial challenges in rats. *Acta Physiol Scand Suppl* 1997;640:65-68.
3. Lawler JE, Barker GF, Hubbard JW, Schaub RG. Effects of stress on blood pressure and cardiac pathology in rats with borderline hypertension. *Hypertension* 1981;3:496-505.
4. Sanders BJ, Lawler JE. The borderline hypertensive rat (BHR) as a model for environmentally-induced hypertension: a review and update. *Neurosci Biobehav Rev* 1992;16:207-217.
5. Anderson DE, Kearns WD, Worden TJ. Potassium infusion attenuates avoidance-saline hypertension in dogs. *Hypertension* 1983;5:415-420.
6. Hundley WG, Lange RA, Clarke GD, et al. Assessment of coronary arterial flow and flow reserve in humans with magnetic resonance imaging. *Circulation* 1996;93:1502-1508.
7. Stergiopoulos N, Meister JJ, Westerhof N. Simple and accurate way for estimating total and segmental arterial compliance: the pulse pressure method. *Ann Biomed Eng* 1994;22:392-397.
8. Pedersen EM, Kozerke S, Ringgaard S, Scheidegger MB, Boesiger P. Quantitative abdominal aortic flow measurements at controlled levels of ergometer exercise. *Magn Reson Imaging* 1999;17:489-494.
9. Steeden JA, Atkinson D, Taylor AM, Muthurangu V. Assessing vascular response to exercise using a combination of real-time spiral phase contrast MR and noninvasive blood pressure measurements. *J Magn Reson Imaging* 2010;31:997-1003.
10. Dedovic K, Renwick R, Mahani NK, Engert V, Lupien SJ, Pruessner JC. The Montreal Imaging Stress Task: using functional imaging to investigate the effects of perceiving and processing psychosocial stress in the human brain. *J Psychiatry Neurosci* 2005;30:319-325.
11. Dickerson SS, Kemeny ME. Acute stressors and cortisol responses: a theoretical integration and synthesis of laboratory research. *Psychol Bull* 2004;130:355-391.
12. Muthurangu V, Lurz P, Critchely JD, Deanfield JE, Taylor AM, Hansen MS. Real-time assessment of right and left ventricular volumes and function in patients with congenital heart disease by using high spatiotemporal resolution radial k-t SENSE. *Radiology* 2008;248:782-791.
13. Lurz P, Muthurangu V, Schievano S, et al. Feasibility and reproducibility of biventricular volumetric assessment of cardiac function during exercise using real-time radial k-t SENSE magnetic resonance imaging. *J Magn Reson Imaging* 2009;29:1062-1070.
14. Chida Y, Steptoe A. Greater cardiovascular responses to laboratory mental stress are associated with poor subsequent cardiovascular risk status: a meta-analysis of prospective evidence. *Hypertension* 2010;55:1026-1032.
15. Steptoe A, Siegrist J, Kirschbaum C, Marmot M. Effort-reward imbalance, overcommitment, and measures of cortisol and blood pressure over the working day. *Psychosom Med* 2004;66:323-329.
16. Bosma H, Peter R, Siegrist J, Marmot M. Two alternative job stress models and the risk of coronary heart disease. *Am J Public Health* 1998;88:68-74.
17. Kuper H, Singh-Manoux A, Siegrist J, Marmot M. When reciprocity fails: effort-reward imbalance in relation to coronary heart disease and health functioning within the Whitehall II study. *Occup Environ Med* 2002;59:777-784.

Author Proof

APPENDIX 4

J.A. Steeden, D. Atkinson, A.M. Taylor, and V. Muthurangu

Split-Acquisition Real-time CINE Phase-Contrast MR Flow Measurements

Magnetic Resonance in Medicine, 2010. 64(6): p. 1664.

Split-Acquisition Real-Time CINE Phase-Contrast MR Flow Measurements

Jennifer A. Steeden,^{1,2} David Atkinson,¹ Andrew M. Taylor,² and Vivek Muthurangu^{2*}

The temporal and spatial resolution of real-time phase-contrast magnetic resonance (PCMR) is restricted by the need to acquire two interleaved phase images. In this article, we propose a split-acquisition real-time CINE PCMR technique, where the acquisition of flow-encoded and flow-compensated data is divided into separate blocks. By comparing magnitude images, automatic matching of data in cardio-respiratory space allows subtraction of background phase offsets. Thus, the data is acquired in real-time but with phase correction originating from a different heart beat. This effectively doubles the frame rate, allowing either higher temporal or spatial resolution. Two split-acquisition sequences were tested: one with high-temporal resolution and one with high-spatial resolution. Both sequences showed excellent agreement in stroke volumes in 20 adults when validated against cardiac-gated PCMR and interleaved real-time PCMR (cardiac gated: 95.2 ± 20.0 mL, interleaved real-time: 96.2 ± 20.7 mL, high-temporal resolution: 95.6 ± 20.1 mL, high-spatial resolution: 95.5 ± 20.4 mL). In six children, the high-spatial resolution sequence provided more accurate flow measurements than interleaved real-time PCMR, when compared with cardiac-gated PCMR (cardiac gated: 20.6 ± 7.6 mL, interleaved real-time: 24.3 ± 9.2 mL, high-spatial resolution: 20.8 ± 7.8 mL), due to the increased spatial resolution. The matching technique is shown to be accurate (truth: 94.6 ± 21.8 , split-acquisition: 95.0 ± 21.9 mL) and quantitative image quality (signal-to-noise ratio, velocity-to-noise ratio and edge sharpness) is acceptable. *Magn Reson Med* 64:1664–1670, 2010. © 2010 Wiley-Liss, Inc.

Key words: phase-contrast; real-time imaging; flow quantification

Phase-contrast magnetic resonance (PCMR) is a proven method of measuring blood flow in the clinical environment (1). Traditionally, PCMR data is acquired using cardiac-gated sequences. However, these sequences are time consuming and difficult to perform in patients with irregular heart rates. An alternative approach is real-time PCMR, which can be performed quickly, during free breathing and in patients with irregular heart rates. To ensure adequate temporal resolution, these real-time PCMR sequences often use EPI (2,3) or spiral trajectories (4–7), as well as *k*-space under-sampling strategies, e.g., SENSE (3,6–9).

However, a more fundamental problem with PCMR is the need to acquire two phase images to produce a single PC flow image. This limits the available spatial or temporal resolution, which is particularly problematic for real-time imaging. In children with congenital heart disease, high-resolution imaging is necessary to ensure accuracy at higher heart rates and in smaller vessels. Thus, real-time imaging is not commonly used in this population. Nevertheless, fast, free breathing acquisitions are still desirable as they could significantly improve patient compliance.

Reference-less PCMR sequences that use a single flow-encoded data set to measure flow have been investigated (10–12). In these studies, background phase offsets are predicted by fitting a low-order model through the phase of static tissue surrounding the vessel of interest. Unfortunately, these methods do not perform well for intra-thoracic vessels due to the lack of stationary, surrounding tissue.

In this article, an alternative split-acquisition real-time CINE approach is considered. Flow-encoded and flow-compensated data are acquired continuously at high-temporal resolution (HTR) in separate short blocks. By comparing magnitude images, the closest flow-compensated frame in the cardio-respiratory cycle is determined for each flow-encoded frame. These matched flow-compensated frames are used to subtract out background phase offsets from the flow-encoded phase data. Thus, the data is acquired in real-time but with the background phase correction originating from a different heart beat. This effectively doubles the frame rate compared with conventional interleaved real-time PCMR, allowing either higher temporal or spatial resolution.

The aims of this article are: (i) to validate the split-acquisition real-time CINE PCMR sequence against both conventional interleaved real-time PCMR and cardiac-gated PCMR in an adult population as well as (ii) to demonstrate the utility of split-acquisition real-time CINE PCMR in a pediatric population.

MATERIALS AND METHODS

Proposed Split-Acquisition Technique

Accurate phase subtraction relies on correct spatial alignment (matching in the cardio-respiratory cycle) of flow-compensated and flow-encoded data. The proposed split-acquisition strategy relies on the fact that the cardiac and respiratory cycles have different frequencies. Thus, data from adjacent R-R intervals is likely to be in similar positions in the respiratory cycle. This means that flow-compensated and flow-encoded data can be acquired continuously in consecutive short blocks and

¹Centre for Medical Image Computing, UCL Department of Medical Physics and Bioengineering, London, United Kingdom.

²Centre for Cardiovascular MR, UCL Institute of Child Health, London, United Kingdom.

Grant sponsor: UK EPSRC.

*Correspondence to: Vivek Muthurangu, MD, Cardiovascular Unit, Great Ormond Street Hospital, Great Ormond St., London WC1N 3JH, United Kingdom. E-mail: v.muthurangu@ich.ucl.ac.uk

Received 24 March 2010; revised 28 July 2010; accepted 30 July 2010.

DOI 10.1002/mrm.22615

Published online 11 October 2010 in Wiley Online Library (wileyonlinelibrary.com).

© 2010 Wiley-Liss, Inc.

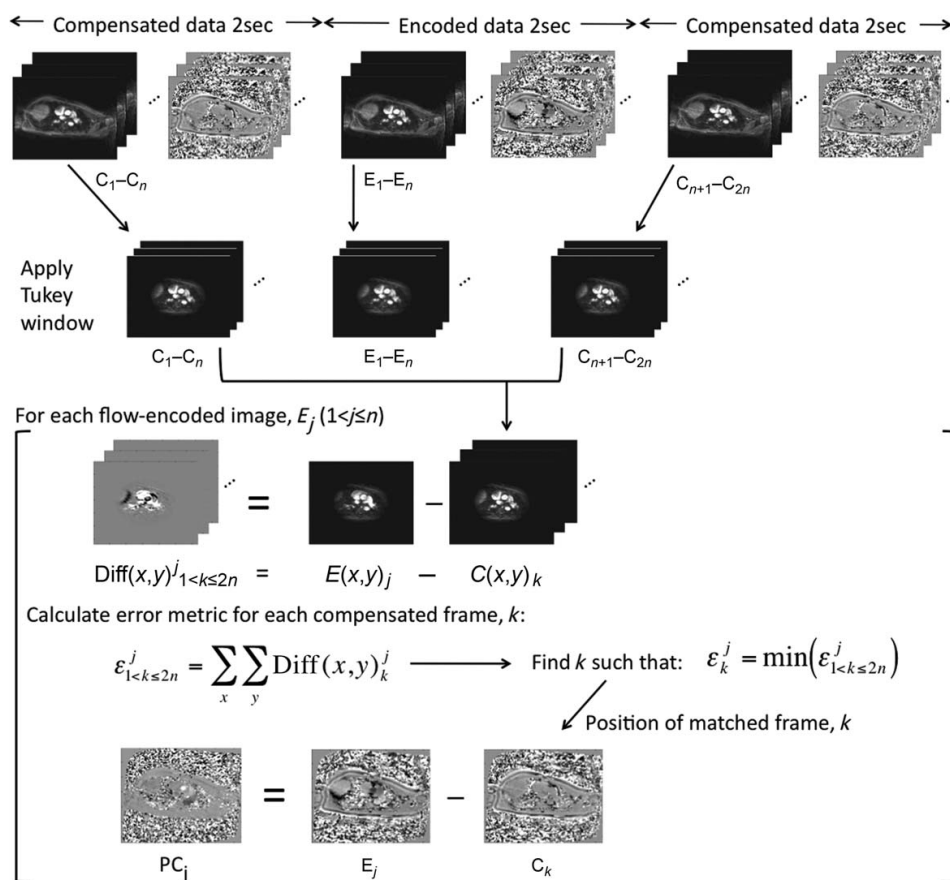


FIG. 1. Pipeline of data acquisition and reconstruction for the proposed split-acquisition real-time CINE PCMR technique.

still be matched in the cardio-respiratory cycle. The split-acquisition sequence used in this study was divided into three blocks of two seconds each (compensated—encoded—compensated) to ensure that at least one whole cardiac cycle was captured in each block. Two flow-compensated blocks were used to increase the likelihood of at least one flow-compensated measurement being acquired at a similar point in the respiratory cycle to each flow-encoded measurement. Before matching, an adapted 2D Tukey window was applied to all magnitude images to attenuate signal at the edge of the image. Each windowed flow-encoded frame was then matched to a windowed flow-compensated frame from either of the two blocks, using the following scheme (Fig. 1):

1. Pixel-wise subtraction of the flow-encoded frame (windowed magnitude reconstruction) from every flow-compensated frame (windowed magnitude reconstruction, from both blocks) to produce a set of difference images.
2. A matching error metric (ϵ) was calculated by summing all the absolute pixel values in each difference image.
3. Identification of the “matched” flow-compensated frame that is associated with the lowest ϵ value.

4. Phase subtraction of the flow-encoded frame with its matched flow-compensated frame to remove background phase offsets and produce the final PC image.

A similar global minimum, matching technique has previously been shown to be accurate for tracking of catheters using magnetic resonance imaging data (13).

Study Population

This study consisted of two parts: an adult validation study and a pediatric study to demonstrate the utility of the split-acquisition sequence. The adult population consisted of 15 healthy volunteers (seven male, eight female: median age 39.8: range 25.2–57.9 years), and five patients with congenital heart disease (one male, four female: median age 23.4: range 15.2–37.7 years). The pediatric population consisted of six patients with congenital heart disease (three male, three female: median age 4.8: range 0.2–8.3 years). Exclusion criteria were: (i) aortic regurgitation, (ii) aortic surgery, (iii) contraindications for MR such as MR-incompatible implants, or (iv) pregnancy. The local research ethics committee approved the

Table 1
Adult Study—Sequence Parameters and Flow Volumes for all Four Sequences Tested

	Cardiac-gated PCMR	Standard real-time PCMR	HTR split-acquisition PCMR	HSR split-acquisition PCMR
TE/TR	2.7/7.0 msec	1.9/7.3 msec	1.9/7.3 msec	1.9/6.3 msec
Spiral readouts	—	12	12	24
Acceleration factor	—	4	4	4
Matrix size	256 × 192	128 × 128	128 × 128	192 × 192
FOV	~320 mm	500 mm	500 mm	500 mm
Rectangular FOV	75%	100%	100%	100%
Slice thickness	6 mm	6 mm	6 mm	6 mm
Flip angle	30°	25°	25°	25°
Pixel bandwidth	390 Hz/pixel	1860 Hz/pixel	1860 Hz/pixel	1860 Hz/pixel
VENC	180 cm/sec	180 cm/sec	180 cm/sec	180 cm/sec
NSAs	3	—	—	—
Total scan duration	~2.5 min	6 sec	6 sec	6 sec
Voxel size	1.3 × 1.3 mm	3.9 × 3.9 mm	3.9 × 3.9 mm	2.6 × 2.6 mm
Temporal resolution	30 msec	44 msec	22 msec	38 msec
Stroke volume (mL)	95.2 ± 20.0	96.2 ± 20.7	95.6 ± 20.1	95.5 ± 20.4
Bias ^a (mL)	—	1.0	0.4	0.3
Limits of agreement ^a (mL)	—	-2.2 to 4.1	-3.9 to 4.7	-3.2 to 3.7
Correlation coefficient ^a (<i>r</i>)	—	0.998	0.994	0.997

^aCalculated with cardiac-gated PCMR sequence.

study and written consent was obtained from all volunteers and patients/guardians.

MR Protocol

All imaging was performed on a 1.5 T MR scanner (Avanto, Siemens Medical Solutions, Erlangen, Germany) using 2 three-element spine coils and 2 three-element body-matrix coils. All reconstructions were performed online in the Siemens reconstruction environment (ICE VB15, two AMD Opteron processors, clockspeed: 3.2 GHz, cache: 6 MB). The imaging plane for aortic flow assessment was located in the ascending aorta as it passes the bifurcation of the pulmonary arteries. In the adult study, flow was measured using four sequences: (i) cardiac-gated PCMR, (ii) interleaved spiral real-time PCMR, (iii) split-acquisition real-time CINE PCMR with a HTR; 22 msec (spatial resolution; 3.9 mm × 3.9 mm), and (iv) split-acquisition real-time CINE PCMR with a higher spatial resolution (HSR); 2.6 mm × 2.6 mm (temporal resolution; 38 msec). In the pediatric study, flow was measured with three sequences: (i) cardiac-gated PCMR, (ii) interleaved spiral real-time PCMR, and (iii) split-acquisition real-time CINE PCMR with a HSR; ~1.9 mm × 1.9 mm (temporal resolution; ~43 msec). All imaging was performed without breath-holds.

Cardiac-gated PCMR was performed using a retrospectively gated, velocity-encoded, Cartesian, gradient echo sequence (parameters shown in Tables 1 and 2). This sequence has been validated in many previous studies against the stop-watch cylinder method of measuring flow (14,15). Thus, flow measurements made using this sequence were considered to be the reference standard.

Interleaved spiral real-time (Standard real-time) PCMR was performed using a uniform density spiral PC sequence with 12 readouts, undersampled by a factor of four (parameters shown in Tables 1 and 2). The flow-compensated and flow-encoded data were interleaved in

their acquisition. The sampling pattern was rotated for each frame so that four consecutive phase-contrast frames comprised a fully sampled *k*-space with 12 spiral readouts. This undersampled data was reconstructed online using an iterative SENSE algorithm (16). All coil sensitivity and regularization information required for the reconstruction process was calculated from the sum-of-squares of the coil data over all flow-compensated time frames. To accurately reconstruct undersampled spiral data, the field of view must be larger than the object. Maxwell correction was performed to remove the effects of concomitant gradients, originating from the flow encoding gradients (17). This sequence has been validated previously (7). Magnitude and phase images for the uncombined flow-compensated and flow-encoded data were output, along with the combined PC data. Six seconds of real-time data was acquired to perform the “accuracy of matching” experiment detailed below.

Split-acquisition real-time CINE PCMR was carried out using the same sequence as the standard real-time PCMR sequence, except that flow-compensated and flow-encoded data were split into separate blocks, as described above. In the adult study, two split-acquisition real-time CINE flow assessments were carried out: one with a HTR and the second with a HSR (parameters shown in Table 1). In the pediatric study, a HSR split-acquisition real-time CINE sequence was used (parameters shown in Table 2).

Data Analysis and Image Quality Assessment

All images were processed using in-house plug-ins for the open-source software OsiriX (the OsiriX Foundation, Geneva, Switzerland). All results are expressed as the mean ± standard deviation (SD), and for adult study, the data is combined for the volunteers and patients. Comparison of means was performed by using repeated measures ANOVA tests with Bonferroni correction for

Table 2
Pediatric Study—Sequence Parameters and Flow Volumes for all Three Sequences Tested

	Cardiac-gated PCMR	Standard real-time PCMR	HSR split-acquisition PCMR
TE/TR	~2.5/7.0 msec	2.1/~7.7 msec	2.1/~7.1 msec
FOV	~250 mm	~350 mm	~350 mm
VENC	~210 cm/sec	~210 cm/sec	~210 cm/sec
Total scan duration	~2.5 min	6 sec	6 sec
Voxel size	~1.0 mm × 1.0 mm × 5.0 mm	~2.8 mm × 2.8 mm × 5.0 mm	~1.9 mm × 1.9 mm × 5.0 mm
Temporal resolution	~32 msec	~46 msec	~43 msec
Stroke volume (mL)	20.6 ± 7.6	24.3 ± 9.2 ^b	20.8 ± 7.8
Bias ^a (mL)	—	3.7	0.3
Limits of agreement ^a (mL)	—	−0.2 to 7.6	−2.1 to 2.7
Correlation coefficient ^a (<i>r</i>)	—	0.990	0.995

^aCalculated with cardiac-gated PCMR sequence.

^bValue is significantly different from cardiac-gated PCMR ($P < 0.05$).

multiple comparisons. All statistical analysis was performed using GraphPad Prism (GraphPad Software Inc., San Diego, CA).

For each aortic stroke volume measurement, the aorta was manually segmented using the modulus images. Bland-Altman analysis was performed to give measurements of agreement with the cardiac-gated flow sequence (18). Additionally, the correlation coefficients were calculated.

Image quality was assessed using measures of signal-to-noise ratio (SNR), velocity-to-noise ratio (VNR), and edge sharpness. True quantification of SNR and VNR in images acquired using non-Cartesian parallel imaging is nontrivial due to the uneven distribution of noise (19,20). Therefore, in this study, noise in the signal intensity (σ_S) was estimated from a region of interest placed in approximately stationary tissue as close to the vessel of interest as possible. For each pixel within the region of interest, the SD of the magnitude data was calculated over all measurements and the average σ_S over all pixels was determined. An estimate of SNR was then calculated by dividing the mean pixel intensity inside the vessel of interest (during peak systole) by the estimated signal noise (19).

Similarly, an estimate of VNR was calculated by dividing the mean velocity inside the vessel of interest (during peak systole) by an estimate of velocity noise (σ_V). The estimated velocity noise was calculated from the same region of interest as used above to select stationary tissue. For each pixel within the region of interest, the SD of the phase data was calculated over all measurements and averaged over all pixels to provide a velocity noise SD σ_V (11).

A quantitative edge sharpness measure was calculated by measuring the maximum relative gradient of pixel intensities across the border of the vessel of interest (20). Sharp edges in the images are represented by a high gradient of the pixel intensities. To prevent noise providing artificially high gradients, the pixel intensities were fitted to a fifth-order polynomial before differentiation (20). In all adult subjects, edge sharpness was measured in two consecutive frames during peak systole and an average used in the analysis.

Adult Study

Three experiments were carried out within the adult study: (i) to assess the accuracy of the matching tech-

nique, (ii) to compare image quality between the sequences, and (iii) to validate the split-acquisition technique.

The purpose of the “accuracy of matching” experiment was to test the assertion that data from adjacent blocks could be matched with sufficient precision to accurately calculate flow. This was achieved by reconstructing the standard real-time PCMR data in two ways. The first reconstruction (“conventional” reconstruction) used interleaved flow-encoded and flow-compensated images for subtraction and production of the final phase image. For the second reconstruction (“simulated split-acquisition” reconstruction), the real-time PCMR data was divided into three blocks (of two seconds each). Only the flow-compensated data was used from the first and third blocks, whereas only flow-encoded data was used from the second block. The “simulated split-acquisition” data then underwent the matching process described above. Flow measurements from the same data using the two reconstruction methods were then compared in all adult subjects.

Image quality was compared between all sequences using measures of SNR, VNR, and edge sharpness, as described above.

The split-acquisition sequences were validated in vivo, by calculating the aortic stroke volume for each of the four sequences described above. The stroke volumes calculated from each of the real-time sequences were compared with those from the gold-standard cardiac-gated flow sequence.

Pediatric Study

To demonstrate the need for higher spatial and temporal resolution in the pediatric population, aortic stroke volumes were compared between cardiac-gated PCMR, standard real-time PCMR, and HSR split-acquisition PCMR.

RESULTS

Reconstruction for each standard real-time PCMR sequence and each split-acquisition sequence took ~5 min, within the Siemens reconstruction environment. For the split-acquisition reconstructions, ~90% of the total reconstruction time was taken by the non-Cartesian parallel imaging reconstruction, and ~2% of the time taken by the matching algorithm.

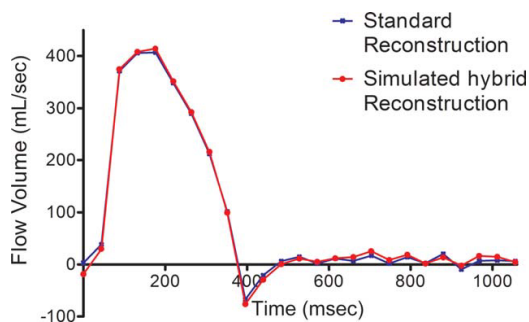


FIG. 2. Comparison of flow profiles from one interleaved real-time PCMR adult patient data set, reconstructed using the “conventional” and “simulated split-acquisition” reconstruction methods. [Color figure can be viewed in the online issue, which is available at wileyonlinelibrary.com.]

Adult Study

Mean aortic stroke volumes assessed using the “conventional” reconstruction method and the “simulated split-acquisition” reconstruction method were 94.6 ± 21.8 mL vs. 95.0 ± 21.9 mL ($r = 0.996$, $P < 0.0001$), respectively. From Bland-Altman assessment, the bias was 0.5 mL with limits of agreement of -3.3 to 4.3 mL. Figure 2 shows comparable flow profiles obtained using the two reconstruction methods.

Figure 3 shows examples of the image quality from all four tested sequences. No residual aliasing artifacts were seen over the vessel of interest, in any standard real-time

PCMR images or split-acquisition PCMR images. Some image blurring was observed (see Fig. 3), and this was attributed to the sensitivity of the spiral trajectories to off-resonance effects and small k -space trajectory errors.

Quantitative image quality metrics can be seen in Table 3. The cardiac-gated PCMR images had the highest estimated SNR in adults, compared with both standard and split-acquisition real-time CINE PCMR data. The HSR split-acquisition images had the lowest estimated SNR and VNR. Estimated velocity noise and VNR were not significantly different in the other three sequences.

Edge sharpness was significantly greater in the cardiac-gated PCMR images compared with all of the real-time images (Table 3). However, the cardiac-gated sequence had the highest SD over all adults. The standard real-time and HTR split-acquisition images had very similar edge sharpness measures. The HSR split-acquisition images had slightly higher edge sharpness than the other real-time images, although this was not found to be statistically significant. A visual improvement in the edge sharpness for this HSR proposed sequence can be seen in Fig. 3, making segmentation of the images easier.

To validate the split-acquisition technique, the average stroke volumes for all sequences were calculated and Bland-Altman assessment was carried out—these results can be found in Table 1. An excellent agreement in stroke volumes between all sequences was found, with no statistical differences between any of the sequences. A slight overestimation was found in all real-time sequences; however, this was not a clinically significant difference. Comparable flow profiles for all sequences can be seen in Figure 4. The average heart rate for all adults was 69 beats per minute.

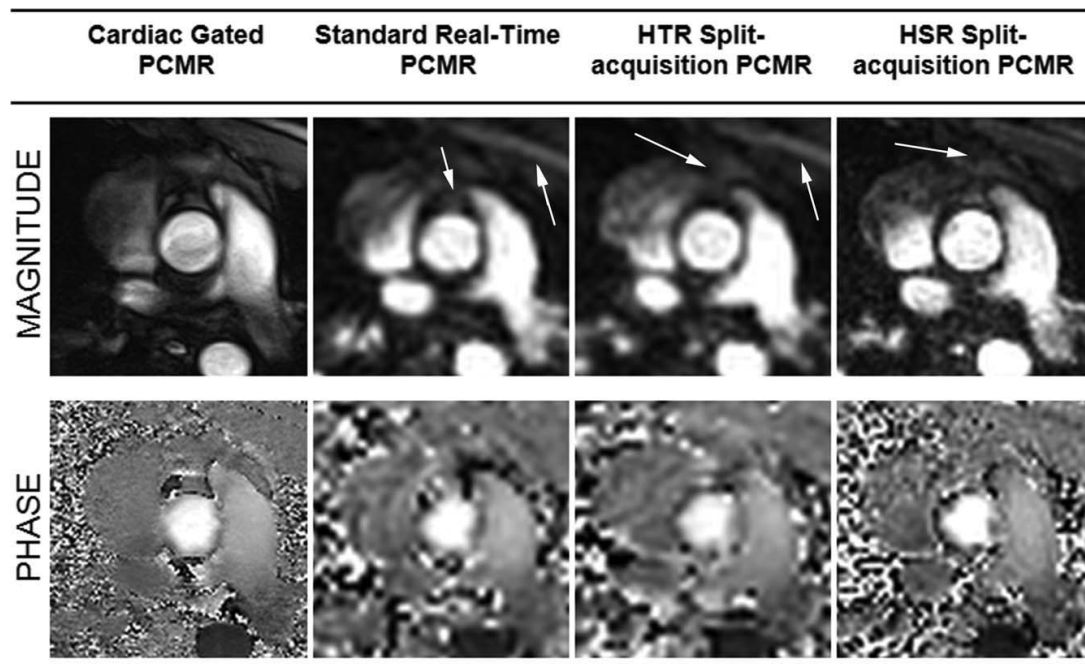


FIG. 3. Comparison of image quality from the sequences. Arrows indicate image blurring.

Table 3
Adult Study—Estimated SNR, VNR, and Edge Sharpness Measures for All Four Sequences

	Cardiac-gated PCMR	Standard real-time PCMR	HTR split-acquisition PCMR	HSR split-acquisition PCMR
Estimated signal variation: σ_S	4.5 ± 1.1	5.6 ± 1.2^a	6.0 ± 1.6^a	6.3 ± 1.1^a
σ_S/σ_S^{PC}	1	1.3 ± 0.4	1.4 ± 0.5	1.5 ± 0.5
Estimated SNR	50.3 ± 16.1	34.5 ± 10.9^a	32.5 ± 10.9^a	28.8 ± 8.1^a
Estimated velocity variation: σ_V (cm/sec)	5.8 ± 1.9	5.5 ± 2.1	5.2 ± 1.8	$7.3 \pm 2.0^{a,b}$
σ_V/σ_V^{PC}	1	0.96 ± 0.16	0.92 ± 0.22	1.31 ± 0.24
Estimated VNR	14.9 ± 9.0	15.7 ± 9.0	16.3 ± 11.0	$11.2 \pm 5.1^{a,b}$
Edge sharpness (mm^{-1})	0.97 ± 0.50	0.43 ± 0.21^a	0.46 ± 0.21^a	0.58 ± 0.26^a

^aValues are significantly different from cardiac-gated PCMR ($P < 0.05$).

^bValues are significantly different from standard real-time PCMR ($P < 0.05$).

Pediatric Study

The average stroke volumes and Bland-Altman assessment from the pediatric study can be seen in Table 2. There was excellent agreement in stroke volumes between the gold-standard cardiac-gated PCMR sequence and the split-acquisition real-time CINE PCMR sequence in the pediatric study, with no statistical differences between these two sequences. The standard real-time sequence overestimated the stroke volume when compared to the cardiac-gated PCMR sequence. The average heart rate for all children was 87 beats per minute.

DISCUSSION

We have demonstrated the feasibility and accuracy of a novel split-acquisition real-time CINE PCMR sequence. Unlike standard real-time PCMR, flow-compensated and flow-encoded data are acquired in separate short blocks and retrospectively matched in the cardio-respiratory cycle. The resulting sequence has the benefit of an effective doubling of the temporal resolution or an increase in the spatial resolution when compared with standard interleaved, real-time PCMR.

The reliability of matching was assessed in adults by comparing both “conventional” and “simulated split-acquisition” reconstructions of the same real-time PCMR data. The excellent agreement in stroke volumes and flow curves, supports the assumption that it is possible to remove background phase offsets using matched data acquired in separate blocks.

Although, matching in the cardiac cycle could be performed using an electrocardiograph signal (4,21,22), image subtraction allows matching in both the cardiac and respiratory cycles in one step (13). This is not only more efficient but also obviates the need for electrocardiograph monitoring, which is in keeping with a philosophy of more simple magnetic resonance imaging (23). Alternatively, data from different blocks could be matched using image-based navigators along with motion correction, which has previously been demonstrated in retrospective enhanced real-time imaging (24).

Real-time imaging often trades image quality for speed of acquisition (9). It was observed that in adults the real-time sequences all had significantly lower estimated SNR and edge sharpness than the cardiac-gated sequence. Nevertheless, the estimated VNR in adults was not significantly different ($P > 0.05$) between the HTR split-acquisition sequence and cardiac-gated sequence. The similar

SNR, VNR, and edge sharpness between the standard real-time and HTR split-acquisition images in adults suggests that image quality is not seriously affected by matching data from different R-R intervals. The lower SNR and VNR seen in the HSR split-acquisition images are to be expected, given the smaller pixel dimensions.

In adults, there was good agreement between stroke volumes measured using the four different sequences. Importantly, this was true in patients and volunteers, suggesting that matching also works in subjects with less regular respiratory patterns. In gated PCMR, variations in stroke volume from breathing are averaged out; however, when analyzing the real-time stroke volumes, a single flow cycle was chosen for comparison. This may explain some of the differences in flow volumes found between the real-time techniques and the gated technique. In children, standard real-time PCMR was found to overestimate stroke volume, probably due to inadequate spatial resolution. However, there was excellent agreement between the cardiac-gated PCMR sequence and the split-acquisition real-time CINE sequence that had a HSR.

Currently, cardiac-gated PCMR is considered the reference standard method of measuring flow in vivo. It has been validated in numerous studies (13,14,24), and due to the high spatial and temporal resolution, it is accurate in the pediatric population. However, it is time consuming as it is usually acquired with several signal averages to compensate for respiratory motion. Breath-hold, cardiac-gated PCMR is commonly used; however, for adequate spatial and temporal resolution, the breath-hold time is long. This is problematic when imaging children with congenital heart disease as they are often unable to

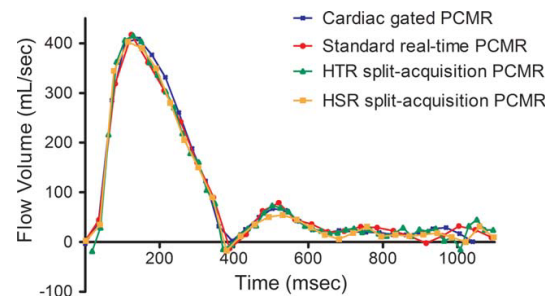


FIG. 4. Comparison of flow profiles from all four sequences for one adult volunteer.

perform long breath holds. Another approach is real-time PCMR, which can be acquired during free breathing in a relatively short length of time. However, as shown in this study, the lower spatial and temporal resolution of standard real-time imaging reduces its accuracy in the pediatric population. The split-acquisition PCMR technique described has all the benefits of standard real-time PCMR, but with improved spatial or temporal resolution. Thus, the split-acquisition technique is accurate even in children and it may be of particular use in the assessment of pediatric heart disease.

Limitations

This study has shown that split-acquisition real-time CINE PCMR technique is accurate in a population of 15 volunteers and 11 patients. Further work is needed to validate this technique in a larger patient population. In particular, the split-acquisition sequence needs to be tested in patients with irregular breathing patterns. Irregular patterns might make it more difficult to match data from different blocks in cardio-respiratory space and may reduce the accuracy of the technique.

In this initial feasibility study, the split-acquisition technique was only tested in the aorta, as flow quantification has been well validated using magnetic resonance imaging in this vessel. One advantage of this technique over other real-time techniques may be its ability to measure flow in smaller vessels, as a HSR can be achieved. Further work is required to test this technique in other smaller vessels.

In the future, it may be advantageous to interleave many blocks of flow-compensated and flow-encoded data. This was not carried out in this study due to the long reconstruction times, of ~5 min per measurement. These long reconstruction times are a drawback, as although the data is acquired in real-time, the images cannot be viewed in real-time. Reconstruction times could be improved by the use of newer multiprocessor graphics cards (25,26), which are well suited to complex iterative reconstruction. This may also allow more complex matching techniques, which may involve some image registration

CONCLUSIONS

In conclusion, we have demonstrated the accuracy and reliability of a novel split-acquisition phase-contrast MR technique in both adults and children. The technique divides the acquisition of flow-compensated and flow-encoded data into separate blocks, and performs automatic matching of this data in cardio-respiratory space. This allows an increase in the temporal or spatial resolution of real-time phase-contrast MR. Split-acquisition PCMR opens up the possibility of real-time scanning of smaller vessels, in patients with higher heart rates, which will be useful in the assessment of congenital heart disease.

REFERENCES

- Beerbaum P, Korperich H, Barth P, Esdorn H, Gieseke J, Meyer H. Noninvasive quantification of left-to-right shunt in pediatric patients: phase-contrast cine magnetic resonance imaging compared with invasive oximetry. *Circulation* 2001;103:2476–2482.
- Klein C, Schalla S, Schnackenburg B, Bornstedt A, Fleck E, Nagel E. Magnetic resonance flow measurements in real time: comparison with a standard gradient-echo technique. *J Magn Reson Imaging* 2001;14:306–310.
- Korperich H, Gieseke J, Barth P, Hoogeveen R, Esdorn H, Peterschroder A, Meyer H, Beerbaum P. Flow volume and shunt quantification in pediatric congenital heart disease by real-time magnetic resonance velocity mapping: a validation study. *Circulation* 2004;109:1987–1993.
- Gatehouse PD, Firmin DN, Collins S, Longmore DB. Real time blood flow imaging by spiral scan phase velocity mapping. *Magn Reson Med* 1994;31:504–512.
- Nayak KS, Pauly JM, Kerr AB, Hu BS, Nishimura DG. Real-time color flow MRI. *Magn Reson Med* 2000;43:251–258.
- Nezafat R, Kellman P, Derbyshire JA, McVeigh ER. Real time high spatial-temporal resolution flow imaging with spiral MRI using auto-calibrated SENSE. In: *Engineering in Medicine and Biology Society, 2004. IEMBS '04 26th Annual International Conference of the IEEE*; 2004. Vol. 1, pp 1914–1917.
- Steeden JA, Atkinson D, Taylor AM, Muthurangu V. Assessing vascular response to exercise using a combination of real-time spiral phase contrast MR and noninvasive blood pressure measurements. *J Magn Reson Imaging* 2010;31:997–1003.
- Thunberg P, Karlsson M, Wigström L. Accuracy and reproducibility in phase contrast imaging using SENSE. *Magn Reson Med* 2003;50:1061–1068.
- Beerbaum P, Körperich H, Gieseke J, Barth P, Peuster M, Meyer H. Blood flow quantification in adults by phase-contrast MRI combined with SENSE—a validation study. *J Cardiovasc Magn Reson* 2005;7:361–369.
- Man L-C, Pauly JM, Nishimura DG, Macovski A. Nonsubtractive spiral phase contrast velocity imaging. *Magn Reson Med* 1999;42:704–713.
- Nielsen J-F, Nayak KS. Referenceless phase velocity mapping using balanced SSFP. *Magn Reson Med* 2009;61:1096–1102.
- Rieke V, Vigen KK, Sommer G, Daniel BL, Pauly JM, Butts K. Referenceless PRF shift thermometry. *Magn Reson Med* 2004;51:1223–1231.
- Bakker CJG, Seppenwoolde J-H, Bartels LW, van der Weide R. Adaptive subtraction as an aid in MR-guided placement of catheters and guidewires. *J Magn Reson Imaging* 2004;20:470–474.
- Muthurangu V, Taylor A, Andriantsimiavona R, Hegde S, Miquel ME, Tulloh R, Baker E, Hill DLG, Razavi RS. Novel method of quantifying pulmonary vascular resistance by use of simultaneous invasive pressure monitoring and phase-contrast magnetic resonance flow. *Circulation* 2004;110:826–834.
- Lee VS, Spritzer CE, Carroll BA, Pool LG, Bernstein MA, Heine SK, MacFall JR. Flow quantification using fast cine phase-contrast MR imaging, conventional cine phase-contrast MR imaging, and Doppler sonography: in vitro and in vivo validation. *Am J Roentgenol* 1997;169:1125–1131.
- Pruessmann KP, Weiger M, Bornert P, Boesiger P. Advances in sensitivity encoding with arbitrary k-space trajectories. *Magn Reson Med* 2001;46:638–651.
- Bernstein MA, Zhou XJ, Polzin JA, King KF, Ganin A, Pelc NJ, Glover GH. Concomitant gradient terms in phase contrast MR: analysis and correction. *Magn Reson Med* 1998;39:300–308.
- Bland JM, Altman DG. Statistical methods for assessing agreement between two methods of clinical measurement. *Lancet* 1986;i:307–310.
- Dietrich O, Raya JG, Reeder SB, Reiser MF, Schoenberg SO. Measurement of signal-to-noise ratios in MR images: influence of multichannel coils, parallel imaging, and reconstruction filters. *J Magn Reson Imaging* 2007;26:375–385.
- Muthurangu V, Lurz P, Critchely J, Deanfield J, Taylor A, Hansen MS. Real-time assessment of right and left ventricular volumes and function in patients with congenital heart disease by using high spatiotemporal resolution radial k-t SENSE. *Radiology* 2008;248:782–791.
- Lanzer P, Botvinick E, Schiller N, Crooks L, Arakawa M, Kaufman L, Davis P, Herfkens R, Lipton M, Higgins C. Cardiac imaging using gated magnetic resonance. *Radiology* 1984;150:121–127.
- Nayak KS, Hu BS. Triggered real-time MRI and cardiac applications. *Magn Reson Med* 2003;49:188–192.
- Larson AC, White RD, Laub G, McVeigh ER, Li D, Simonetti OP. Self-gated cardiac cine MRI. *Magn Reson Med* 2004;51:93–102.
- Kellman P, Ched'hotel C, Lorenz CH, Mancini C, Arai AE, McVeigh ER. Fully automatic, retrospective enhancement of real-time acquired cardiac cine MR images using image-based navigators and respiratory motion-corrected averaging. *Magn Reson Med* 2008;59:771–778.
- Hansen MS, Atkinson D, Sorensen TS. Cartesian SENSE and k-t SENSE reconstruction using commodity graphics hardware. *Magn Reson Med* 2008;59:463–468.
- Sorensen TS, Schaeffer T, Noe KO, Hansen MS. Accelerating the nonequispaced fast Fourier transform on commodity graphics hardware. *IEEE Trans Med Imaging* 2008;27:538–547.

APPENDIX 5

J.A. Steeden, D. Atkinson, A.M. Taylor, and V. Muthurangu

Rapid Flow Assessment of Congenital Heart Disease Using High Spatio-Temporal Gated Spiral Phase Contrast MR

Radiology, 2010. In Press.

Rapid Flow Assessment of Congenital Heart Disease Using High Spatio-Temporal Gated Spiral Phase Contrast MR

Jennifer A Steeden^{1,2}, MEng, David Atkinson¹, PhD, Michael S Hansen^{2,3},
PhD, Andrew M Taylor², MD, Vivek Muthurangu², MD

¹ Centre for Medical Image Computing, UCL Department of Medical Physics & Bioengineering, London, UK. WC1E 6BT

² Centre for Cardiovascular MR, UCL Institute of Child Health, London, UK. WC1N 1EH

³ National Institutes of Health, NHLBI, Bethesda, MD 20814

Manuscript type: Original research

Advances in Knowledge:

- High spatio-temporal resolution phase contrast MRI is achievable using spiral fast trajectories and sensitivity encoding (SENSE) acceleration.
- Breath-hold times can be significantly reduced, compared to standard Cartesian, breath-hold phase contrast MRI.
- Measurement of stroke volumes, pulmonary-to-systemic flow ratio (Q_p/Q_s) and ratio of right-to-left pulmonary artery flow (RPA/LPA) are more accurate with spiral breath-hold PCMR imaging, compared to standard Cartesian, breath-hold PCMR imaging.
-

Implications for Patient Care:

- In subjects who are unable to perform long breath-holds, spiral, sensitivity encoding (SENSE), phase contrast (PC), MR may be used to significantly decrease breath-hold time.
- Spiral SENSE PCMR could significantly reduce total scan time in patients with congenital heart disease, without compromising accuracy of the flow assessment.

ABSTRACT

Purpose: The aim of this paper was to compare flow volumes and image quality measured using: a) reference free-breathing, retrospectively cardiac-gated, Cartesian, phase-contrast magnetic resonance imaging (PCMR), b) standard breath-hold, retrospectively cardiac-gated, Cartesian, PCMR, and c) prospectively cardiac-triggered, spiral, sensitivity encoding (SENSE), breath-hold PCMR.

Materials and Methods: The local research ethics committee approved this study and written consent was obtained from all patients. Stroke volume, regurgitation fraction, Q_p/Q_s and RPA/LPA ratios were quantified using the three sequences from 40 patients with congenital heart disease. These functional parameters were compared using repeated-measures ANOVA tests, Bland-Altman analysis and correlation coefficients. Signal-to-noise ratio (SNR), velocity-to-noise ratio (VNR) and edge sharpness were also compared using repeated-measures ANOVA tests.

Results: Scan time was significantly reduced for the breath-hold spiral PCMR sequence, compared to the standard breath-hold PCMR sequence (~5 vs. ~18 seconds, respectively). There was an excellent agreement in stroke volume, Q_p/Q_s and RPA/LPA ratios between all sequences, however the spiral breath-hold sequence was found to be superior to the standard breath-hold sequence in terms of limits of agreement and correlation. There was a small but statistically significant underestimation of regurgitation fraction using the spiral sequence. SNR and VNR were lower for the spiral breath-hold sequence compared with the standard breath-hold sequence, however the edge sharpness was greater for the spiral breath-hold sequence.

Conclusion: Flow volumes can be accurately and reliably quantified using a spiral SENSE PCMR sequence, with high spatio-temporal resolution in a short breath-hold.

INTRODUCTION

Cardiac gated phase-contrast magnetic resonance (PCMR) is a proven method of measuring blood flow in the clinical environment (1-3). It is particularly useful in patients with congenital heart disease (4), where flow assessment often guides clinical decision-making.

PCMR is intrinsically slow because each line in k -space must be acquired twice (with different velocity-encodings) in order to perform background phase subtraction. Unfortunately, this prolongs acquisition time and prevents high spatio-temporal resolution PCMR from being performed in a breath-hold. Hence, gated PCMR often relies on multiple signal averages to compensate for respiratory motion. This results in scan times of approximately 2 minutes and thus in congenital heart disease, complete flow assessment can take up to 10 minutes. If spatio-temporal resolution is lowered, gated PCMR can be performed in a breath-hold (5). However, in children with congenital heart disease, high resolution is necessary to assess smaller vessels at higher heart rates. Furthermore, the breath-hold times are often too long (>15seconds) for children or sick adults. Thus, in the congenital population there is a need for a high spatio-temporal resolution gated PCMR sequence that can be performed within a short breath-hold.

One possible method of achieving this is to use efficient spiral trajectories. Furthermore, spiral trajectories can be combined with parallel imaging techniques, such as sensitivity encoding (SENSE), to further accelerate acquisition (6-9). Using both these techniques, it is possible to perform real-time PCMR (6, 10-12). Unfortunately, real-time PCMR comes at the cost of low spatio-temporal resolution and is not well suited to the pediatric population. Nevertheless, cardiac gated, spiral PCMR, accelerated with parallel imaging should provide the necessary high resolution, in a short breath-hold.

The aim of this paper is to validate a prospectively-triggered, spiral PCMR sequence accelerated with SENSE, in a population of children and adults with

congenital heart disease. This has been achieved by comparing image quality and flow volumes measured using: a) breath-hold spiral SENSE PCMR, b) standard breath-hold Cartesian PCMR and c) reference free-breathing PCMR.

MATERIALS AND METHODS

Patient population

In July and August 2010, 40 consecutive children and adults (22 male, 18 female) referred for cardiac MR imaging, were enrolled in this study. The median age was 21.4 ± 13.8 years (range: 3.0 to 61.3 years, 17 of whom were less than 16 years old). Diagnosis; repaired tetralogy of Fallot/ pulmonary atresia with ventricular septal defect - 15, coarctation of the Aorta - 7, cardiomyopathy exam - 6, pulmonary stenosis - 4, transposition of the great arteries repair - 2, atrial septal defect - 2, dilated aortic root - 2, left pulmonary artery stenosis - 1, and bicuspid aortic valve - 1. Of these, 5 children were imaged whilst under general anesthetic. The sample size was chosen to detect a mean difference in stroke volumes of 2 mL (means and standard-deviation assumed from literature values (5)), with a statistical power of 80% and a P-value of .05. This analysis was performed using open-source software (G*power 3; University of Dusseldorf, Dusseldorf, Germany) (13) which gave an estimated sample size of 36 (which was increased to 40 for this study).

Inclusion criteria were: a) clinical referral for cardiac MR imaging. Exclusion criteria were: a) contraindications for MR such as MR-incompatible implants, b) pregnancy, or c) irregular heart rate. The local research ethics committee approved the study and written consent was obtained from all subjects/guardians.

MR protocol

Imaging was performed on a 1.5T MR scanner (Avanto, Siemens Medical Solutions, Erlangen, Germany) using two spine coils and one body-matrix coil (giving a total of 12 coil elements). A vector electrocardiographic (ECG) system was used for cardiac gating.

All patients underwent a standard clinical cardiac MR examination for diagnostic purposes. Flow imaging was performed in the following vessels as per clinical need, with stented vessels excluded:

- Ascending aorta, AAO (N=40, including 4 with regurgitation)
- Main pulmonary artery, MPA (N=38, including 12 with regurgitation)
- Right pulmonary artery, RPA (N=22, including 10 with regurgitation)
- Left pulmonary artery, LPA (N=24, including 14 with regurgitation)

Flow assessment was performed in each vessel using three sequences (parameters shown in *Table 2*), before moving to the next vessel.

Reference free-breathing sequence – The reference standard was a retrospectively-gated, free-breathing, Cartesian, gradient echo PCMR sequence (provided by the manufacturer). Respiratory motion was compensated by the acquisition of three signal averages (NSA). This sequence had high spatial and temporal resolution (*Table 2*) and is well-validated *in-vitro* and *in-vivo* (2, 14-17).

Standard breath-hold sequence – The standard breath-hold sequence was a retrospectively-gated, Cartesian PCMR sequence (provided by the manufacturer). This sequence was the same as the free-breathing flow sequence described above. However, in order to acquire the data within a breath-hold, spatio-temporal resolution was lowered (*Table 2*).

Spiral SENSE breath-hold sequence – The spiral sequence was a prospectively-triggered, segmented PCMR sequence, which was developed in-house to provide high spatio-temporal resolution imaging in a short breath-hold. A uniform density spiral trajectory was used, with 36 spiral interleaves,

undersampled by a factor of three (so only 12 spiral interleaves were acquired for each cardiac phase). Two spiral interleaves were acquired per RR-interval, meaning that six RR-intervals were used to acquire all of the data. One additional RR-interval was required at the beginning of the scan to reach a steady state. The sampling pattern was rotated for each cardiac phase so that three consecutive cardiac phases comprised a fully-sampled k-space with 36 spiral readouts.

This data was reconstructed online using an iterative SENSE algorithm (18). The coil-sensitivity information was calculated from the time-averaged (flow-compensated) data from each coil, divided by the sum-of-squares of the time-averaged coil data (12).

The field-of-view (FOV) was not optimized for children, as this would have resulted in a reduction in temporal resolution.

Table 2: Imaging parameters

	Free-Breathing PCMR	Standard Breath- hold PCMR	Spiral Breath- hold PCMR
TE/TR (ms)	~2.2 / 7.0	~2.2 / 7.0	2.1 / 8.0
Spiral Readouts	-	-	36
Acceleration factor	2 (GRAPPA)	2 (GRAPPA)	3 (SENSE)
Matrix Size	256 x 192	192 x 113	256 x 256
FOV (mm)	200 - 400	290 - 400	400
Rectangular FOV (%)	75	66	100
Readouts per segment	3	4	2
Slice Thickness (mm)	5	5	5
Flip Angle	30°	30°	25°
Pixel bandwidth (Hz/pixel)	543	543	1220
VENC (cm/s)	180 - 400	180 - 400	180 - 400
NSAs	3	1	1
Total Scan Duration (s)	44 - 144	11 - 24	3 - 8
Voxel Size (mm)	~ 0.8 – 1.5	~ 1.5 – 2.1	1.6
Temporal resolution	~ 30.0 ms	~ 40.0 ms	32.0 ms

Functional assessment

All images were processed using the open-source software OsiriX (the OsiriX Foundation, Geneva, Switzerland). For each flow measurement, the vessel-of-interest (VOI) was segmented using the modulus images. Segmentations were propagated using a semi-automatic technique.

In the prospectively-triggered spiral PCMR sequence, the acquisition window was automatically calculated from the average RR-interval, minus two-times the standard-deviation of the RR-interval. This meant that data was not acquired in ~80 ms at the very end of diastole. The missing flow data was predicted by performing a linear interpolation between the last calculated point and the first point, so that the flow profile filled the entire RR-interval. This is not important in patients with normal flow profiles, however is important in patients with regurgitant flow during diastole.

For each flow measurement the stroke volume (net forward flow) and regurgitation fraction were calculated. Additionally, where flow was measured in both the MPA and AAO (N=38), the Q_P/Q_S ratio was calculated, and where flow was measured in both the pulmonary branch vessels (N=20), the RPA/LPA ratio was calculated.

In 10 randomly selected patients, the AAO flow data was reanalyzed for all three sequences (JAS – 3 years experience) to determine intra-observer variability. This data was also analyzed by a second operator (VM – 8 years experience) to determine inter-observer variability.

Image quality analysis

Image quality was assessed for all three sequences using measures of signal-to-noise ratio (SNR), velocity-to-noise ratio (VNR) and edge sharpness. All image quality analysis was carried out using in-house plug-ins for OsiriX.

True quantification of SNR and VNR in images acquired using non-Cartesian parallel imaging is non-trivial in the clinical environment, due to the uneven

distribution of noise (19-21). Therefore, in this study estimated signal-noise (σ_S) and velocity-noise (σ_V) were calculated in the same way as (22) and (21). In summary, a region-of-interest (ROI) was drawn in stationary tissue, and estimated noise was calculated as the average standard-deviation of the pixel intensity (σ_S) or velocity (σ_V) through all cardiac phases. σ_S was calculated after correcting for exponential signal decay, from a non-steady state, in all images. Final estimates of SNR were made from the corrected mean signal intensity, and VNR from the mean velocity, within a ROI drawn in the vessel during peak systole, divided by σ_S or σ_V , respectively.

A quantitative edge sharpness value was calculated by measuring the maximum gradient of the normalized pixel intensities across the border of the VOI (20, 22). To reduce noise providing artificially high gradients (representing sharp edges), the pixel intensities were filtered using a Savitzky–Golay filter (23) (window size: 6, polynomial order: 3) prior to differentiation. Edge sharpness was calculated for all cardiac phases, and the average value was used for comparison.

Statistical analysis

All statistical analysis was performed using GraphPad Prism (GraphPad Software Inc., San Diego, CA). The results were combined for all subjects, and were expressed as the mean \pm standard-deviation. Comparison of means was performed by using repeated-measures ANOVA tests, with Bonferroni correction for multiple comparisons. A P-value of less than .05 indicated a significant difference. Bland-Altman analysis was performed to give measures of agreement with the free-breathing PCMR sequence (24). Additionally, the correlation coefficients were calculated.

RESULTS

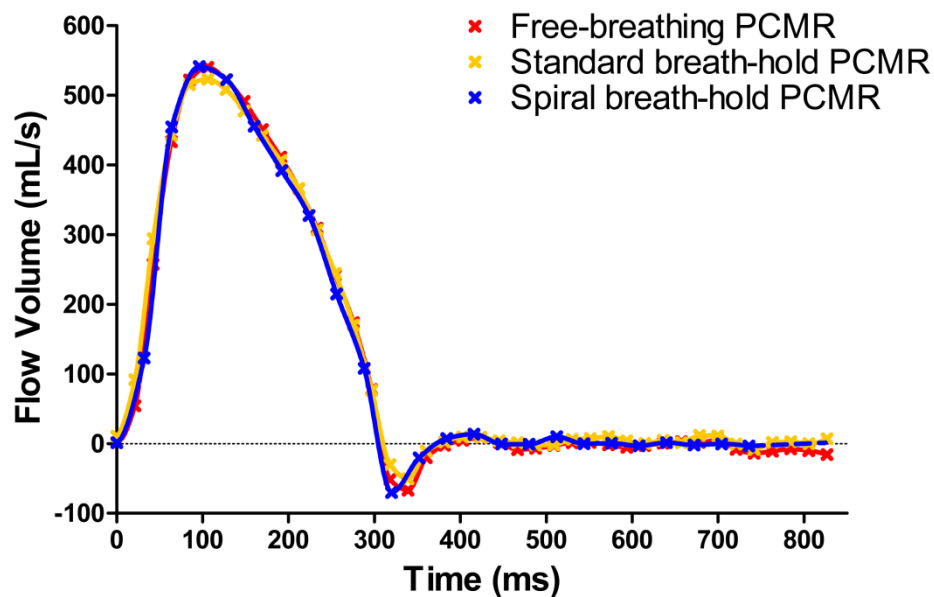
The average heart rate was 76 ± 12 beats per minute (range: 50 to 111 bpm). For the reference free-breathing sequence, data was acquired over 108 heartbeats, which was 91 ± 17 seconds (range: 44 to 144 seconds). In the standard breath-hold sequence, data was acquired over 18 heartbeats, which

was 16 ± 3 seconds (range: 11 to 24 seconds). For the spiral breath-hold sequence, data was acquired over 7 heartbeats, which was 5 ± 1 seconds (range: 3 to 8 seconds).

Functional assessment

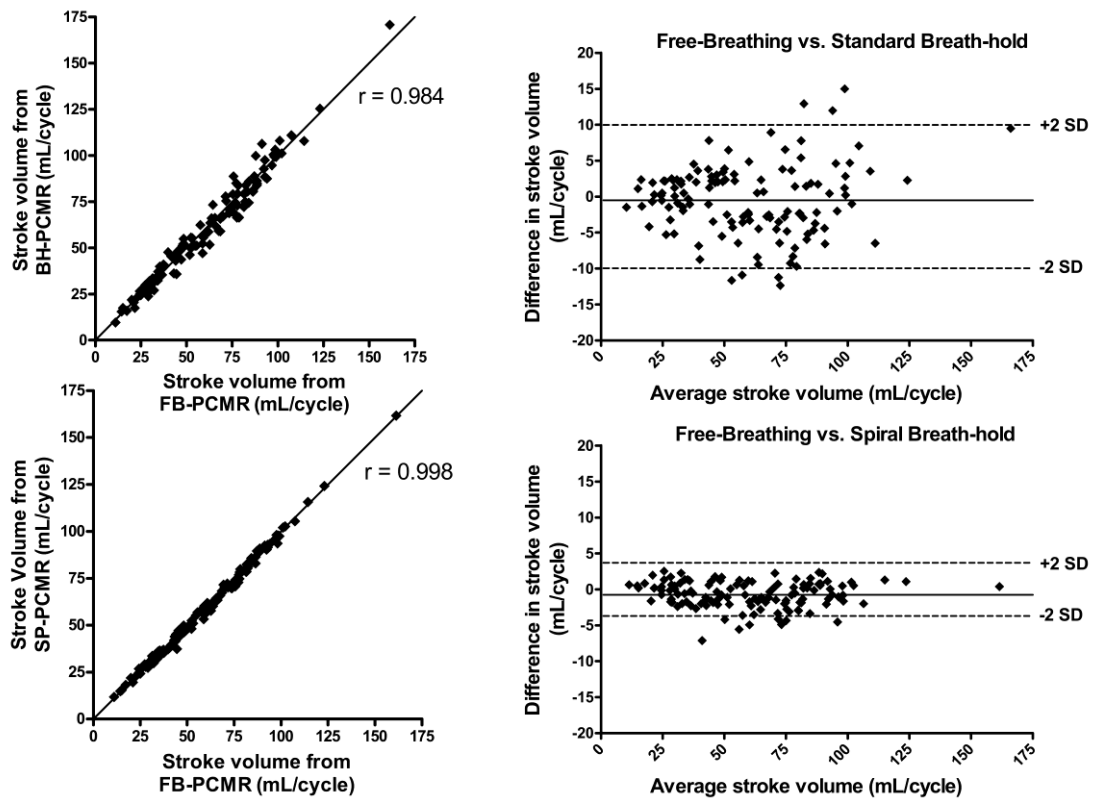
Good agreement was seen throughout the cardiac cycle for all sequences, as can be seen in *Figure 6*.

Figure 6: Comparison of flow profiles from all three sequences for the AAO of one patient



Combining all vessels ($N=124$), there were no statistical differences in mean stroke volume calculated from the reference free-breathing sequence (60.3 ± 27.3 mL), the standard breath-hold sequence (59.8 ± 27.6 mL) and the spiral breath-hold sequence (59.5 ± 27.1 mL). Bland-Altman analyses comparing the breath-hold sequences to the reference free-breathing sequence are shown in *Figure 7*. There was no clinically significant bias using either breath-hold sequence (spiral breath-hold: -0.7 mL, standard breath-hold: -0.5 mL). However, the limits of agreement were smaller and the correlation better for the spiral breath-hold compared to the standard breath-hold sequence (-4.4 to 2.9 mL vs. -10.3 to 9.3 mL, $r = 0.984$ vs. $r = 0.998$, respectively).

Figure 7: Comparisons of stroke volumes in all vessels between free-breathing PCMR (FB-PCMR) and standard breath-hold PCMR (BH-PCMR) (top), and between free-breathing PCMR and spiral breath-hold PCMR (SP-PCMR) (bottom). Scatter plots shown on the left and associated Bland-Altman analysis shown on the right.



Separate mean stroke volumes, Bland-Altman analysis and correlations for the AAO, MPA and branch pulmonary arteries are shown in *Table 3*. There were no statistically significant differences in stroke volumes calculated between any of the sequences. Bland-Altman analysis found only a small bias in stroke volume between the free-breathing and both the breath-hold sequences. For all vessels, limits of agreement were smaller and the correlation was greater for spiral breath-hold acquisition, compared to the standard breath-hold acquisition.

Table 3: Comparison of Stroke volumes calculated from the three sequences

	Free-Breathing PCMR	Standard Breath- hold PCMR	Spiral Breath- hold PCMR
AORTA			
Stroke Volume (ml)	68.6 ± 19.6	67.3 ± 19.6	67.7 ± 19.9
Bias* (ml)	-	-1.3	-0.9
Limits of agreement* (ml)	-	-11.1 to 8.5	-4.6 to 2.8
Correlation coefficient* (r)	-	0.968	0.996
MPA			
Stroke Volume (ml)	76.6 ± 27.6	76.2 ± 29.1	75.9 ± 27.7
Bias* (ml)	-	-0.5	-0.8
Limits of agreement* (ml)	-	-13.1 to 12.1	-4.4 to 2.8
Correlation coefficient* (r)	-	0.976	0.998
PULMONARY BRANCHES			
Stroke Volume (ml)	39.5 ± 18.5	39.7 ± 19.2	38.9 ± 18.1
Bias* (ml)	-	0.2	-0.6
Limits of agreement* (ml)	-	-6.5 to 6.8	-4.2 to 3.1
Correlation coefficient* (r)	-	0.985	0.995

* Compared to free-breathing PCMR sequence

Regurgitant flow was found in 40 vessels (see Table 4.8). For free-breathing vs. standard breath-hold PCMR there was no significant difference in regurgitation. However, a small but statistically significant difference was found between the free-breathing and spiral breath-hold PCMR sequences. Despite this, the correlation coefficient was found to be higher and limits of agreement to be lower with the spiral breath-hold acquisition, compared to the standard breath-hold acquisition.

Q_p/Q_s and RPA/LPA ratios were calculated where possible (see Table 4.8). No significant differences were found between any of the sequences. Bland-Altman analysis found a slightly lower bias, and smaller limits of agreement with the spiral breath-hold acquisition compared to the standard breath-hold acquisition.

Table 4: Comparison of regurgitation, Q_p/Q_s and RPA/LPA calculated from the three sequences

	Free-Breathing PCMR	Standard Breath- hold PCMR	Spiral Breath- hold PCMR
REGURGITATION (N=40)			
Regurgitation fraction (%)	31.1 ± 14.7	30.0 ± 15.0	29.1 ± 14.2 †
Range (%)	11.16 to 60.8	6.4 to 60.4	8.6 to 55.7
Bias* (%)	-	-1.1	-2.0
Limits of agreement* (%)	-	-8.2 to 5.9	-6.8 to 2.8
Correlation coefficient* (r)	-	0.971	0.986
Q_p/Q_s (N=38)			
Q_p/Q_s ratio	1.13 ± 0.29	1.15 ± 0.34	1.14 ± 0.30
Range	0.81 to 2.64	0.78 to 2.92	0.83 to 2.73
Bias*	-	0.018	0.006
Limits of agreement*	-	-0.23 to 0.27	-0.08 to 0.10
Correlation coefficient* (r)	-	0.933	0.989
RPA/LPA (N=20)			
RPA/LPA ratio	1.44 ± 0.59	1.42 ± 0.65	1.39 ± 0.53
Range	0.55 to 2.78	0.44 to 2.62	0.54 to 2.70
Bias*	-	-0.049	-0.050
Limits of agreement*	-	-0.32 to 0.21	-0.22 to 0.12
Correlation coefficient* (r)	-	0.973	0.991

* Compared to free-breathing PCMR sequence

† Value is significantly different from free-breathing PCMR ($p < 0.05$)

For 10 randomly selected subjects, the AAO data from all three sequences was reevaluated by the same observer (JAS). The mean difference in stroke volumes from the free-breathing sequence was 0.5 ± 1.2 % (range: -1.1 to 2.9 %, $P=0.25$), for the standard breath-hold sequence was 0.9 ± 2.4 % (range: -3.6 to 5.6 %, $P=0.20$) and for the spiral breath-hold was -0.3 ± 1.2 % (range:

-2.6 to 1.6 %, P=0.22). There were no statistically significant differences between the repeated measures for any of the sequences.

These data sets were also independently reviewed by a second observer (VM), to assess inter-observer variability. The mean difference in stroke volumes from the free-breathing sequence was 0.1 ± 1.5 % (range: -2.5 to 3.4 %, P=0.75), for the standard breath-hold sequence was 0.7 ± 2.3 % (range: -3.9 to 3.6 %, P=0.40) and for the spiral breath-hold was -0.5 ± 1.5 % (range: -2.7 to 2.5 %, P=0.21). There were no statistically significant differences between the repeated measures for any of the sequences.

Image quality analysis

Figure 8 shows examples of the image quality from all three tested sequences in the AAO and MPA. Quantitative image quality metrics can be seen in Table 4.

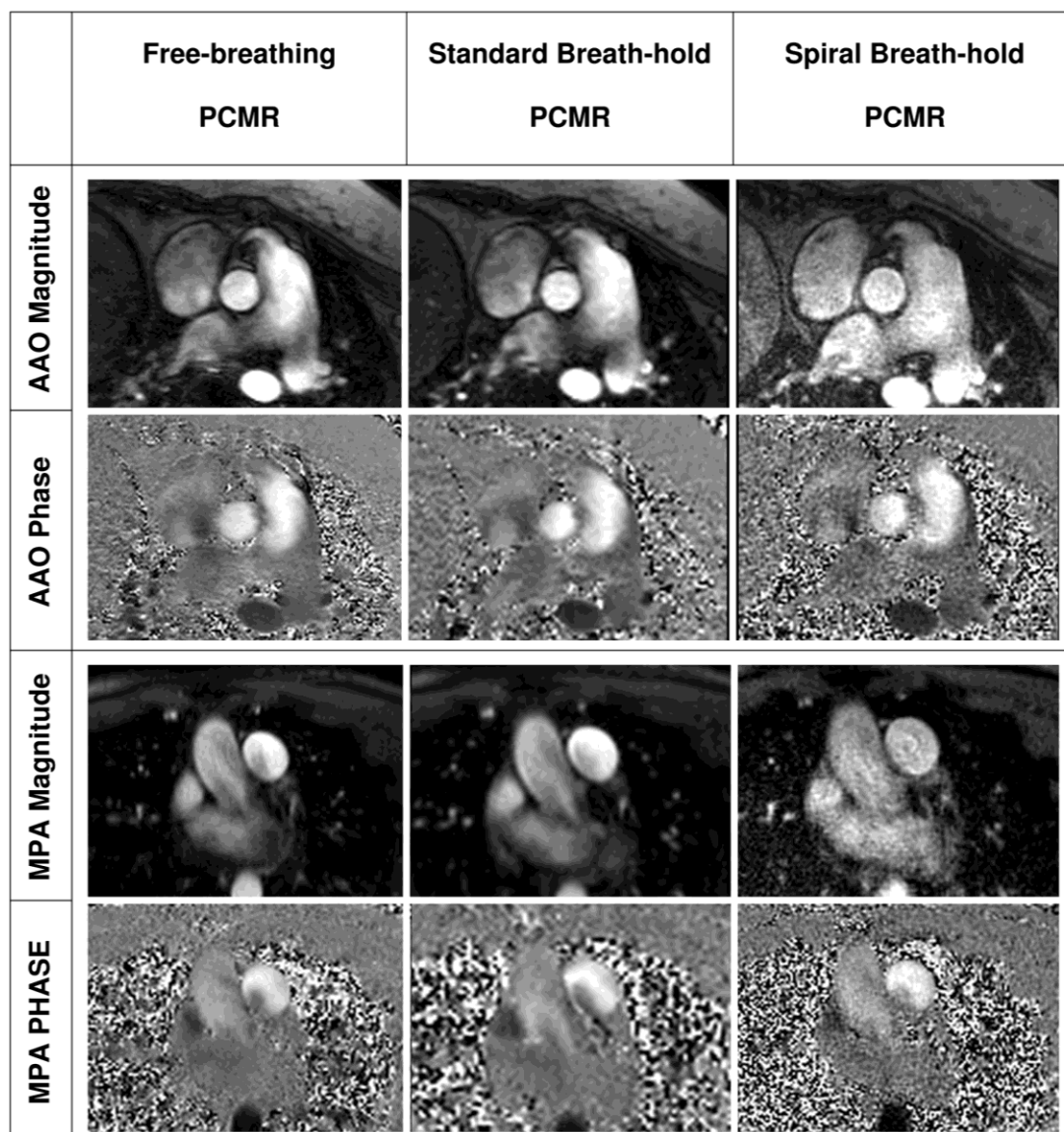
Table 5: Image Quality - estimated SNR, VNR and edge sharpness measures for all sequences

	Free-Breathing PCMR	Standard Breath-hold PCMR	Spiral Breath-hold PCMR
Estimated signal variation: σ_S	5.4 ± 1.4	$5.9 \pm 1.5^\dagger$	$8.6 \pm 2.2^{\dagger\ddagger}$
$\sigma_S / \sigma_S^{\text{Free-breathing}}$	-	1.1 ± 0.3	1.7 ± 0.6
Estimated SNR	45.6 ± 14.9	$41.7 \pm 14.2^\dagger$	$31.9 \pm 11.6^{\dagger\ddagger}$
Estimated velocity variation: σ_V (cm/s)	17.6 ± 9.1	$19.5 \pm 10.5^\dagger$	$19.7 \pm 7.7^\dagger$
$\sigma_V / \sigma_V^{\text{Free-breathing}}$	-	1.1 ± 0.4	1.2 ± 0.4
Estimated VNR	8.4 ± 4.8	$7.4 \pm 3.9^\dagger$	$6.7 \pm 3.1^{\dagger\ddagger}$
Edge Sharpness (mm^{-1})	0.78 ± 0.36	0.74 ± 0.34	0.78 ± 0.35

[†] Value is significantly different from free-breathing PCMR (p<0.05)

[‡] Value is significantly different from standard breath-hold PCMR (p<0.05)

Figure 8: Examples of image quality from the three sequences



The free-breathing PCMR images had the highest estimated SNR and VNR compared to both of the breath-hold PCMR sequences ($p < 0.05$). The spiral breath-hold PCMR images had the lowest estimated SNR and VNR compared to the free-breathing and standard breath-hold PCMR images ($p < 0.05$).

Edge sharpness was not significantly different between any of the sequences (Table 5). However, the free-breathing PCMR images and the spiral breath-hold PCMR images had the same average edge sharpness, whereas the edge sharpness was slightly lower in the standard breath-hold PCMR images.

DISCUSSION

We have demonstrated that it is possible to use a prospectively-triggered, undersampled spiral PCMR sequence with a SENSE reconstruction algorithm to accurately and reliably measure flow within a short breath-hold. Currently, the reference standard method of measuring flow in patients with congenital heart disease is high spatio-temporal resolution, free-breathing, cardiac gated PCMR. Unfortunately, due to multiple signal averaging, each flow assessment can take more than 2 minutes to perform. Thus in congenital cardiac MR, where between 4 and 8 separate flow assessments are necessary, flow imaging can take a significant proportion of the total scan time. The spiral breath-hold sequence used in this study should be able to reduce the total duration of flow imaging from an average of 10 minutes, to less than 1 minute. This would lead to a marked reduction in total scan time and has implications for patient throughput and compliance for congenital cardiac MR scanning.

Spiral SENSE PCMR

Achieving high spatio-temporal resolution PCMR in a short breath-hold requires efficient filling of k -space. In this study, spiral trajectories were used to significantly speed up acquisition time. Imaging was further accelerated with non-Cartesian SENSE. The resultant sequence had a breath-hold time of ~5 seconds, compared to ~16 seconds for a standard Cartesian breath-hold PCMR sequence. Furthermore, unlike the standard breath-hold sequence, spatio-temporal resolution was not compromised in order to achieve the short breath-hold. This makes this spiral sequence extremely useful in both children and sick adults who are unable to perform long breath-holds. There are some disadvantages to spiral trajectories and parallel imaging, including off resonance effects and trajectories errors, as well as reduced signal-to-noise. However, these were not seen to affect the accuracy of the spiral PCMR sequence in this study.

Comparison of sequences

For stroke volumes, Q_P/Q_S and RPA/LPA ratios, there was an excellent agreement between the spiral breath-hold sequence and the reference free-breathing sequence. Furthermore, the spiral breath-hold sequence was found to be superior to the standard breath-hold sequence in terms of limits of agreement and correlation. This is most likely to be due to the higher temporal and spatial resolution of the spiral breath-hold sequence. It may also be attributed to the shorter breath-hold times, which may prevent residual breathing, as well as limiting heart rate variability during the scan. In addition the intra-observer and inter-observer variability seen in the spiral breath-hold PCMR sequence was good.

There was, however, a small, but statistically significant difference in the regurgitation fractions calculated from the free-breathing PCMR sequence and the spiral breath-hold sequence. This was probably due to the interpolation of the flow curve at the very end of diastole to in the prospectively triggered spiral sequence. However, it should be noted that the difference in regurgitant fraction was on average only 2% and this would not be considered clinically important.

Image quality

The edge sharpness of the spiral breath-hold sequence was found to be similar to the free-breathing sequence, and higher than the standard breath-hold sequence. This is most likely due to the lower spatial resolution of the standard breath-hold PCMR sequence. The good edge sharpness of the spiral breath-hold sequence may have benefits in terms of either manual or automatic segmentation of the vessels compared to standard breath-hold sequences.

However, the spiral breath-hold sequence had a lower estimated SNR and VNR than the free-breathing and standard breath-hold sequences. This is due to: i) the higher acceleration factor used compared to the other two sequences, ii) the much higher bandwidth used compared to the other two sequences, iii) no use of signal averages (unlike the free-breathing PCMR

sequence), and iv) the higher spatial resolution compared to the standard breath-hold sequence.

Limitations

The main limitation of using an undersampled spiral trajectory is the need for a large FOV, in order to prevent wrapping of signal and ensure accurate reconstruction of the undersampled data. As we do not use a selective excitation, it is necessary for the FOV to be larger than the object being scanned. In the future, the FOV could be reduced by the use of improved coil configurations, or RF-shielding of the arms and torso. Additionally, a spatially-selective RF pulse, or saturation bands could be used, however these would increase the scan time, or reduce the temporal resolution.

As seen from the image quality analysis, the spiral breath-hold PCMR sequence has a significantly lower SNR and VNR than the standard breath-hold PCMR sequence, or the free-breathing sequence. Although this is a limitation of the sequence it did not affect the accuracy of the stroke volume measurements made in this study.

CONCLUSION

Currently, MR flow assessment can take more than 10 minutes in patients with congenital heart disease. Thus it often represents almost 25% of total scan time. Using the spiral breath-hold sequence validated in this study, all flow imaging could be performed in less than 1 minute. This would significantly reduce total scan time without compromising the accuracy of the flow assessment. The benefits of this would be twofold. Firstly, in the pediatric population a shorter total scan time would be less demanding on the patients and improve compliance. Secondly, shorter scan times should improve patient throughput. Therefore, we believe that this sequence is has significant benefits in congenital CMR.

REFERENCES

1. Firmin DN, Nayler GL, Klipstein RH, Underwood SR, Rees RSO, Longmore DB. In Vivo Validation of MR Velocity Imaging. *Journal of Computer Assisted Tomography*. 1987;11(5):751-6.
2. Beerbaum P, Korperich H, Barth P, Esdorn H, Gieseke J, Meyer H. Noninvasive Quantification of Left-to-Right Shunt in Pediatric Patients : Phase-Contrast Cine Magnetic Resonance Imaging Compared With Invasive Oximetry. *Circulation*. 2001;103(20):2476-82.
3. Van Rossum AC, Visser FC, Peels KH, Valk J, Roos JP. An in vivo validation of quantitative blood flow imaging in arteries and veins using magnetic resonance phase-shift techniques. *European Heart Journal*. 1991;12(2):117.
4. Rees S, Firmin D, Mohiaddin R, Underwood R, Longmore D. Application of flow measurements by magnetic resonance velocity mapping to congenital heart disease. *The American Journal of Cardiology*. 1989;64(14):953-6.
5. Sakuma H, Kawada N, Kubo H, et al. Effect of breath holding on blood flow measurement using fast velocity encoded cine MRI. *Magnetic Resonance in Medicine*. 2001;45(2):346-8.
6. Steeden JA, Atkinson D, Taylor AM, Muthurangu V. Assessing vascular response to exercise using a combination of real-time spiral phase contrast MR and noninvasive blood pressure measurements. *Journal of Magnetic Resonance Imaging*. 2010;31(4):997-1003.
7. Nezafat R, Kellman P, Derbyshire A, McVeigh E, R. . Real-time blood flow imaging using autocalibrated spiral sensitivity encoding. *Magnetic Resonance in Medicine*. 2005;54(6):1557-61.
8. Nayak KS, Pauly JM, Kerr AB, Hu BS, Nishimura DG. Real-time color flow MRI. *Magnetic Resonance in Medicine*. 2000;43(2):251-8.
9. Qian Y, Zhang Z, Stenger VA, Wang Y. Self-calibrated spiral SENSE. *Magnetic Resonance in Medicine*. 2004;52(3):688-92.
10. Gatehouse PD, Firmin DN, Collins S, Longmore DB. Real time blood flow imaging by spiral scan phase velocity mapping. *Magnetic Resonance in Medicine*. 1994;31(5):504-12.
11. Korperich H, Gieseke J, Barth P, et al. Flow Volume and Shunt Quantification in Pediatric Congenital Heart Disease by Real-Time Magnetic Resonance Velocity Mapping: A Validation Study. *Circulation*. 2004;109(16):1987-93.
12. Nezafat R, Kellman P, Derbyshire JA, McVeigh ER. Real Time High Spatial-Temporal Resolution Flow Imaging with Spiral MRI using Auto-Calibrated SENSE.

- Engineering in Medicine and Biology Society, 2004 IEMBS '04 26th Annual International Conference of the IEEE. 2004;1:1914-7.
13. Faul F, Erdfelder E, Lang A-G, Buchner A. G*power 3: A flexible statistical power analysis program for the social, behavioral, and biomedical sciences. *Behavior Research Methods*. 2007;39(2):175-91.
 14. Powell AJ, Maier SE, Chung T, Geva T. Phase-Velocity Cine Magnetic Resonance Imaging Measurement of Pulsatile Blood Flow in Children and Young Adults: In Vitro and In Vivo Validation. *Pediatric Cardiology*. 2000;21(2):104-10.
 15. Evans AJ, Iwai F, Grist TA, et al. Magnetic Resonance Imaging of Blood Flow with a Phase Subtraction Technique: In Vitro and In Vivo Validation. *Investigative Radiology*. 1993;28(2):109-15.
 16. Frayne R, Steinman DA, Rutt BK, Ethier CR. Accuracy of MR phase contrast velocity measurements for unsteady flow. *JOURNAL OF MAGNETIC RESONANCE IMAGING*. 1995;5(4):428-31.
 17. Meier D, Maier S, Bösiger P. Quantitative flow measurements on phantoms and on blood vessels with MR. *Magnetic Resonance in Medicine*. 1988;8(1):25-34.
 18. Pruessmann KP, Weiger Mk, Bornert P, Boesiger P. Advances in sensitivity encoding with arbitrary k-space trajectories. *Magnetic Resonance in Medicine*. 2001;46(4):638-51.
 19. Dietrich O, Raya JG, Reeder SB, Reiser MF, Schoenberg SO. Measurement of signal-to-noise ratios in MR images: Influence of multichannel coils, parallel imaging, and reconstruction filters. *Journal of Magnetic Resonance Imaging*. 2007;26(2):375-85.
 20. Muthurangu V, Lurz P, Critchely J, Deanfield J, Taylor A, Hansen MS. Real-time Assessment of Right and Left Ventricular Volumes and Function in Patients with Congenital Heart Disease by Using High Spatiotemporal Resolution Radial k-t SENSE. *Radiology*. 2008;248(3):782-91.
 21. Nielsen J-F, Nayak KS. Referenceless phase velocity mapping using balanced SSFP. *Magnetic Resonance in Medicine*. 2009;61(5):1096-102.
 22. Steeden JA, Atkinson D, Taylor AM, Muthurangu V. Split-Acquisition Real-time CINE Phase-Contrast MR Flow Measurements *Magnetic Resonance Imaging*. 2010;In press.
 23. Savitzky A, Golay MJE. Smoothing and Differentiation of Data by Simplified Least Squares Procedures. *Analytical Chemistry*. 1964;36(8):1627-39.
 24. Bland JM, Altman DG. Statistical methods for assessing agreement between two methods of clinical measurement. *Lancet*. 1986;i:307-10.